CONSOLIDATION OF WC-Co NANOCOMPOSITES SYNTHESISED BY MECHANICAL ALLOYING

STEPHEN A. HEWITT BEng

A thesis submitted in partial fulfilment of the
requirements of the University of Wolverhampton
for the degree of Doctor of Philosophy

May 2009

This work or any part thereof has not previously been presented in any form to the University or to any other body whether for the purposes of assessment, publication or for any other purpose (unless otherwise indicated). Save for any express acknowledgements, references and/or bibliographies cited in the work, I confirm that the intellectual content of the work is the result of my own efforts and of no other person.

Signature……

Date…….

Abstract

The influence of mechanical alloying (MA) milling time, temperature, sintering method and microstructure on the mechanical properties of a tungsten carbide-cobalt (WC-Co) hardmetal, based on 10wt% Co, has been established.

The effects of high-energy milling for 30, 60, 180 and 300 min and the interrelation between milling time and powder properties, and the resultant effects on the mechanical properties of the consolidated WC-10Co material, has been obtained for a horizontally designed ball mill. Nanostructured WC-10Co powder was synthesised after 60 min cyclic milling at room temperature with an average WC domain size of 21 nm. In direct comparison, a WC-10Co composition MA at -30°C for 60 min produced an average WC domain size of 26 nm with a higher lattice strain. WC domain size showed a slight increase with milling time, measured at 27 nm after 300 min ball milling. Extended ball milling (300 min) reduced the mean particle size from 0.148 μm for 60 min milling to 0.117 μm. Thermal analysis showed that the onset temperature of the WC-Co eutectic was related to particle size with increased milling time reducing the onset temperature from 1344°C after 60 min milling to 1312°C after 300 min milling. Onset temperature was further reduced by the addition of vanadium carbide (VC), reducing the onset temperature to 1283°C after 300 min milling. Powder contamination increased with increased milling time with Fe content measured at ~ 3wt% after 300 min ball milling. Milling at -30°C reduced Fe contamination to an almost undetectable level. Increased ball milling time resulted in decreased levels of green density with the powders milled

for 30 and 300 min achieving 62.5% and 59.5% TD, respectively. Relative density increased for the powder milled at -30°C compared to the RT milled powder due to its flattened, slightly rounded morphology. A large difference in VC starting particle size compared to WC and Co led to non-uniform dispersion of the inhibitor during milling.

Densification and hardness reached optimum levels for the 60 min milled powder for both pressureless sintering and sinter-HIP. Both properties decreased with increased milling time, regardless of the sintering method. Low temperature milling resulted in a higher hardness value of 1390 HV30 compared to 1326 HV30 for the 60 min, RT milled material after pressureless sintering. Densification levels of the doped materials were restricted to < 90% TD for both sintering methods due to inhomogeneity in the microstructures.

Palmqvist fracture toughness (W_K) of the RT milled powders increased with increased milling time and increasing WC grain size for both sintering methods. W_K reached 11.6 $MN.m^{3/2}$ with 300 min milling after pressureless sintering but reached 16.1 $MN.m^{32}$ for the same material after sinter-HIP due to the effect of mean WC grain size and binder phase mean free path. The -30°C milled powder exhibited higher fracture toughness for both sintering methods than the 60 min, RT milled material.

Spark plasma sintering (SPS) showed that the onset of densification was dependent upon particle size with the powder from 300 min milling showing an onset temperature of ~ 800°C compared to ~ 1000°C for the 60 min milled powder. The low temperature milled powder showed an onset temperature of ~ 980°C, which suggested that low temperature milling provided enhanced densification kinetics.

Table of Contents

4. Experimental procedure

1. Introduction

1.1 Overview

Describing a product invented in the early 1920s, the word hardmetal is a translation of the German "hartmetall," with a very distinct meaning. It defines probably the most important powder metallurgical product of the last century. In most hardmetals, the hard carbide component is tungsten carbide (WC) and the metallic binder is cobalt (Co), exactly the combination invented by Karl Schröter at the Osram Works in Berlin all those many years ago. There are now many other variants, including borides and nitrides, which are seldom employed alone, and silicides very rarely indeed (Brookes 2002). Because the material is sintered, the usual product is alternatively termed "sintered carbide" and, because Co acts as a kind of cement, as "cemented carbide".

Increasing demands for materials that can offer improved properties over traditional materials have led to the design and development of advanced materials. Advanced materials may be defined as those where consideration is firstly given to the systematic synthesis and control of the structure of the materials in order to provide a precisely tailored set of properties for demanding applications (Bloor and Cahn 1994). An emerging and rapidly growing class of materials are the so-called nanostructured materials, which include a further classification of nanocrystalline materials. These materials are assembled from nanometre-sized building blocks that may have incoherent or coherent interfaces depending on the atomic structure, crystallographic orientation,

and the chemical composition of adjacent crystallites. The materials assembled from nanometre-sized building blocks need to be microstructurally heterogeneous, as this is crucial for many of their properties (Gleiter 2000). When the grain size of nanocrystalline materials is below a critical value (~ 10 to 20 nm), then more than 50 vol% of atoms are associated with grain boundaries or interfacial boundaries (Tjong and Chen 2004). The unique properties of these materials can be attributed to two basic phenomena (Yao, Stiglich and Sudarshan 1998): (i) the number of atoms at the surface and/or grain boundaries of these materials is comparable to those located in the crystal lattice, therefore the chemical and physical properties are increasingly dominated by the atoms at these locations; (ii) the 'quantum-size effect' or 'quantum confinement effect'. When particles approach the nanometre size range, their electronic and photonic properties can be significantly modified, as a result of the absence of a few atoms in the lattice and the resulting relaxation of the lattice structure. For example, compared with conventional materials, nanomaterials can offer improved transparency, hydrophobicity, photoluminescence, toughness and hardness, chemical sensing and bioavailability (Lines 2008).

Despite competition from new materials, WC-Co materials remain the material of choice in terms of cost, tool life, and productivity. The development of new hardmetals during the past 10 years has focused strongly on fine, ultra-fine and nanostructured materials. Significant innovations have occurred and the move towards 'nano'-grained hardmetals is attracting ever more attention.

Consumption has increased steadily since the first commercial production of hardmetals in 1926. This growth shows no sign of slowing, and in 2006, hardmetal inserts for the German market showed a 9% increase over 2005, driven by increased vehicle production, and also partly by record levels of machine tool utilisation (Berg 2007).

The range of applications in which hardmetals are used has also continued to grow, driven by competitors' requirements for improved performance. Improved mechanical properties, for example toughness, have enabled hardmetals to compete in applications previously held to be the reserve of other cutting tool materials. A vital requirement is cost effective performance; advanced tools provide longer life or productivity gains by increasing the rate at which workpieces can be processed.

Over the past decade, development, for metal cutting in particular, has concentrated on reducing grain size, with the aim of improving hardness (Fig. 1.1 and Table 1.1), and hence, abrasive wear resistance, in addition to qualities such as surface finish. It is well known that the properties of hardmetals critically depend on the grain size of the microstructure. The finer the grain size then the harder and more wear-resistant the sintered product. Ultra-fine carbide powders, with grain sizes of 0.2-0.5 μm, are now routinely available by a number of processing routes. Finer powders (termed nanosized at <0.2 μm, from criteria developed by the German Fachverband für Pulvermetallurgie) are commercially available and there is now market demand for powders <0.1 mm. As shown in Fig. 1.2, control of grain growth during sintering is an important issue that will become ever more relevant as powder size is reduced. Doping, for example with

vanadium (VC) or chromium carbide (Cr_3C_2), allows fine, uniform structures to be maintained during sintering. Markets for these ultra-fine grained materials include wear parts (low binder contents for increased hardness), microdrills (Fig. 1.1), and knives for paper cutting (a growing market: binder content is increased to 10-16% to increase toughness).

Fig. 1.1 Hardness of WC-Co hardmetals as a function of Co content and WC grain size (Berg 2007).

Table 1.1

Designation and properties of WC-10Co for different WC grain sizes (Richter, Ruthendorf and Drobniewski 1995).

Designation	WC grain size (μm)	Hardness HV_{10} (WC-10Co)
Nano	< 0,2	> 2000
Ultrafine	0,2 – 0,5	1800
Submicron	0,5 – 0,8	1600
Fine	0,8 – 1,3	1400
Medium	1,3 – 2,5	1300
Coarse	2,5 – 6,0	1150
Extracoarse	> 6,0	1000

Fig. 1.2 Micrographs showing WC grain growth in sintered WC-6wt%Co hardmetals (a, b) without carbide dopant and (c, d) with dopant (Berg 2007).

1.2 Statement of research problem

In recent years, ultra-fine grained hardmetals have drawn increasing interest as:

- tools and components made from these alloys are harder and more wear resistant than conventional WC-Co alloys for a given binder content;
- for a given hardness level, these alloys, with higher binder content, should be significantly tougher than their coarser grained counterparts.

The worldwide hardmetals cutting tool industry has approached the problem of higher mechanical properties for their cutting tools by altering composition levels primarily in the direction of increased carbide content (Stiglich, Yu and Sudarshan 1996). However, at the level of 94 to 97 wt% carbides, fracture toughness and strain tolerance fall below acceptable levels, and excessive brittleness results.

One answer to this dilemma is to reduce the average grain size of the hard carbides, thus reducing the mean free path between carbide particles. These superfine-grained WC-Co materials have superior properties, such as hardness and wear resistance, compared to coarser, sub-micron WC-Co materials (Daub *et al*. 1995). This improvement in properties is achieved because the matrix is now exposed to the abrasive/corrosive environment over much smaller dimensions, even though the WC-Co composition has not changed. By means of the particle size reduction process, the fracture toughness and strength can be increased significantly. Nanostructured WC-Co offers hope for a new

generation of hardmetals that have high hardness and high toughness. A comparison of the Vickers hardness of various WC-Co alloys as a function of composition and WC grain size (McCandlish *et al*. 1994) illustrates the potential offered by these new materials, Fig. 1.3. However, despite this potential, the industry has failed to live up to early predictions of widespread use of nanoscale powders. In spite of undoubtedly useful properties, their implementation in press-and-sinter processing remains extremely limited, almost to niche (though important) markets such as tungsten carbide microtools and circuitboard drills. Barriers to their use include powder cost, contamination, handling difficulties, low packing densities and rapid grain growth during sintering.

For a nanosize powder material, the classical powder manufacture and alloy consolidation techniques do not suffice, since uniform phase dispersion is difficult. Therefore, innovative processing techniques are required that can show a substantial cost or performance benefit in order to displace established press-and-sinter processes.

Fig. 1.3 Effect of binder content and WC grain size on Vickers hardness of WC-Co hardmetals (McCandlish *et al*. 1994).

1.3 Technical barrier(s)

A commonly used technique for the production of WC-Co materials is cold compaction followed by sintering. The powder compact is exposed to elevated temperature in order for densification to occur. In theory, pressureless sintering of ultra-fine powder particles is an easy method of preparing nanocrystalline WC-Co materials: one simply packs together the ultra-fine powder and heats it. In practice, however, it is often very difficult to control grain growth, Fig. 1.4, at the same time as attempting to stimulate densification. Further development of nanostructured WC-Co materials is currently

stalled because of a lack of sintering technologies that can produce bulk WC-materials with true nanometre grain sizes.

Fig. 1.4 Grain growth of nanoscale WC during heat-up to conventional sintering temperature for a WC-10wt%Co composition (Wang, Fang and Sohn 2008).

1.4 Project objectives

Considering the challenges outlined above, present work is intended to improve knowledge of the synthesis of nanostructured hardmetals by mechanical alloying (MA) and the consolidation of such materials using conventional and non-conventional techniques in order to minimise WC grain growth whilst promoting densification.

The method for developing the nanostructured hardmetal is a horizontal, high-energy ball milling system, which allows precise control of some of the MA process

variables including milling temperature and atmosphere, and also system specific variables including repetitious, cyclic operation. Consolidation of the synthesised powders is investigated using conventional, cold press and sinter routes and also by a novel processing technique involving an externally applied, pulsed electric current.

Due to the complexity of the MA process and hardmetal sintering, the aim of a reasonably short-term research study cannot fully address all the variables of both processes that have a bearing on the final bulk material. Rather, this work focuses on two of the most crucial variables of MA and characterises their variation on the consolidation processes.

In summary, this thesis has the following objectives:

1. determine the optimum processing parameters and conditions to produce WC-Co nanostructured powders by MA. These parameters include:
   - milling time
   - milling temperature
2. understand the effects on WC grain growth and densification for:
   - time/temperature/pressure sintering relationships
   - grain growth inhibitor (VC)

2. Solid state synthesis of nanostructured WC-Co powder

2.1 Hardmetals

The unique properties accessible for the transition-metal carbides are of great importance for several industrial applications, due to their excellent high temperature strength and good corrosion and fracture resistance, whilst being chemically and thermally very stable even at high temperatures. Among the hard alloys and refractory carbides, hardmetals find a wide range of industrial applications, being used extensively in commercial applications such as tips for cutting and drilling tools, extrusion and pressing dies, and wear-resistant surfaces in many types of machines. Cemented tungsten carbide is a material of worldwide importance and has a world market of close to $9-billion a year (Luyckx 2004).

The constant need for higher productivity and improved financial return across industrial manufacturing has continually spurred the development of tool materials, and hardmetals are no exception. Deeper study of application conditions, wear mechanisms and failure modes of carbide tools became necessary to find ways of improving their performance. In many studies it was found that reducing tungsten carbide (WC) grain size to sub-micron levels yielded significant gains in performance. Of the 38,000 tonnes of hardmetal produced worldwide in 2004, an estimated 40 per cent had submicron WC grain size (Grearson *et al*. 2005). This growth has been driven by developments in user industries such as electronics, precision engineering, micro-machining, and metal

forming that exploit the exceptional properties of these alloys that include wear resistance, strength, stiffness and edge sharpness. The need for hardmetals with improved properties, particularly increased hardness and strength coupled with increased toughness, has focused attention on the development of increasingly finer-grained hardmetals (Lassner and Schubert 1999).

An example of a nanostructured cemented carbide product already on the market is that developed by Sumitomo Electric Hardmetal Corp. and A.L.M.T. Corp. This is an "ultra-super-micrograin cemented carbide", which has a WC particle size of 90 nm (http://www.sei.co.jp/sn/2004/321/2a.html). The product has been given the name "XF1", and was developed using a technique of direct carbonisation of WO_3, in order to satisfy the requirements (breakage resistance, wear resistance) for micro-diameter printed circuit board (PCB) drills having a diameter of 0.05-0.2 mm.

2.2 Mechanical alloying (MA)

Synthesis and assembly strategies of nanopowders involve precursors from the solid, liquid, or gaseous state. The more conventional solid-state synthesis or "top-down" approach is to bring the solid precursors into close contact through controlled, mechanical attrition and to subsequently heat treat this mixture at high temperatures to facilitate diffusion of atoms or ions. To release the potential of these materials, cost effective preparation and retention of the nanostructure into bulk materials remains a key challenge. MA of powder particles has been developed as a versatile alternative to

other processing routes in preparing nanostructured materials with a broad range of chemical composition and atomic structure. Although there are numerous techniques to produce nanostructured materials, MA has become a popular method to fabricate nanocrystalline materials due to its simplicity, relatively inexpensive equipment and its potential for large-scale production (El-Eskandarany 1998; Koch 1997).

However, this process is considered by some companies to be a high cost powder manufacturing route and consolidation of MA powders can be difficult due to the high surface area from reduced particle size and entrapped gases. Additionally ball-milled powders may cause substantial grain growth during high temperature consolidation because of high interfacial energies. However, synthesis methods using the "bottom up" approach require alternative and much more expensive techniques, such as gas-phase synthesis and spray conversion processing.

2.2.1 Mechanism of grain size reduction by MA

Comminution or multiple rupture of the particles resulting in a reduction of their size and the simultaneous increase in the specific surface area, and the formation of structural defects during milling, are just some of the examples of the numerous phenomena that occur as a result of high-energy ball impacts.

The MA process was developed in 1966 at the International Nickel Company (INCO) as part of a program to produce a material combining oxide dispersion strengthening with gamma prime precipitation hardening in a nickel-based superalloy intended for gas

turbine applications. The pioneering work of Benjamin (1970) led to the evolution of MA as a solid state processing route that, for example, enabled previously unobtainable alloys of complex, oxide dispersion-strengthened (ODS) materials to be produced.

The principle of the technique is that powders are continually welded and fractured by the action of the milling medium, to produce a homogeneous, finely dispersed, composite powder. The MA process of this brittle-ductile (WC-Co) component system can be visualised schematically, as shown in Fig. 2.1. MA powders allow lower processing temperatures owing to their higher surface activation and stored energy. Consolidation is achieved more rapidly, and higher density and finer microstructures may also be obtained (Lee *et al*., 2003).

Fig. 2.1 Schematic showing the various stages of the MA process for a brittle-ductile component system (Fogagnolo *et al*. 2003).

The raw materials used for MA are widely available commercially pure powders that have particle sizes in the range of 1-200 μm (Suryanarayana, 2001). The raw powders fall into the broad categories of pure metals, master alloys, pre-alloyed powders, and refractory compounds.

Since large plastic deformations are induced into the powder particles during MA, each crystal is heavily strained and deformation occurs in a rather inhomogeneous manner. With a longer duration of MA, shear bands, which are ~ 1 μm thick at the initial stage of milling, grow over large areas and eventually the entire powder particle disintegrates into subgrains with a final grain size of a few nm (Fecht 1994).

For nanocrystalline powders prepared using conventional processes and consolidated by elevated temperature techniques, the compacts are found to consist of nanosized grains that are dislocation-free. On the other hand, the nanocrystalline grains in the powders synthesised using MA are separated by grain boundaries containing a large density of dislocations. Hence, nanocrystalline powders produced by MA will possess different properties from those prepared by conventional techniques since there are about 50% of the atoms located in the grain boundaries (Lu and Lai 1998). This new solid state manifests considerable changes in physical and mechanical properties.

Every time two grinding balls collide they trap powder particles between them. The force of the impact deforms the particles, creating atomically clean, new surfaces. When the clean surfaces come into contact, they weld together. Since such surfaces readily oxidise, milling is carried out in an inert atmosphere or vacuum. To facilitate interparticle welding, there must be adequate compressive energy imparted to the

grinding medium during milling and usually the presence of a malleable constituent that can act as a binder for the other material.

In the early stages of the process, the metal powders show a tendency to weld together, as at this stage they are not sufficiently work-hardened for fracturing to take place. A broad range of particle sizes develops, with some particles two to three times larger in diameter than the original ones. As the process continues, the particles become harder through work hardening and their ability to withstand deformation without fracturing decreases. After milling for a certain length of time, steady-state equilibrium is attained when a balance is achieved between the rate of welding, which tends to increase the average particle size, and the rate of fracturing, which tends to decrease the average composite particle size. Smaller particles are able to withstand deformation without fracturing and tend to be welded into larger pieces, with an overall tendency to drive both very fine and very large particles towards an intermediate size (Benjamin 1976). At this stage, each particle contains the starting ingredients in the proportion they were mixed together and the particles reach saturation hardness due to the accumulation of strain energy. The particle size distribution at this stage is narrow, because particles larger than average are reduced in size at the same rate that fragments smaller than average grow through agglomeration of smaller particles, Fig. 2.2, (Lee, Yang and Lin 1998).

Fig. 2.2 Narrow particle size distribution caused by a tendency of the small particles to weld together and large particles to fracture under steady-state conditions (Lee, Yang and Lin 1998).

2.2.2 Factors affecting the MA process

The MA process is a complex process and is greatly affected by a number of factors that play very important roles in the fabrication of homogeneous materials. The more complete the control and monitoring of the milling conditions then the better the end product (El-Eskandarany *et al*. 1992). These factors include the following:

- Type of mill

- Milling materials
- Milling atmosphere
- Ball-to-powder weight ratio
- Milling temperature
- Milling time and speed
- Process control agent (PCA)

2.2.3 Type of mill

There are a number of different types of mills for conducting MA and they differ in their capacity, speed of operation, and their ability to control the operation. Examples include attritor, shaker, drum, planetary, and horizontal mills. The motion of the milling medium and the charge varies with respect to the movement and trajectories of individual balls, the movement of the mass of balls, and the degree of energy applied to impact, shear attrition, and compressive forces acting on powder particles. The attritor mill, Fig. 2.3, is preferred by most workers because of its operational flexibility, and consists of a water-cooled stationary vessel with a centrally mounted vertical shaft with impellers radiating from it. The mill was invented in the 1920s by Szegvari as a means of quickly attaining fine sulphur dispersion for use in rubber vulcanisation (Gilman and Benjamin 1983). In this mill, the milling procedure takes place by the stirring action of an agitator, which has a vertical, rotating central shaft with horizontal arms (impellers). When the shaft rotates, the arms stir the balls causing them to lift up and fall back. Thus,

there is a differential movement between the balls and materials being milled, giving a much higher degree of surface contact. The rotating charge of balls and powder form a vortex at the upper end of the stirring shaft into which the milling product and balls are drawn. Attritors have a number of associated advantages:

1. milling is achieved by impact and shear forces, and is very intensive because the force restoring the media downward is the weight of all the media above it;
2. the high impact energy allows the use of smaller diameter balls, thereby creating powder with a narrow size distribution;
3. as the greatest milling action is at 2/3 chamber-radius away from the shaft, there is little contamination due to wear of the tank or shaft.

However, the drawback with these mills is the relatively low product output. They also need more power and can be difficult to run and maintain cost effectively.

Fig. 2.3 Example of a Szegvari-type attritor ball mill

(http://www.sut.ac.th/Engineering/Metal/facilities/powderlab.html).

The planetary mill, Fig. 2.4, is one of the most popular mills used in MA research. This type of mill can generate considerable high energy, because the milling media come off the inner wall of the vessel and the effective centrifugal force reaches up to twenty times gravitational acceleration (El-Eskandarany 2001). The centrifugal forces caused by the rotation of the supporting disc and autonomous turning of the vessel act on the milling media (balls and powders). Since the turning directions of the supporting disc and the vessel are opposite, the centrifugal forces are synchronised and opposite alternately. Therefore, the milling media roll on the inner wall of the vessel, and are lifted and thrown across the bowl at high speed, as schematically presented in Fig. 2.4 (b).

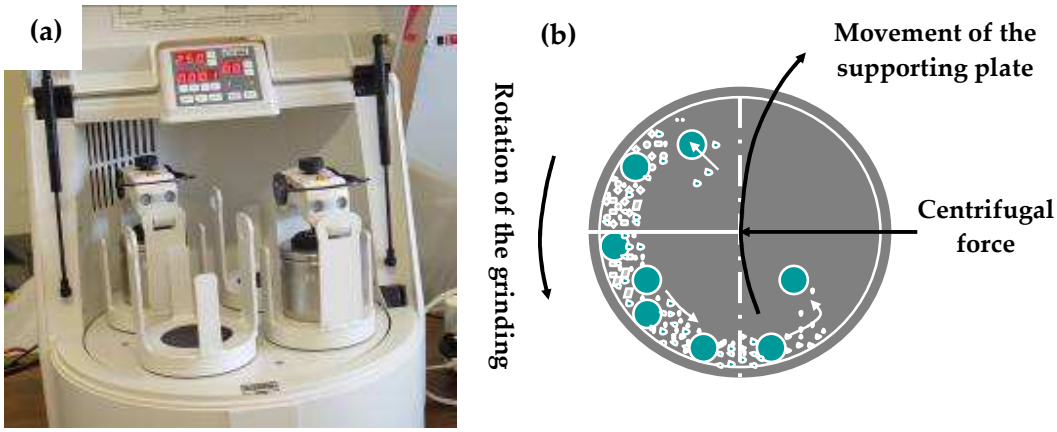

Fig. 2.4 (a) Example of a planetary ball mill (Fritsch P5); (b) schematic representation of the displacement of the milling media inside the vessel.

The tumbler ball mill, Fig. 2.5, dates back to 1876 and is defined as cylindrically-shaped shells, which rotate about a horizontal axis. The capacities of these mills are governed by several variables, for example, the ratio of mill length to diameter, speed of mill, size of balls, and particle size. With its simplified design, this type of mill provides lower maintenance requirements. On the downside, this type of low-energy mill can lead to an increase in the overall milling time for a complete MA process.

Fig. 2.5 A heavy duty tumbler mill showing three milling drums (http://www.lapidary-solutions.com/shop/page/category/Category/24203382f170f81e2d6dbbe89b880763.html).

Shaker mills such as SPEX mills, Fig. 2.6 (a), which mill about 10-20 g of the powder at a time, are most commonly used for laboratory investigations and for alloy screening purposes. The most common variety of the mill has one vessel, containing the sample and grinding balls, secured in the clamp and swung energetically back and forth several thousand times a minute. The back-and-forth shaking motion is combined with lateral movements of the ends of the vessel, so that the vessel appears to be describing a 'figure of 8' as it moves. With each swing of the vessel, the balls impact against the powder and the end of the vessel, both milling and mixing the sample. With the amplitude (about 5

cm) and speed (about 1200 rpm) of the clamp motion, the ball velocities are high (on the order of 5 m s^{-1}) and consequently the force of the ball's impact is unusually great. Therefore, these mills are classed as high-energy.

Fig. 2.6 (a) SPEX 8000 shaker mill in the assembled condition, (b) WC vessel set consisting of the vessel, lid, gasket, and balls (www.spexcsp.com/sampleprep/catalog/aid4.html).

2.2.4 Milling materials

The material used for the milling container and balls is important as impacts of the grinding medium on the inner walls of the container, (and in such cases where impellers are used), may remove material, which then becomes incorporated into the powder. Hardened steel, tool steel, hardened chromium steel, tempered steel, stainless steel, WC-

Co, and bearing steel are the most common types of materials used for the grinding medium (Suryanarayana 2001). By minimising the milling time and using the purest metal powders available, a thin coating of the milling tools by the respective powder material can be obtained, which reduces Fe-contamination tremendously.

2.2.5 Milling atmosphere

For all nanocrystalline materials, surface and interface contamination constitutes a major problem. The major effect of the milling atmosphere is on the contamination of the powder since a small amount of O_2 or H_2O may have a large influence on the final product. Therefore, the powders are milled in vessels that have been either evacuated or filled with an inert gas such as argon or helium. Atmospheric contamination can be minimised or eliminated by sealing the vessel with a flexible "O"-ring. Very fine powders have relatively large surface areas (El-Eskandarany *et al*. 1992) and, thus, are highly reactive not just with O_2 but also with other gases such as hydrogen or nitrogen (Campbell and Kaczmarek 1990). High-purity argon is the most common ambient to prevent oxidation and/or contamination of the powder. Although milling in argon can prevent powder contamination, it has been found that entrapped argon can cause micropores during annealing of MA ferritic steels (Jaeger and Jones 1994).

2.2.6 Ball-to-powder weight ratio

An increase in ball-to-powder ratio (BPR) reduces the mean free path of motion, whilst a low BPR minimises collision frequency. At a high BPR, the number of collisions per unit time increases because of an increase in the weight proportion of the balls and consequently more energy is transferred to the powder particles, thereby increasing the rate of alloying. The BPR also has a significant effect on the time required to achieve a particular phase in the milled powder with a high BPR reducing the time required. BPR has been varied from as low as 1:1 (Chin and Perng 1997) to as high as 220:1 (Kis-Varga and Beke 1996). Generally speaking, a ratio of 10:1 is most commonly used for small capacity mills.

2.2.7 Milling temperature

Milling temperature is another important parameter in deciding the constitution of the milled powder. Since diffusion processes are involved in the formation of alloy phases irrespective of whether the final product phase is a solid solution, intermetallic, nanostructure, or an amorphous phase, it is expected that the temperature of milling will have a significant effect in any alloy system (Suryanarayana 2001).

Although the maximum temperature reached during MA is dependent on several factors, such as the type of ball mill used, speed of rotation employed and properties of the powder particles to be mechanically alloyed, measurements have shown that the

global temperature is relatively low (Lu and Lai 1995). Unfortunately, the dynamic nature of the ball milling process precludes direct measurement of the transient temperature at the ball-powder interface during milling. Therefore, considerable efforts have focused on modelling and other indirect methods in order to ascertain the possible temperature rise. A wide variation in the predicted temperature rise is observed from the literature, with temperatures ranging from 47°C (Schwarz and Koch 1986) to 347°C (Bhattacharya and Arzt 1993). All of the models are guided by various assumptions and approaches, for example, one study demonstrated that the ball diameter as well as the presence of powder coating on the milling media during milling, has a significant influence on the ball temperature (Kwon, Gerasimov and Yoon 2002). However, the actual deformation of the ball surface due to collision and the influence of the coating thickness were not considered. A later work tried to quantify these effects for a ternary blend of AlNiFe with the model predicting a temperature rise of 200°C within 4-6 h of MA, but although the model showed that the temperature rise is related to the surface density of powder on the grinding balls, it seems reasonable to assume that the density would change during the various stages of MA. Also, these models are based upon the planetary ball mill, which, by the very nature of its design, incorporates a dual mode of energy transfer involving a considerable fraction of frictional energy together with impact energy whereas the ball mill configuration used in this study is considerably different.

Heat dissipation would depend on the mass of the milling vessel, ball diameter, BPR, and powder particles. An increase in milling temperature certainly plays a very

important role in MA, not only in the diffusion process, but also in controlling the size of the particles. Two major phenomena can contribute to an increase in milling temperature; friction during collision and localised plastic deformation.

A study of CoZr intermetallic showed that the nanocrystalline structure formed more rapidly at lower milling temperatures (Koch, Pathak and Yamada 1993). The variation of grain size with milling time for CoZr milled for different times in a shaker mill is shown in Fig. 2.7. It can be seen that reduction in grain size is much more rapid at cryo-temperatures than at higher temperatures. Cooling the mill chamber promotes fracturing and establishment of steady-state processing. With a cryogenic temperature (~ -50°C) and the high-speed rotation of the milling balls, the size of the powder particles can be reduced into the nano- scale in a relatively short time period.

Fig. 2.7 Variation in grain size with milling time and temperature for CoZr milled in a shaker mill (Koch, Pathak and Yamada 1993).

It has also recently been reported that milling at low temperatures can produce WC nanocrystalline structures with enhanced thermal stability during sintering, with growth occurring at 600°C and the average particle size remaining less than 100 nm after 4 h at 1000°C (He, Ajdelsztajn and Lavernia 2001).

Cryomilling is a mechanical attrition technique in which powders are milled in a slurry formed with milling balls and a cryogenic liquid (Witkin and Lavernia 2006). The vast majority of previous studies have involved wet milling in liquid nitrogen to produce nanostructured materials from a variety of systems including Ni (Lee *et al*. 2001; Chung *et al*. 2003), Zn (Zhang *et al*. 2001; Zhu *et al*. 2003), Fe (Birringer 1989), Al (Luton *et al*. 1989), and Fe-Al (Huang, Perez and Lavernia 1998). The beneficial aspects of this technique for a number of these material systems include the in-situ formation of dispersoids (Luton *et al*. 1989), reduced oxygen contamination (Suryanarayana 2001), enhanced thermal stability (Lau *et al*. 1996), and dynamic recrystallisation (Zhu *et al*. 2003), with a NiCrAlY alloy for example, showing greatly increased creep resistance under service life for thermal barrier coatings (TBCs) (Ajdelsztajn *et al*. 2007). The improved resistance was a result of *in-situ* formed dispersoids from the cryomilling process, with the nano-scale dispersoids contributing to the thermo-mechanical stress distribution. Cryo-temperatures have also been utilised with dry milling, whereby the

cryogenic fluid flows around the outside of the vessel and therefore does not come into direct contact with the powder material (Zhu *et al*. 2003).

Early problems encountered in cryomilling of Al and Al alloys using standard Szegvari-type attritors, Fig. 2.3, included poor powder quality and low powder yield. Additionally, formation of dead zones in the tank, excessive powder loss due to liquid nitrogen evaporation and flow control, excessive seal wear, jamming of the stir arms, and freezing of the apparatus were some of the problems that had to be overcome (Suryanarayana 2001). Nowadays, modified attritors have minimised the above problems. Milling of powders at cryogenic temperatures has been shown to minimise welding, most probably due to the increased brittleness of the powder particles at such low temperatures (Hwang *et al*. 1992; Huang *et al*. 1996).

Whilst the advantages of cryomilling have enhanced certain material systems, an investigation of cryomilled WC-Co-VC powders (Lee *et al*. 2003) showed that high oxygen and nitrogen contents in the nano-powders led to carbon deficiency during subsequent sintering due to the slightly decarburising nature of vacuum sintering.

2.2.8 Milling time and speed

Milling time and speed are two of the most important variables to be considered. Generally, milling time is chosen to achieve a steady state between the fracturing and cold welding mechanisms. The time required will vary according to the type of mill used, milling intensity, BPR, milling temperature, and the powder system. Very low

rotational speeds lead to increased periods of milling, thereby inducing a large inhomogeneity in the powder due to inadequate kinetic energy input and insufficient localised heat input for alloying (Soni 2000). Conversely, very high speeds could lead to excessive heating of the vessel, high wear of the balls causing increased contamination, and lower powder yields. The level of contamination increases if the powder is milled for longer times than required, for example, 20 at% Fe has been found in a W-C mixture milled for 310 h and 33 at% Fe in pure W milled for 50 h in a SPEX mill (Wang *et al*. 1997). Heating may be advantageous in some cases where diffusion is required to promote homogenisation and/or alloying in the powders but, in some cases, an increase in temperature may be a disadvantage because the increased temperature accelerates the transformation process and results in the decomposition of supersaturated solid solutions, for example, Fe-Cu (Kaloshkin *et al*. 1997).

Altering the milling speed, and thereby the kinetic energy, can alter the constitution of the powder. For example, when vanadium and carbon powders were milled at very low milling energy (or speed), the powder consisted of nanometre-sized grains of vanadium and amorphous carbon, which on annealing formed V_2C or a mixture of V + VC. At an intermediate energy level, the as-milled powder contained a nanostructure, which on annealing transformed to VC. At the highest energy level, VC formed directly on milling (Calka, Nikolov and Ninham 1993).

2.2.9 Process control agents (PCAs)

Using organic surfactants, termed PCAs, for example, oxalic acid, methanol, stearic acid, and ethylene bis disteramide, are one way of achieving the critical balance between cold welding and fracturing, whilst also enhancing process efficiency (Gilman and Nix 1981). The PCAs help by preventing fresh surface contact by coating the powder particles and inhibit agglomeration. During the MA process, the PCA is embedded and finely distributed among the layers of flaky powder. PCAs also help in alleviating the tendency of ductile powder particles towards powder-to-ball/vessel welding. The use of a surfactant can reduce milling medium contamination by at least a factor of 10 (Radlinski *et al*. 1991). Thus, use of a PCA may be of practical significance, provided it does not pose a contamination problem itself. The majority of these compounds decompose during milling, interact with the powder and form compounds, which get incorporated in the form of inclusions and/or dispersoids into the powder particles. In general, organic PCAs contaminate the milled powder with residual carbon and oxygen (Gilman and Nix 1981) resulting in the formation of carbides and oxides which are uniformly dispersed in the matrix. These are not necessarily harmful to the alloy system since they can contribute to dispersion strengthening of the material resulting in increased strength and higher hardness (Murty, Koczak and Frazier 1987). Organic PCAs also form hydrogen during MA, which remains in the particles, necessitating a de-gassing step.

2.3 Synthesis of WC-based powders by MA

Elemental W, Co and C powders have been used as the starting material in MA to synthesise nanostructured WC–Co composites (Mi and Courtney 1997; El-Eskandarany *et al*. 2000). Typically, the process consists of milling a mixture of W, C and Co powders at room temperature, followed by hot isostatic processing (HIP) of the milled powder. After ~ 82 h milling, a complete single phase of *hcp*-WC was obtained, and further milling (120 h) led to nanocrystalline WC grains of < 5 nm diameter. The addition of Co powders increased oxygen contamination in the bulk samples to a level of 1.44 at%, as determined by the fusion-thermal conductivity method, due to the fresh Co surfaces reacting with oxygen.

Generally, grain size reduction in ball milling is mainly due to the comminution, dislocations' annihilation, and recombination to small angle grain boundaries separating individual grains (Fecht 1995). WC-Co, when deformed by compression, showed that dislocations with Burgers vectors [0001], 1/3[$1\bar{2}13$] and 1/3[$1\bar{2}10$] appeared in the WC phase (Greenwood, Loretto and Smallman 1982). The dislocation vector 1/3[$1\bar{2}13$] can also be observed when WC is deformed by indentation (Hibbs and Sinclair 1981). High-energy ball milling can also partially change *hcp*-WC into an orthorhombic phase by introducing stacking fault 1/6[$\bar{1}2\bar{1}3$] onto the plane of {$10\bar{1}0$} (Yang *et al*. 2001). Sufficient ball-milling intensity of a WC-10wt%Co composition has been shown to transform *fcc*-Co into *hcp*-Co by a mechanically induced allotropic transformation (Zhang, Wang and Zhu 2003). After 10 h of milling, the grain size of WC was reduced to

11 nm from a starting size of 5.6 μm, with a severe internal strain introduced. At the edge of one WC particle, a number of straight planes were observed, which were attributed to the $\{10\bar{1}0\}$ plane of WC, the main slip and fracture plane. In one arbitrarily selected WC particle, dislocations with Burgers vector $1/3[1\bar{2}10]$ and high dislocation density were found. The high stored energy in nanocrystalline metals has been attributed to the high dislocation density (Zhang, Wang and Zhu 2003) and grain boundary strains (Oleszak and Shingu 1996).

2.4 Characterisation of nanostructured WC-Co powder

2.4.1 X-ray diffraction (XRD)

When X-ray radiation is directed on a sample, the X-rays are scattered ("diffracted") by electrons present in the material. Diffraction occurs when each electron in a periodic array scatters radiation coherently, producing concerted constructive interference at specific angles.

If the atoms in the material are arranged in a regular structure, i.e. if the material is crystalline, then this scattering results in maxima and minima in the diffracted intensity. The signal maxima follows Bragg's law, $n\lambda = 2d\sin\theta$ where n is an integer, λ is the X-ray wavelength, d is the distance between crystal lattice planes and θ is the diffraction angle (see Fig. 2.8). Bragg's law is a simplistic model to understand what conditions are

required for diffraction. Thus, for each lattice spacing d, Bragg's law predicts a maximum at a characteristic diffraction angle θ. For parallel planes of atoms, with a space d_{hkl} between the planes, constructive interference only occurs when Bragg's law is satisfied.

During an XRD measurement, the angles of incidence and detection are scanned. When the intensity of detected X-rays is plotted as a function of angle θ, an X-ray diffraction pattern is obtained, which is a characteristic of the sample material. The space between diffracting planes of atoms determines peak positions whilst the peak intensity is determined by what atoms are in the diffracting plane. At slightly higher θ than the Bragg angle, each plane gives a "lag" in the diffracted beam. For many planes, these end up cancelling each other and, thus, the net diffraction is zero. In small crystals, there are relatively fewer planes, so there is a "remanent" diffraction.

XRD can also supply information about deformation of a crystalline sample. Deformation (also referred to as strain) of a crystal lattice will result in a change in the inter-atomic distances. The effect on a diffraction pattern depends on whether the deformation occurs on a local (microscopic) or on a global (macroscopic) scale. Microscopic deformation, i.e. local variation of the interatomic distances in a sample, is referred to as micro-strain. In this case, XRD analysis of an entire sample will display a range of deviations from the expected interatomic distances (d). This leads to peak broadening.

Fig. 2.8 Schematic representation of the diffraction of X-rays in a crystalline material (Graat 2004). Bragg's law is satisfied when the pathlength difference of the X-rays (indicated in green) is equal to $n\lambda$. The diffraction angle θ is half the angle between the incident and diffracted X-rays.

The width of a diffraction peak is also influenced by the crystallite size: a large crystallite size causes sharp reflections, whereas a small size leads to broad reflections. Although both size and strain result in peak broadening, their effects can be separated since their angular dependence is different.

Crystallite size determination is one of the most important applications in powder diffractometry for materials characterisation. Unfortunately, crystallite size is a quantity that cannot be measured directly, as explained below. In addition, there is confusion in the literature concerning the definition of particle size, crystal size, crystallite size, and domain size, Fig. 2.9.

A typical particle is represented in Fig. 2.9 (a), which may consist of one or more crystals ("primary grains"). The different crystals may be separated, for example, by large angle boundaries, amorphous or crystalline interfaces. Typical methods used for particle

size determination are light microscopy, laser size analysis, sieving etc. Complications may arise due to the fact that particles can agglomerate. Several crystals are shown in Fig. 2.9 (b). For crystal size, the same principles are true as for particle size. Methods for crystal size determination are the same as for particle size determination, but agglomeration effects can also hamper crystal size analysis. The size of a crystal is, in general, equal or less than the particle size. Each crystal may consist of one or more crystallites, as shown in Fig. 2.9 (c). The size of a crystallite is, in general, equal or less than the crystal size. Crystallite size can be determined by means of powder diffraction, but not directly as mentioned and explained further. Each crystallite may consist of one or more coherently reflecting domains, which need not be connected. In Fig. 2.9 (d) a crystallite is shown, which is "broken" into two domains as a result of stacking fault twinning ABCBA (dashed line) as may be found in fcc-structures. For a reflection hkl, represented by the diffraction vector $\vec{a}$, there are two domains, but only one crystallite. In contrast to this, for a reflection hkl represented by the diffraction vector $\vec{b}$, there may be two domains and two crystallites. It is important to realise that line broadening is due to domain size, which cannot be determined by powder diffraction, although in rare cases a "domain structure" can be deduced (Coelho 2007). The size of a domain is in general equal or less than the crystallite size.

(a) (b) (c) (d)

Fig. 2.9 Schematic representation of (a) particle or grain size, (b) crystal size, (c) crystallite size, and (d) domain size (Coelho 2007).

As mentioned, crystallite size is a quantity that cannot be measured directly. Measurable quantities are so-called 'column heights', as illustrated in Fig. 2.10. As the scattering power of a column is dependent on its volume then it is appropriate to use volume weighted mean column heights, L_{Vol}. For example, only h00 reflections for a cube give a column height L_{Vol} that is identical with the edge-length L_0 of the cube (crystallite size for h00) as shown in Fig. 2.10. For any other hkl, a column height distribution will be observed with a mean less than the crystallite size. This is illustrated in Fig. 2.10 for a sphere, where for any given hkl, a column height distribution is observed. For any given hkl, L_{Vol} will not be identical with the diameter of the sphere, but can be derived from the known crystallite shape:

$$L_0 = 4 L_{Vol} / 3 \qquad (2.1)$$

With powder diffraction, only column heights can be determined. To obtain the true crystallite size, the true mean shape of the crystallites must be known in order to derive and apply a correction to the column height of each hkl.

Fig. 2.10 Schematic representation of a square and a circular cross-section of a crystallite built up of columns perpendicular to the lattice planes (Coelho 2007); (d = d-spacing; L_0 = edge length and sphere diameter respectively).

In 1918, Scherrer noted that line breadth varies inversely with crystallite size, leading to:

$$\beta = \lambda / \varepsilon \cos\theta \qquad (2.2)$$

where λ is the wavelength, θ the Bragg angle, β the FWHM of the instrument corrected line profile and ε is an "apparent crystallite size" dependent on the "true crystallite size" and hkl and has no direct physical interpretation; nevertheless it may be used as a measure for crystallite size. The Scherrer constant, *k*, allows a relationship between ε and volume weighted mean column height L_{Vol}, to give:

$$\beta = k\lambda / L_{Vol} \cos\theta \qquad (2.3)$$

An integral breadth (β_i) method was later developed (Stokes and Wilson 1942), which gave a more generalised treatment of domain-size broadening, which is independent of the crystallite shape:

$$\beta_i = \lambda / L_{Vol} \cos\theta \qquad (2.4)$$

This conception leads directly to a formula identical with eq. 2.3, except that the constant *k* assumes a value of unity.

Lattice strain (microstrain) represents variable displacements of atoms from their sites in the idealised crystal structure, Fig. 2.11, caused by any lattice imperfection, for

example, dislocations, vacancies, interstitials, substitutionals, and similar defects. Strain e_0, is conceived by considering two extreme values of the lattice spacing d, namely $d + \Delta d$ and $d - \Delta d$, with $e_0 = \Delta d / d$. By equating FWHM β with the angular range corresponding to $d + \Delta d$ and $d - \Delta d$, and by assuming that Bragg's law holds over this range (implying that parts of the specimen with spacings $d + \Delta d$ and $d - \Delta d$ diffract independently, i.e. incoherently), it follows that:

$$\beta = 4e_0 \tan\theta \qquad (2.5)$$

Fig. 2.11 Schematic representation of lattice strain (Haberkorn 1999).

2.5 Chapter summary

The solid state processing method of MA has been developed as a versatile alternative to other processing routes in preparing nanostructured WC-based materials with a broad range of chemical compositions. The advantage of using MA for the synthesis of nanostructured WC-based materials lies in its ability to produce bulk quantities of

material in the solid state using simple equipment and at room temperature. The minimum grain size achievable by milling is determined by the competition between the plastic deformation via dislocation motion and the recovery and recrystallisation behaviour of the material.

MA is a complex process that involves many variables, of which many of them are interdependent. Therefore, modelling of the MA process is very difficult. In spite of some success, one has to go much further in developing models that can reach the final goal of predicting the nature of phases produced under a given set of milling conditions.

The range of synthesis techniques that use the "bottom-up" approach to develop nanostructured WC-Co powders, for example gas-phase synthesis and spray conversion processing, involve much more expensive technologies. Some of this extra cost is related to the lower volumes of powder produced and the inefficiencies of the processes. Many of these processes have only been developed on a laboratory scale. It remains to be seen whether their technologies can be transferred, cost effectively, to large scale production.

In a recent study (Esawi 2005), the cost-benefit analysis of replacing conventional WC-Co powder with nanostructured WC-Co was about four times the cost of conventional powders, and at current prices, cannot compete with conventional powder, in spite of the anticipated improved performance. For nanoscale powders to become commonplace in press-and-sinter operations, they need to be produced at much lower cost or to provide a much larger improvement in property performance.

Further significant R&D investment is necessary if the challenges of synthesising nanostructured materials are to be efficiently and cost-effectively met. Although the

thermochemical-based synthesis methods have an economical advantage over conventional processing by eliminating the mechanical milling step, their processing route is, however, relatively complicated. If, as predicted, the use of nanostructured materials becomes more widespread and this, coupled with the development of more efficient, higher yield synthesis techniques starts to reduce their cost, then they could become a viable replacement for conventionally produced powder. The technical challenge remains two-fold; (i) synthesis of nanostructured particles; and (ii) uniform retention of the extremely fine microstructures in the consolidated materials. Much research is currently underway to optimise the consolidation of nanostructured WC-Co powders using a variety of novel fabrication techniques, for example spark plasma sintering (SPS). This consolidation technique is detailed further in Chapter 3.

3. Consolidation of nanostructured WC-Co powders

3.1 Introduction

Consolidation of hardmetals involves numerous operations in which almost every factor is critical. The basic hardmetal production technique is a typical powder-metallurgical process in which the starting product (fine WC and metallic Co powders) are blended by ball milling. The powder is then compacted into a raw shape (often called a green body), which is then exposed to elevated temperature in order for densification to occur.

The initial step in most densification processes is to compact powders at room temperature, or cold compaction, to form a green body. Final sintering results are largely dictated by the green compact structure. A large number of initial point contacts, small pores in a high green density compact, and a uniform pore distribution favour high final density, thereby permitting shorter sintering times and lower sintering temperatures. Conversely, many sintering defects may be traced to the green compact structure. Inhomogeneities in density, packing, and particle size in green compacts limit the final sintered density. Generally, nanostructured materials are less forgiving of defects in green compacts than are conventional powders (Groza 2007). The most common problem is the elimination of large pores that originate from the green compact. This elimination requires high temperatures upon subsequent sintering, promoting undesired grain growth and loss of the desired nanosize features.

The demand for finer WC-Co materials is growing rapidly, mainly due to new machining technologies which require carbide materials with enhanced properties. As the carbide industry converts to superfine (< 0.5μm) WC powders to meet this demand, their existing manufacturing processes will have to be optimised to ensure production of high quality WC-Co materials. The critical issues and concerns associated with processing of these superfine powders include the selection and content of grain growth inhibitors; mixing/milling conditions; overall carbon stoichiometry; and sintering temperature, and these issues are already a major concern in the carbide industry for the fabrication of sub-micron (0.5-1 μm) materials (Carroll 1997; Carroll and Conner 1997). However, with the processing of nano WC powder (< 0.2 μm), the range of acceptable compositions and processing conditions will be tightened further due to the increased activity of the nanosize WC grains.

Based on the above, the key requirement of a nanopowder consolidation process will be to achieve densification without microstructural coarsening. To date, the synthesis of raw nanomaterials (powders) has progressed further than the formation of bulk parts, with nanoscale powders of metals, ceramics, polymers, and composites now available, sometimes in tonnage quantitities (Groza 2007). The densification of nanopowders poses significant additional challenges including powder agglomeration, high reactivity (leading to contamination), grain coarsening, and an inability to fabricate large and dense parts. The lower temperatures required to minimise grain growth may hinder good intergranular bonding, thus compromising the expected high levels of strength. Grain coarsening for example, has to some extent been addressed through the use of

grain growth inhibitors and/or the development of consolidation techniques that allow nanopowders to be fabricated at temperatures much lower than conventional sintering.

This chapter firstly covers some aspects involved in cold compaction of nanopowders, including powder particle distribution. This is followed by a brief review of the techniques to improve green density for hardmetals. Finally, this chapter reviews the sintering process of WC-based nanoparticles, which is divided into pressureless (conventional) and pressure-assisted sintering and also features non-conventional sintering methods.

3.1.1 Powder packing and distribution

The formation of a high quality green body is key to obtaining acceptable final product microstructures and properties. There are many difficulties in consolidating nanopowders, which are related to their low apparent density; low flow rate; high absorbed gases; high surface area relative to their volume; and large interparticle friction. In ideal systems, particles of a constant size would be uniformly packed and thus pores of the same size would be uniformly distributed. Densification and shrinkage of powder compacts would, therefore, occur uniformly throughout the compacts. However, in real powder compacts, particle sizes are variable, and pore size and distribution are non-uniform. As a direct result, differential sintering and densification occur and particles may move, which can cause the generation of pores that are larger than the initial pores (Petzow and Exner 1976; Liniger and Raj 1987). Particle packing

and distribution are, therefore, important parameters in the sintering kinetics of real powder compacts.

A high green density compact is desirable for higher densification kinetics, which will provide an increased number of contact points and, therefore, a greater number of transport paths. Green density is highly dependent on the friction forces among powder particles. These forces are a result of electrostatic, van der Waals, and surface adsorption forces that become much more significant with decreasing particle size. With nanoparticles, grain boundaries tend to be irregular and agglomerate formation is favoured by the tendency to minimise surface energy (Groza and Dowding 1996).

One parameter which substantially affects packing density, especially when working with undeformable (e.g. carbide, ceramic) powders, is the arrangement of the individual particles. There is a noticeable difference in the compaction (and sintering) behaviour of powders in which each individual powder particle is free and independent of its neighbours, and those in which the primary particles, or crystallites, are chemically or physically bonded together to form larger units, termed agglomerates or aggregates (Mayo, Chen and Hague 1996). An example of an agglomerated powder is shown in Fig. 3.1. Agglomerates of ~ 1 μm have been found in 10 nm metallic powders (Trusov *et al*. 1989).

Fig. 3.1 Schematic diagram of an agglomerated powder (Mayo, Chen and Hague 1996).

3.1.2 Cold pressure forming

Of the many powder shaping methods, cold pressing in metal dies is the most widely used industrially because it lends itself admirably to automation and mass production.

The way a powder behaves when it is compacted in a die is dependent upon a large number of factors, including particle size, particle shape, chemical composition, plasticity, and the presence of surface films. Compaction induces very complex stress states in the powder. Lubrication, powder height in the die, compaction rate and stress triaxiality strongly influence the compaction process and, thus, affect the properties of the products obtained (Briscoe and Rough 1998).

When a metal powder is poured into a die, it will take on a certain packing density with the particles adopting a loose, random packed state with the manner of filling. Upon application of punch pressure, the first stage of densification begins by movement of particles to provide a better packing density. The extent to which this occurs depends largely on those factors already mentioned, i.e. fine powders having poor flow properties are liable to form bridges and the first slight pressure will tend to cause their collapse (Sands and Shakespeare 1966). Abrasion of surface films (oxide, adsorbed water vapour, CO_2, etc.) is a further effect of interparticle movement. These films must be removed before direct metal contact can take place. The initial areas of contact between particles are so small that, even at very low punch loads, pressures on these areas are high, which means that surface films at the areas of contact are soon broken. The particles can experience extensive shear deformation as powder flows around the punches. The constitutive response of the powder during the early stages of compaction and flow determines the evolution of the density distribution in the die (Wu *et al*. 2003) and can significantly influence its evolution during subsequent stages of the consolidation process.

Frictional forces between the powder and the die wall can become sufficient to inhibit the transmission of pressing loads throughout the compact and the general effect is a variation in density throughout the compact. The density decreases with increasing distance from the punch face and there is also a density distribution in the horizontal plane due to frictional effects dropping-off away from the die wall. Pressure transmission can be improved by reducing frictional effects through the use of a

lubricant. Application of lubricant to the die walls is as effective in improving green density as is the admixture of lubricant with the powder (Sands and Shakespeare 1966).

Carbide powders flow very poorly during compaction, thus limiting the intricacy of geometrical shape that may be produced. The flaws induced by compaction (density gradients, densification faults) are the main causes of non-conformity of sintered parts, which include residual porosity, cracks, and dimensional defects (Roure *et al*. 1999). Thus, the control of this step is of prime importance. Due to the friction between the powder and the die, the state of stress within the powder is not homogeneous during die pressing.

The optimal compacting conditions used for nano-sized powders are known to be considerably different from those used for micron-sized powders due to the increased total surface area of such powders. In the case of nano-sized powders obtained by mechanical milling, a major processing concern is the nature and amount of impurities that contaminate the powders, which can include entrapped gases such as oxygen and nitrogen, and particles from the milling medium. Thus, a higher compacting pressure is generally required to bring these powders into direct contact with each other in order to facilitate effective sintering.

Green density has a significant influence on the final density and microstructure of a material in the nanoscale and a high green density can enhance the densification process through increased particle-particle contact. Compaction pressures of several GPa are commonly used in nanoscale systems (Ahn *et al*. 1997; Gao *et al*. 2001). The practice of this principle, apart from the greater engineering demands, creates other problems, such

as the development of nonhomogenous density distributions and the formation of internal cracks during the stored stress release of the sample during ejection.

Very fine particles do not have the necessary free-flowing properties to facilitate effective manufacture since they spontaneously agglomerate due to Van der Waals attractive forces (Özkan and Briscoe 1996). A powder flows freely when the inertial forces exceed the attractive forces between particles. The inherent flowability of powder is required during the handling stage of the material and during die filling in the compaction stage. In order to create free-flowing particles with a reproducible size and shape, fine powders are commonly agglomerated by a suitable granulation technique. Weak agglomerates are disrupted in handling and produce unwanted 'fines'. However, if the agglomerates are too hard or tough, the large interstices between the agglomerates (inter-agglomerate pores, Fig. 3.1) will not be readily eliminated during the compaction process, and it will then be often impossible to eliminate these large pores during the subsequent sintering process. As a result, the mechanical properties of the final sintered compact will not be satisfactory since the resulting inter-agglomerate pores will provide the strength-limiting flaws.

In principle, this problem may be resolved by the application of very high compaction pressures but as previously stated, this in itself creates further challenges.

3.1.3 Improved green density techniques applied to hardmetals

In the nanoscale particle size range, green strength is very sensitive to compaction pressure. Small particles have inhibited packing due to agglomeration concomitant with their high surface area and large inter-particle friction (German 1989) and as a result, resist compression and exhibit lower green density and strength than their micron and sub-micron counterparts. Smaller particles also exhibit a tendency toward delamination under increasing compaction pressure (German and Olevsky 2005). Organic binders could be used to increase green strength but contamination issues can arise. A pre-heat treatment applied to nano hardmetal powders (0.2 μm average grain size) prior to cold uniaxial compaction can improve green density from ~ 51.5% for un-treated WC-Co powder to ~ 59% for a powder mixture treated at 1000°C for 1 h (Jung and Kang 2005). However, pre-treatment at such a high temperature increased agglomerate size from ~ 3 μm to ~ 10μm. The magnitude of the reported increase in green density was achieved through a 1:1 mixing ratio of heat treated and un-treated powders, which shows that a broad particle size distribution can enhance particle packing density. However, this is in contrast to Furnas' packing model (Furnas 1928), which predicted that particle packing was most efficient when the system consists of uniform, small-sized powders (<50%). Despite the stated improvement in densification, no mention was given to the effect of the lubricant (paraffin wax) on green density, which was mixed with both powder systems.

Lubricants are added to the powder as well as the die wall to reduce deleterious effects of both die-wall and inter-particle friction during compaction. High wall-friction creates high stress gradients within the powder, thus causing significant density fluctuations. Lubricants added to the powder can be classified as internal and external. Internal lubricants are added to the slurry during spray drying and serve to reduce inter-particle friction and promote better flow under high pressures. Internal lubricants significantly increase the green density, and thereby reduce the defects in the green body, whilst increasing the strength at a given green density (Motyl 1963). External lubricants serve to lubricate the die and punch surfaces giving increased tool life and a more uniform green body.

Techniques have been developed that incorporate die compaction pressure combined with a very fast current discharge that effectively consolidates the powder mixtures in one step. Further discussion of these consolidation techniques are given in section 3.4.3. In a more traditional route, very high cold compaction pressures followed by a fast, furnace heating rate (> 500°C min^{-1}) have been used to fabricate nanocrystalline WC-Co (Park, Johnson and German 2006). The optimum process conditions achieved a relative density of 98.9 % and a WC grain size of 240 nm at a compaction pressure of 2760 MPa, with a standard heating rate (10°C min^{-1}) and a sintering temperature of 1400°C. The high die compaction pressure helped by increasing density without exaggerated grain growth and also helped to break up agglomerates. However, one would have to weigh up the relative merits of this technique against the tooling costs as one of the major difficulties in die-compaction at high pressure is related to the fact that

the compaction tools in service are submitted to high stresses and, as such, excessive wear occurs. As a consequence, the service life of the compaction tools becomes extremely critical.

3.2 Thermodynamic and kinetic effects of nanopowder consolidation

Thermodynamically, nanopowders are far from equilibrium, sometimes by as much as 10–50 kJ/mol (Groza 2007). The sintering process is driven by the tendency to reduce the excessively large surface area per unit volume. The extra energy of a surface with a radius of curvature R may be expressed as a stress (σ) in a Laplace equation:

$$\sigma = \gamma / R \tag{3.1}$$

where γ is the surface energy. In nanomaterials, the sintering stress may as large as 300 MPa in 10 nm particles, compared to only 3 MPa for 1 μm particles, if γ has a typical value of 1.5 J/m^2 (Porter and Easterling 1992). The altered local atomic arrangement at the surface of nanocrystals may result in surface energy values different from those in conventional powders. This was shown in the case of amorphous, surface oxide layers on Al nanoparticles (Luo *et al*. 1995; Phung *et al*. 2003). As Cahn infers, the different nature of the surface oxide on nanopowders may be an indication of a different surface structure (Cahn 1992). The interfacial energy may also be modified by any distortion of surface structure, such as by segregation or adsorption of impurities. Impurities dictate

the thermodynamics of surfaces and surface behaviour of nanoparticles (Groza 2007). Modelling of ceramics (e.g. SiC) has supported these findings, showing a high dependency of grain boundary formation on initial surface structures (Tsuruta, Totsuji and Totsuji 2000). Particle stabilisation can be affected by the formation of surface oxides, which leads to lower surface energy values for nanosize particles (Rabe and Wasche 1995).

Significantly enhanced kinetics are expected for processes that display direct grain size dependence (Groza 2007). A recent work showed that decreasing grain size by three orders of magnitude (e.g., from micrometer to nanometer) could enhance sintering rates by up to 12 orders of magnitude (Hansen *et al*. 1992). During sintering of nanopowders, enhanced diffusivity is observed initiating the sintering process at temperatures lower than those required for coarse-grained polycrystalline powders, with the WC-Co liquid phase system a prime example, which will be detailed later in this chapter.

3.3 Sintering mechanisms and phase relationship in the W-Co-C system

The most crucial aspect of the sintering of nanostructured WC-Co grades is retaining the nanostructure of WC in the consolidated (dense) material. Only if this aim is both successfully and reliably achieved can a pronounced technical advantage, (e.g. higher hardness, better wear resistance, higher strength), be realised over the submicron (0.5-1 μm) and ultrafine (0.1-0.5 μm) alloys, which are coarser, but less WC growth sensitive during the manufacturing process.

In the following section, the most important aspects of sintering with reference to nanoscale WC powders will be discussed.

3.3.1 Phase relationship

There are many factors that have a direct influence on the microstructure of cemented carbides, including:

- Chemical composition of both hard and binder phases
- Shape, size and distribution of WC particles
- Control of the carbon level
- Processing technology, e.g. ball milling and sintering including the purity of raw materials

Tungsten carbide has a highly anisotropic structure and therefore develops anisotropic crystal shapes during growth, which can be described as flat, triangular prisms with truncated edges (Exner 1979). In technical hardmetals, this shape is not fully developed due to coalescence and impingement with other crystals. However, most of the crystal sections observed in a polished cross- section can easily be interpreted by this equilibrium configuration (Hara, Nishikawa and Nishimoto 1970; Exner 1979). Two crystallographic planes play an important role in the formation of tungsten carbide

interfaces; the $\{10\bar{1}0\}$ prismatic plane and the $\{0001\}$ basal plane, which are the main facets of WC crystals.

Cobalt is the most widely used binder in WC-based hardmetals and exists in the microstructure as a continuous thin film separating the WC grains. There are two allotropic modifications of cobalt, a close-packed hexagonal form, ε, stable at temperatures below approximately 400°C, and a face centred cubic form, α, stable at higher temperatures. The temperature of the allotropic transformation depends critically on purity and on the rate of temperature change, but for the highest purity material, ~ 99.998%, and slow temperature change, the transformation temperature was found to be 421.5°C (Betteridge 1982). Grain size also affects the stability of the two allotropes with a finer grain size favouring the cubic form. In cobalt powder, typically, a mixture of approximately the same amounts of both phases exists. During milling, the amount of ε-cobalt increases up to 100% (Hinnuber, Rudiger and Kinna 1961; Fischmeister and Exner 1965). Insufficient milling results in a large cobalt pool in the microstructure and may cause porosity (Lardner and Bettle 1973; Amberg and Doxner 1977).

Although some differences exist amongst the various phase diagrams presented in the literature, some of the common similarities are:

- For compositions corresponding to a W/C atomic ratio close to one, the WC phase, β (binder) and liquid are stable.
- At lower carbon contents, a ternary brittle phase (η) occurs.

- At a W/C atomic ratio below one, primary carbon will precipitate and remain in equilibrium with WC and Co-rich β phase in solidified alloys.
- The two-phase WC-β exists only in a narrow range of carbon concentration.

These phases can only exist within specific temperature ranges, which are detailed in Table 3.1 for a W-C-10Co alloy. The η phase is a ternary compound of tungsten, cobalt and carbon. It can exist in two forms, either M_6C carbide ranging from $Co_{32}W_{28}C$ to Co_2W_4C (Hellsing *et al*. 1983) or an $M_{12}C$ carbide of fixed composition Co_6W_6C (Johansson and Uhrenius 1978). Both M_6C and $M_{12}C$ are indistinguishable physically, but in commercial tungsten carbide alloys with a relatively fast cooling rate, presence of M_6C is more likely to occur (Bolton and Keely 1982). A calculated phase diagram of the W-C-10Co system is shown in Fig. 3.2, and accordingly, caution is needed in its interpretation. A stoichiometric mixture of WC + 10 wt. % Co corresponds to 5.519 wt. C; the value which is placed inside the desirable two-phase region (FCC + WC) for the temperatures below the solidus. In practice, carbon is often added to the mixture of WC and Co, since some carbon inevitably reacts with oxygen during sintering.

With minor carbon deficiency levels, 'η' phase is not produced at the sintering temperature but forms on subsequent cooling (i.e., WC + liq. $\rightarrow$ WC + η + liq.), and in doing so occurs as isolated concentrated areas in which considerable volumes of WC and Co binder phase are locally consumed during its growth. As shown by the vertical section of the ternary W-C-Co system (Fig. 3.2), a very tight composition range is available to generate the two-phase WC-Co mixture. The carbon content range suitable

to generate the two-phase field {WC+liquid} at the sintering temperature and the two-phase field {WC+Co} after cooling is very tight, in between ~ 5.4 and 5.5% (Uhrenius 1994).

The morphologies of the 'η' phase range from finely dispersed particles at low carbon deficiency to large areas of 'η' concentration in highly carbon deficient alloys. For carbon deficient alloys, the relationship between density, σ_{sc} and carbon content is given by the lines drawn as carbon axes corresponding to different Co levels as shown in Fig. 3.3. The dashed line defines the boundary of the *η*-phase region.

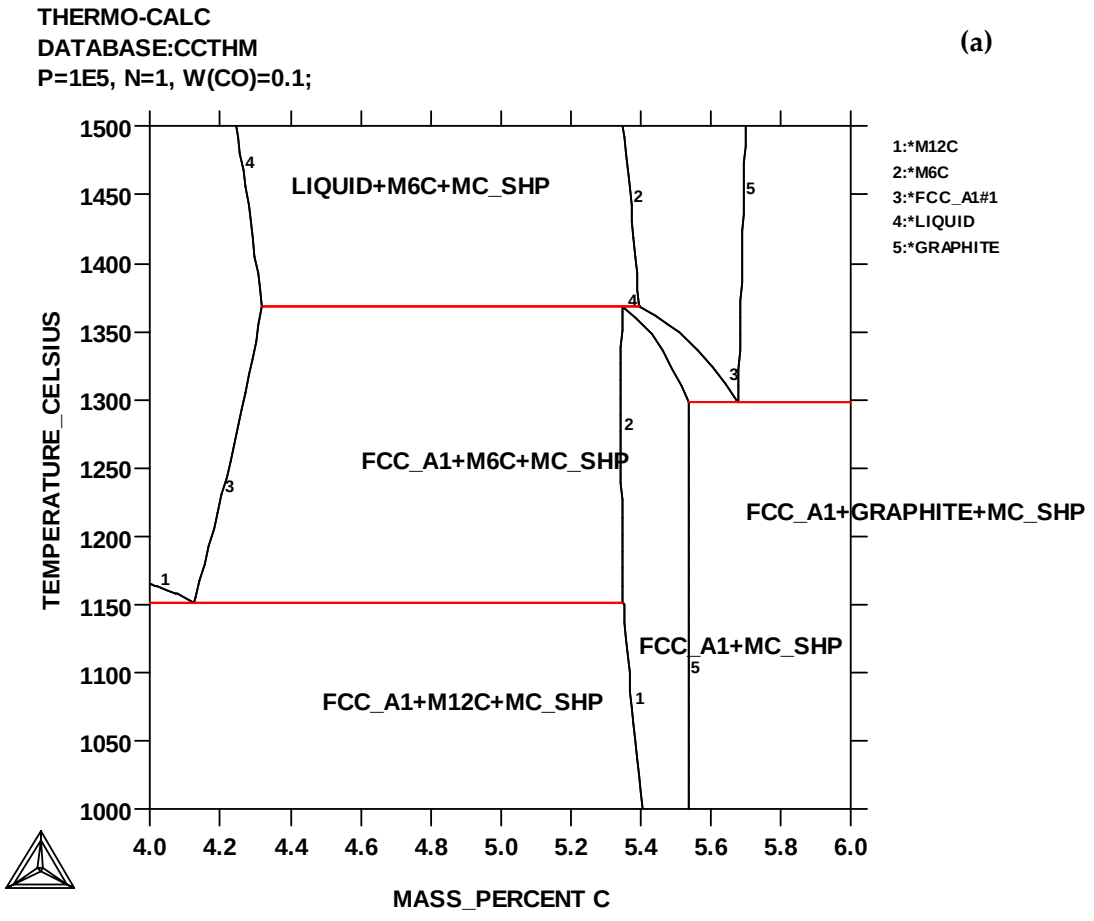

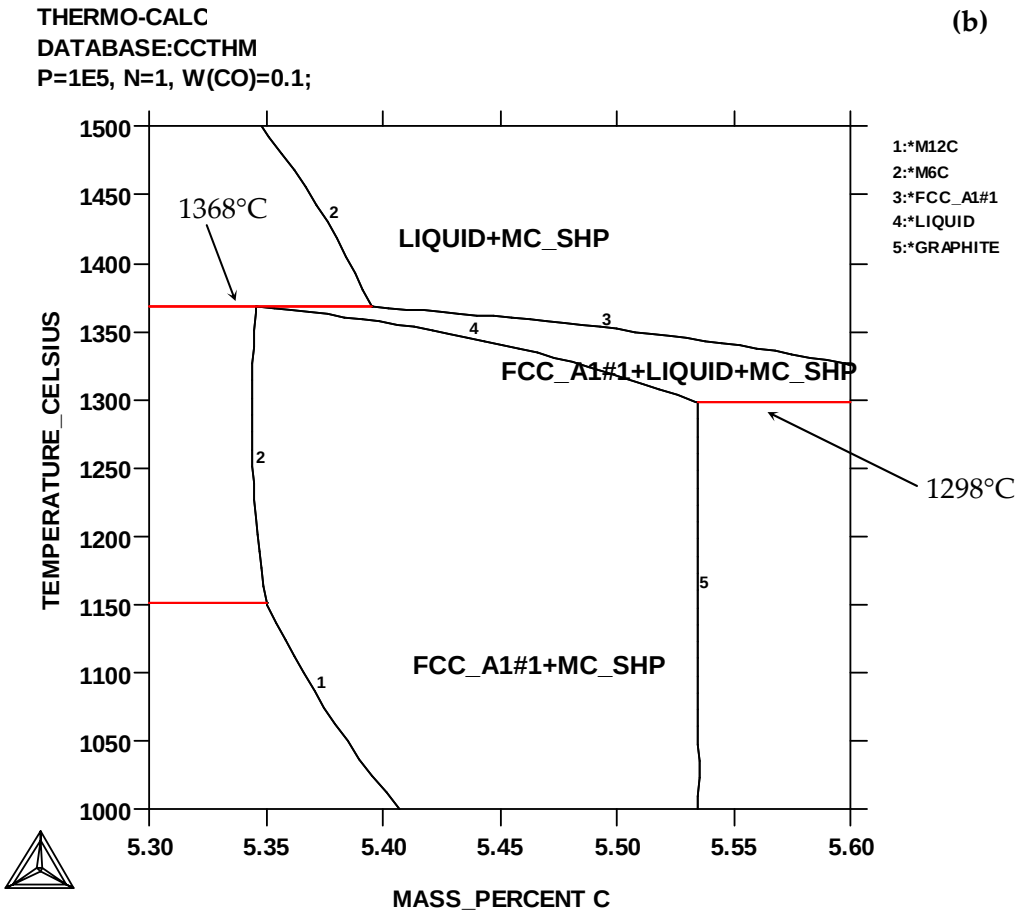

Fig. 3.2 Vertical section of (a) the tungsten-cobalt-carbon (W-Co-C) ternary system, calculated with Thermo-Calc coupled with the CC THM thermodynamic database, with (b) showing an extended section of the diagram. The cobalt content is kept constant at 10 wt%.

Table 3.1

Temperature range for W-C-10Co ternary system phases.

Phase	Temperature (°C)
η ($M_{12}C$)	<1150
η (M_6C)	>1150
liquid+WC	>1330
fcc+liquid+WC	>1298<1368
graphite	<1298

The gross carbon content of the alloy also plays an important role in the complex alloy system MeC/WC/Co/C. It can strongly influence the eutectic temperature and equilibrium saturation concentration ratio of both Me_xC_y and WC in the binder (Hayashi, Fuka and Suzuki 1972). Higher solubility and lower eutectic temperature are important for better grain refining of cemented carbides by VC and Cr_3C_2 as compared to Ti, Nb and Ta additions, Table 3.2.

Precipitates generally observed in the microstructure may include non-metallic impurities, graphite, carbides, and intermetallic compounds precipitated during cooling or heat treatment in the solid state. Local concentration gradients can arise due to the slow diffusion of tungsten in cobalt, which can result in the formation of Co_3W. It is more likely that the transformation of the α-Co into the ε-Co phase is the reason for the

formation of the intermetallic due to the sudden decrease of tungsten solubility in the binder phase.

Fig. 3.3 Density-specific magnetic saturation diagram: interrelationship of cobalt and carbon content in cemented carbide (Fang and Eason 1993).

Table 3.2 Eutectic temperatures for the Me_xC_y–Co systems and solubilities of the carbides in the cobalt phase (Upadhyaya 2001).

Inhibitor compound MeC	Eutectic temperature Me_xC_y–Co (°C)	Solubility in Co binder Mol.% Me_xC_y at 1400°C
TiC	1360	1.5
ZrC	1360	6
HfC	1370	3
VC	1330	10
NbC	1380	6
TaC	1370	3
Cr_3C_2	1245	12

3.3.2 Driving force

The primary driving force for sintering is a decrease of the specific surface energies (Δ_γ) of the system resulting from the energies involved:

$$\Delta_\gamma = \gamma_S + \gamma_L - \gamma_{SL} \qquad (3.2)$$

γ_S = specific surface energy solid/gas

γ_L = specific surface energy liquid/gas

γ_{SL} = specific phase boundary energy solid/liquid

An energy decrease only takes place when:

$$\gamma_{SL} < \gamma_S + \gamma_L \tag{3.3}$$

thus, liquid phase sintering (LPS) is successful only in good wetting systems (e.g. WC-Co), in which γ_{SL} is low. These energies are correlated in the Young-Dupré equation with wetting angle ω, Fig. 3.4 (a) to give:

$$\cos\omega = \frac{\gamma_S - \gamma_{SL}}{\gamma_L} \tag{3.4}$$

Fig. 3.4 Schematic showing (a) wetting (ω) angle and (b) dihedral angle (Φ) (Thümmler and Oberacker 1993).

Combining these equations gives:

$$\Delta_\gamma = (1 + \cos\omega) \cdot \gamma_L \qquad (3.5)$$

The higher cos ω (i.e. the smaller ω), the higher the driving force Δ_γ. The angle for complete wetting is 0°, occurring at very low γ_{SL} values, as observed in the hardmetal systems WC with Co, Ni or Fe. γ_{SL} is very sensitive to impurities, especially thin oxide films, which may change the wetting angle considerably. The liquid phase may also penetrate the solid grain (or phase) boundaries, when the boundary energy:

$$\gamma_{SS} > 2\gamma_{SL} \qquad (3.6)$$

The resulting angles between the liquid and two solid particles are called dihedral angles (Φ), Fig. 3.4 (b). Small dihedral angles result in very low γ_{SL} and grain boundary energies γ_{SS}, leading to a disintegration of solid (multigrained) particles during LPS. This supports densification by solid phase rearrangement.

Unlike solid state sintering (SSS), the microstructure change during liquid phase sintering (LPS) is fast because of fast material transport through the liquid. Considerable densification usually occurs in the solid state during heating to the LPS temperature; the initial microstructure of LPS is strongly affected by the SSS stage (Park *et al*. 1989). For simplicity, solid-state densification is considered to be accomplished through three

stages: initial, intermediate, and final, Fig. 3.5. The initial stage involves gradually increasing densification. The second but extremely rapid densification stage is where a large fraction of densification is achieved, and the third stage, where the densification rate decreases as the material approaches full density. The smaller the grain size i.e. the higher the internal interface areas, then the higher the solid-state sintering intensity. Although Fig. 3.5 resembles the classic sintering behaviour of many materials, it is important to note that densification occurs during heat-up at solid-state temperatures based on equilibrium phase diagrams, instead of isothermal holding. In fact, not only does it start at solid-state temperatures, most of the densification is completed at solid-state temperatures. In other words, only a minor fraction of densification actually takes place during LPS. This is just one of a number of studies that report a significant level of densification of nanocrystalline WC-Co powders occurring at solid-state temperatures (Porat, Berger and Rosen 1996; Goren-Muginstein, Berger and Rosen 1998; Arato *et al*. 1998).

Fig. 3.5 Densification of WC-10Co with different initial WC grain sizes as a function of temperature. The dashed line represents the WC-Co eutectic (~ 1320°C) (Fang *et al*. 2005).

Once a liquid phase forms during heating of a powder compact, liquid then flows into fine capillaries due to the capillary pressure difference between the fine and coarse channels between solid particles. The solid particles can be redistributed by the flow of liquid (Huppmann and Riegger 1975; Kang *et al*. 1984; Lee *et al*. 1999) and in LPS models this phenomenon is referred to as 'particle rearrangement'. The possibility of particle rearrangement by liquid flow relies upon various factors including liquid volume fraction, dihedral angle, extent of sintering at the moment of liquid formation and particle size (Lee and Kang 2001). At temperatures above 1200°C, the densification mechanism can be described as a global diffusion in the Co phase (diffusional creep) under the action of capillary forces with WC particle rearrangement caused by spreading of the binder phase into pores. This spreading process may be preceded by the rapid surface diffusion of a thin film of Co onto WC grains (Missiaen and Roure 1998). Enhanced surface and boundary diffusion of metallic atoms has been mentioned in

hardmetals when the carbide is soluble in the metallic phase (Meredith and Milner 1976). At temperatures lower than 1200°C, diffusion in the Co phase is inhibited, thereby limiting binder phase spreading into pores. Densification would then only be facilitated by a solution-precipitation mechanism. The nature of this inhibition is understood to be due to the high WC-Co interfacial tension at low temperatures (Missiaen and Roure 1998) and could be related either to the low solubility in the binder phase (solubility increases from 0.8 to 3 at% WC when the temperature increases from 1000° to 1200°C (Guillermet 1988)) or to the presence of an oxide layer on the WC surfaces (oxygen cleaning of WC surfaces under vacuum ends in the 1000° to 1200°C temperature range (Ågren *et al*. 1996)). Inhibition of Co spreading could be partial, with a critical pore radius r_c, as encountered in LPS (Park, Kwon and Yoon 1986). Spreading would stop as soon as pores smaller than r_c are filled. The critical radius can increase with temperature as the WC-Co interfacial tension decreases. Microstructural analyses have shown that small pores are eliminated first, with increasing pore size eliminated with increasing temperature (Roure and Missiaen 1995). Any inhomogeneity of Co binder distribution or local fluctuations of green density, WC surface area or grain size, causes local fluctuating densification and results in micropores or pores, Fig. 3.6.

Fig. 3.6 Stages 1 (initial) and 2 (intermediate) of solid state sintering (Gille *et al*. 2002).

In summary, the primary driving force for sintering of nanostructured hardmetals, as for any sintering system, is a reduction in the interface energy of the system. This is accomplished by reducing the area of the surfaces and interfaces of the compact, which happens mainly by a combination of two concurrent processes (Schubert, Bock and Lux 1995), namely densification and WC grain growth. The latter process is of particular importance during the sintering of nanostructured alloys and will be discussed in the following section. Based upon statistical analysis, the order of critical parameters for densification of nanocrystalline WC-Co powders is reported to be sintering temperature >> die compaction pressure > powder selection > heating method (Park, Johnson and German 2006).

3.3.3 Grain growth

Grain growth in nanostructured materials is primarily driven by the excess energy stored in the grain or interphase boundaries. As grain growth involves the transport of atoms across and presumably also along the boundaries, the activation energy of the

process is frequently compared with that of grain boundary diffusion (Gleiter 2000). Grain growth in nanostructured WC-Co occurs predominantly due to the high interface between the WC phase and the Co phase by the solution-reprecipitation process (Bock, Schubert and Lux. 1992).

Success in nanopowder consolidation is intimately related to the control of the competition between densification and grain coarsening. In the case of densification, minimisation of the internal energy drives WC grain growth whereas a reduction of the total WC-Co interface area is the driving force of WC coarsening. In practice, continuous as well as discontinuous (local or exaggerated) grain growth must be considered and suppressed as much as possible.

Because of the capillary pressure exerted on a particle, the activity of the atoms in the particle and, hence, its solubility in the matrix, increases as the particle size decreases (Kang 2005). Therefore, the atoms dissolved in the matrix from small particles are transported to large particles, resulting in growth of large grains. Continuous grain growth during LPS may be considered as an Ostwald ripening process. Smaller WC particles dissolve due to their higher dissolution potential and reprecipitate after diffusion through the binder at coarser WC grains. The intensity of this dissolution–reprecipitation process and, therefore, the WC growth rate, is increased by high carbon content and essentially decreased by addition of grain growth inhibitors such as Vanadium carbide (VC), Chromium carbide (Cr_3C_2), Niobium carbide (NbC) etc., which will be detailed further in section 3.3.3. All these grain growth additives are soluble in the Co binder and can segregate at the WC/Co interfaces or as separate particles during

sintering. It is believed that the additives alter the WC/Co interfaces by forming mixed crystals or new phases, reducing the interface energy and therefore the driving force of grain growth (Gille *et al*. 2002). As with densification, WC grain growth is not restricted to liquid-phase sintering but occurs to a remarkable extent during SSS (Schubert, Bock and Lux 1995; Schubert, Bock and Lux 1999).

To suppress discontinuous grain growth and exaggerated WC grains is a fundamental prerequisite to obtain high strength and high performance hardmetals. Apart from impurities or inhomogeneities arising from the raw materials or processing, one reason for discontinuous grain growth is the difference in interface energies on basal (001) and prismatic (100) WC planes (Schubert, Bock and Lux 1995). Although face oriented grain growth may be used successfully for toughening of coarse grained hardmetals with platelet structures (Saito *et al*. 1998), in ultrafine hardmetals it may also cause exaggerated, platelet shaped WC grains, which can degrade strength, wear resistance and other performance related properties. Additionally, the microstructure of the carbide can significantly influence grain growth behaviour, including such features as densities of stacking faults, dislocations and vacancies. A highly distorted WC lattice shows a tendency towards stronger grain growth in the solid state as well as in LPS (Gille *et al*. 2002).

Full density or rapid sintering of nanosize powders is achieved when the green structure contains a narrow pore size distribution, which is similar to conventional powders. Conversely, densification is retarded or inhibited when pore size distribution is wide. In this case, big pores become larger and only small pores shrink. The removal

of large pores is a lengthy process and requires higher temperatures. Therefore, the overall effect of large pores is to slow densification and induce undesirable coarsening. A thermodynamic model of pore shrinkage was developed by Kingery, Bowen and Uhlmann (1976), which was based on pore curvature, and predicted the pore size for the transition between pore shrinkage and pore growth. A complicating event is the separation of large pores from the grain boundaries that occur in the final sintering stages. This was incorporated in pore size-grain size maps (Brook 1969), which designated the regions where such pore separation from grain boundary would occur. When pore-grain boundary breakaway takes place, the detached pores will no longer benefit from easy transport paths such as grain boundaries. Instead, transport is by slower volume diffusion and, as a consequence, densification occurs at a slower rate. This is the stage when open porosity breaks down and pores become closed. Since grain boundary migration is no longer restricted by pores, grain coarsening takes place; or pinning of grain boundary migration due to residual pores is no longer effective. Therefore, in the final sintering stage, densification is hindered and significant grain growth occurs.

The influence of pores on grain coarsening has been well documented theoretically (Lange 1989; Zhao and Harmer 1992; Sweeney and Mayo 2002; Mortensen 1997). The presence of open pores in nanopowders inhibits grain growth in a similar way that pores prevent grain coarsening in ceramics of ordinary grain size (Groza 2007). As soon as pore isolation occurs, grain growth becomes unrestricted but the pinning action of the pores is difficult to predict. It follows the same principles as in coarse grained materials.

In summary, whilst at lower densities, the pores themselves retard grain growth effectively. However, stronger grain growth occurs when the majority of pores have been removed and the rest have separated from grain boundaries. Before this stage, sintering additives remaining heterogeneous and finely distributed significantly retard grain growth and at the same time enhance densification.

3.3.4 Grain growth inhibitors

The addition of grain growth inhibitors to ultra-fine WC-Co compositions is one of the essential factors in preventing WC grain growth during sintering. Inhibitors cause a decrease in the rate of solution-reprecipitation by a diminution of the interfaces through a modification of the liquid phase (Kim and Accary 1980).

The most commonly used grain growth inhibitors in the hardmetal industry are Cr_3C_2, TaC and VC. The choice of inhibitors is based on their overall effectiveness, which has been shown to be VC > Cr_3C_2 > NbC > TaC > TiC > Zr/HfC (Bock, Schubert and Lux 1992; Wittmann, Schubert and Lux 2002) in order from most effective to least effective. It has also been reported that an addition of VC inhibitor below 0.5 wt.% for nanoscale WC-Co powders, and below 1.3 wt.% TaC, 1.0 wt.% VC/TaC, can lead to abnormal WC grain growth and facetted crystals due to a lack of grain growth inhibitor (Kim *et al*. 1998). This would suggest that higher levels of inhibitor may be required when WC is reduced into the nanoscale.

The presence of VC in a Co matrix has also been found to have a negative influence on the solubility of W in Co (Seo, Kang and Lavernia 2003), thus inhibiting the dissolution and growth of WC. The solubility of VC in the Co binder is 8.19 wt.% (Falkovsky *et al*. 2001) with the content in WC-Co usually kept around 0.7 wt.%, in order to avoid embrittlement due to (V,W)C precipitation at the WC-Co interface (Jaroenworaluck *et al*. 1998; Egami, Ehira and Machida 1993) during cooling. Cr_3C_2 remains in solution in Co during cooling, although it tends to diffuse towards the WC-Co boundaries (Yamamoto *et al*. 2001). Both VC and Cr_3C_2 have been found to lower the onset temperature of the eutectic reaction in WC-Co. In the case of VC it was found to decrease by 25-30°C (Luyckx *et al*., 1996), as illustrated in Fig's 3.7 (a) and (b), and in the case of Cr_3C_2, by approximately 40°C (Okada *et al*. 1998). Later work has suggested that VC is a more effective grain refiner because a smaller amount of VC is required to obtain the same WC grain size, and that it also allows the attainment of extremely fine grain sizes, which can only be obtained by adding much larger amounts of Cr_3C_2 (Luyckx and Alli 2001). VC is equally effective in limiting continuous grain growth for all temperatures within the temperature range 1300 to 1575°C, Fig. 3.8, (Fang and Eason 1995; Morton *et al*. 2005) and was also found to be the most effective inhibitor of discontinuous grain growth (Morton *et al*. 2005).

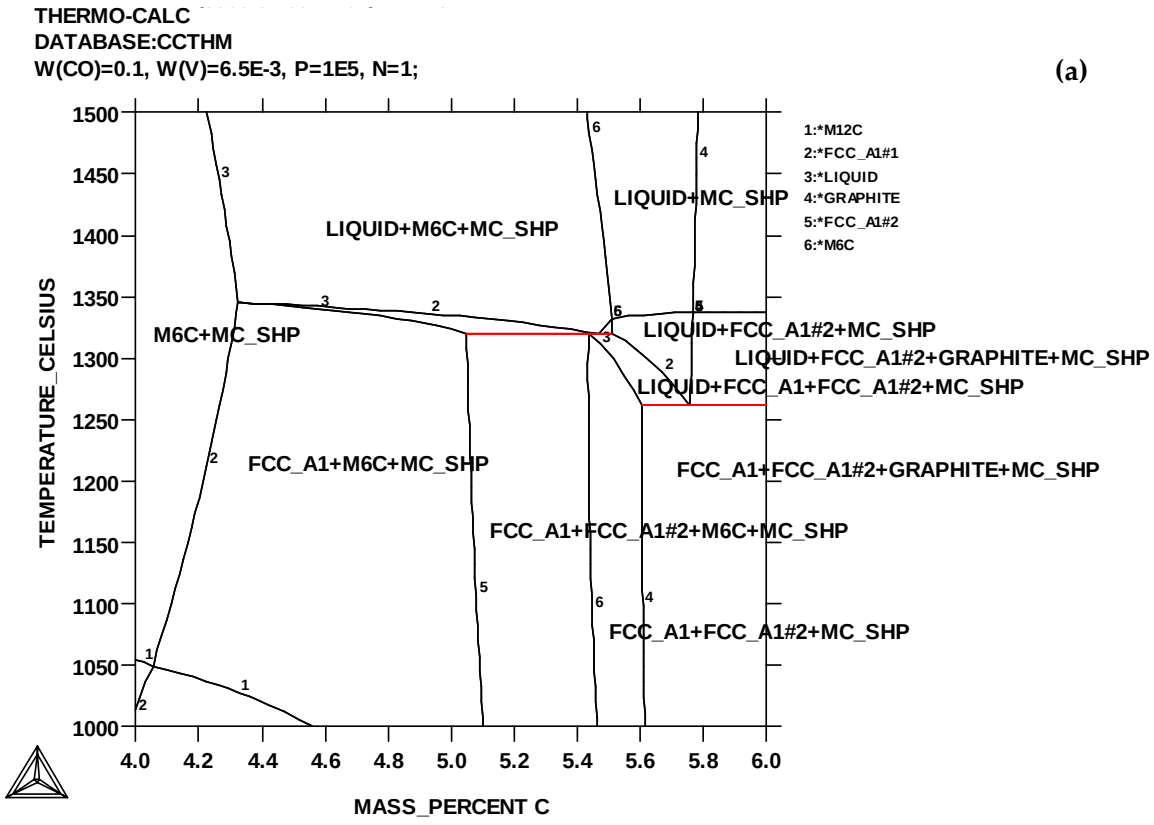
THERMO-CALC
DATABASE:CCTHM
W(CO)=0.1, W(V)=6.5E-3, P=1E5, N=1;
(a)
1:*M12C
2:*FCC_A1#1
3:*LIQUID
4:*GRAPHITE
5:*FCC_A1#2
6:*M6C
LIQUID+M6C+MC_SHP
LIQUID+MC_SHP
M6C+MC_SHP
LIQUID+FCC_A1#2+MC_SHP
LIQUID+FCC_A1#2+GRAPHITE+MC_SHP
LIQUID+FCC_A1+FCC_A1#2+MC_SHP
FCC_A1+M6C+MC_SHP
FCC_A1+FCC_A1#2+GRAPHITE+MC_SHP
FCC_A1+FCC_A1#2+M6C+MC_SHP
FCC_A1+FCC_A1#2+MC_SHP
TEMPERATURE_CELSIUS
MASS_PERCENT C
1500
1450
1400
1350
1300
1250
1200
1150
1100
1050
1000
4.0
4.2
4.4
4.6
4.8
5.0
5.2
5.4
5.6
5.8
6.0

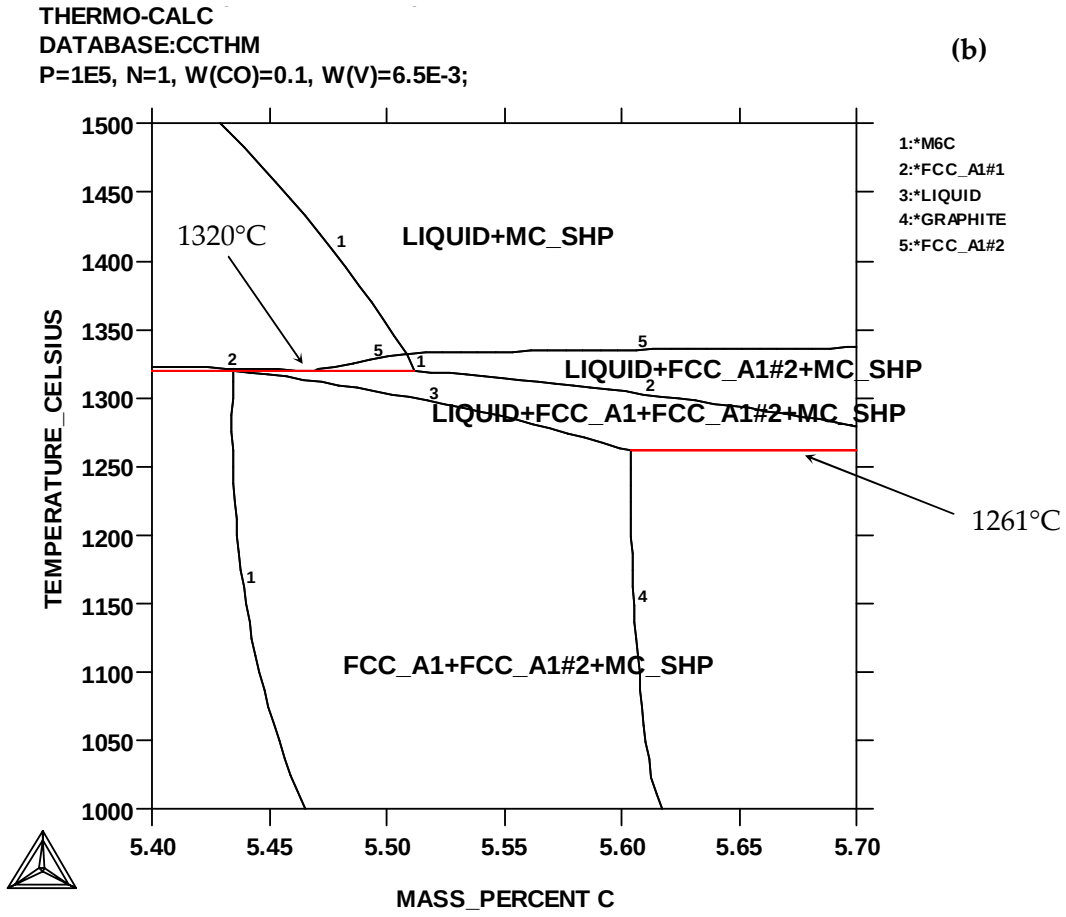

Fig. 3.7 Vertical section of the (a) tungsten-cobalt-carbon-vanadium (W-Co-C-V) quaternary system, calculated with Thermo-Calc coupled with the CC THM thermodynamic database with (b) showing an extended section of the diagram. The cobalt content is kept constant at 10 wt%.

Fig. 3.8 Effects of temperature on the magnetic coercivity (*Hc*) of carbon saturated WC-10Co samples with various grain growth inhibitors. Magnetic coercivity is approximately proportional to the inverse grain size (Morton *et al*. 2005).

It is generally accepted that the effectiveness of grain growth inhibitors is dependent upon the availability of the inhibitor at the WC-Co interface. The higher the availability, the greater the potential effect on the interfacial free energy and the more probable the blocking of nucleation sites. The availability of the inhibitor is affected by the total inhibitor content, inhibitor solubility in the binder phase, WC particle size, binder content and inhibitor distribution (Bock, Schubert and Lux 1992). Sintering under pressure may be another effective means to suppress grain growth. This approach will be discussed in the following section.

3.4 Densification of nanostructured WC-Co powders

3.4.1 Conventional sintering

Sintering of nanopowders is expected to take place at significantly lower temperatures due to enhanced driving force and kinetics in nanosize powders. These lower temperatures may minimise or even eliminate the use of grain growth inhibitors.

Nanostructured WC-Co powders have been fully consolidated with minimal grain growth by conventional sintering, but the final grain size was on the order of 100-200 nm (Wu, Kim and Kear 1993; Fang and Eason 1995; McCandlish, Kim and Kear 1992). This was attributed to the liquid-phase mechanism, which typically promotes grain growth. Approaches to restrict grain growth in WC-Co are the use of inhibitors or exploration of the sintering temperature to possibly achieve densification only in the solid state.

3.4.2 Pressure-assisted consolidation

An applied stress adds a new component to the curvature-related driving force for densification. The applied mean stress, known as the hydrostatic stress, induces new plasticity-driven sintering mechanisms, as well as a stress-assisted diffusion mechanism (Groza 2007) with both mechanisms enhancing the densification rate. The shear component of the applied stress causes particle rearrangement and collapse of large pores. Particle rearrangement and macroscopic deformation of pores increases the number of particle contacts. This alteration in pore size and distribution is more

amenable to pore removal than in pressureless sintering (Lange 1989; Hague and Mayo 1997). The main benefit is the elimination of large pores in agglomerated powder, which is the cause of exaggerated grain coarsening at densities above 90%.

Sinter-HIP is a procedure that combines vacuum sintering with HIP technology by utilising gas pressure treatment immediately after the sintering process and at the same high temperature. This type of process requires distinctly lower pressures (6-10 MPa) than HIP alone, and therefore entails lower procurement and operating costs. Also, the supplementary application of pressure takes place during the final phase of the sintering process when the carbide structures are still soft. The pressure applied in this process is below that necessary to overcome capillary action, but above that necessary for gross structural movement (Lueth 1974). This prevents any voids or porosity from being filled with Co but rather from the surrounding structure by gross movement.

Although this technique is now widely used in the hardmetal industry to produce ultrafine materials, its reported use with nanoscale WC-Co is limited due to the elevated temperatures involved (> 1310°C binary eutectic temperature WC-Co) with reported studies (Shao *et al*. 2003; Shi *et al*. 2006) showing an increase in WC grain size to over 0.2 μm.

3.4.3 Non-conventional sintering technique

In the last decade, methods based on field sintering that involve pulsed current discharge and resistance heating, seem to have been the most active processing

technique for WC-Co nanopowder densification (Kim *et al*. 2004; Michalski and Siemiaszko 2006; Cha, Hong and Kim 2003; Sivaprahasam, Chandrasekar and Sundaresan 2006; Jia *et al*. 2005; Zhang, Shen and Sun 2004). The main purpose in using these methods is to enhance densification, thus reducing the sintering temperature or time with the ultimate benefit of preserving the initial nanoscale grain size.

Spark plasma sintering (SPS), sometimes termed field-activated sintering technique (FAST), or pulsed electric current sintering (PECS) works by creating electrical sparks between powder particles in the sintered body. The main characteristic of the SPS process is that a pulsed DC current passes directly through a graphite die, as well as the powder compact in the case of conductive samples. Therefore, heat is generated internally, which facilitates a very high heating rate and, hence, a very fast sintering process. Compared to other techniques, such as HIP or pressureless sintering, full density of the material can be achieved at lower temperatures and shorter holding times at maximum temperature, saving time and energy.

The enhanced densification is most noticeable at lower temperatures or when multiple discharges of current through the powder compact are applied. Densification in nanostructured WC-Co during SPS was shown to begin around 800°C (solid phase sintering) with liquid phase beginning at 1000°C and ending at 1150°C, with a WC grain size of 0.3μm (Wang *et al*. 2006). A small addition of phosphorus (0.3 wt.%) enhanced densification rates through the chemically-activated sintering effect of P, achieving full densification at 1000°C (Zhang, Shen and Sun 2004), which is substantially lower than those temperatures used in conventional techniques, such as sinter-HIP.

In summary, the most distinctive features of the sintering process of nanosized powders are the high driving force and enhanced kinetics due to large curvature effects. Grain growth in nanostructured materials is primarily driven by the excess energy stored in the grain or interphase boundaries. The boundaries move toward their centres of curvature and the rate of movement varies with the amount of curvature. Densification during liquid phase sintering of the WC-Co system is largely dependent on pore size and distribution. Since pore filling occurs as a result of grain growth, sintering time for densification is governed by grain growth kinetics. Densification of WC-Co nanopowders takes place at temperatures consistently below those of coarser-grained powders by many hundreds of degrees. There are numerous benefits from using lower sintering temperatures, including not only material-related benefits, such as the elimination of sintering aids but also reduced processing costs.

Consolidation of nanocrystalline powders into fully dense material must not alter the nanostructure in order to retain the unique properties of fine particles. Consolidation of WC-Co nanopowders under the applications of temperature and pressure can, generally, yield nearly fully dense compacts. However, recrystallisation and grain growth occur readily during high temperature consolidation of nanocrystalline powders. The science and practice of pressure application, consolidation techniques that can retain the original nanostructure are still in the developmental stage.

3.5 Characterisation of consolidated WC-Co

3.5.1 Electron backscatter diffraction (EBSD)

The acquisition of EBSD (or backscatter Kikuchi diffraction) patterns in the scanning electron microscope (SEM), is a very powerful method for the microstructural characterisation of crystalline materials. Recent developments in instrumentation and software now enable grain structures >0.1 μm to be quantitatively characterised by EBSD (Humphreys 2004). EBSD is based on the acquisition of diffraction patterns from bulk samples in the scanning electron microscope. A further development includes the use of EBSD in conjunction with field emission gun scanning electron microscopes (FEGSEM) (Humphreys 1999). It is this last factor which has made EBSD viable as a technique for characterising sub-micrometre grain structures. Accurate measurement of grain size and phase distribution is necessary to assess the physical properties of WC hard metals.

A phosphor screen is used to intercept the backscattered electrons diffracted from the sample and an EBSD pattern, such as the one shown in Fig. 3.8 (a), is formed on the phosphor screen. An image of the EBSD pattern is then acquired using a video imaging system. The EBSD pattern constitutes a number of Kikuchi bands. Inspection of Fig. 3.9 (a) reveals that each band comprises of a pair of parallel Kikuchi lines, the formation of which is illustrated in Fig. 3.9 (b).

Fig. 3.9 (a) an example of an electron backscattered pattern (EBSP); (b) schematic showing the formation of Kikuchi lines (http://level2.phys.strath.ac.uk/ssd/chartech/ebsd/emrs2000/emrs2000.htm).

Backscattered electrons that satisfy Bragg's law for a given plane emanate in diffraction cones from both the front and back surface of the plane. When these cones intersect the phosphor screen, Kikuchi lines are formed. The Kikuchi lines appear as almost straight lines because the cones are very shallow as the Bragg angle θ_D is of the order of 1° ($\lambda \approx 0.008$ nm for a 25 keV electron beam). Each Kikuchi band is effectively the trace of the plane from which it is formed. The EBSD pattern is therefore a 2-D projection of the crystal structure. Each Kikuchi band subtends an angle of $2\theta_D$ with the sample (Troost, Van der Sluis and Gravesteijn 1993). EBSD is carried out on a specimen that is tilted between 60° and 70° from the horizontal and provides 3 main types of information:

- the absolute 3D orientation of the crystal lattice;

- discrimination between phases based on their crystallographic differences (for example, austenite (fcc) and ferrite (bcc) in steel;
- identification of unknown phases when used in conjunction with EDS.

The most common method of obtaining the size of grains and subgrains from an EBSD map, Fig. 3.10, is by linear intercept methods. The boundaries in the map are identified from the orientations of adjacent data points (pixels) in the map, and may be classified if required as 'high'- or 'low'-angle boundaries. The intercept spacings are then analysed to obtain grain sizes and size distributions in a similar manner to traditional metallographic methods (e.g. DeHoff and Rhines 1968; Underwood 1970). Important considerations in obtaining accurate data by EBSD include the size of the grain/subgrain relative to the spatial resolution of the technique, and the pixel step size (Humphreys 2001). The advantages of EBSD over optical microscopy for quantitative metallography include improved spatial resolution, more accurate data and more complete microstructural characterisation.

Fig. 3.10 EBSD orientation map of WC-6wt%Co with WC grains represented by different colours and Co represented in white (Farooq and Clement 2004).

4. Experimental procedure

4.1 Powder preparation

The chosen compositions and the main characteristics of the starting powders used in this study are shown in Tables 4.1 and 4.2, respectively. Only commercially available powders have been used for this experimental work. All of the powders were supplied by William-Rowland Ltd, Sheffield, UK, apart from the grain growth inhibitor VC, which was supplied by New Metals & Chemicals Ltd, Essex, UK. All of the compositions were ball-milled in a Zoz Simoloyer CM01 (Zoz GmbH, Germany) horizontal milling machine, Fig. 4.1. The powder compositions, together with 5 mm diameter stellite balls, were sealed in a 2l capacity, stellite vessel with a ball-to-powder weight ratio of 10:1. Vacuum pumping to 10^{-2} Torr was repeated three times, followed by Ar gas charging. The ball-milling profile consisted of variable rotation rates and repetitious circulation with a 30 min cyclic operation, detailed in Fig. 4.2. Additional ball-milling times of 60, 180, and 300 min were achieved by simply repeating the cyclic stage with all profiles carried out at room temperature. The cyclic profile was created and controlled by the Simoloyer's control and data acquisition system, Maltoz®, which also monitored process parameters such as rotational speed, temperature, torque, and total energy consumption. The vessel and rotor bearing were cooled by water circulation throughout the cycle and the process temperature was monitored by a thermocouple, which was attached to the inner wall of the vessel, Fig. 4.4.

Table 4.1

Compositions of the powders ball-milled on the CM01.

	Elements (wt%)		
Compositions	WC	Co	VC
WC/Co	90	10	
WC/Co + VC	89	10	1

Table 4.2

Characteristics of the starting powders.

	Powder			
	WC		Co	VC
Mean particle size (μm)	3.50 (FSSS) * 3.72 (LD) *		1.50 (FSSS)	10 (FSSS)
Chemical analysis (ppm)		Chemical analysis (wt%)		
Co	< 5			
C				
Fe	13		0.0067	0.05
Mo	36			
Al				0.004
Ca				0.006
Ni	< 5		0.056	
O_2	160			

* FSSS = Fisher sub-sieve size; LD = Laser diffraction

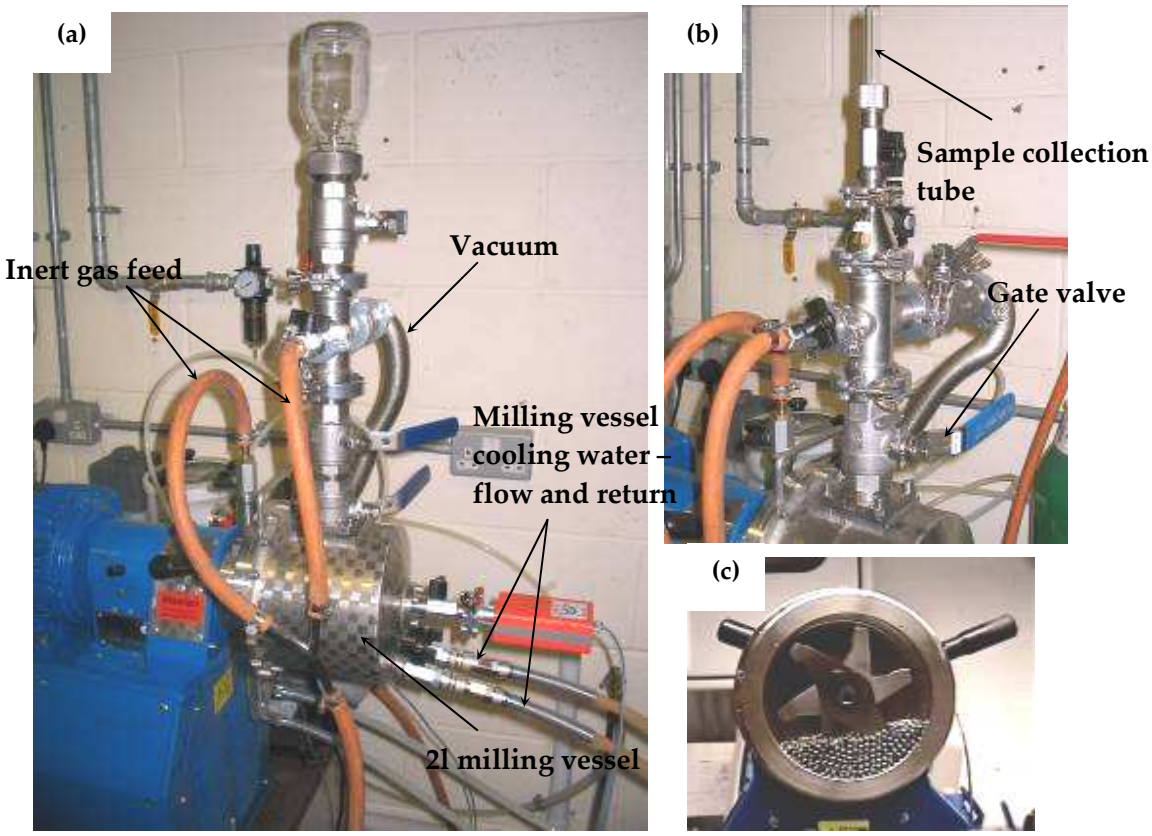

Fig. 4.1 (a) Zoz Simoloyer CM01 horizontal ball mill, shown in the operating position; (b) inert gas and vacuum attachments with powder sample collection tube; (c) view inside the milling head showing the rotor and milling medium.

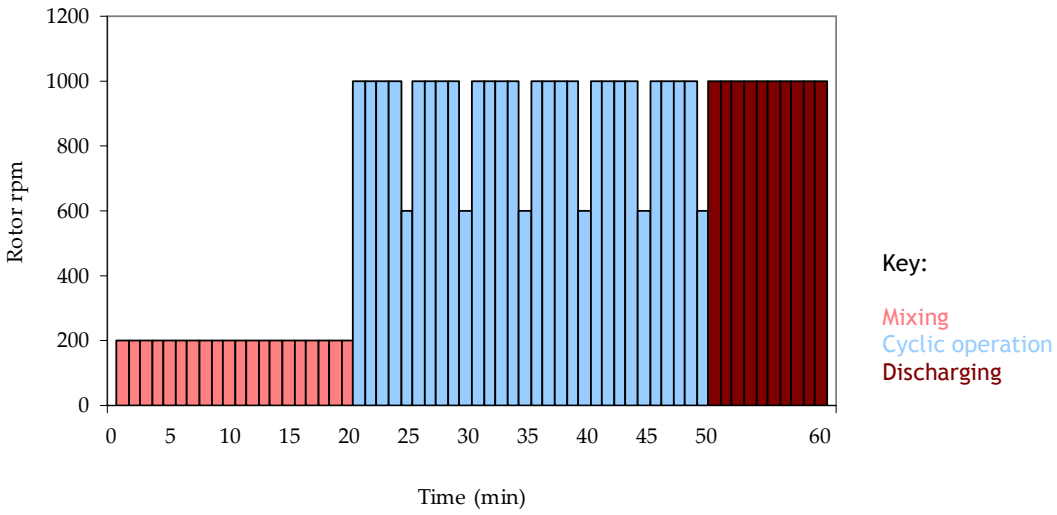

Fig. 4.2 Ball milling profile, (30 min cyclic sequence shown), including a 20 min mixing stage followed by cyclic operation and a 10 min powder discharging stage.

4.1.1 Powder discharging

For cyclic/normal operation, the Simoloyer was operated in the position shown in Fig. 4.1 (a), with the main valves 'closed' and specifically positioned as shown in Fig. 4.1 (b). In order to discharge the powders after completion of the test profile, a specially designed draingrating valve, Fig. 4.3 (a), allowed powder to pass through the screengrating, but prevented any milling balls from passing during discharging. This valve also incorporated a second ball valve (without a screengrating), which provided further air-lock enhancement as the first ball valve was very close to the screengrating, Fig. 4.3 (a).

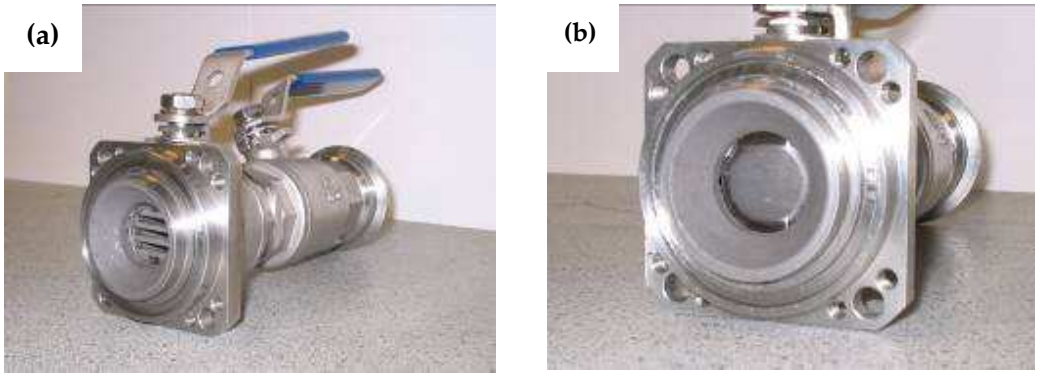

Fig. 4.3 A specially designed draingrating valve showing (a) the valve open and (b) closed.

Before commencement of the powder discharging stage, the test profile was paused to allow the main valves to be opened before the vessel was rotated anticlockwise from the cyclic/normal operating position to the position shown in Fig. 4.4. Opening the valves in the cyclic/normal operating position prevented any powder from becoming trapped behind the ball valve due to gravitational effects.

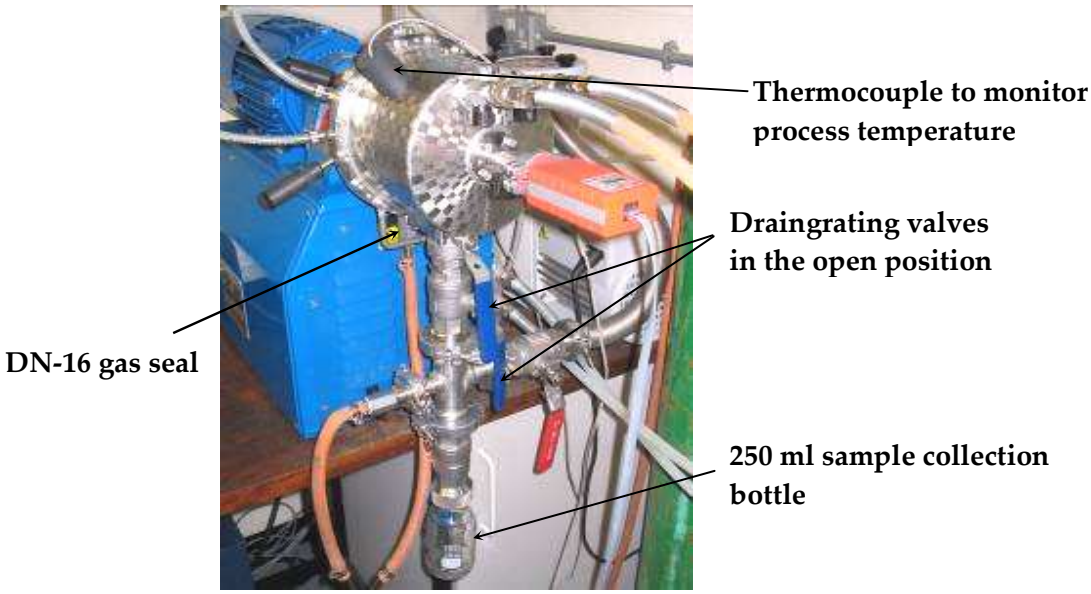

Fig. 4.4 Simoloyer shown in the powder discharging position with all valves open with the sample collection tube replaced with a 250 ml collection bottle.

The test profile was recommenced and the powders were discharged under inert gas as the total system was still air-locked. After powder discharging, the ball valve shown in Fig. 4.1 (b) was closed to allow separation from the system whilst maintaining the powders in an inert atmosphere.

4.1.2 Preparing the vessel

The ball-milling test matrix is shown in Table 4.3. After completion and discharging of a powder composition, for example, WC-10Co, the Simoloyer vessel and ball valves were

cleaned to prevent any cross contamination of the powders. The vessel was returned to the cyclic/normal operating position and all the attachments were removed. A mixture of 500 ml sawdust, 100 ml Al_2O_3, and 2 g zinc stearate was added into the vessel, which was then sealed using a blanking cap. This mixture was milled to a fine powder using a simple profile of 1000 rpm constant rotor speed for 30 min. The cap was removed and replaced with a plastic bottle after which the vessel was then rotated to the discharging position. The profile was re-started to allow all the waste powder to be discharged under gravitational effects. This procedure was repeated 3 times.

Table 4.3

Ball milling test matrix for the CM01.

Composition	Milling time (min)			
	30	60	180	300
WC-10Co	•	•	•	•
WC-10Co+1VC		•	•	•
WC-10Co (-30°C milling)		•		

Following this procedure, the collection bottle and ball valve assembly was attached to the vessel before which, 200 ml of ethanol was added. This was used to remove any remaining powder material and to allow fast evaporation. Once again, a constant profile was used, starting with 500 rpm for 5 min. The used ethanol was discharged and the procedure repeated using 750 rpm and then 1000 rpm for 5 min. At this stage, the colour

of the ethanol was checked to determine whether or not any further ethanol cleaning was required, as it was almost impossible to get clear alcohol again. Once the colour became brighter, or in other words, the content of powder decreased, then ethanol cleaning was complete. A visual inspection inside the vessel verified whether or not the cleaning operation had been successful, with a metallic gloss inside the vessel providing a positive indication. It was important that the vessel was completely dry. To facilitate this, small pieces of cotton wool were added into the vessel and the unit was allowed to run at 200 rpm for 2 min. Once complete, the unit was emptied and run at 1000 rpm for 10 min. The DN-16, gas seal flange at the decompression chamber, Fig. 4.4, was removed and air dried to complete the cleaning procedure.

4.1.3 Altering the milling temperature

A WC-10Co composition was also milled using a modified 2l vessel coupled to a Thermo scientific, Haake phoenix II C40P refrigerated bath. The modified vessel was, in essence, exactly the same apart from modified seals, which allowed the unit to operate within a range of temperatures, and modified inlet/outlet ports. To reduce thermal losses, the flow and return pipework from the bath was insulated using domestic pipe lag and the vessel itself was also insulated, Fig. 4.5. Vessel powder charging was carried out using the same procedure as outlined in section 4.1. Vessel temperature was monitored by the Haake C40P rather than the thermocouple attached to the Simoloyer due to Maltoz® software limits. A mixture of 70% ethylene glycol to 30% water was used as the cooling

medium. System temperature was allowed to stabilise overnight at -30°C after which an identical cyclic operation (Fig. 4.2) was run for 60 min. The powder was discharged under inert atmosphere.

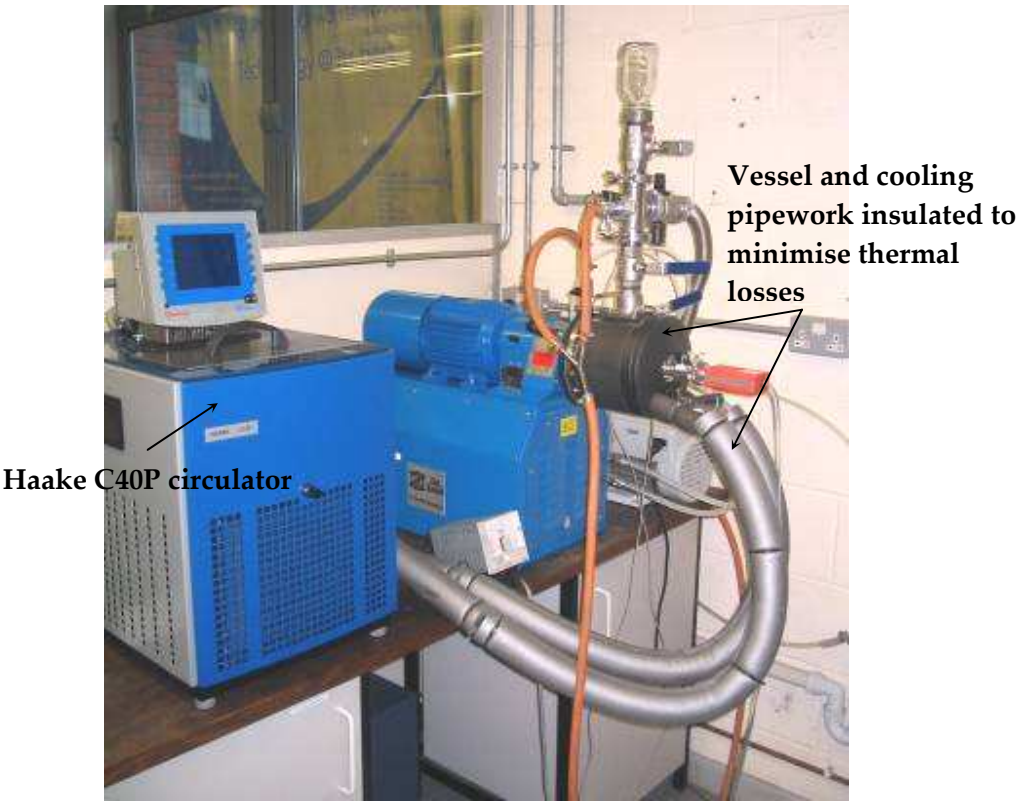

Fig. 4.5 Setup for low temperature milling showing the Simoloyer vessel connected to a Haake C40P refrigerated bath.

4.2 Powder characterisation

4.2.1 X-ray diffraction (XRD)

The microstructure of the ball-milled powders was characterised by X-ray diffraction using a Bruker D8 diffractometer with CuKα radiation. The XRD patterns of the MA samples were recorded in the range 2θ = 25-90°, using a step size of $\Delta 2\theta$ = 0.02° and a counting time of 10 s per step. The divergence slit angle, the antiscatter slit angle in the diffracted beam and the receiving slit width were set to 1/4°, 1/4° and 0.2 mm, respectively. Instrumental broadening was characterised by measuring a suitable sample that shows a minimal amount of physical line broadening caused by defects and small crystallite size, in this case, standard reference material (SRM660) LaB_6 from the National Institute of Standards and Technology (NIST). The measured intensity data was analysed using Bruker Axs TOPAS V4.1 profile and structure analysis software (Bruker 2008).

4.2.2 Thermal analysis – DSC/TG

Onset temperature of the WC/Co eutectic for the powders milled for 60, 180, and 300 min was determined by using a differential scanning calorimeter (DSC 1500) at the University of Loughborough. Calibration of the equipment was carried out prior to sample testing using an empty alumina crucible. New alumina crucibles were used for each sample analysis. A heating/cooling rate of 10°C min^{-1} was used from 25°C up to a

maximum temperature of 1400°C within a flowing N_2 atmosphere, which was set at 30 ml^{-1}.

Thermogravimetric (TG) analysis was carried out on 2 samples ball milled for 60 min, including WC-Co samples milled at RT and -30°C using a TGA/DSC 1, Mettler Toledo International Inc., Columbus, US. In the TG analysis, the percent weight loss of the test sample is recorded whilst the sample is heated at a uniform rate in an appropriate environment. The weight loss over specific temperature ranges provides an indication of the composition of the sample, including impurities such as oxides, as well as indications of thermal stability. For each test, ~ 10-20 mg of powder was used with a new alumina crucible. Heating/cooling rate was set at 10°C min^{-1} from 25°C to 1400°C for each test with N_2 gas flow set at 30 ml^{-1}. Temperature calibration was performed using the precise melting point of a certified reference standard.

4.2.3 Powder morphology and structure

Powder morphology was examined by using an Evo 50, Carl Zeiss SMT AG, Oberkochen, Germany, scanning electron microscope (SEM) operated at 20 kV, with powder from each composition tipped onto a sticky carbon pad. As synthesised WC-Co composite powder particles were mixed with bakelite and hot mounted, followed by the grinding and polishing procedure given in Table 4.7, to allow cross sections of the composite particles to be viewed by SEM.

4.2.4 Particle size

Particle size was characterised using an LM10, Nanosight Ltd, Wiltshire, UK, which uses a laser light source to illuminate nano-scale particles as they move under Brownian motion. A finely focussed, 635 nm laser beam is passed through a prism-edged optical flat, the refractive index of which is such that the beam refracts at the interface between the flat and a liquid layer placed above it. Due to the refraction, the beam compresses to a low profile, intense illumination region in which nanoparticles present in the liquid film can be easily visualised via a long-working distance, x20 magnification microscope objective fitted to a conventional microscope. Mounted on a C mount, a CCD camera, operating at 30 frames per second, is used to capture a video field of view approximately 100 um x 80 um. The nanoparticle tracking analysis (NTA) programme simultaneously identifies and tracks the centre of each particle on a frame-by-frame basis throughout the length of the video. The average distance each particle moves in x and y in the image is automatically calculated. From this value, the particle diffusion coefficient, Dt, can be obtained and, knowing the sample temperature T, and solvent viscosity η, the particle hydrodynamic diameter d is identified. The 3-dimensional Brownian movement is tracked only in 2 dimensions (x and y) and is accommodated by the use of the following variation of the Stokes-Einstein equation 4.1:

$$\left(\frac{x,y}{4}\right)^2 = Dt = \frac{TK_B}{3\pi\eta d} \qquad (4.1)$$

where K_B is Boltzmann's constant. Upper size limits are approached when the Brownian motion of a particle becomes too limited to track accurately, typically 1-2 μm diameter.

Powders from 60 min RT, -30°C, and 300 min milling were analysed by dispersing the powders in 500 μl of water before being inserted into the viewing unit. A 'system flush' was carried out between each analysis. The samples were dispersed in water in order to enable a sufficient number of particles to be analysed within an acceptable time period (in this case 60 seconds) from which a statistically meaningful and reproducible particle size distribution profile could be obtained. A particle size upper limit of 1 μm was used for each analysis.

4.2.5 X-ray fluorescence (XRF)

A quantitative analysis of powder contamination after each stage of ball milling was carried out using a Spectro Xepos X-ray spectrometer, Spectro Analytical Instruments GmbH & Co. KG, Germany, based on the method of energy-dispersive-X-ray-fluorescence analysis (ED-XRF). Sample preparation involved binding 8.5 g of powder with 1.5 g of wax under compression to produce a cylindrical compact.

4.3 Powder compaction

The synthesised powders were cold compacted using a Zwick/Roell 250 kN capacity cylinder, Fig. 4.6. Displacement and pressure application of the cylinder was controlled by a Dartec 9600 series controller, linked to Zwick/Roell workshop '96 software (Zwick/Roell 1996).The software allowed 4 ramps or stages to be incorporated into the test profile, with the cylindrical compaction profile shown in Table 4.4.

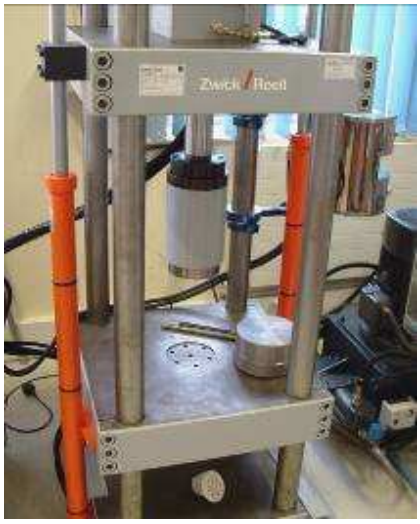

Fig. 4.6 Zwick/Roell 250 kN capacity hydraulic cylinder.

Two tooling geometries were manufactured from BS4659 BD2 tool steel, consisting of a set of 15 mm dia cylindrical punches and die, and a set of rectangular punches and die, 30 x 17 mm. In order to minimise pressing cracks and ease ejection of the samples from the dies, a 1° taper was machined onto both die openings, commencing 10 mm from the top die face (Fig. 4.7), which allowed elastic expansion to progressively take place. The

dies were also designed as two-piece parts, to allow easy removal for re-machining or replacement. A compaction pressure of 250 MPa was used to produce both cylindrical and rectangular compacts for post processing. A mixture of zinc stearate and ethanol was used as a die wall lubricant and was thinly applied to the die wall with a small brush. Compaction experiments using the cylindrical tooling were carried out at a range of pressures from 100 MPa to 400 MPa using only WC-Co milled powders.

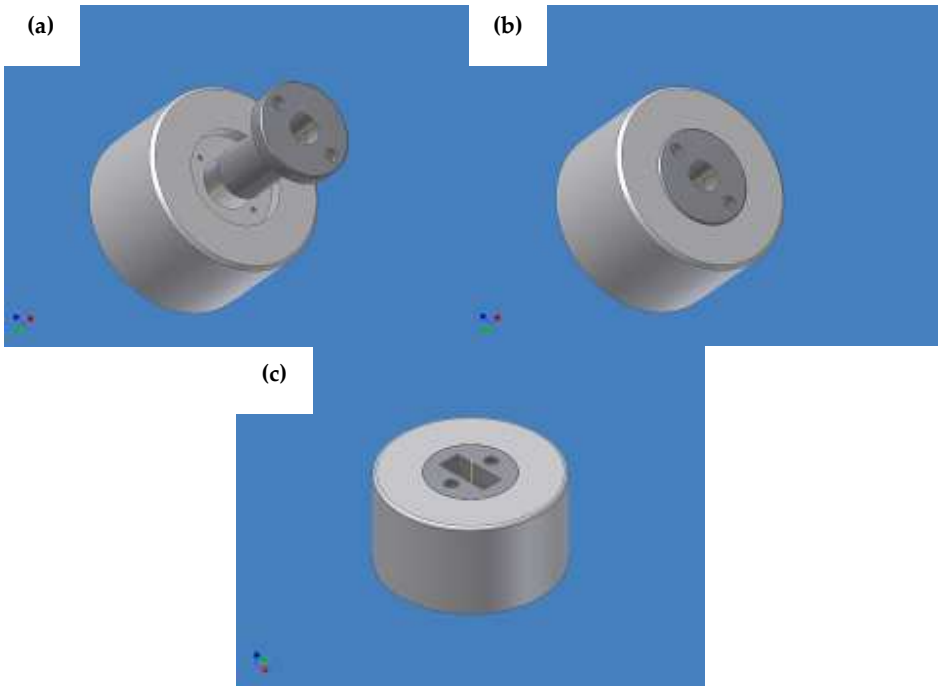

Fig. 4.7 3-D models of (a) and (b) cylindrical die and (c) rectangular die, showing a two part design structure.

The test procedure for producing compacted, cylindrical samples began with aligning the top and bottom punches. Once aligned, a thin layer of lubricant was applied

onto the die wall, which was then allowed to dry. A powder mass of 6.4 g was then carefully poured into the die, Fig. 4.8. The punches and die were arranged as shown in Fig. 4.9, with the die sitting on spacers that positioned the lower punch approximately halfway inside the bore. The test procedure then followed the 4 sequential ramps shown in Table 4.4. The control mode 'Bigstroke' refers to position control of the cylinder and '250 kN' refers to load control. Ramp 2 signifies the application of a pre-load of 5 kN. The load limit shown for ramp 3 signifies a compaction pressure of 250 MPa for the geometry of the cylindrical tooling. The final ramp removed pressure from the compacted sample at a slow, controlled rate in order to try and minimise any possibility of stress-related cracking. After full retraction of the upper punch, the spacers were removed and used to aid removal of the sample, as shown in Fig. 4.10, by pushing the die off the lower punch. Once the die was removed, the sample was easily extracted, Fig. 4.11. All the tooling was then cleaned with ethanol and the procedure repeated five times to generate sufficient samples for green density measurements (section 4.3.1).

Fig. 4.8 Powder mass poured into the lubricated cylindrical die.

Fig. 4.9 Assembly arrangement of the punches and die showing the starting position of the top punch.

Table 4.4

An example of the ramp sequence for controlling the 250 kN Zwick/Roell cylinder to produce cylindrical samples.

	Ramp 1	Ramp 2	Ramp 3	Ramp 4
Control mode	Bigstroke	250 kN	250 kN	Bigstroke
Rate	2.0 mm^{-1} s	0.2 kN^{-1} s	2.0 kN^{-1} s	0.1 mm^{-1} s
Limit	60.3 mm	-5.0 kN	-44.0 kN	100.0 mm

Fig. 4.10 Removal of the die using the top punch and aluminium supports.

Fig. 4.11 Compacted sample after retraction of the top punch and die.

Compaction of rectangular samples for transverse rupture strength testing (TRS), section 4.5.6, was carried out using the same overall procedure as that used for cylindrical compaction. The tooling was aligned and checked for parallelism using feeler gauges with the die resting on spacers once again. A powder mass of 19 g was poured into the die, which was pre-lubricated with a zinc stearate and ethanol solution, Fig. 4.12. The 4 stage ramp sequence is shown in Table 4.5. Pre-load at ramp 2 was increased to -20 kN (50 MPa compaction pressure) with the final compaction pressure (ramp 3) increased to – 100 kN (250 MPa compaction pressure). The spacers were used to push the die off

the bottom punch, Fig. 4.13, leaving the sample easily accessible, Fig. 4.14. The tooling was cleaned and the procedure repeated three times as the green sample was of sufficient size to allow two TRS samples to be cut out.

Fig. 4.12 Assembly arrangement of the punches and die showing the starting position of the top punch for rectangular compacts.

Table 4.5

An example of the ramp sequence for controlling the 250 kN Zwick/Roell test cylinder to produce rectangular samples.

	Ramp 1	Ramp 2	Ramp 3	Ramp 4
Control mode	Bigstroke	250 kN	250 kN	Bigstroke
Rate	2.0 mm^{-1} s	0.2 kN^{-1} s	2.0 kN^{-1} s	0.1 mm^{-1} s
Limit	63.5 mm	-20.0 kN	-100.0 kN	100.0 mm

Fig. 4.13 Spacers used to push the die off the bottom punch.

Fig. 4.14 Top punch fully retracted leaving easy access to the compacted sample.

4.3.1 Determination of green density

All compacted samples were weighed individually for mass using a precision Ps-200 balance, Thermo Fisher Scientific Inc., Leicester, UK. Sample dimensions were measured using vernier callipers and a micrometer with density, ρ, calculated from:

$$\rho = m/v \tag{4.2}$$

where m is sample mass in g, and v is volume in cm^3. The percentage of theoretical density (TD%) is:

$$\frac{\rho_s}{\rho_{th}} \times 100 \qquad (4.3)$$

where ρ_s is the apparent density (green or sintered), and ρ_{th} is the density of the pore free material (14.5 g cm^{-3} for WC-10Co).

4.4 Consolidation

4.4.1 Pressureless sintering

Cylindrical and rectangular green compacts were pressureless sintered using an EHF 17/8, elevator hearth furnace, Lenton, Hope Valley, UK. Samples were placed on graphite trays, which were kept inside an inverted crucible, Fig. 4.15, during sintering. The crucible sat in a groove in the hearth with additional sealing against air ingress provided by a layer of silica sand around the base of the crucible. Optimum temperature uniformity was obtained by the inclusion of molybdenum disilicide heating elements, positioned around the walls of the chamber ensuring uniform heating of the crucible. Heat-up rate inside the crucible was checked against furnace temperature by using a type B thermocouple fed through the gas pipe. The crucible was evacuated before each

sintering run with Ar, which was left flowing at ~ 2l min^{-1} throughout the run. Heat-up and cooling rates were kept constant at 10°C min^{-1} for all sintering runs.

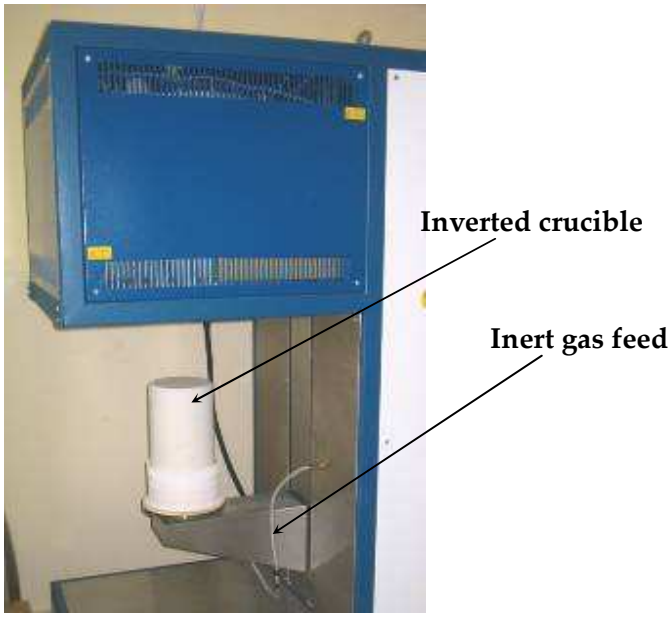

Fig. 4.15 Pressureless sintering furnace showing the inverted crucible and inert gas attachment.

4.4.2 Sinter-HIP processing

The complete test matrix of both types of samples were also sintered by using an industrial based, sinter-HIP (hot isostatic pressure) furnace at Marshalls Hardmetals Ltd, Sheffield, UK. As this was a production process, there was no flexibility with the thermal

cycle. The cycle itself consisted of 10°C min^{-1} to 1390°C under vacuum with an isothermal hold of 60 min under 0.001 MPa partial pressure Ar followed by 5 min at 40 MPa pressure.

4.4.3 Spark plasma sintering (SPS)

SPS was carried out in a HPD 25/1 type furnace, manufactured by FCT Systeme, Rauenstein, Germany. The equipment was based at the School of Engineering and Materials Science, Queen Mary, University of London and is shown in Fig. 4.16. The powder mixture was poured into a 20 mm dia graphite die, set-up with graphite paper inserts. Each test was carried out in vacuum with temperature controlled by a pyrometer (Impac, 400–2300°C) focused at the bottom of a central core hole in the upper punch, situated about 2 mm from the top surface of the sample. Thermal carbon felt insulation was used around the die to avoid thermal gradients inside the sample during sintering. Table 4.6 presents the milled powders and SPS parameters used in this study. SPS sample size was based on 20 mm dia x ~ 5 mm for each test.

Fig. 4.16 SPS facility (a) used to consolidate the hardmetal powders, with (b) a spark plasma reaction shown in the furnace. (Pictures courtesy of the School of Engineering and Materials Science, Queen Mary, University of London).

Table 4.6

SPS test parameters and powder samples used in the study.

Material	MA condition	Heat up rate (°C min $^{-1}$)	Temp. (°C)	Axial press. (MPa)	Hold time (min)	Cooling rate (°C min $^{-1}$)
WC-10Co	RT, 300 min	150	1100	50	10	150
WC-10Co	RT, 60 min	150	1100	100	10	150
WC-10Co	-30°C, 60 min	150	1100	100	10	150
WC-10Co	-30°C, 60 min	150	1150	100	5	150
WC-10Co	-30°C, 60 min	300	1200	100	3	100

4.5 Determination of mechanical properties

4.5.1 Density

Density of consolidated, cylindrical samples was determined by Archimedes method following ISO 3369:1975. Individual samples were suspended by wire on a Mettler H51AR balance and the weight recorded. The sample was then weighed in liquid, in this case, distilled water with a couple of drops of wetting agent (washing liquid), and the weight recorded. Density, ρ, of the sintered sample was calculated from:

$$\rho = \frac{m_1}{m_2} \frac{x}{} \frac{\rho_1}{} \qquad (4.4)$$

where ρ_1 is the density in air of the liquid in g cm^{-3}, m_1 is the mass in g of the sintered sample in air, and m_2 is the mass in g of the liquid displaced by the test piece.

4.5.2 Metallographic preparation

All sintered cylindrical samples were hot mounted in bakelite in order to prepare the surfaces for hardness measurements (section 4.5.4) and metallographic examination. Four samples at a time were ground and polished on a Pedemax-2, Struers, Solihull, UK, using the preparation technique shown in Table 4.7. All the grinding discs, polishing cloths, and suspension fluids were supplied by Struers. Stage 8 was included and/or

excluded depending on the required metallographic examination with a 1 μm diamond finish used for the determination of hardmetal phases and porosity levels and a SiO_2 finish used for image analysis techniques.

Table 4.7

Metallographic preparation technique.

Stages	Time (min)	Force (N)	Disc	Medium
1. Grinding	5	15	120 grit diamond disc	Water
2. Grinding	5	15	220 grit diamond disc	Water
3. Grinding	10	15	600 grit diamond disc	Water
4. Grinding	10	15	1200 grit diamond disc	Water
5. Polishing	10	10	MD Dac	6 μm diamond
6. Polishing	10	10	MD Dac	3 μm diamond
7. Polishing	10	10	MD Dac	1 μm diamond
8. Polishing	30	10	MD Nap	SiO_2 suspension

4.5.3 Determination of hardmetal phases and porosity

The microstructure of selected samples was examined by the gradual development of phases by etching, following ISO 4499:1978. For the determination of deleterious type phases (η, and free graphite), the samples were etched for 5 s in Murakami's reagent (100 ml distilled water, 10 g KOH, 10 g $K_3Fe(CN)_6$). To reveal WC grain boundaries, samples were further etched in Murakami's for 3 – 4 min followed by 10 s in 50:50 HCl and H_20. Presence, type, and distribution of porosity was estimated following ISO 4505:1978 by referencing photomicrographs given in the standard as shown in Figs. 4.17 and 4.18.

Fig. 4.17 Type A apparent porosity (x200) from ISO 4505:1978.

Fig. 4.18 Type B apparent porosity (x100) from ISO 4505:1978.

4.5.4 Determination of magnetic properties

Magnetic measurements are widely used by the hardmetal industry for non-destructive quality control. Both coercive force and magnetic moments are measured for this purpose. If interpreted corectly, they can be linked to the Co composition and hence, overall properties and performance.

In two-phase WC/Co hardmetals, coercive force is proportional to the interface area between the Co binder phase and the WC hard phase. The interface area is related to the WC grain size and thus, measurements of coercive force are an indirect method for monitoring this parameter.

Tungsten carbide/cobalt hardmetals generally contain 5-20 wt% Co as a binder phase. The Co binder phase contains both tungsten and carbon in solution. The amount of tungsten dissolved in the binder phase can be assessed by measurement of the magnetic saturation or magnetic moment of the hardmetal because the saturation value of Co decreases linearly (Roebuck and Almond 1988; Freytag, Walter and Exner 1978) with the addition of tungsten and is not affected by the amount of carbon in solution. The term 'magnetic saturation' is an abbreviation for the saturation (or maximum) value of magnetic induction that can be obtained in a testpiece in a strong magnetic field.

The measurements were carried out by Marshalls Hardmetals Ltd, Sheffield, UK. The coercive force measurements were made on a Forster Instruments Koercimat, model 1.095. Calibration was carried out using a known WC-6 wt% Co sample of hardmetal having a coercive force in the range 141-143 oersteds (11.22-11.38 kA m^{-1}, SI unit). The

magnetic saturation measurements were made on a Setaram Sigmameter, model D6025, again using a known 6 wt% Co hardmetal sample for calibration of size 16 mm diameter x 25 mm long, which gave a value of 157-158 gauss cm^3 $gram^{-1}$ (15.7-15.8 μT m^3 kg^{-1}, SI unit). In both cases, the measurements of magnetic properties of the materials used in this study were obtained purely to identify any variations as opposed to obtaining absolute values.

4.5.5 Hardness measurement

The polished sintered cylindrical samples were Vickers hardness tested following ISO 3878:1983 using a force of 294.2N (HV_{30}) with five hardness determinations for each sample, with the mean values used in eq. 4.4. In order to ensure a completely flat surface so that the indentation is of regular geometry, all the sintered samples were ground and polished using the preparation technique given in Table 4.7. Flatness was confirmed after the indentation was made by measuring the diagonals of the Vickers indentation in orthogonal directions. If the diagonals differed by more than 1% then the surface was not flat and the test was declared invalid.

The diagonals of the diamond indenter were measured, as shown in Fig. 4.19, using an optical microscope Polyvar Met, Reichert-Jung, Germany at a magnification of 500 x with Vickers hardness (HV_{30}) calculated from (Roebuck *et al*. 1998):

$$HV_{30} = \frac{1.8544P}{[(d_1 + d_2)/2]^2} \qquad (4.5)$$

where P is applied load (kgf), and d_1 and d_2 are the indentation diagonals (mm).

4.5.6 Palmqvist toughness

The Palmqvist toughness method is widely used for measuring the fracture toughness of hardmetals. There is no standard available for this test method. For the purpose of the toughness method used in this study, the good practice guide for measuring Palmqvist toughness in hardmetals, (Roebuck *et al*. 1998), was followed as it represents a technical precursor to a common standard. In this method, Palmqvist fracture toughness, W_k, is obtained by measuring the total length of cracks emanating from the four corners of a Vickers hardness indentation.

Palmqvist fracture toughness was determined at room temperature using the direct crack measurement method with cracks generated by the Vickers indenter from a single load of 294.2 N (30 kgf). An important prerequisite for reproducible crack length measurement in Palmqvist testing is the removal of the stressed surfaces, which form after grinding of the specimens. Following the work of Exner [4], Viswanadham [5], and Shetty *et al.* [6] this can be done by progressive polishing of the sample. After face grinding, the specimens were polished with successively finer polishes using the schedule shown in Table 4.7 and tested after each polishing stage until the crack lengths became constant.

Each Vickers indentation presented two pairs of radial cracks emerging from each corner with crack lengths measured from five indentations for each sample. Crack length was measured from the corner of the indentation to the crack tip using a Polyvar Met microscope, Reichert-Jung, Germany, a stage graticule and image analysis software. Crack lengths were measured at x500 magnification. The summation of crack lengths gave a total crack length, *T*. If more than one crack was observed emanating from the indentation tip then the indentation was ignored. If the total crack length was less than 40 μm then the test was considered invalid. For a 60 kgf load, this corresponds to a toughness value, W_G, of 7360 N m^{-1} (or 25 MN $m^{-3/2}$ for W_k) for a material with a hardness of 1100 HV_{60} (Roebuck *et al*. 1998). This type of material is likely to have a coarse structure and the individual crack lengths at each indentation corner will be no more than one or two grains long. This is too short to be confident that the crack is sampling a representative volume of hardmetal. W_k was obtained using the formula (Shetty *et al*.):

$$W_k = A\sqrt{HV}\sqrt{W_G} \qquad \text{(MN m}^{-3/2}\text{)} \qquad (4.6)$$

For the toughness to be expressed in MN $m^{-3/2}$ the value of A is 0.0028 (Shetty), HV is the hardness in N mm^{-2}, W_G (N mm^{-1}) is given by P/T where P is the indentation load in N, in this case 294.2 N, T is the total crack length (mm). The schematic diagram, Fig. 4.19, shows the method used to measure crack length and toughness, W_k.

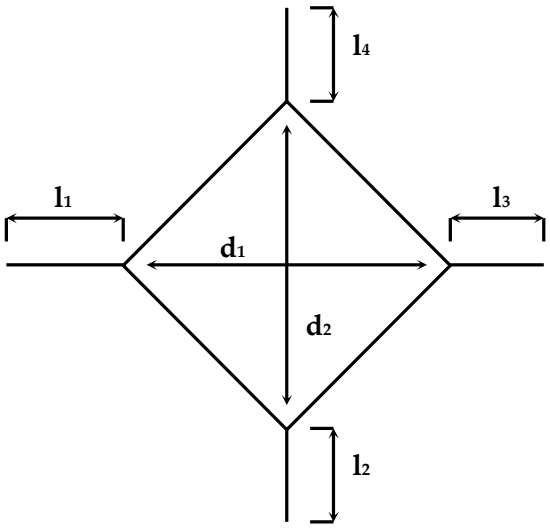

Total crack length, $T = l_1 + l_2 + l_3 + l_4$

$W_G = P/(l_1 + l_2 + l_3 + l_4)$

Fig. 4.19 Schematic diagram and definitions for Palmqvist test method.

4.5.7 Transverse rupture strength (TRS)

Sintered rectangular samples were prepared according to ISO 3327:1982. To bring the samples into line with the required dimensions and surface preparation characteristics of the standard, they were firstly cut in half along their length using a Struers Accutom 50 cut-off machine. The samples and cutting disc were flooded with coolant during cutting to minimise any localised heat build up. In order to grind all four faces parallel to the length within set tolerances, the samples were adhered to a flat disc from a Struers Pedemax-2 using a wax adhesive, which was melted onto the disc to secure the TRS samples, Fig. 4.20. Each parallel face was ground and polished up to stage 5 of the metallographic preparation technique shown in Table 4.7. The four long edges of each sample were chamfered to 0.15 to 0.20 mm using a specially designed jig, Fig. 4.21 that

positioned the sample at 45°. The chamfers were applied by holding the jig against a 220 grit diamond disc with copious quantities of water, with chamfer size and angle checked on a shadowgraph. The purpose of applying chamfers is to reduce stress concentrations caused by damage along the edges of the rectangular section test-pieces.

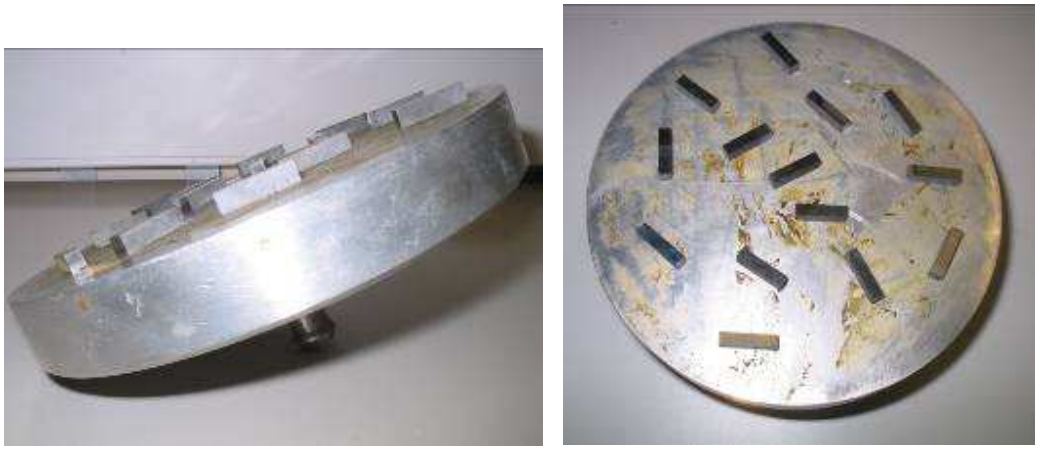

Fig. 4.20 Sintered TRS samples secured onto a grinding/polishing disc.

Fig. 4.21 A simple vee-block jig for gripping Type B, TRS test pieces for chamfering.

None of the standards attempts to give more than a schematic of the design of a test-jig because different test machines may require different types of fixtures. A number of the main features of the TRS test-jig, Fig. 4.22, were designed with reference to "The measurement good practice guide for flexural strength testing of ceramics and hardmetals" (Morrell 1997). The test-jig was designed for type B test pieces (ISO 3327:1982) with a span between the hardmetal support cylinders of 14.5 ± 0.5 mm. A key requirement of the design was to minimise frictional effects by allowing the support and loading rollers freedom to rotate. The designed incorporated 'loose' cylinders as they have the advantage that they are easy to remove and inspect for damage, and economical to replace if necessary. The disadvantage is that they normally have to be gently restrained into known start positions in the test-jig in order to define the spans and the symmetry of the loading roller to the support roller. The method of restraint chosen for the test-jig involved a slight angle of the support plate, Fig. 4.22 (b), such that they rolled to 'stops' at the correct positions. To ensure a uniform distribution of load across the test piece face and to prevent any twisting, a degree of articulation (± 1°) was used in the design of the loading unit relative to the support unit, Fig. 4.23. For well-machined test-pieces and test-jigs, articulation is needed only for the loading unit relative to the support unit (Morrell 1997). The test-jig design allowed the loading roller to be centrally positioned between the support rollers.

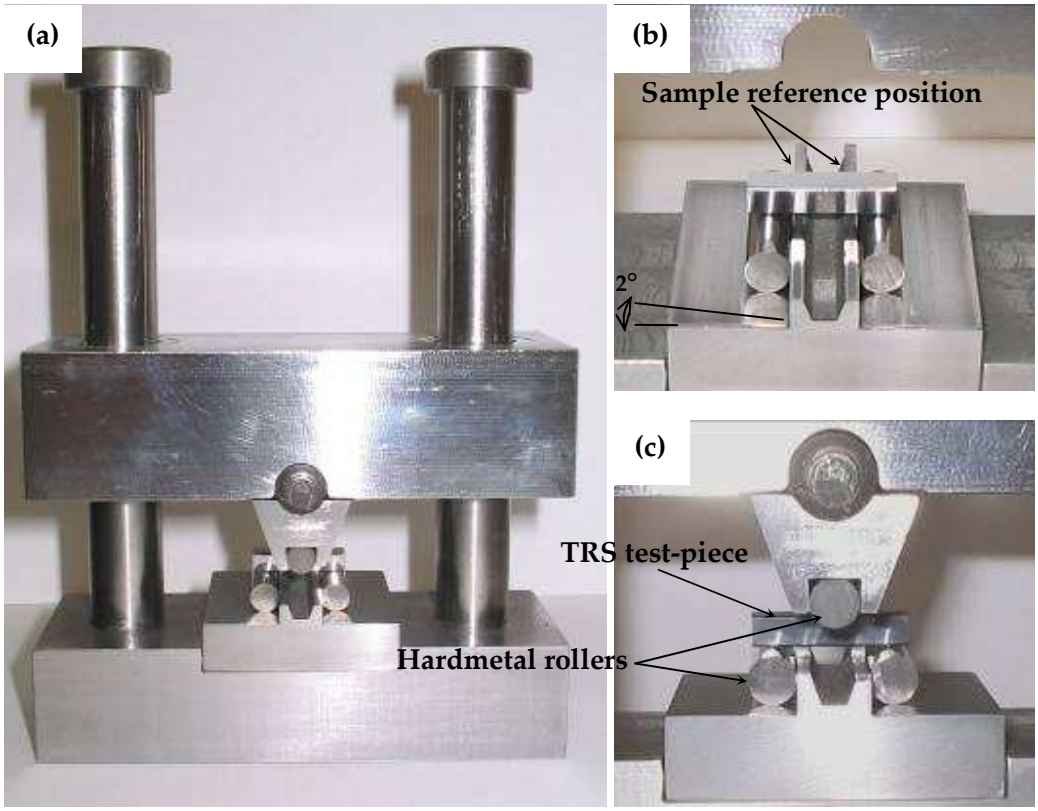

Fig. 4.22 (a) TRS (3-point bending) test-jig using rolling rollers and articulation of the loading roller. Test-jig (b) also shows the rollers held in their start positions using a slight slope on the support surface and the sample reference position, with (c) the TRS test-piece under load.

The test itself was carried out by using a calibrated Zwick/Roell 100 kN static test machine with the test-jig arranged as shown in Fig. 4.24. The test routine involved the application of a small pre-load 0.2 kN followed by an increasing rate of 0.25 kN s^{-1} to failure. TRS, R_{bm}, is expressed in N mm^{-2} and is given by the formula (ISO 3327:1982):

$$R_{bm} = \frac{3xkxFxl}{2xbxh^2} \qquad (4.7)$$

where k is the chamfer correction factor, F is the force required to fracture the test piece in N, l is the distance between the supports in mm, b is width of the test piece in mm, and h is the height of the test piece in mm.

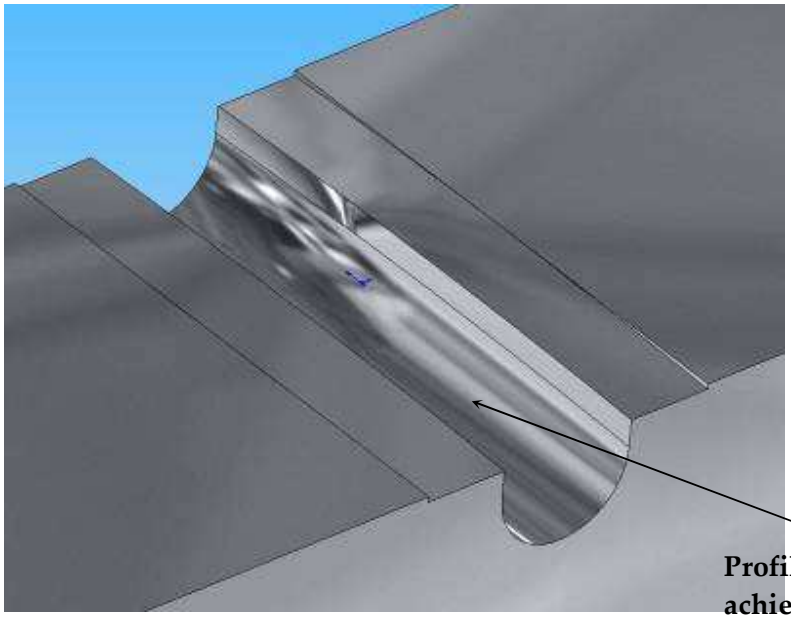

Fig. 4.23 3D model of the loading unit showing the profiled design used to achieve articulation.

Fig. 4.24 Test setup of the TRS rig on a Zwick/Roell 100 kN static test machine.

4.6 Image analysis techniques

4.6.1 Electron backscatter diffraction (EBSD)

The samples shown in Table 4.8 were characterised by EBSD at the National physical laboratory (NPL) using a Zeiss Supra 40 FEGSEM using an HKL (Oxford Instruments) Nordlys II detector and Channel 5 software. EBSD conditions were optimized for each sample, but typically, examination was at 20 kV with a 2 nA probe current and a step size of 0.05 μm with a 60 μm aperture.

The sample polishing used conventional mechanical metallographic techniques, finishing with colloidal silica polish for 30 min, removing approximately 200 μm in total. This technique can give an adequate finish to the samples for EBSD analysis of the WC phase but it is difficult to remove polishing damage from the softer Co binder, so identification of crystallographic orientation from this phase is often not possible, or only to a limited extent and as such, was not measured in this study. High resolution maps and grain size distribution data were obtained for each sample.

Table 4.8

Samples characterised by EBSD.

Composition (wt%)	Milling time (min)	Compaction pressure (MPa)	Sintering technique
WC-10Co	180	250	Sinter-hip
WC-10Co	300	250	Sinter-hip
WC-10Co-1VC	300	250	Sinter-hip

4.6.2 Line intercept method

The most direct way to measure the WC grain size is to polish and etch a cross-section of the microstructure and then use quantitative metallographic techniques to obtain a mean value for the grain size either by point or area counting, by linear

intercept techniques (Heyn method) or by measurement of the number of grains per unit area (Jeffries method). In this study, the grain size and size distributions of the WC-10Co hardmetals were measured manually using the Heyn method.

SEM micrographs of sintered, cylindrical polished samples were taken using a Zeiss Evo 50 operated at 20 kV. These micrographs were used to quantify the mean WC grain size for each composition and sintering process by using Image pro plus software V4.5 (MediaCybernetics 2006). Three concentric circles were overlaid against the micrograph being analysed. Lines were drawn where the grain network crossed the circles. The circles were then automatically disconnected at the specified intersections followed by ASTM E 112 grain size measurements.

The analysis routine used to determine mean WC grain size consisted of the following software sequence:

1. calibration – using the SEM micron marker stored on the image (which is checked during each routine SEM service by Zeiss UK);
2. remove background;
3. edge detection;
4. prune edges – superfluous edges removed;
5. connect edges – detected edges connected to form a continuous network;
6. apply pattern – 3 concentric circles.

5. Results and discussion

5.1 Influence of ball milling time and cyclic operation

5.1.1 WC grain size and strain

The X-ray diffractogram of the unmilled WC-10wt%Co powder is shown in Fig. 5.1. Reflections of the Co phase indicated the presence of fcc-Co, which partially changed to hcp-Co after 60 min of milling due to a mechanically induced transformation. This phenomenon has also been reported in other ball-milling studies and was directly linked to ball-milling intensity (Zhang, Wang and Zhu 2003; Huang, Wu and Ye 1995). The fcc-Co phase is a high temperature phase and is metastable at room temperature, which suggests that 60 min MA induced a partial fcc→hcp transformation at room temperature. The diffractograms of the powders milled for 60 and 300 min at RT are shown in Fig. 5.2 with Fig. 5.2 (a, c) showing the observed data and modelled data from the TOPAS-Academic software, assuming there was no size to strain broadening of the WC peaks. The WC peaks were then allowed to broaden due to size and strain, shown in Fig. 5.2 (b, d). An accurate description of the profile shapes in a powder diffractogram is critical to the success of any profile fitting application. Profile shapes are the convolution product of instrument and sample contributions to the diffraction process.

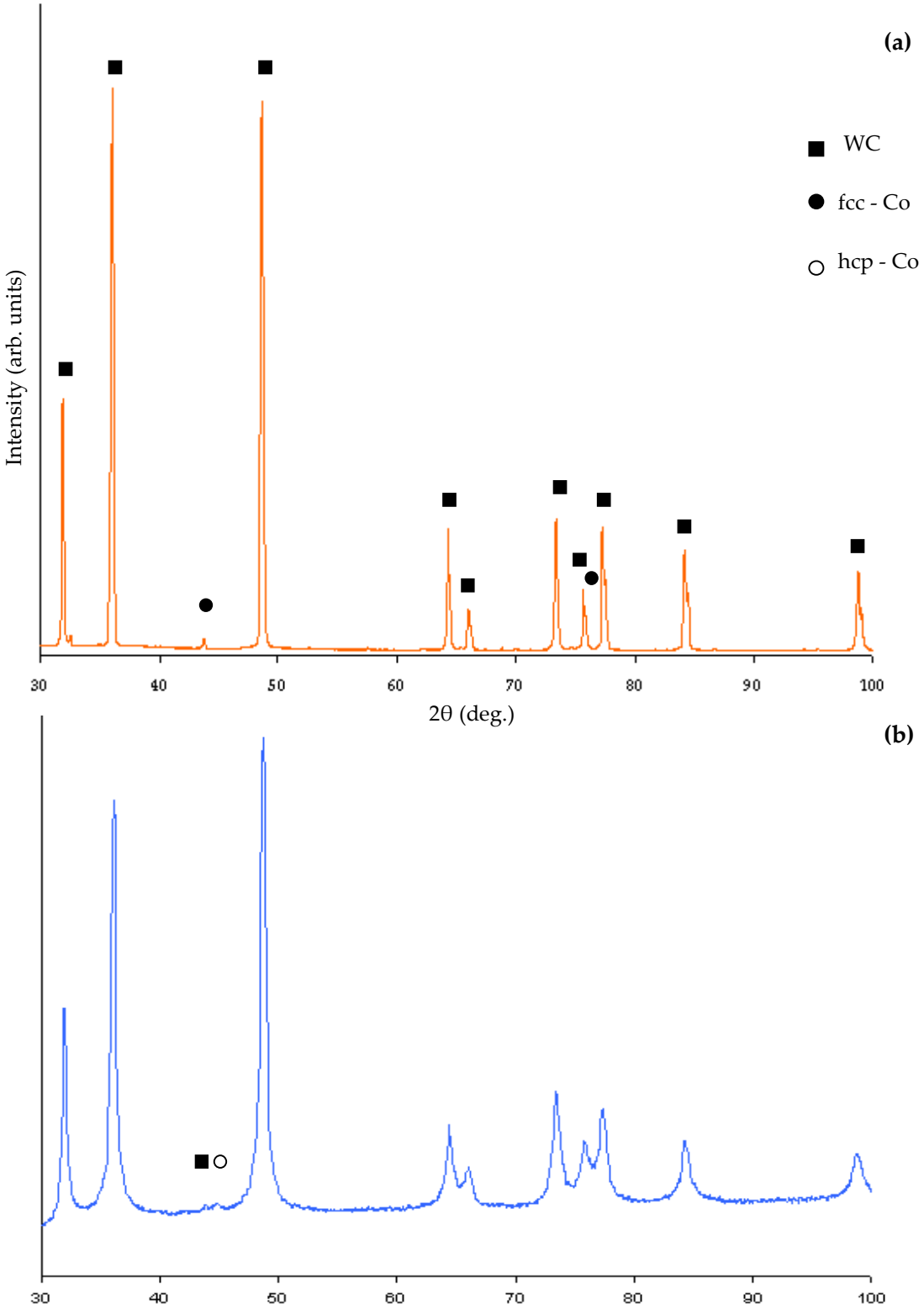

Fig. 5.1 X-ray diffractograms of the (a) unmilled WC-10Co starting powder and (b) after 60 min milling.

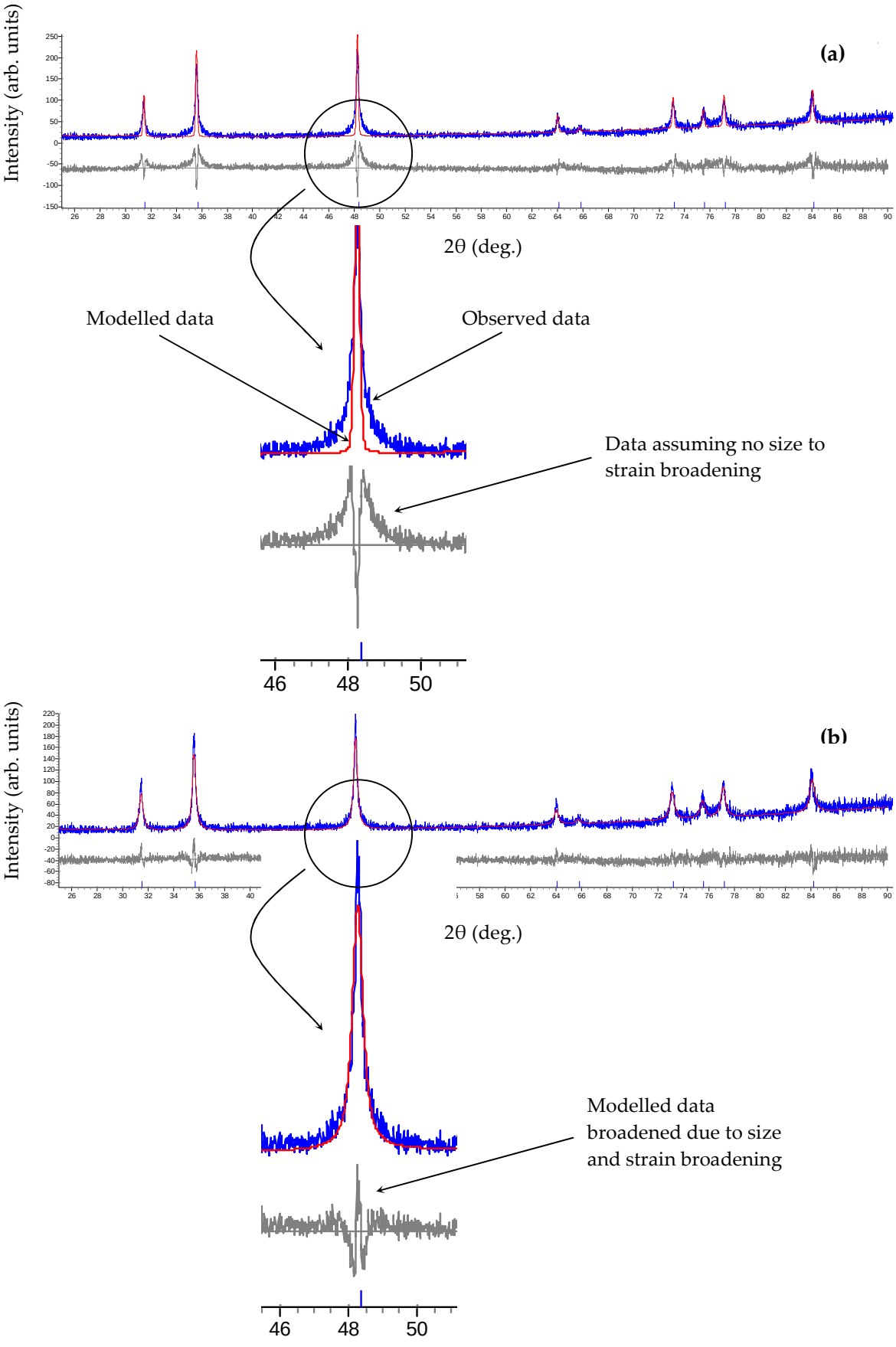
Intensity (arb. units)
(a)
2θ (deg.)
Modelled data
Observed data
Data assuming no size to strain broadening
46
48
50
Intensity (arb. units)
(b)
2θ (deg.)
Modelled data broadened due to size and strain broadening
46
48
50

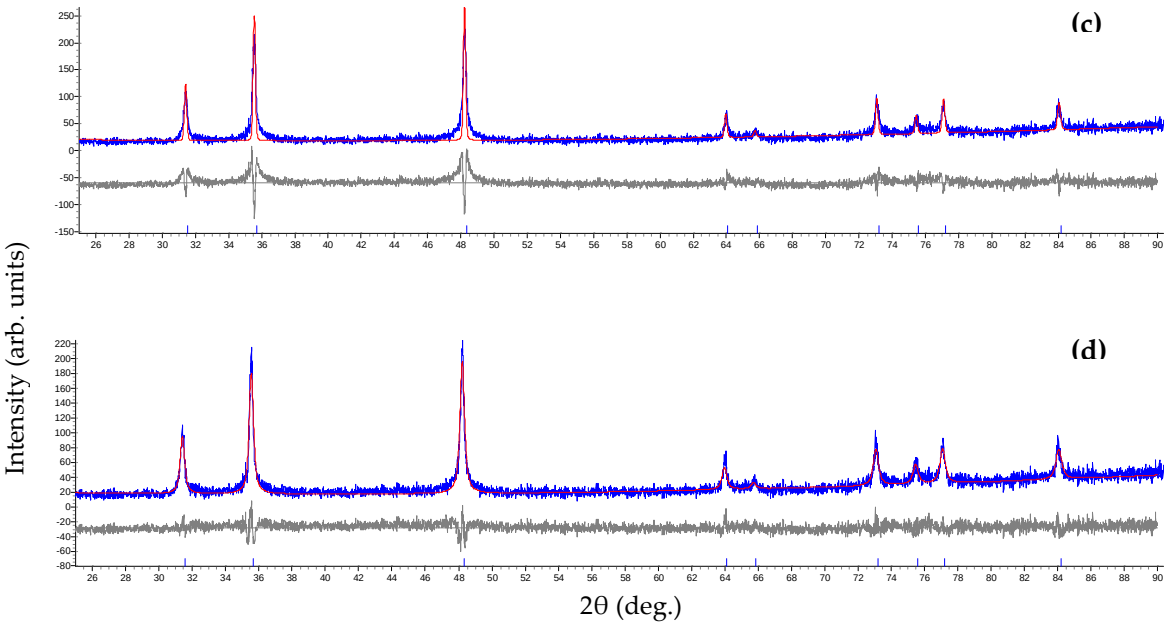

Fig. 5.2 X-ray diffractograms of WC-10Co powder after (a, b) 60 min milling and (c, d) 300 min. The diffractograms shown in (a, c) exhibit the observed data and modelled data, assuming there was no size to strain broadening of the WC peaks, whilst (b, d) show the broadened WC peaks due to size and strain.

TOPAS uses a direct convolution approach whereby profiles are generated by convolution. Various functions are convoluted to form the observed profile shape. For a convolution of n functions, this process is written as:

$$Y(2\theta) = W \otimes F_1(2\theta) \otimes F_2(2\theta) \otimes \ldots \otimes F_i(2\theta) \otimes F_n(2\theta) \qquad (5.1)$$

where $Y(2\theta)$ is the observed line profile shape, W is the source emission profile, and $\otimes$ denotes the convolution process. In powder diffractometry, the functions $F_i(2\theta)$ can

be interpreted as both the aberration functions of the diffractometer (Wilson 1963) as well as the various specimen contributions.

In the literature, convolution based profile fitting is typically associated with microstructure analysis where the specimen contribution is separated from the instrument contribution (Howard and Preston, 1989; Snyder, 1993). It can, however, also be used in an empirical manner to provide a greater variety of profile shapes resulting in better fits. The two general areas of application for convolution based profile fitting are:

1. The purely empirical parameterisation of line profile shapes by convolution of appropriate functions $F_i(2\theta)$ according to eq. (5.1); a schematic of which is shown in Fig. 5.3;
2. The explicit discrimination of instrument and specimen contributions (Jones, 1938):

$$Y(2\theta) = W \otimes G \otimes S \tag{5.2}$$

where G and S are instrument and sample contributions respectively, which are modelled separately using appropriate $F_i(2\theta)$ functions according to eq. 5.1. In general, instrumental setup $(W \otimes G)$ is seen as an entity called the instrument function I(2θ), which can either be measured (conventional approach) or calculated. In the conventional convolution approach, an instrument function is determined experimentally from a standard material, in this case LaB_6 (Fig. 5.4), which ideally should (but does not) meet

the following requirements; (i) large crystallite size to minimise size broadening; (ii) small crystallite size to give sufficient particle statistics; (iii) no strain and (iv) possess the same linear absorption coefficient as the specimen. The instrument function is then convoluted with specimen related functions to represent the "real" specimen properties. Obviously, the requirement to have both large and small crystallites simultaneously is a contradiction and limits the accuracy of microstructure analysis at small levels of specimen broadening.

Fig. 5.3 Schematic representation of the convolution approach as given in eq. 5.2. The final profile Y(2θ) is described by the selection of appropriate functions $F_i(2\theta)$ and convoluting them on top of the emission profile W. Note the capabilities of this approach to add functions before convoluting them as shown for the sum of two hat functions as well as to convolute split-type functions (Coelho 2007).

The broadening of diffraction lines occurs for two principal reasons; instrumental effects and physical origins. The latter can be divided into diffraction-order-independent (size) and diffraction-order dependent (strain) broadening in reciprocal space. Instrumental peak broadening was determined by measuring LaB_6, which showed a minimal amount of physical line broadening caused by defects and small grain size. A model of lognormal size distribution of spherical grains was used to account for line broadening. The lognormal size distribution function can be represented as (Popa and Balzar 2002):

$$f(R) = R^{-1}[2\pi \ln(1+c)]^{-1/2} x \exp\{-\ln^2[R\bar{R}^{-1}(1+c)^{1/2}]/[2\ln(1+c)]\} \quad (5.3)$$

$\bar{R}$ is the average radius of the grains and the dimensionless ratio c is defined as:

$$c = \sigma_R^2 / \bar{R}^2 \quad (5.4)$$

where σ_R^2 is the distribution dispersion. From the distribution parameters $\bar{R}$ and c, volume weighted average apparent domain size is:

$$D_v = 3\bar{R}(1+c)^3 / 2 \quad (5.5)$$

The double-Voigt approach (Balzar 1999) was used to calculate volume weighted mean crystallite sizes based on integral breadth of WC peaks and a mean strain value (ε0), based on individual crystallite size and strain contributions to line profile shapes versus 2θ in terms of Lorentzian and Gaussian type line broadening.

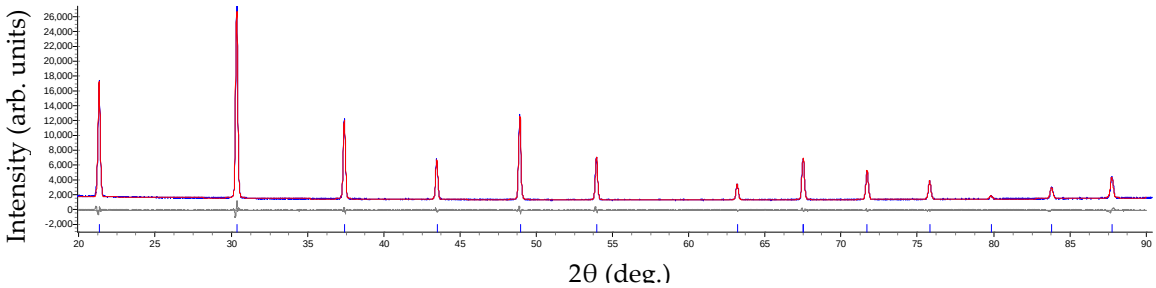

Fig. 5.4 X-ray diffractogram of the LaB_6 standard reference material.

Domain size and mean square strain of fcc-Co and hcp-Co could not be determined due to the intensity weakness of the reflections. X-ray structural analysis of the phase composition of the WC particles showed that WC was the only phase present (spatial symmetry group $P\bar{6}m2$). The diffraction peaks of WC, shown in Fig. 5.5, markedly broaden and decrease in intensity with increasing milling time. After 60 min milling, peak shift was observed towards lower Bragg angles, as shown in Fig. 5.5, with lattice parameters increasing, Table 5.1. The small angular shift is usually attributed to first order internal stresses induced by milling. These stresses act at the macroscopic level by modifying the lattice parameter and consequently produce an angular shift of the XRD peak (Castex et al. 1981). In this case the shift has been caused by Co atoms diffusing into

the WC lattice. This shift is well defined for 60 min milling and increases with milling time.

In this study, WC domain size was reduced to 21 nm after 60 min ball-milling and compares favourably with other studies of ball-milled WC-Co, especially when compared against studies incorporating planetary ball-milling, which took more than 10 h to achieve an equivalent WC size (Xueming and Gang 1996; El-Eskandarany *et al*. 2000; Zhang, Wang and Zhu 2003). In a similar study using a horizontal ball-mill with hardmetal milling media (Sun, Zhang and Shen 2003), WC domain size was reduced to ~ 20 nm after 60 min of cyclic milling, which is very similar to results obtained in this study using stainless steel/stellite milling media. This suggests that milling intensity is not heavily influenced by the milling media material. The favourable milling time to WC domain size reduction also suggests that horizontal, cyclic milling can effectively generate higher kinetic energy, and therefore, a higher impact velocity, which in turn leads to a lower, overall processing time. It also suggests that variable rotation rates and repetitious circulation can enhance the milling efficiency, (Table 5.2), as the variation in processing can periodically break-up the balance of impact and welding forces. Much longer times are required to generate equivalently-sized nanocomposite WC-Co or WC powders using conventional milling techniques.

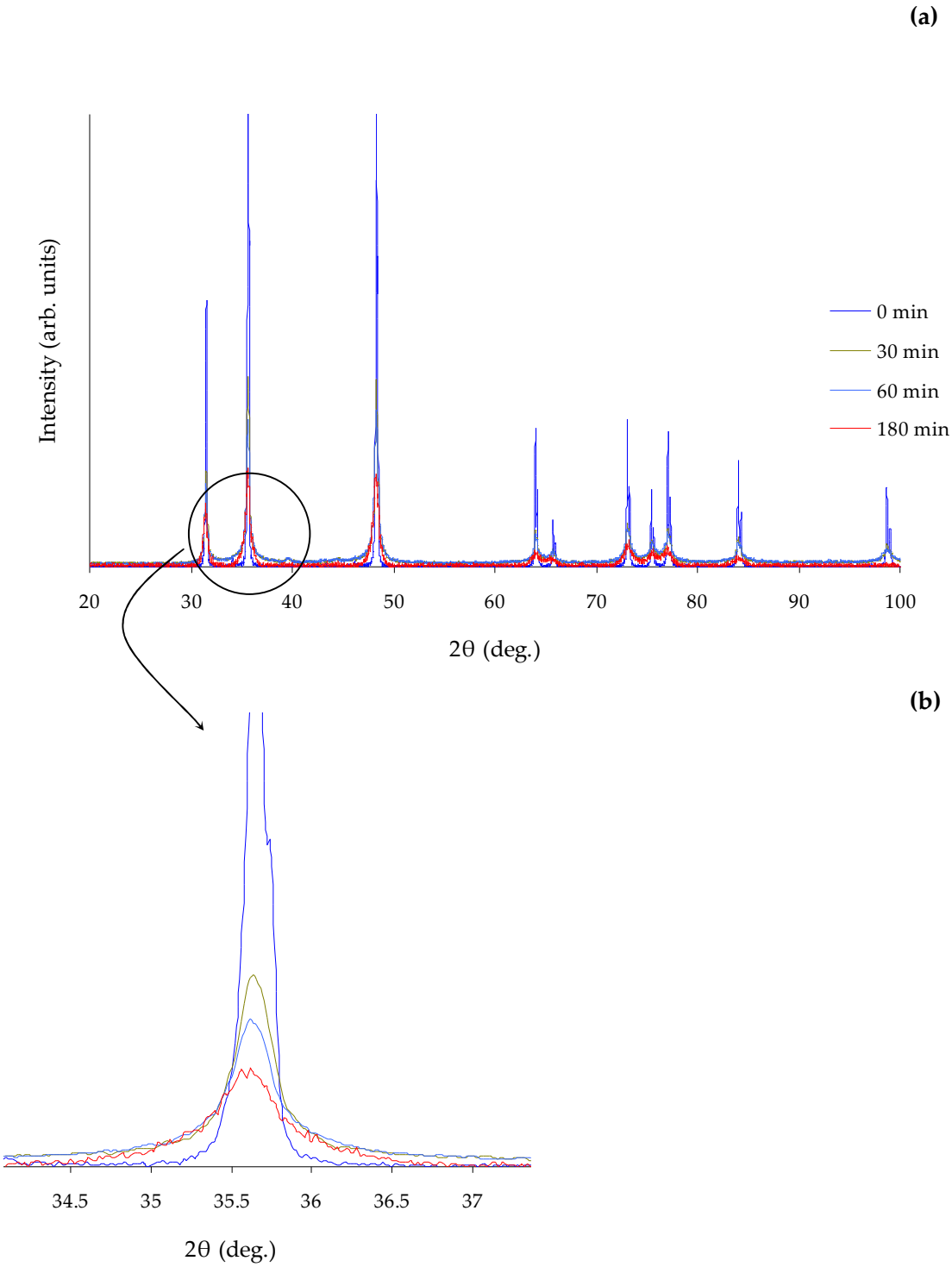

Fig. 5.5 X-ray diffractograms of WC-10Co powder after (a) 0, 30, 60, and 180 min milling. An expanded section of the diffractogram is displayed in (b), which shows WC (1 0 0) peak shift.

Table 5.1

Peak shift and lattice parameter determined from the (1 0 0) reflection.

Milling time (min)	2θ peak shift (deg.)	Lattice parameter (Å)
0	35.66	2.5219
30	0	0
60	-0.02	+0.0014
180	-0.08	+0.0055

Table 5.2

WC domain size and strain with milling time.

Composition	Milling technique	Milling time (min)	D_v (nm)	$\varepsilon 0$ ($x10^{-4}$)	Ref.
WC-10Co	Simoloyer (St. steel milling medium)	60	21	6	This work
WC-10Co	Simoloyer (St. steel milling medium)	300	27	4	This work
WC-10Co-0.8VC-0.2Cr_3C_2	Simoloyer (WC-Co milling medium)	32	25	-	(Sun *et al*. 2003)
WC-Co	Spex 8000	2400	10	-	(Changhui 1999)
WC-Co	Planetary (WC-Co milling medium)	600	11	-	(Zhang *et al*. 2003)

D_v: average volume weighted domain size; $\varepsilon 0$: mean square strain

MA processes reach a steady state after a certain milling time, (Chapter 2), when the welding and fracture mechanisms come into balance, and the size of the particles becomes constant within a narrow range (Benjamin 1976). As with the case of all horizontal milling systems, the effect of gravity on the milling media has to be overcome. In this case, the design of the rotor allows it to be run at 2 to 3 times higher rotational speeds than conventional vertical attritors (Zoz 1995; Zoz and Ernst 1997; Davis, McDermott and Koch 1988), thereby generating a higher kinetic energy impact. In addition, cyclic operation can have a tremendous influence on particle size reduction, grain refinement, as well as grain-growth behaviour after heat treatment compared to the refinement effects from constant operation (Kim *et al*. 2000). This is due to the fact that the periodical changes of the milling velocity in cyclic operation break the balance of deformation, fracture and welding in the process and maximise the effect of fracture. Mean square strain reached a maximum of 0.06% after 60 min of milling and showed no further increase with continued milling. The maximum strain is lower than that reported in a similar study of WC-10Co (Zhang, Wang and Zhu 2003) where a mean strain of 1.44% was determined, which may have been due to the higher ball-to-powder weight ratio. A higher ball-to-powder weight ratio would increase the kinetic energy of the balls per unit mass of powder but this, in turn, would affect contamination levels from the milling media. In the present study, mean square strain showed a slight decrease with milling time, which may be due to dynamic recovery during extended milling (Kim *et al*. 2000) caused by thermal processes. Koch (1997) indicated that the total strain rather the milling energy is responsible for determining the nanocrystalline grain size. However, in

this study, it appears that the opposite is more applicable from the mean square strain measurements (Table 5.2). During MA processing, a maximum reduction in domain size at a certain strain level is thought to be the result of a change in the deformation from plastic deformation, via the generation and movement of dislocations, to grain boundary sliding (Hellstern, Fecht and Johnson 1989). Therefore, this may be the predominant deformation mechanism taking place with extended milling time (> 180 min), which would prevent the microstructure from being further refined.

5.1.2 Particle morphology and size

The SEM micrographs of the starting powders are shown in Fig. 5.6. The WC particles exhibit a rounded, slightly elongated morphology with some agglomeration, whereas the Co particles show a spherical morphology with a narrow particle size distribution. Vanadium carbide (VC) particle size is ~ 10 μm, with the particles showing an irregular, agglomerated structure.

The morphology and size of the MA WC-10Co powders after ball milling for 30, 60, 180 and 300 min are shown in Fig. 5.7. During the MA process, the powders are subjected to high-energy collision, which causes plastic deformation, cold welding and fracture of the powders. Plastic deformation and cold welding are predominant during the initial stage of ball milling, in which deformation leads to a change in particle shape, and cold welding leads to an increase in particle size and the formation of layered structures with an average size of ~ 10 μm, Fig. 5.7 (a, b). After 30 min milling, the

spherical Co powder had become flattened due to the impact forces exerted on the powder by the milling medium. At this stage of milling, the hard WC particles are randomly embedded into the deformed, soft Co matrix to form coarse composite WC-Co powders, Fig. 5.8 (a). In contrast to the Co particles, the WC particles decreased in size to form finer particles of ~ 1 μm or less. Even at this stage, the hard embedded WC particles had, essentially, lost their starting morphology, indicating intensive deformation occurred in a short milling period. The predominant mechanism in this stage is plastic deformation and cold welding. Plastic deformation of WC particles occurs through multiplication and slippage of dislocations, whilst the accumulation of dislocations and their subsequent readjustment is accompanied by disoriented regions within the particle structure (Paul *et al*. 1994). With further milling, the ability of the particle to accept further plastic deformation is diminished; therefore, fracturing becomes a significant process, which leads to a decrease in particle size, Fig. 5.7 (c, d).

During this stage, the agglomerated particles were subjected to continuous fragmentation to form finer particles with a narrower particle size distribution. As welding is the predominant mechanism in this stage, particle morphology is altered by flattened particle pile-up. Welding and fracture mechanisms then reach equilibrium, promoting the formation of composite particles with randomly orientated interfacial boundaries (Fogagnolo *et al*. 2003).

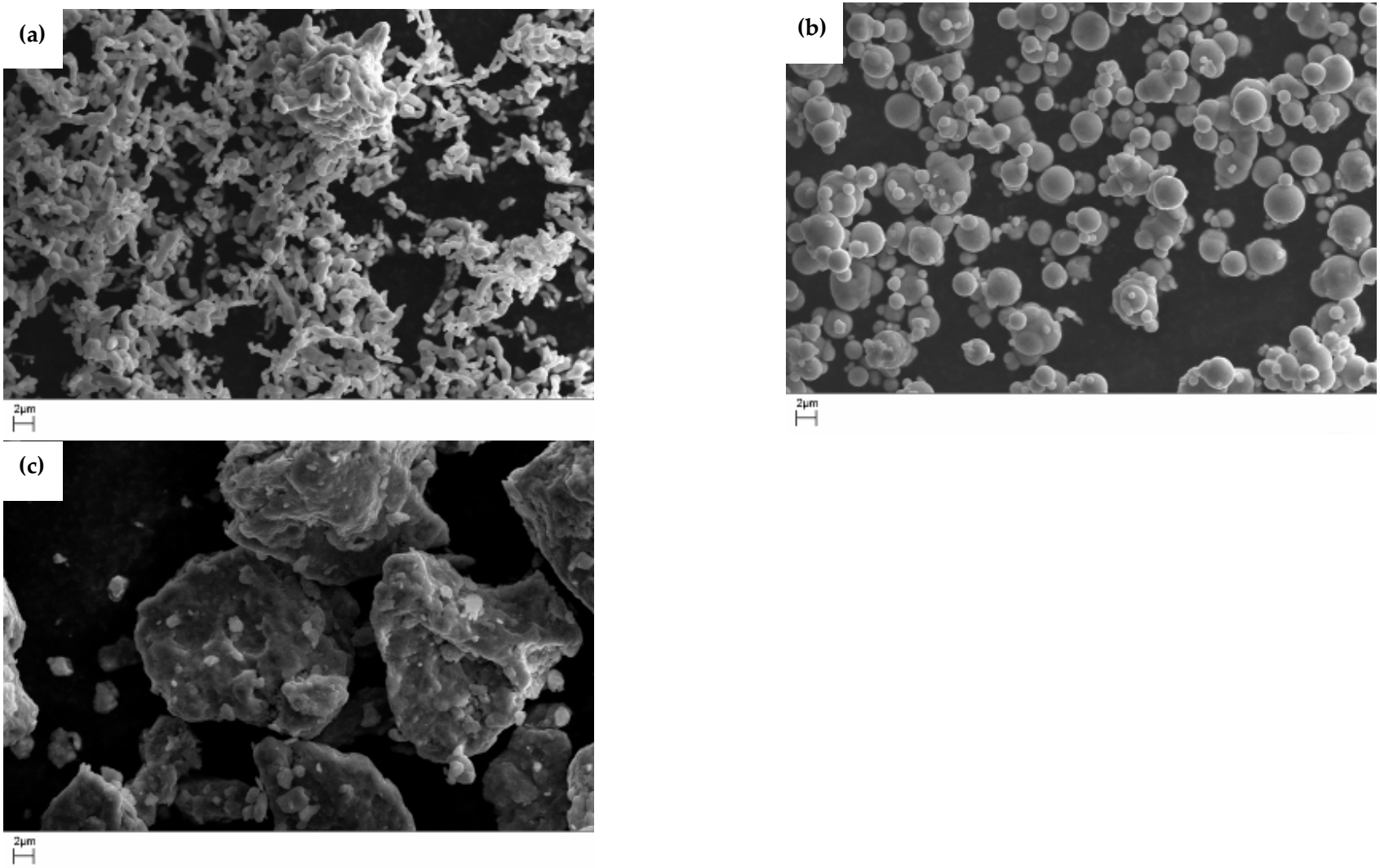

Fig. 5.6 SEM micrographs of (a) WC, (b) Co and (c) VC starting powders.

The latter stages of the milling process involve particle fracture, and results in further deformation and/or fragmentation of the particles. Towards the end of this stage (180 min), the hard WC particles become finer and are more uniformly distributed in the Co matrix, Fig. 5.8 (c). At this stage, particle agglomeration was still evident. The flake-like morphology and particle size distribution is consistent with previous studies of WC-Co ball milling (El-Eskandarany *et al*. 2000).

For brittle materials such as WC, particle fracture can be described by the Griffith theory. According to the theory, the stress, σ_F, where crack propagation reaches catastrophic failure (fracture) in the particle, can be approximated by:

$$\sigma_F \approx \sqrt{\frac{\gamma E}{c}} \tag{5.6}$$

where c is the crack length, E is the modulus of elasticity, and γ is the surface energy to create new fracture surfaces of the milled substance. When stress at the crack tip equals the strength of cohesion between atoms, the crack becomes unstable and propagates, leading to fracture (Kuhn 1984). With decreasing fragment size, particle agglomeration increases thereby increasing the resistance to fracture. Particle fineness approaches a 'limit' as milling continues and maximum energy is expended (Kim *et al*. 2000). Increasing resistance to fracture and increasing cohesion between particles, with decreasing particle size causing agglomeration, are just two of the major factors contributing to the 'limit' (Harris 1968). With the formation of more free surfaces and

grain boundaries, surface diffusion, which is driven by the reduction in surface area and the radius of the crack tip, dominates during MA. After 300 min ball milling, a number of the WC-Co composite particles showed a slightly rounded morphology with fewer fine fragments agglomerated on the particle surfaces, Fig. 5.7 (d). A homogeneous distribution of fine WC grains in the Co matrix was formed after 60 min of milling, Fig. 5.8 (b).

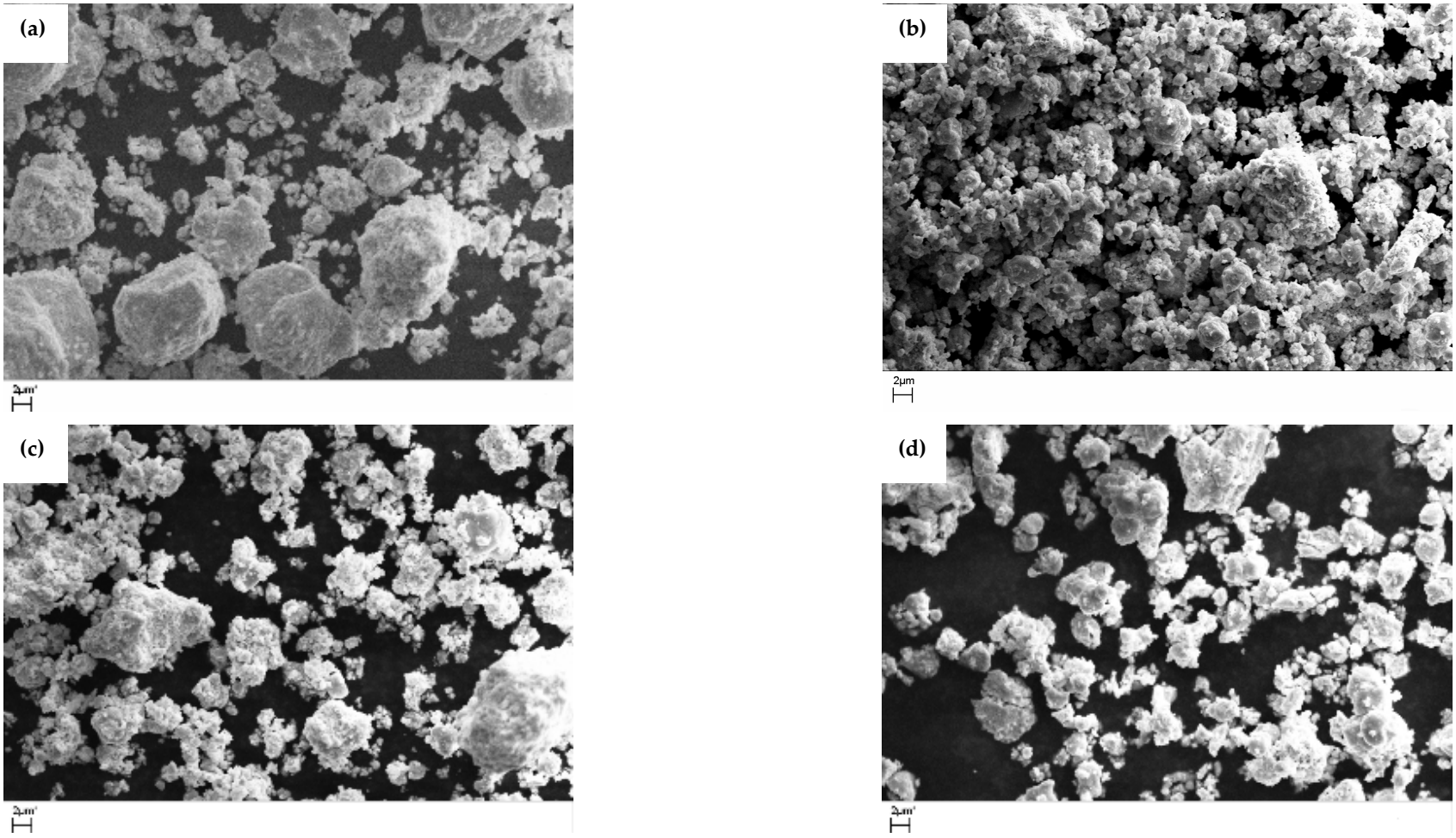

Fig. 5.7 SEM micrographs of the WC-10Co powders after (a) 30 min, (b) 60 min, (c) 180 min and (d) 300 min milling.

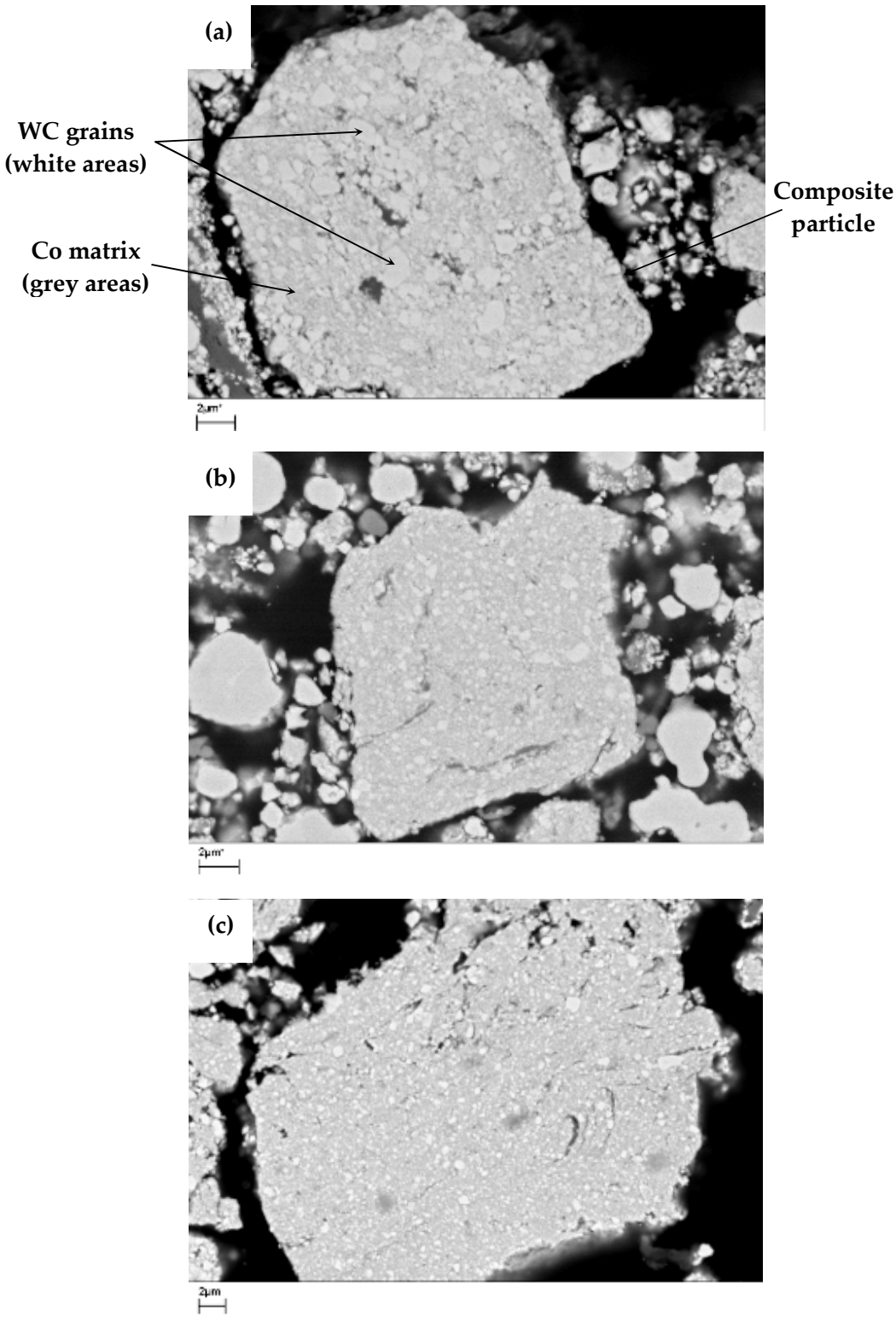

Fig. 5.8 SEM micrographs of a polished x-section through WC-Co composite particles after (a) 30 min, (b) 60 min, and (c) 180 min of ball milling.

Particle size measurements of WC-10Co powders after 60 and 300 min ball milling are shown in Fig. 5.9. The measurements were obtained by NanoSight's nanoparticle tracking analysis (NTA) software, which automatically tracked and sized the particles on an individual basis as they moved under Brownian motion using a laser light source. It should be noted that a particle detection threshold was set for the measurements to exclude particles > 1 μm. In order to quantify particle size distribution, the milled powder agglomerates (Fig. 5.7) were dispersed in water to break the particle-particle interactive forces. In as much as agglomerates are porous, capillary pressure-driven infiltration occurs upon contact with a processing fluid (Boyle, Manas-Zloczower and Feke 2005). Results, within the measured range, showed a mean particle size of 0.117 μm after 300 min ball milling compared with 0.148 μm after 60 min. The number of superfine (<0.5 μm) particles increased considerably and the size distribution shows more nanosize (<0.2 μm) particles were generated with increasing milling time. However, the particle size measurements appear to contradict the SEM results, Fig. 5.7, with the micrographs suggesting considerably coarser mean particle sizes for both milling times. A representative sample was taken from both powders for particle size analysis and although the powders were well dispersed in water prior to the analysis, some 'settling' of the larger and, therefore, heavier particles may have occurred, which would have prevented them being injected into the viewing unit. On the other hand, the dispersion process may have disrupted the inter-particle attractive forces for some of the particles leaving any larger agglomerates to be excluded by the upper analysis limit. The

analysis may well have measured non-agglomerated fine particles/fragments representative of both milling times.

Particle size measurements suggested that the milling 'limit' was reached under 300 min, as a five-fold increase in ball milling time shifted the mean particle size by just 0.03 μm. This small reduction in the mean particle size with milling time suggests strong interparticle bonding in the agglomerates, i.e. hard agglomerates. WC domain size also increased upon extended milling time (Table 5.2), which suggests that the local collision temperature between milling balls may have increased to such an extent as to promote recovery processes of the sub-grain structure generated during MA. Ball temperatures increase with increasing milling power and can reach several hundred degrees (Kwon, Gerasimov and Yoon 2002; Schwarz and Koch 1986; Bhattacharya and Arzt 1993), although this would surely be dependent on the characteristics of the material being milled and the energy generated by the milling system.

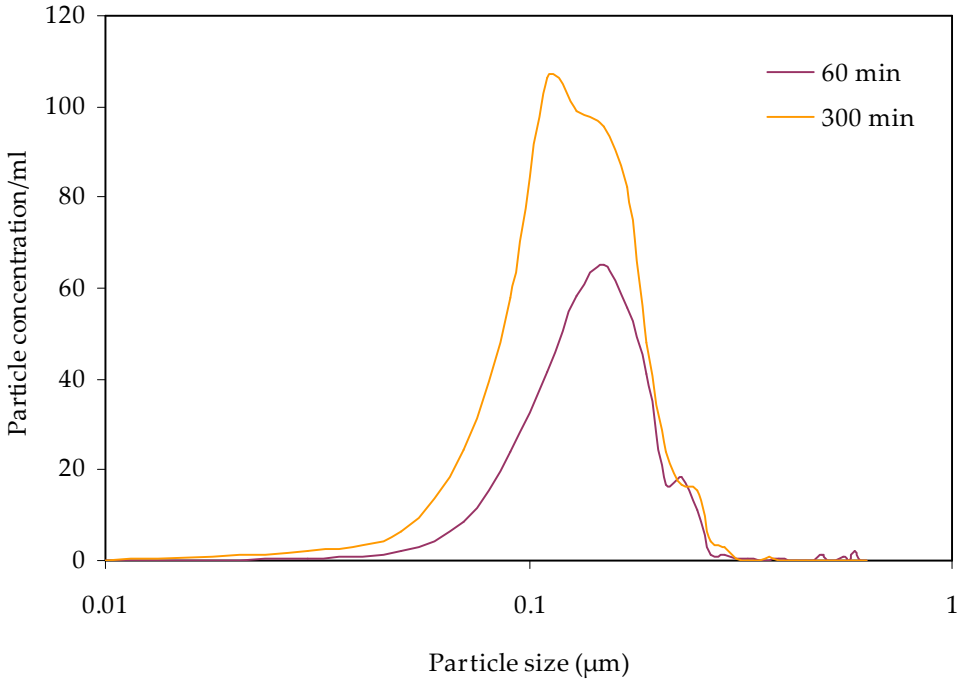

Fig. 5.9 Particle size measurements for WC-10Co powders ball milled for 60 and 300 min.

5.1.3 Effect of milling time on WC-Co eutectic temperature

Differential scanning calorimetry (DSC) was used to detect the release of interfacial grain boundary enthalpy during grain growth processes and also to determine the effect of particle size on the WC-Co eutectic temperature (section 3.3.1). A DSC heating scan for the powders after ball milling for 60, 180, and 300 min is shown in Fig. 5.10. When the grain size of nanocrystalline materials is below a critical value (~ 10 to 20 nm), more than 50 vol % of atoms are associated with grain boundaries or interfacial boundaries (Tjong and Chen 2004). By cold working, the metal particles are plastically deformed with most of the mechanical energy expended in the deformation process converted into heat, but

the remainder is stored in the particles, thereby raising internal energy (Bever, Holt and Titchener 1973). This energy is released during heating to elevated temperatures due to grain boundary recovery and relaxation processes along with grain growth. In general, the stored enthalpy can reach values up to several kJ/mole (Moelle *et al*. 1996) and corresponds to a major fraction of the enthalpy of fusion ΔH_f. Thermodynamically, these materials are far from equilibrium. As a result, during heating to elevated temperatures the relaxation and growth processes provide a driving force towards equilibrium leading to a concurrent increase in grain size. The DSC scans show a change in stored energy of the powders with increasing ball milling time. A substantial amount of enthalpy can be stored in nanocrystalline materials due to their large grain boundary area (Suryanarayana 2001). MA introduces high energy into the material being processed and this energy can be stored in the material as atomic disorder and/or grain boundaries. Upon heating to elevated temperatures, the stored energy can normally revert to a lower energy state by structural evolution during recovery (Humphreys and Hatherly 1996). The largest release of energy is shown by the powder milled for 180 min. After further milling (300 min), the energy release decreased to a level below that of the powder milled for 60 min, which, along with the WC domain size results (Table 5.2), would suggest that MA steady-state equilibrium, i.e. when a balance is achieved between the rate of welding and the rate of fracturing, was reached between 60 and 180 min.

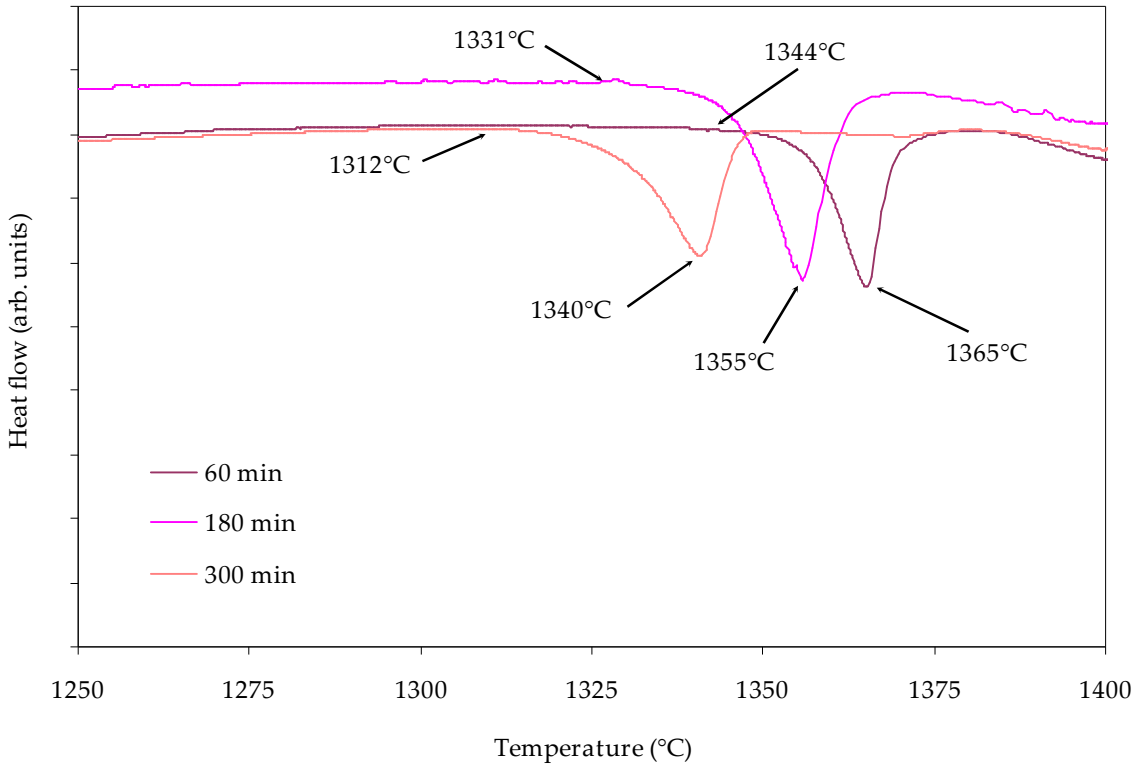

Fig. 5.10 DSC heating scan of the WC-10Co powders after ball milling for 60, 180, and 300 min with the onset and completion of melting shown for each powder.

The DSC scans show that the onset temperature of the WC-Co eutectic was reduced with increasing milling time with an onset temperature of 1344°C, 1331°C, and 1312°C recorded after 60, 180, and 300 min milling, respectively, which fits within the solidus-liquidus lines calculated for the WC-10Co phase diagram, Fig. 3.2. The phenomenon of melting point depression of nanoscale metal particles has been studied since the 1960s, when it was noticed that extremely thin evaporated particles of metal have a lower melting point than the bulk material (Wronski 1967). As the dimensions of a material decrease towards the atomic scale, the melting temperature scales with the material

dimensions. The decrease in melting temperature can be on the order of tens to hundreds of degrees for metals with nanometre dimensions (Sun and Simon 2007; Lopeandia and Rodriguez-Viejo 2007). Changes in melting point occur because nanoscale materials have a much larger surface to volume ratio than bulk materials, drastically altering their thermodynamic and thermal properties. The increased surface to volume ratio means surface atoms have a much greater effect on chemical and physical properties of a nanoparticle. Surface atoms bind in the solid phase with less cohesive energy because they have fewer neighbouring atoms in close proximity compared to atoms in the bulk material. Each bond an atom shares with a neighbouring atom provides cohesive energy, so atoms with fewer bonds and neighboring atoms have lower cohesive energy. The cohesive energy of an atom is directly related to the thermal energy required to free the atom from the solid.

5.1.4 Effect of milling time on impurities

The disadvantage of using ball-milling for producing nanostructured powders is the contamination of products by the milling media (balls and vessel) and atmosphere. The small size of the powder particles, their large surface area, and the formation of fresh, new surfaces during milling, all contribute to the contamination of the powder.

These impurities can be classified into substitutional, for example iron, chromium, and nickel from the milling media, and interstitial impurities such as nitrogen, oxygen, and carbon from either the atmosphere and/or the process control agent (PCA). In this

study, the possibility of introducing any interstitial impurities was reduced by milling in a controlled atmosphere using high purity Ar and without a PCA. The substitutional impurities can either dilate or contract the lattice depending on the relative atomic sizes of these elements with respect to the solvent atoms. The magnitude of contamination appears to depend on the time of milling; the milling intensity; milling atmosphere; and the difference in strength/hardness of the powder and the milling medium. Typically, between 1-4wt% Fe and 1 wt% Cr have been found to be present in powders milled with steel media (Suryanarayana 2001), whereas < 0.03wt% Fe was found for cemented carbide media after 120 min milling (Sun, Shen and Zhang 2003). XRF analysis of the as milled powders, Fig. 5.11, shows small amounts of trace elements from the milling media and increasing Fe content with milling time. The other elements do not show this trend. The chemical composition of the balls, vessel, and rotor tip is shown in Table 5.3. The reason for a high amount of Fe contamination during milling is due to the difference in hardness between the milling media (balls and vessel), and the WC powders as the milling media are made from softer and less wear resistant materials. It is interesting to note that the level of Cr does not increase with milling time given that, typically, stellite 6 contains 29 wt% Cr, which suggests that the harder rotor tip has experienced less wear during milling.

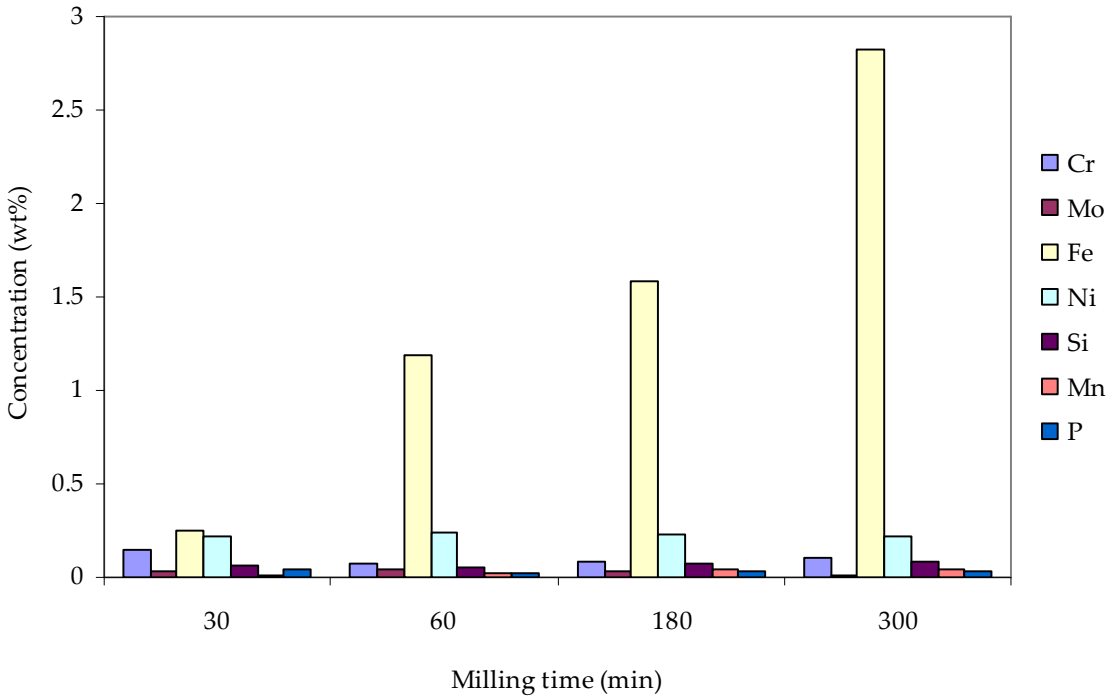

Fig. 5.11 XRF analysis of the ball milled powders.

Table 5.3

Chemical composition of the milling media and milled powders

Chemical analysis (wt%)	Balls (100Cr6)	Rotor tip (Stellite 6)	Vessel (st. steel AISI 304)	Ball milling time (min)			
				30	60	180	300
Cr	1.4 – 1.65	29	18 – 20	0.15	0.078	0.09	0.10
Mo	Nil	0.1	Nil	0.03	0.04	0.03	0.01
Fe	Rest	2.5	Rest	0.25	1.18	1.58	2.82
Ni	Nil	0.3	8 – 10.5	0.22	0.24	0.23	0.22
Si	0.15 – 0.35	0.8	1	0.06	0.06	0.07	0.08
Mn	0.25 – 0.45	0.5	2	0.01	0.03	0.04	0.04
Nb	Nil	6	Nil	-	-	-	-
P	0.03	Nil	0.045	0.04	0.02	0.04	0.03
Co	Nil	Rest	Nil	-	-	-	-

5.1.5 Effect of milling time on green density

Dense, uniform particle packing in a green powder compact is a prime criterion in achieving a high sintered density body with a uniform microstructure. Initial homogeneity of the green compact strongly affects the final homogeneity and integrity of the sintered microstructure. In powder processing, one important consideration is to eliminate agglomerates which are formed as clusters of primary particles bonded strongly (hard agglomerates) or weakly (soft agglomerates) with an interconnective pore network. The presence of agglomerates in powders can reduce particle packing efficiency and suppress sintering activity, which deteriorates sintered properties due to the loss of microstructural homogeneity/integrity and the formation of crack-like voids (Roosen and Bowen 1988; Lange 1989; Lange, Davis and Aksay 1983). A high density green compact is desirable for higher densification kinetics, and to take advantage of the increased number of contact points and therefore, a greater number of transport paths. Green density is highly dependent on the friction forces among powder particles. These forces are a result of electrostatic, Van der Waals and surface adsorption forces that become much more significant with decreasing particle size (Groza and Dowding 1996). Frictional forces between particle-die wall contacts were reduced by the application of a die wall lubricant.

The die compaction behaviour of the ball milled powders is shown in Fig. 5.12. Green density increased linearly with compaction pressure between 100 and 400 MPa. This graph, along with Fig. 5.7, clearly shows the influence of milling time, particle size,

and particle hardness on relative density. Increasing particle hardness stems from increasing ball milling time and the resulting increased levels of cold work. Decreasing particle size (or increasing milling time) results in a decrease in relative density, as shown in Fig. 5.13. This is a direct result of the increase in average surface area of the particles resulting in an increase in interparticle friction. For example, the powder milled for 30 min reached a higher relative density at each compaction pressure due to its larger particle size (Fig. 5.7) (resulting in lower interparticle friction), than the powder milled for 300 min with its fine particle size (Fig. 5.7) and higher interparticle friction. Such a size effect is often ascribed to the increased number of contacts in the fine powder (German 1989). The relative density difference between the fine (300 min) and the coarser (30 min) powder is not reduced with increasing pressure. Much higher pressures would be required for the fine powders to reach the same density. Although increased ball milling time served to break up agglomerates, thereby decreasing the particle size, the downside of this was the creation of harder particles. The influence of powder particle size on compressibility is consistent with other studies (Roure *et al*. 1999; Al-Qureshi, Galiotto and Klein 2005; Poquillon *et al*. 2002; Morsi, Shinde and Olevsky 2006) and the linear relationship for the tested range is also consistent with compaction behaviour attributed to irreversible particle deformation (Poquillon *et al*. 2002). The mechanisms for developing green strength during compaction are generated by two phenomena, namely (i) particle sliding and interlocking and (ii) plastic deformation and fragmentation (Lund 1982). The initial stage of compaction leads to rearrangement of the powder from a loose array to close packing. As the pressure increases, the contact area

between the grains decreases and particles undergo extensive plastic deformation and fragmentation.

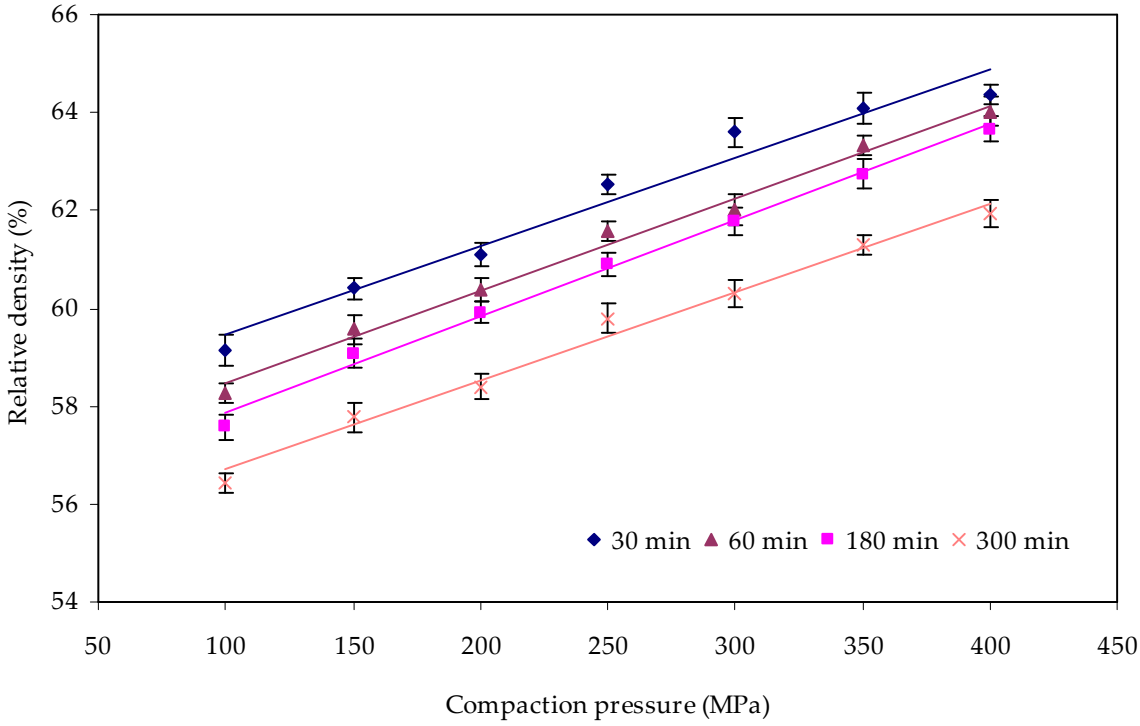

Fig. 5.12 Effect of compaction pressure on the relative density of WC-10Co powders ball milled for 30, 60, 180, and 300 min.

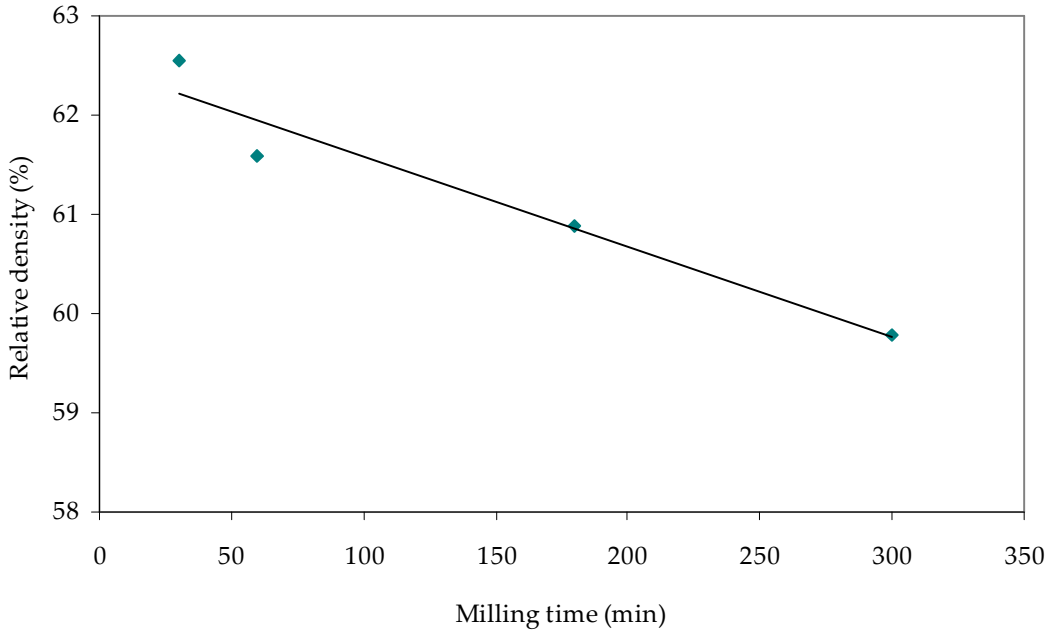

Fig. 5.13 Effect of ball milling time on the relative density of WC-10Co powder compacted at 250 MPa.

A green density of 60% is generally attained for a typical WC-10wt%Co composition using fine (0.5-1 μm) powders (Upadhyaya 1998). For compacts with < 60% relative density, percent shrinkage during sintering is high, and dimensional control is difficult and therefore, a high green density is preferred (Lardner, Spriggs and Wood 1972). It was possible to exceed 60% relative density for all the ball milled powders, provided that compaction pressure was > 300 MPa, as shown in Fig. 5.12.

Considerable effort has been made to characterise powders and their compaction behaviour using a compacting equation (Heckel 1961; Niesz 1996; Shapiro and Kolthoff 1947; Ge 1995; Kawakita and Lüdde 1971). Several equations have been proposed for

modelling the relationship between the main macroscopic parameters, such as compacted material relative density or porosity with applied pressure. A new phenomenological compaction equation has recently been proposed (Panelli and Ambrozio Filho 1998):

$$\ln\left[\frac{1}{1-D}\right] = A\sqrt{P} + B \tag{5.7}$$

where D is the relative density of the compacted material, and P is the applied pressure. However, this equation doesn't consider the effect of compaction pressure on the compacts' properties. Parameter A is related to the plastic deformation capacity of the powder during the compaction process. Parameter B expresses the density without applied pressure, which is the apparent density. Parameter A from eq. 5.7 represents the powder's ability to densify by plastic deformation. The equation proposed by Panelli and Ambrozio Filho contains a square root pressure term, which is different to other compaction equations. Panelli and Ambrozio Filho's equation was originally derived from a general equation correlating q and P:

$$\ln(q) = k\left(1/P\right)^n \tag{5.8}$$

where q is relative porosity, and k and n are constants. Based on this phenomenological equation, a differential equation to describe the porosity-pressure relationship was proposed:

$$\frac{\partial q}{\partial P} = \frac{K_q}{P^m} \tag{5.9}$$

where K and m are constants. By integrating eq. 5.9 from q (porosity at P) to q_0 (porosity at $P = 0$) and applied pressure from 0 to P, a general equation is obtained:

$$\ln \frac{q_0}{q} = C_1 \frac{P^{-m+1}}{-m+1} + C_2 \tag{5.10}$$

This equation has an integration constant C_2 which must be zero to satisfy the condition $q_0 = q$ when $P = 0$. Eq. 5.10 was tested by fitting experimental data to it by linear regression, which gave linear correlation coefficients > 0.99 when $m = 0.5$. This value was adopted for m in eq. 5.10 and was rewritten as:

$$\ln \frac{q_0}{q} = AP^{1/2} \tag{5.11}$$

where $q_0 = (1 - D_0)$, $q = (1 - D)$, D_0 is the relative density of the loose powder at zero pressure, D is the relative density of the compact at pressure P, and A is a constant. Upon substitution, eq. 5.11 becomes:

$$\ln\left(\frac{1-D_0}{1-D}\right) = AP^{1/2} \tag{5.12}$$

Eq. 5.12 has restricted applicability owing to the necessity to determine the parameter D_0, which can be difficult or inconvenient. Eq. 5.12 was simplified by Panelli and Ambrozio Filho to eliminate D_0 by the following:

$$\ln\left(\frac{1}{1-D}\right) = AP^{1/2} + \ln\left(\frac{1}{1-D_0}\right) \tag{5.13}$$

$$\ln\left(\frac{1}{1-D}\right) = AP^{1/2} + B \tag{5.14}$$

where B is a constant.

A useful estimation of the plastic deformation capacity of the powder with ball milling time was obtained by using eq. 5.7. A good linear correlation coefficient (> 0.99) is obtained when the experimental data are fitted by this equation, as shown in Fig. 5.14, for WC-10Co after 30, 60, 180, and 300 min of mechanical milling, with the data also showing slightly different gradients. Plotting parameter A versus milling time for WC-

10Co powders, as shown in Fig. 5.15, indicates the influence of MA on the compaction behaviour of the powders. Parameter A shows a gradual decrease with milling time up to 180 min milling, which suggests that the levels of cold work from the MA mechanisms (repeated welding, fracturing, and re-welding of powder particles) were of sufficient intensity, even after 30 min, to have a gradual effect on the hardness of the powder particles. After prolonged ball milling (300 min), the curve shows a sharp decrease, which indicates an increased level of cold work, producing more brittle powder particles. This is consistent with the morphological changes shown in Fig. 5.7. The curve in Fig. 5.15 also shows that the MA mechanisms did not reach equilibrium.

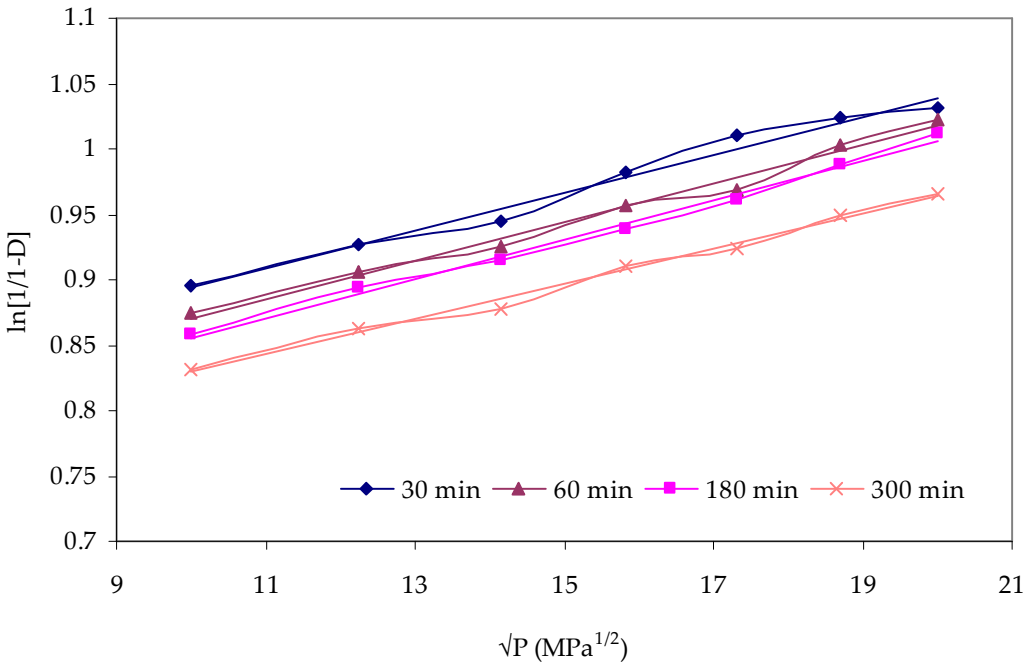

Fig. 5.14 Compressibility curves of the ball milled WC-10Co powders.

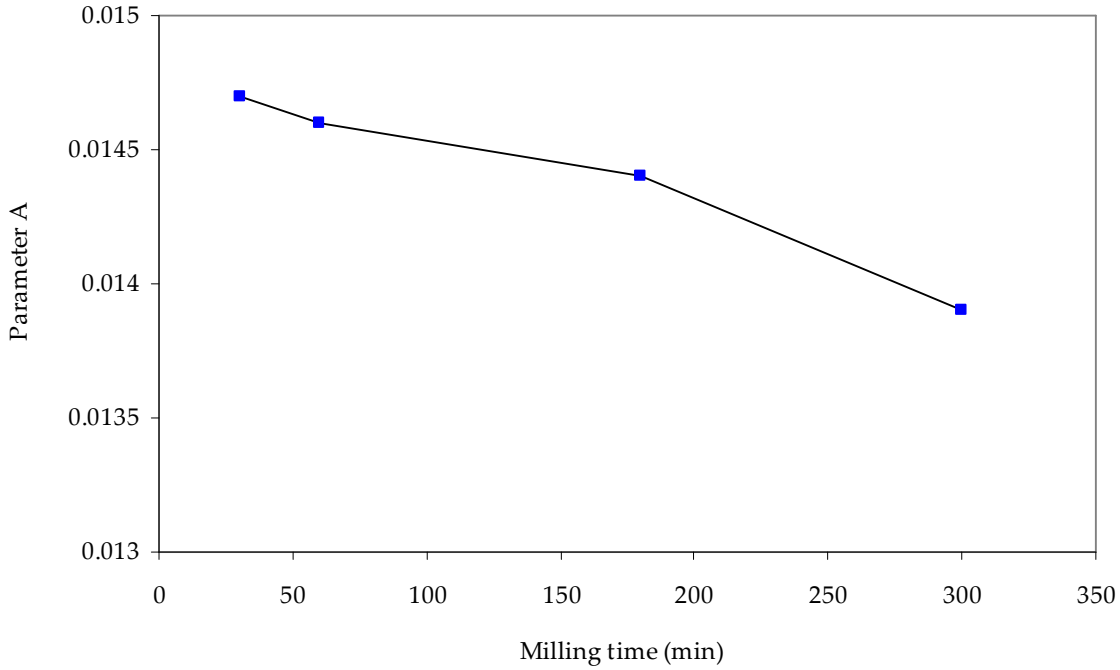

Fig. 5.15 Influence of MA on the compaction behaviour of the powders.

5.2 Effect of milling temperature

5.2.1 WC grain size and strain

The X-ray diffractogram of WC-10Co powder milled for 60 min at -30°C is shown in Fig. 5.16. WC grain size and strain was again determined by TOPAS software using the procedure outlined in Section 5.1.1. A comparison between WC domain size and mean square strain of the WC-10Co powder milled for 60 min at room temperature (RT) is shown in Table 5.4. WC domain size was reduced to 26 nm after ball milling at -30°C compared to 21 nm for the powder milled at RT. Although the magnitude of the measured mean square strain values is relatively small compared to other studies (Lee *et al*. 2003; He, Ajdelsztajn and Lavernia 2001; Back, Lee and Kang 2005), the powder milled

at -30°C exhibited a higher WC lattice strain. These results suggest that milling at -30°C has reduced the extent of WC grain refinement compared with milling at RT with a similar energy level. The higher value of mean square strain suggests that milling at a lower temperature reduced the rate of dynamic recovery, which decreases with increasing mean square strain (Salimon, Korsunsky and Ivanov 1999).

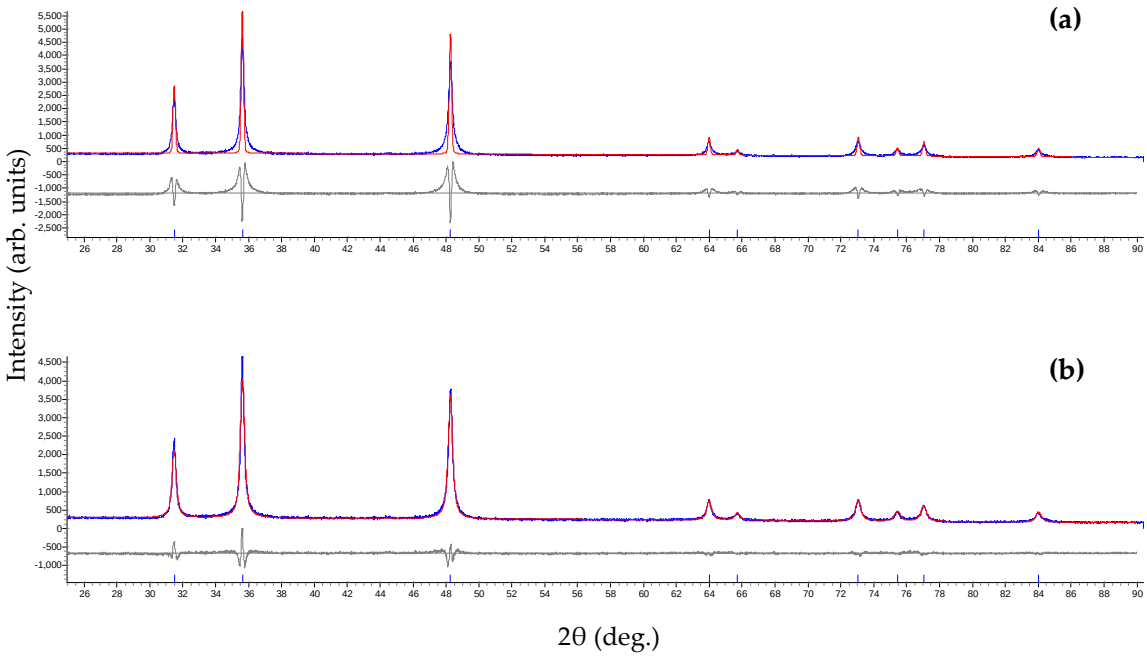

Fig. 5.16 X-ray diffractogram of WC-10Co powder after milling for 60 min at -30°C, showing (a) the observed data and modelled data, assuming there was no size to strain broadening of the WC peaks, whilst (b) shows the broadened WC peaks due to size and strain.

Table 5.4

WC domain size and strain with milling temperature.

Milling condition	Milling time (min)	Dv (nm)	ε0 (x10^{-4})	Ref.
RT	60	21	5	This work
-30°C	60	26	18	This work
-50°C	600	50	-	(Back *et al*. 2005)

Dv: average volume weighted domain size; ε0: mean square strain

Comparative studies of cryomilled WC-Co materials required much longer milling times to achieve a similar reduction in WC domain size (Lee *et al*. 2003; He, Ajdelsztajn and Lavernia 2001; Back, Lee and Kang 2005). However, it should be noted that previous studies have been carried out in vertical attritor® mills, which are not capable of generating the high milling media velocities associated with the Simoloyer (Zoz 1995).

5.2.2 Particle morphology and size

SEM micrographs of the powders milled for 60 min at -30°C and RT respectively are shown in Fig. 5.17. Milling at -30°C produced particles with reduced irregularity and a slightly, rounded morphology, Fig. 5.17 (a, b). The number of fine fragments was reduced, which would suggest that the particles have undergone repeated deformation with increased levels of welding. The particles also seemed to show a high degree of

flattening. Low temperature milling leads to transgranular fracture (Tanaka and Kosugi 1988) with grain refinement caused by fracturing and cold welding by forming new grains at the welding interface from the fragments of the original coarse grains. The morphology and structure of the particles from RT milling, Fig. 5.17 (c, d), suggest that welding and fracture mechanisms have reached equilibrium, whilst the structure of the particles milled at -30°C suggest an imbalance between the mechanisms. The elemental processes leading to grain size refinement during mechanical milling generally include three stages, beginning with the localisation of deformation into shear bands with high dislocation density, which is followed by annihilation and recombination of dislocations, forming nanometre-scale sub-grains. Further milling extends this sub-grain structure throughout the sample. The final stage involves the transformation of the sub-grain boundary structure to randomly oriented, high-angle grain boundaries (Fecht 1994). The annihilation of dislocations can set a natural limit to the dislocation densities that can be achieved by plastic deformation. Steady state deformation is observed when the dislocation multiplication rate is balanced by the annihilation rate (Moelle *et al*. 1996). Dislocation generation in the particles may have increased by ball milling at a low temperature due to the mismatch of thermal expansion coefficients between the Co matrix (13×10^{-6}/K) and the hard WC particles (4.5×10^{-6}/K). If two neighbouring phases have different thermal expansion coefficients, thermal stresses will arise at the interface upon heating or cooling, and result in dislocation formation and/or thermal crack initiation in severe cases (Kumai, King and Knott 1991).

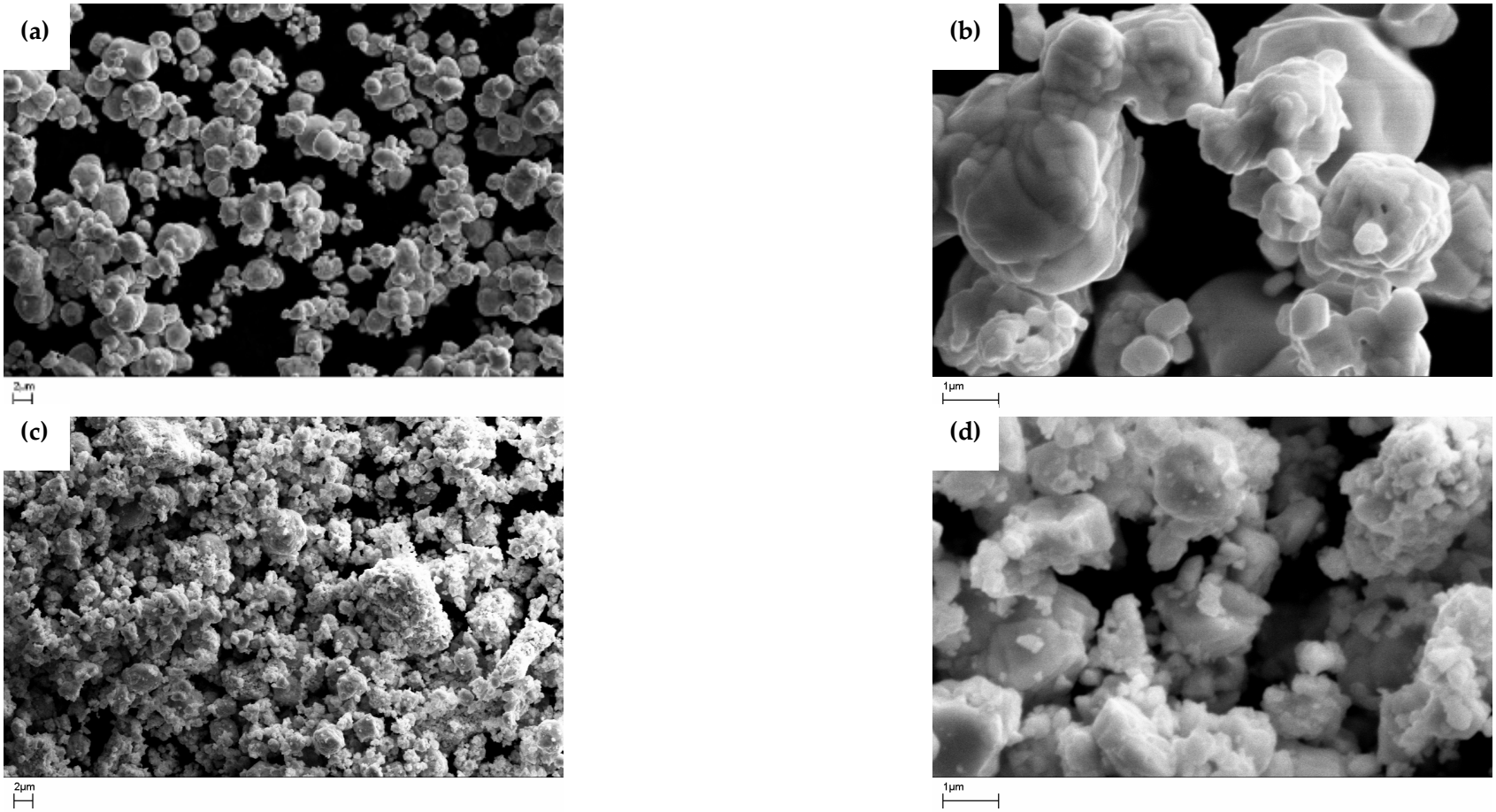

Fig. 5.17 SEM micrographs of the WC-10Co powders after 60 min milling at (a, b) -30°C and (c, d) RT.

Particle sizes after 60 min low temperature milling, Fig. 5.18, were again measured using NanoSight's NTA software. A particle detection threshold was set for the measurements to exclude particles > 1 μm. The milled powder agglomerates were again dispersed in water to break the particle-particle interactive forces. Results, within the measured range, showed a smaller mean particle size for the powder milled at -30°C of 0.129 μm compared with 0.148 μm for the RT milled powder.

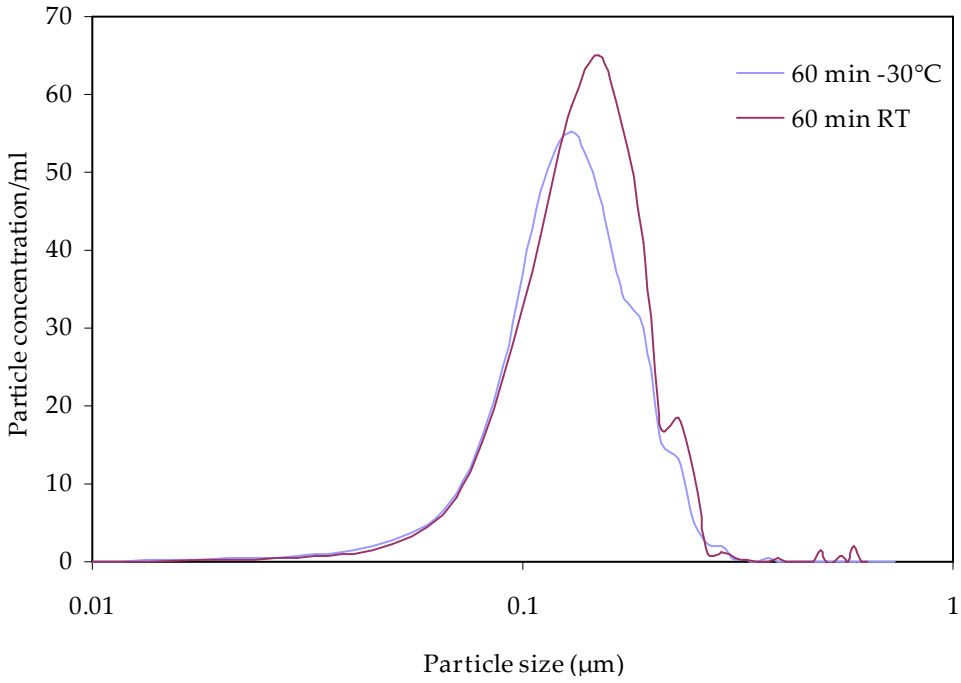

Fig. 5.18 Particle size measurements for WC-10Co powders ball milled for 60 min at -30°C and RT.

5.2.3 Effect of milling temperature on green density

The effect of compacting pressure on relative density for both powders is shown in Fig. 5.19. Both powders exhibited increasing relative density with increasing pressure with the powder milled at -30°C showing higher values at each pressure. At 400 MPa pressure, the powder milled at RT gave a relative density of 64% compared with 65.5% for the powder milled at -30°C. Both powders showed higher densities than those of conventional micron-sized WC-10Co powder. Both particle morphology and hardness influence powder compressibility. During die compaction, a compressive stress is applied on the particles that are in contact with the punch. These particles transmit stress to their neighbouring particles through the contact points between them. In an ideal model of spherical, isosized particles, symmetrical opposite forces appear in the contact points, which promote only compressive deformation of the particles. An irregular morphology of the particles propitiates the formation of asymmetrically opposite forces in the contact points between particles, which results in the shear deformation and, consequently, cold-welding of the powder. As a consequence, an irregular powder is harder to compact than a spherical powder (Schatt and Wieters 1997). The flattened morphology of the particles also provides a higher deformation capacity during powder compacting (Fogagnolo *et al*. 2003). Accordingly, the higher relative density achieved by the powder milled at low temperature was a result of its flattened, slightly rounded morphology, as it allowed higher mechanical interlocking between particles.

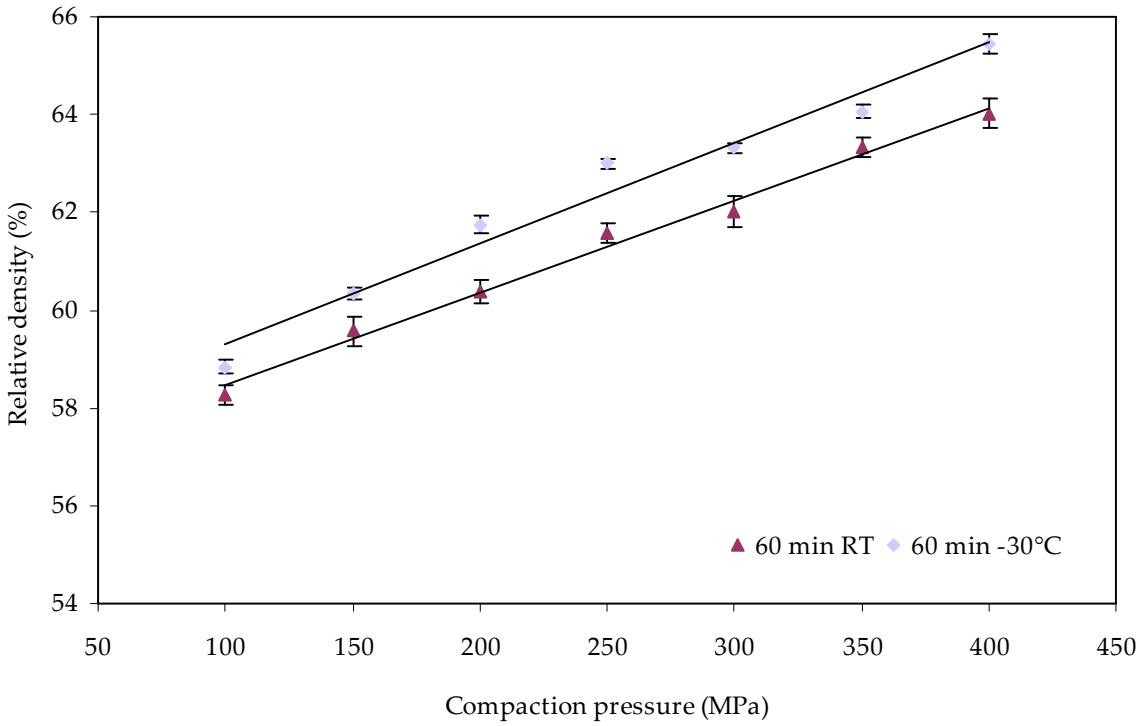

Fig. 5.19 Effect of compaction pressure on the relative density of WC-10Co powders ball milled for 60 min at -30°C and RT.

5.2.4 Effect of milling temperature on WC-Co eutectic temperature

A thermogravimetric TGA/DSC heating scan for the powder ball milled for 60 min at -30°C is shown in Fig. 5.20. For comparative purposes, the powder milled for 60 min at RT is also shown. The powder milled at low temperature shows a greater enthalpy release suggesting a higher level of grain boundary stored energy in the particles. The sample milled at -30°C shows increased weight loss, reaching ~ 0.9% compared with ~ 0.7% for the RT milled powder. From first analysis of the weight loss trace, the powder milled at -30°C behaved quite differently up to ~ 1000°C where a number of thermal

events were observed, which represent the evolution of selected gaseous species. To analyse these events in further detail, reference was made to the mass loss rate curve, Fig. 5.21. The initial weight loss that occurred up to 150°C for both powders is based on the loss of humidity (Cheremisinoff 1990). Analysis of the curve for the powder milled at -30°C shows similar behaviour to the RT milled powder up to ~ 400°C, but the weight loss at this temperature was significantly increased, as the powder particles may have absorbed additional water that could have condensed on the inside of the vessel. It has been reported that water is not completely removed until 450-500°C for mechanically mixed WC-Co powder (Gille *et al*. 2000), which may have accounted for a proportion of the increased weight loss up to that temperature, with the powder milled at -30°C showing more weight loss. However, it is more likely that the mass loss in the 250°C region is related to the removal of the die lubricant, which may have contaminated the powders during the pressing operation. At ~ 400°C, both mass loss curves show similar behaviour, which is related to the evolution of CO_2 from the reduction of oxidic impurities of the Co binder. This is followed by a further reduction process at ~ 470°C, which again corresponds to the evolution of CO/CO_2 from the oxidic impurities, with an increased effect in hardmetals with a higher Co content (Leitner, Gestrich and Gille 1997). From ~ 600°C and 1000°C, both powders exhibited a reduction in the oxidic impurities of the WC phase. A significant shift in the peak, and the number of weight loss peaks was observed. The rate of change also appears to be much faster, suggesting a faster removal of oxides. The mass loss was higher for the powder milled at -30°C, which suggests a higher amount of absorbed CO and CO_2. The low temperature milled

powder showed extensive decomposition occurring at ~ 750°C, which is the typical temperature range for the removal of CO_2 (Gille *et al*. 2000) and CO (Leitner, Gestrich and Gille 1997). It is clear that low temperature milling has significantly increased the oxygen contamination of the hard phase. The use of gas chromatography or mass spectrometry to analyse the effluent gases would provide positive identification. From 1000-1200°C no further mass loss was exhibited by the low temperature milled powder, whereas the RT milled showed a small mass loss at ~ 1200°C. This small change could be due to melting of Fe or other contaminants, Fig. 5.11, introduced as a by-product of ball milling.

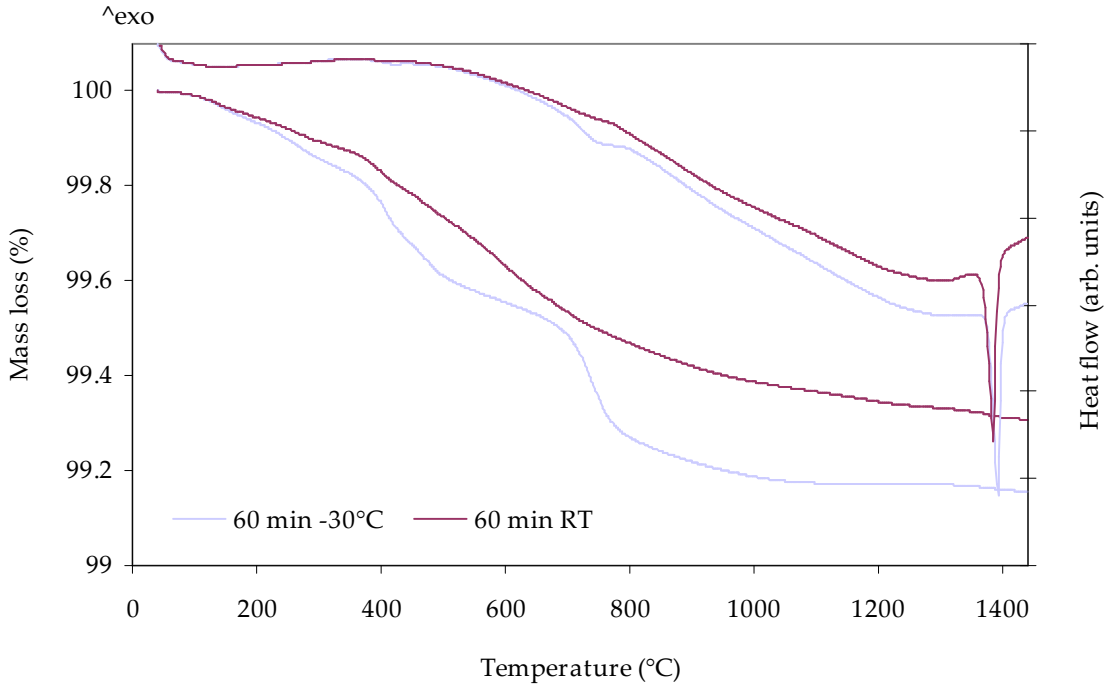

Fig. 5.20 TGA/DSC heating scan for the WC-10Co powders milled at RT and -30°C.

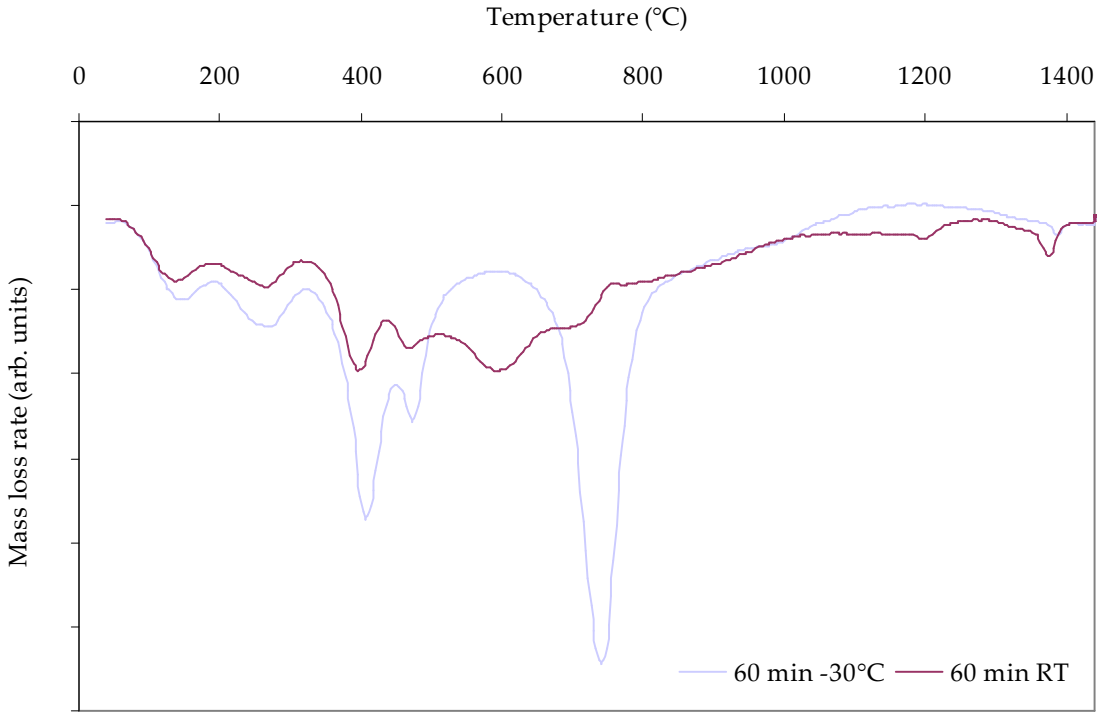

Fig. 5.21 Differential weight change versus temperature for powders milled for 60 min at RT and -30°C.

5.2.5 Effect of milling temperature on impurities

For all nanocrystalline materials prepared by a variety of different synthesis routes, surface and interface contamination is a major concern. In particular, during mechanical attrition contamination by the milling media (Fe) and atmosphere (trace elements of O_2 and N_2) can be a problem. The extent of contamination in mechanical attrition is related, in part, to the processing conditions, as shown in Fig. 5.11. By minimizing the milling time, Fe-based wear debris can be reduced. Other contamination elements usually associated with milling at low temperatures (cryomilling), such as O_2 and N_2, are not

prevalent to the same extent in this study due to the design of the milling vessel and the ability to operate 'dry' at low temperatures. An investigation of cryomilled WC-Co-VC powders showed that high O_2 and N_2 contents in the nano-powders led to carbon deficiency during subsequent sintering processes (Lee *et al*. 2003). The level of impurities measured in the powder ball milled at -30°C compared with the powder milled at RT are shown in Fig. 5.22 and Table 5.5. An interesting phenomenon is observed regarding the level of Fe pick-up, which was almost undetectable after milling at -30° even though the same grades of stainless steel milling media were used for both experiments. This suggests that wear of the milling media was considerably reduced by milling at a low temperature. The temperature rise at the ball-powder interface during MA at RT has been estimated to rise between 47°C (Schwarz and Koch 1986) to 347°C (Bhattacharya and Arzt 1993) (Chapter 2) but this would depend upon the characteristics of the powder being milled and the configuration of the ball mill. It is clearly shown by Fig. 5.22 that the temperature rise at the ball-powder interface during 60 min milling at RT was sufficient enough to 'soften' the stainless steel balls, thereby reducing their resistance to wear from the powder and the impact energy of the impeller.

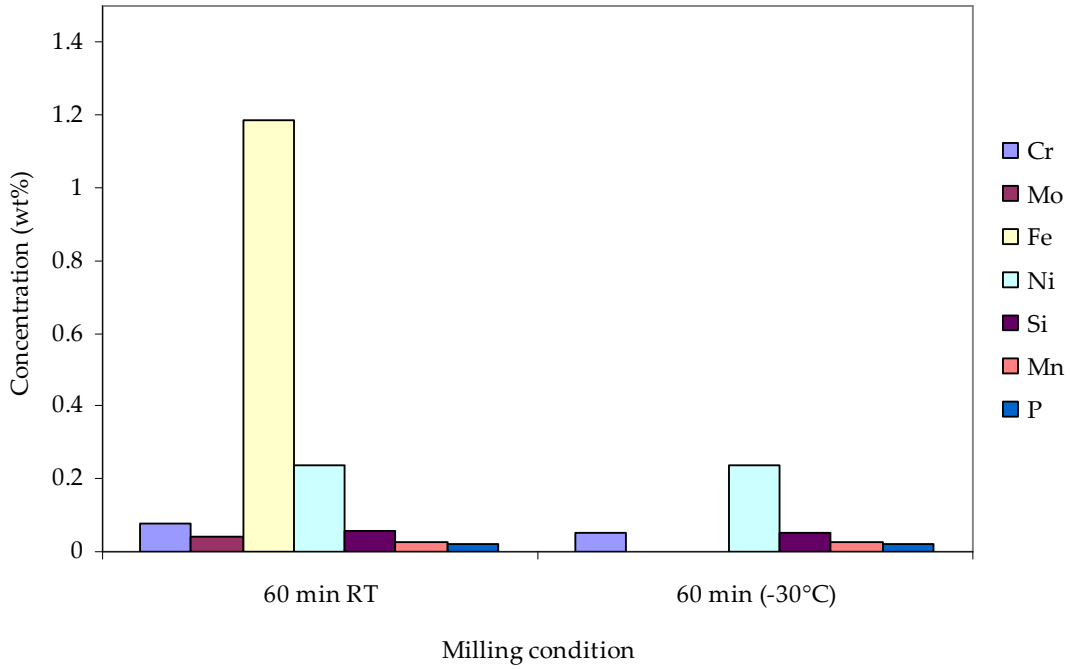

Fig. 5.22 XRF measurement of contamination elements after 60 min ball milling at RT and -30°C.

Table 5.5

XRF analysis of the WC-10Co powders after 60 min at RT and 60 min at -30°C.

Chemical analysis (wt%)	60 min RT	60 min -30°C
Cr	0.077	0.050
Mo	0.041	0.001
Fe	1.183	Nil
Ni	0.239	0.237
Si	0.056	0.050
Mn	0.031	0.025
P	0.022	0.020

5.3 Consolidation

5.3.1 Pressureless sintering – effect of milling time on densification and microstructure

After compaction, a nanocomposite powder can be densified at elevated temperatures without the application of external pressure. This technique, known as pressureless sintering†, uses the reduction of surface energy associated with the surfaces of the internal pores as its driving force. Thus, densification can be specified as the reduction of pore surface area and consequently, pore volume in a powder compact.

† The term 'pressureless sintering' is used for atmospheric pressure sintering without an additional pressure.

The sintering process is normally conducted at temperatures in the range 1400-1500°C, where the Co-rich binder phase is in the liquid state. From classical sintering theory, it is known that surface diffusion leads not to densification but to grain coarsening (German 1996). Then, if surface diffusion is the most sensitive to particle size, reduced low temperature densification should be observed in nanoparticle sintering. From the thermal analysis measurements, Figs. 5.10 and 5.20, it was proven that WC-Co melting temperature could be reduced with increased milling time. To establish the extent of low temperature densification, the 180 min milled powder sample was sintered for 60 min at 1355°C, just above its onset temperature of 1330°C. Densification reached ~ 80% of theoretical density with a sample hardness of 425 HV30, Fig. 5.23. With such a low level of densification, residual porosity was high, as shown in Fig. 5.24. The elimination of pores governs the overall densification kinetics. Temperature was increased in order to detect the completion of the densification process by monitoring sample hardness. For metals with grain sizes > 10 nm, hardness should initially increase with sintering as the microstructural characteristics of a true solid are established (Mayo, Chen and Hague 1996). If hardness begins to decrease with increased sintering then only grain growth processes are occurring and increased sintering will prove unproductive (Fougere *et al*. 1992). Relative density and hardness increased linearly with temperature, Fig. 5.23, and an increase in temperature of 35°C was required to increase density close to theoretical, with a corresponding hardness of 1311 HV30.

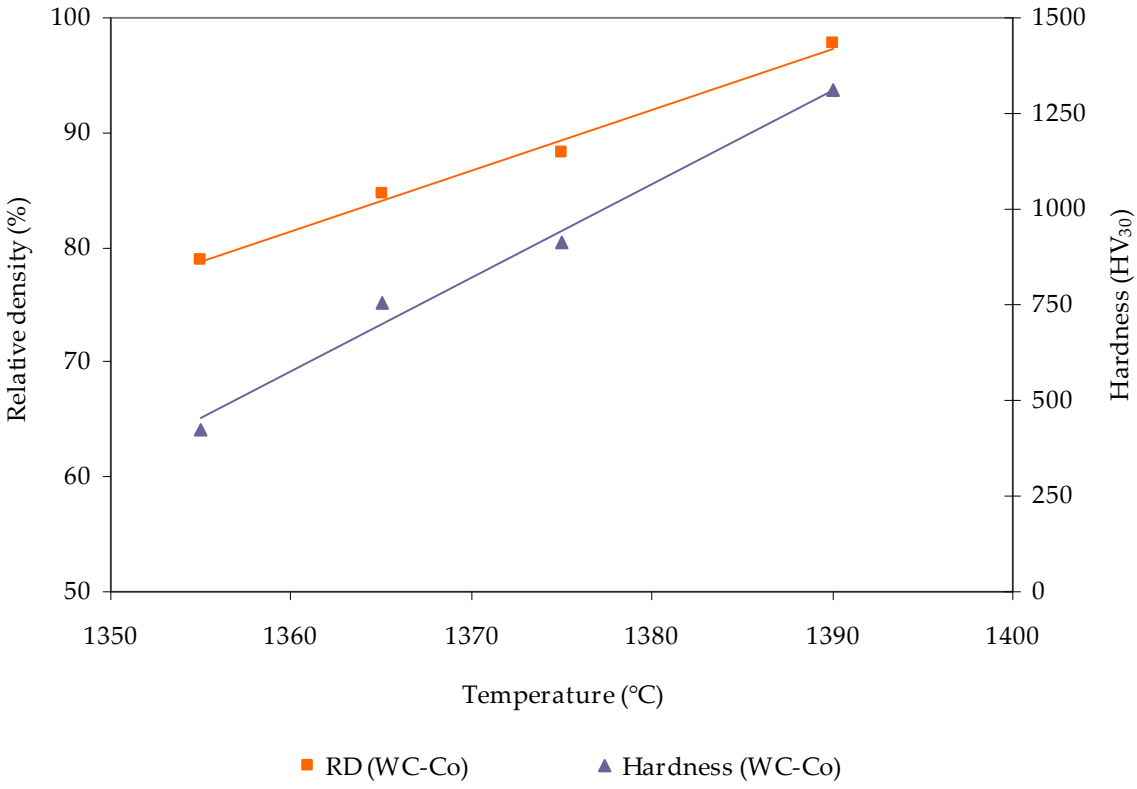

Fig. 5.23 Relative density and hardness as a function of sintering temperature for WC-10Co ball milled for 180 min and cold compacted at 250 MPa.

Residual porosity decreased with increasing temperature, Fig. 5.24, with a porosity rating of >A06 according to ISO standard 4504:1978 (section 4.5.3), after sintering at 1390°C. Some large pores remained typically around 5 μm, which may have been caused by a nonuniform, green compact structure. The effect of this nonuniformity on the final sintering of nanopowders is even less forgiving than for fine grained powders. Large pores usually originate from agglomerated powders. As shown in Fig. 5.17, nanoparticles produced after 180 min ball milling exhibited a high agglomeration tendency. Agglomerated powders have a bimodal pore distribution with small interparticle and large interagglomerate pores. The removal of interagglomerate pores,

based on vacancy diffusion, requires higher temperatures and longer sintering times (Groza 2007). Although the powder exhibited a higher green density, Fig. 5.12, than conventional WC-Co fine powders, this may not necessarily reflect a uniform pore size and distribution. The optimum green density of commercial WC–Co is known to be in the vicinity of 53%. When large agglomerates are present, the green density may be higher than in nonagglomerated powders, similarly to bimodal size powder packing. The powders ball milled for 60 and 300 min and compacted at 250 MPa, were sintered using the same conditions and measured for density, Fig. 5.25.

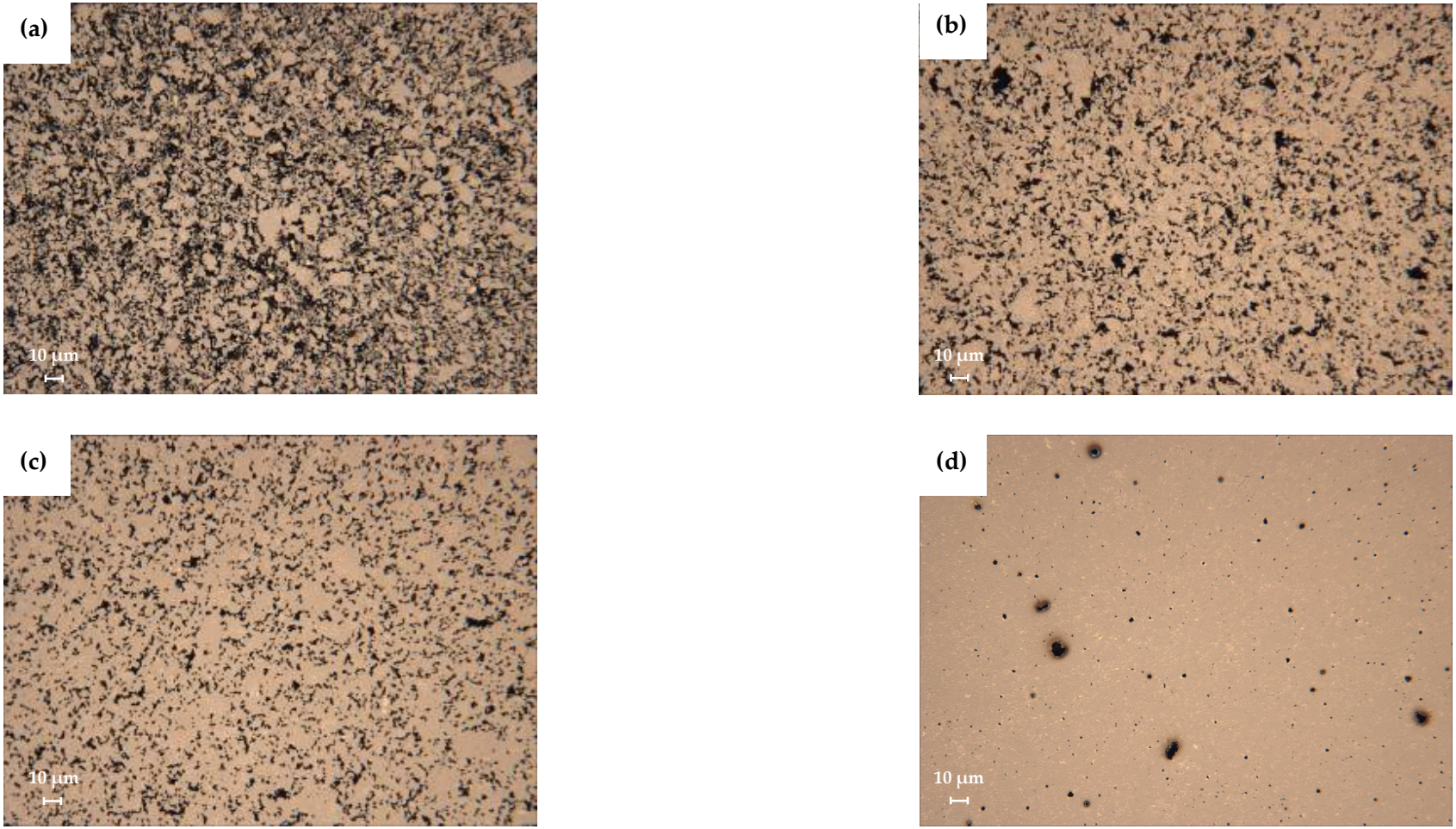

Fig. 5.24 Optical micrographs of residual porosity from 180 min ball milled WC-10Co after pressureless sintering at (a) 1355°C; (b) 1365°C; (c) 1375°C; and (d) 1390°C.

At 1355°C, the powders exhibited behaviour consistent with their thermal analysis measurements, Fig. 5.20. The powder milled for 300 min showed a relatively high level of densification (~ 93%) at 1355°C due to the enhanced temperature in relation to the reduced onset of melting and lower level of agglomeration. This result also suggests that agglomerate size, and not domain size, has the dominant role in determining densification behaviour. Powders with larger, mean agglomerate sizes contain larger interagglomerate pores at the beginning of sintering. These large pores have a low driving force for densification. To compensate for the low driving force and to generate a reasonable rate of densification, the sintering temperature must be increased. The larger the agglomerates, the larger the interagglomerate pores, and the higher the sintering temperature required to reach a given density. It is reasonable to assume that some of the interagglomerate pores would have been closed by plastic flow of the surrounding metal particles during compaction but with increasing milling time, as shown in Fig. 5.12, the particles became harder and as a result, green density decreased. The powder milled for 60 min reached ~ 76% relative density at 1355°C as the sintering temperature was only slightly above the onset temperature (~ 1340°C). Densification increased linearly up to 1390°C with the powders milled for 60 and 180 min showing enhanced rates of densification after their respective eutectic points compared to the powder milled for 300 min. Temperature also has a significant influence on densification rate, due to the exponential (Arrhenius) relationship between densification rate and temperature. Considering the Arrhenius expression for densification, the sintering temperature dependence on the particle size becomes:

$$n\ln(d_1/d_2) = Q/R[(1/T_1) - (1/T_2)] \quad (5.15)$$

where Q is the activation energy for the predominant sintering mechanism, R is the gas constant, d_1 and d_2 are the different powder particle sizes, and T_1 and T_2 are their respective sintering temperatures. However, the exponent n is dependent on the main sintering mechanism and has a value of 3 if the main sintering mechanism is volume diffusion and a value of 4 if the main sintering mechanism is grain boundary diffusion (Groza 2007).

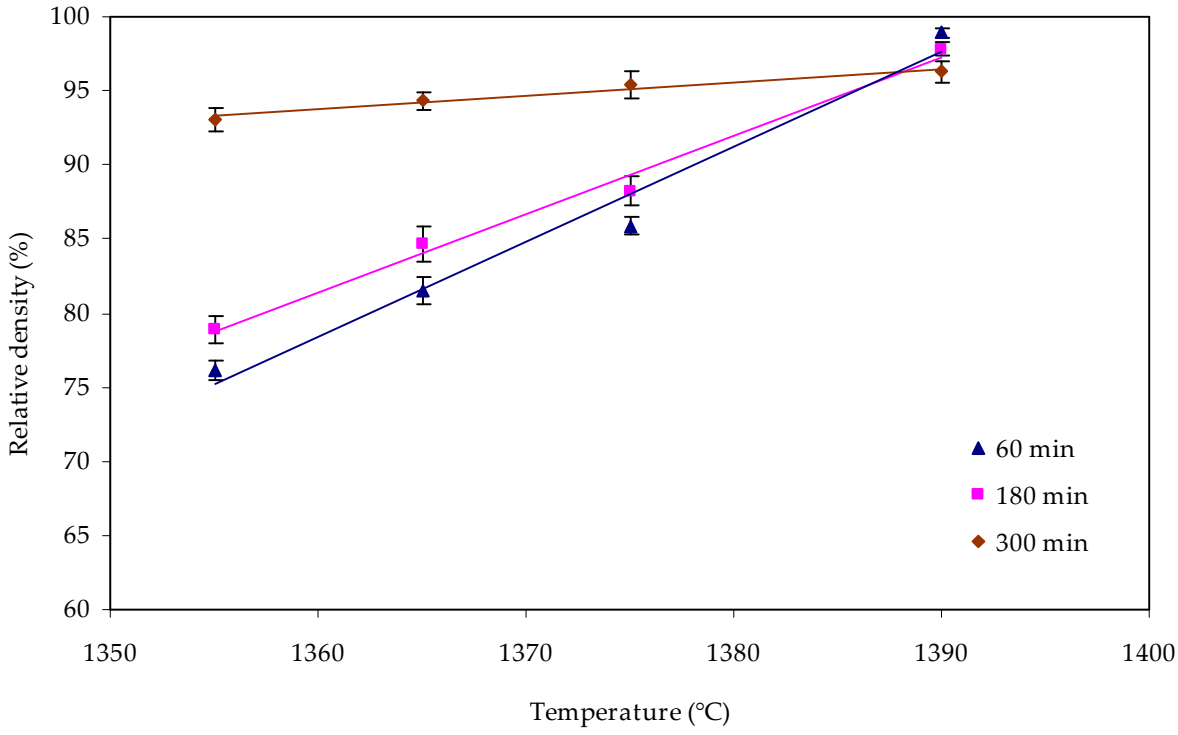

Fig. 5.25 Densification as a function of temperature for ball milled WC-10Co powders after pressureless sintering.

In Fig. 5.26, residual porosity can be seen for each powder after sintering at 1390°C, including 30 min milling. There appeared to be a marked difference in porosity levels between 30 and 60 min milling, Figs. 5.26 (a, b), with the samples rated at >A08 and A06, respectively. This was probably caused by insufficient milling time, as 30 min was not long enough to create a well dispersed, homogeneous two phase structure. Although composite particles had been formed at this stage, Fig. 5.8 (a), the structure of the particles and the particle size distribution would have prevented a uniform pore structure at the green stage and the nonuniform distribution of Co could have caused isolated areas of Co to be formed during sintering. Although this powder exhibited the highest level of relative density at the green stage, due to lower levels of cold work and large agglomerate sizes, it showed the lowest relative density after sintering at 1390°C, Fig. 5.27. Residual porosity reached the lowest level, A06, for the sample milled for 60 min milling, Fig. 5.26 (b), after which pore size and number of pores increased with milling time with the sample milled for 300 min rated at A08. Porosity seals off from the surrounding atmosphere when 90% density is reached. If the gas entrapped is insoluble, then the pores shrink until a balance is attained between surface energy and the excess pressure in the pores (Nelson and Milner 1972).

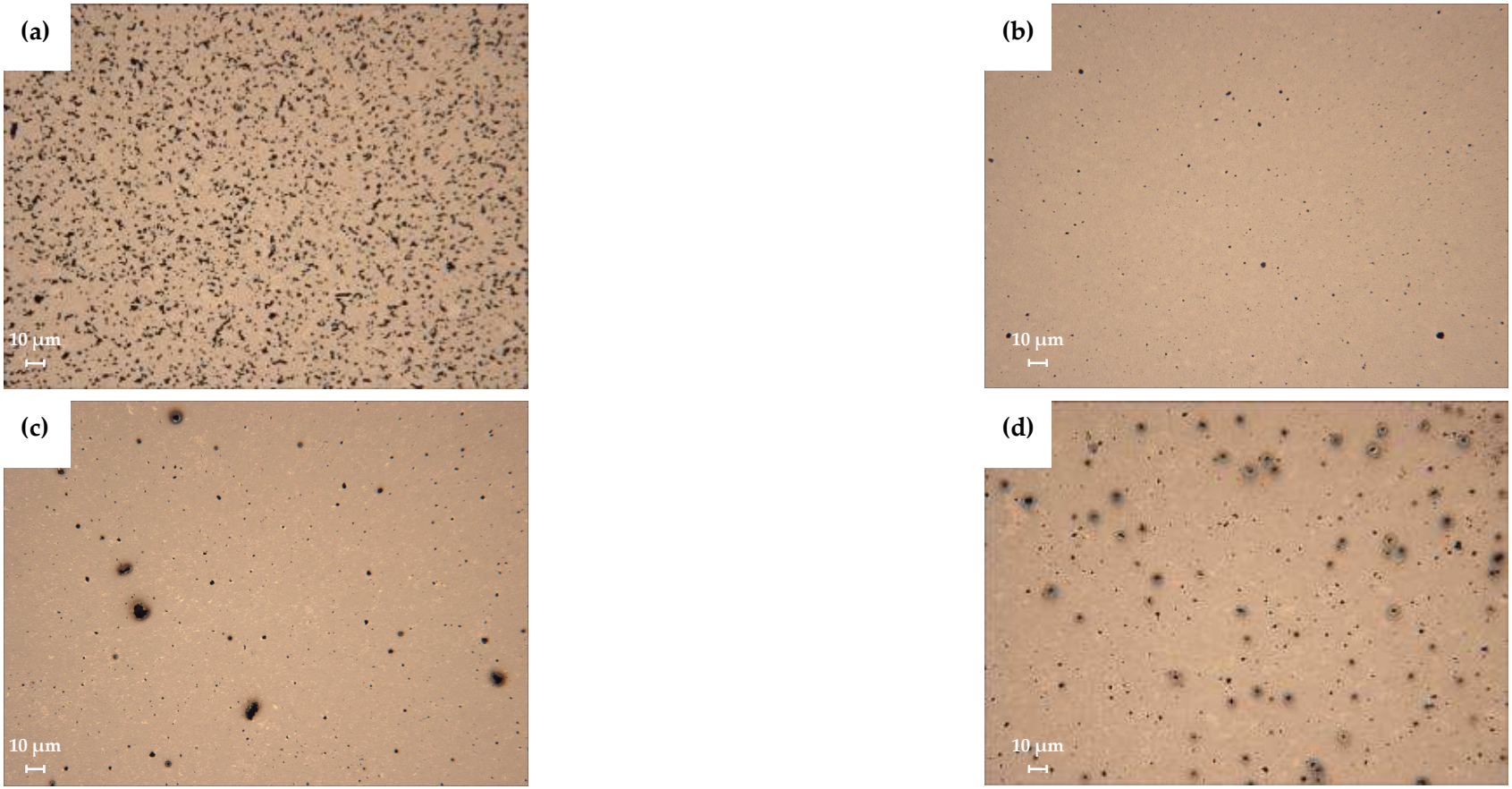

Fig. 5.26 Optical micrographs of WC10Co pressureless sintered at 1390°C/60 min after (a) 30 min, (b) 60 min, (c) 180 min and (d) 300 min ball milling.

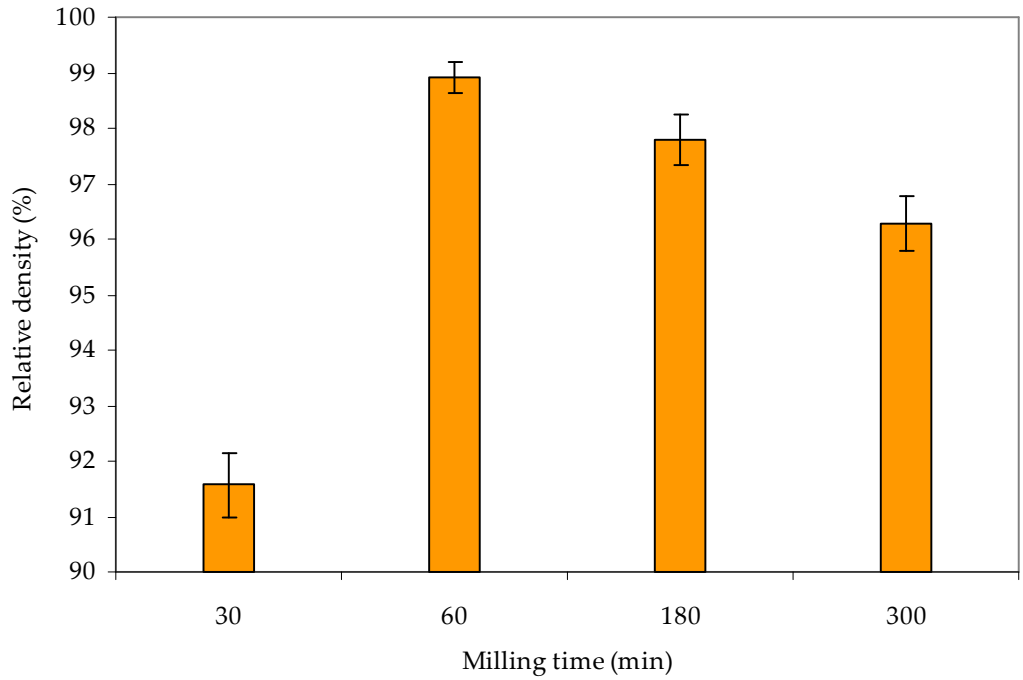

Fig. 5.27 Relative density as a function of milling time for the WC10Co grade pressureless sintered at 1390°C/60 min.

In Fig. 5.28 the effect of ball milling time on relative density and hardness is shown, with both properties reaching optimum levels after 60 min milling. This supports the morphological results from Fig. 5.7, with both pointing towards 60 min ball milling as the ideal conditions for balancing the mechanisms of MA for this WC-10Co material and their effects on post-processing with pressureless sintering. It is clearly shown in Fig. 5.28 that continued ball milling did not enhance densification or hardness levels but in fact, had a detrimental effect.

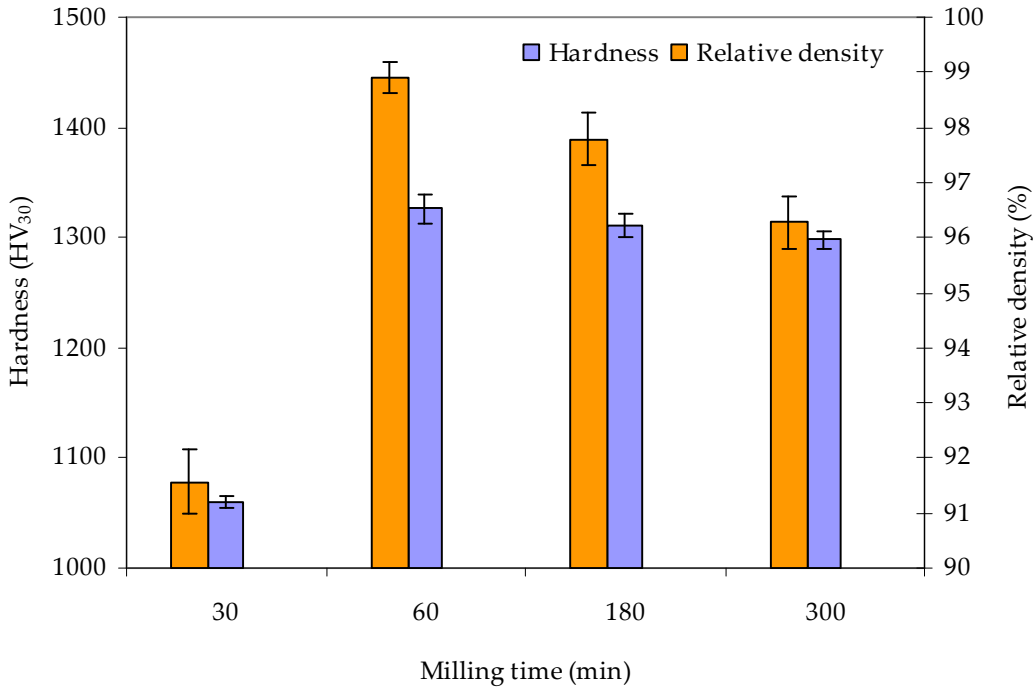

Fig. 5.28 Relative density and hardness as a function of milling time for the WC10Co grade pressureless sintered at 1390°C/60 min.

Normally, die compaction of metal powder undergoes a number of stages with the initial stage involving particle rearrangements (Al-Qureshi *et al*. 2008). The physical properties of the powder particles, such as size and shape, greatly influence this initial stage. This is followed by the elastic-plastic deformation, and here the mechanical properties and the quality of the particles are important factors, which control the compressibility behaviour of the powder. Hence, the work hardening of the particle affects the hardness of the final product. As a result, the powder compacted component is produced with inhomogeneous distributions of density and porosity. This is due to

the frictional forces in between particles (internal friction), and/or between the powder and the die walls (powder/die friction).

A series of hardness measurements were made in order to verify whether the frictional forces between the powder and the die wall had become sufficient to inhibit the transmission of the compaction load through the compact, the general effect of which is to create a variation in density. A cylindrical compact of the 180 min milled powder, cold pressed at 250 MPa and pressureless sintered at 1390°C for 60 min, was sectioned as shown in Fig. 5.29. A hardness profile through the thickness of the sample at the edge and centre positions was generated. The results show that hardness decreases with increasing distance from the punch face, with a larger decrease at the edge of the punch. There is also a density distribution in the horizontal plane due to frictional effects dropping-off away from the die wall.

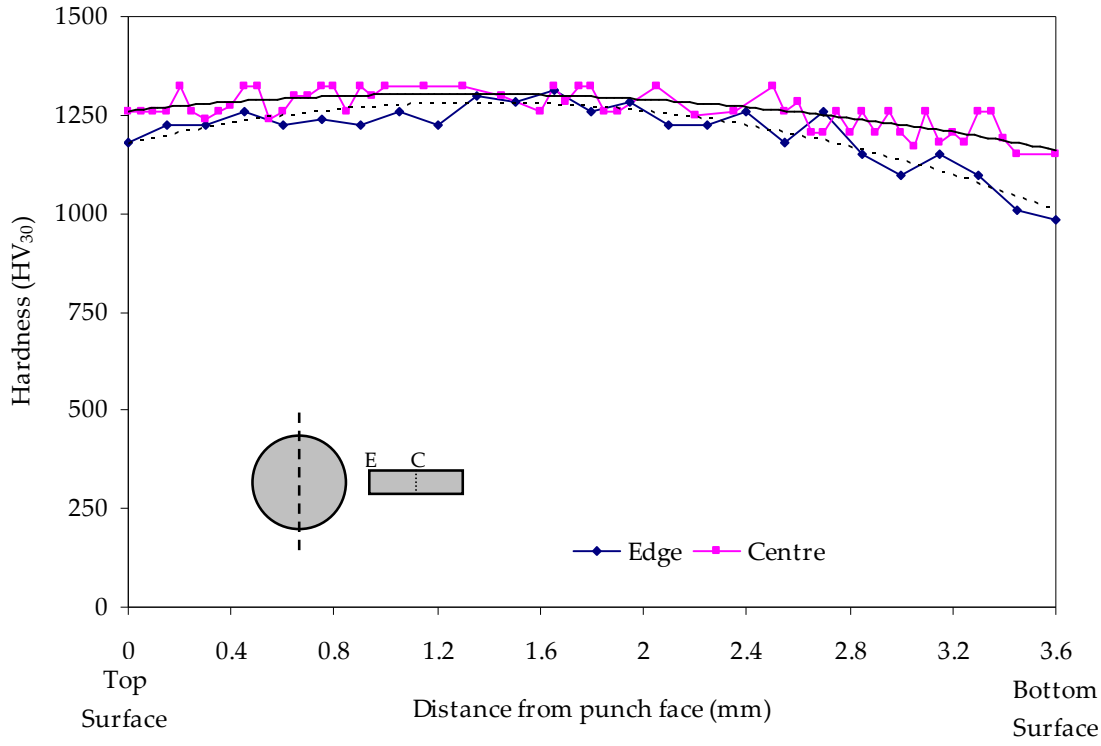

Fig. 5.29 Through-thickness hardness (HV30) profile of a cylindrical compact, cold pressed at 250 MPa and pressureless sintered at 1390°C for 60 min.

Magnetic coercivity measurements are used by the hardmetal industry for non-destructive quality control. The WC/Co interface restricts movement of magnetic domain walls within the ferromagnetic Co binder phase. Thus, the magnetic field required to restore zero magnetisation to a magnetically saturated WC-Co hardmetal is proportional to the interfacial area between the Co binder phase and the WC hard phase, and is thus related to the WC grain size (Porat and Malek 1988; Fang and Eason 1993; Roebuck, Bennett and Gee 1993; Roebuck 1999; Sundin and Haglund 2000; Roebuck 2002). A fine Co matrix will have a lot more residual magnetism, as it will require more force to neutralize all the magnetic nodes (Co pockets) in the matrix. The size of the Co pockets is

a direct measurement of the size of the WC grains, i.e. if the WC grains are small, the Co pockets are small.

The amount of Co present in the sample influences; (i) most predominantly the magnetic saturation M_s of the material; (ii) the binder mean free path thickness; and (iii) the degree of skeleton formation or contiguity of the WC grains. The theoretical M_S value of pure Co reaches 161.8 Am^2/kg at room temperature (Lyndon and Swartzendruber 1991) while that of the highest measured M_S value per gram of Co in the hardmetal alloy reaches 156 Am^2/kg, i.e. 96% that of pure Co. Therefore, the non-magnetic WC particles decrease the overall magnetic saturation of the material. In Fig. 5.30 the effect of ball milling time on coercivity can be seen after the samples were pressureless sintered at 1390°C for 60 min. Coercivity decreases with milling time up to 180 min milling where a sharp increase then occurs with 300 min milling. In this case, the increase in coercivity is not related to a decrease in WC grain size, as typically found for WC-Co hardmetals (Topić *et al*. 2006) but is instead due to the high level of Fe pick up (Fig. 5.11) during ball milling, which would affect the ferromagnetism reading. The typical relationship between increasing coercivity with decreasing grain size is somewhat similar to a Hall-Petch relationship, where a decrease in grain size causes an increase in the strength of the material. The coercivity increase is believed to be attributed not only to WC grain size refinement, but also to a decrease in Co content (Gorkunov, Ulyanov and Chulkina 2004).

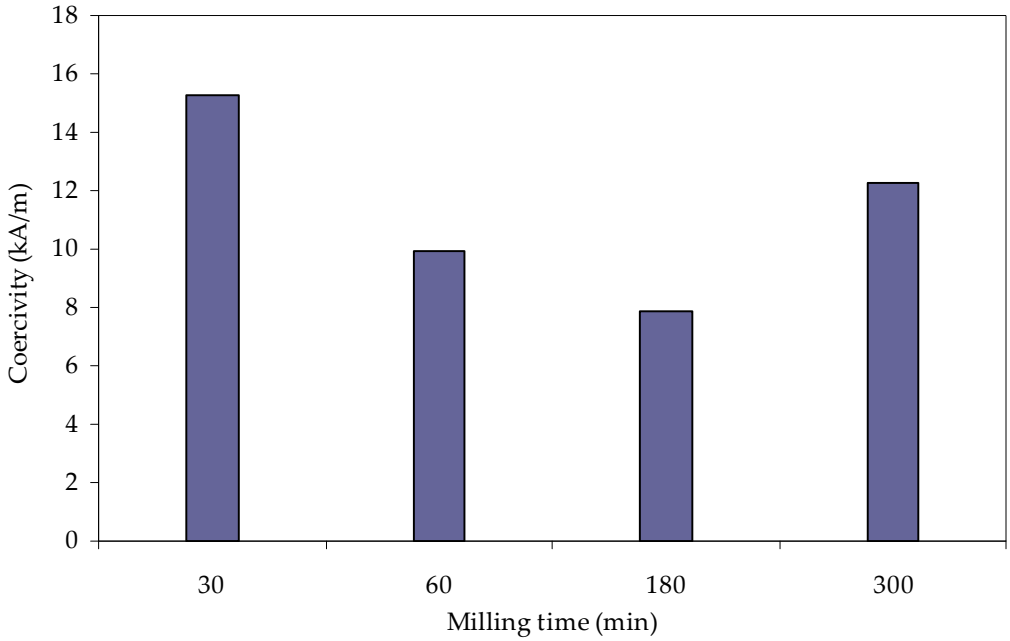

Fig. 5.30 Coercivity as a function of milling time for WC-10Co pressureless sintered at 1390°C/60 min.

Microstructure development during pressureless sintering was monitored by SEM, and the micrographs are shown in Fig. 5.31. The first noticeable feature of the micrographs is the amount of WC grain growth that has taken place during sintering, closely followed by the WC grain size distributions. For all applications of WC-Co hardmetals, the utmost homogeneity in WC grain size and distribution in the binder phase is a prerequisite. Clearly, 30 min ball milling time was insufficient to generate a well dispersed, uniform microstructure as shown in Fig. 5.31 (a) and (b). Whilst there were a number of large, ~ 4 μm WC grains in the microstructure, there did not appear to be any discontinuous, WC grain growth affecting neighbouring grains. During sintering, grain growth in WC-based materials occurs in two ways, by (i) continuous and (ii)

discontinuous grain growth. Continuous grain growth is recognised as uniform growth of individual grains, whilst discontinuous grain growth is known as an undesirable formation of isolated, coarse WC grains that grow faster and larger than their neighbouring grains and have a deleterious effect on the performance of the material (Kishino *et al*. 2002). In Fig. 5.31 (a, b) it can clearly be seen why 30 min milling, combined with the conditions of pressureless sintering, produced a material with poor mechanical properties. An improved microstructure in terms of WC dispersion after 60 min milling is shown in Fig. 5.31 (c, d). However, WC grain size distribution appeared wider with a higher number of grains > 3 μm, with coercivity measurements suggesting a significant increase in WC grain size. Despite this wide distribution and general, coarse structure, mechanical properties were considerably improved due to an enhanced level of densification and correspond with those of a medium-grained conventional WC-10Co hardmetal (Table 1.1) with a hardness of 1326 HV30. Further milling had only a small effect on the microstructures in terms of WC grain size, as shown in Fig. 5.31 (e, f) and (g, h).

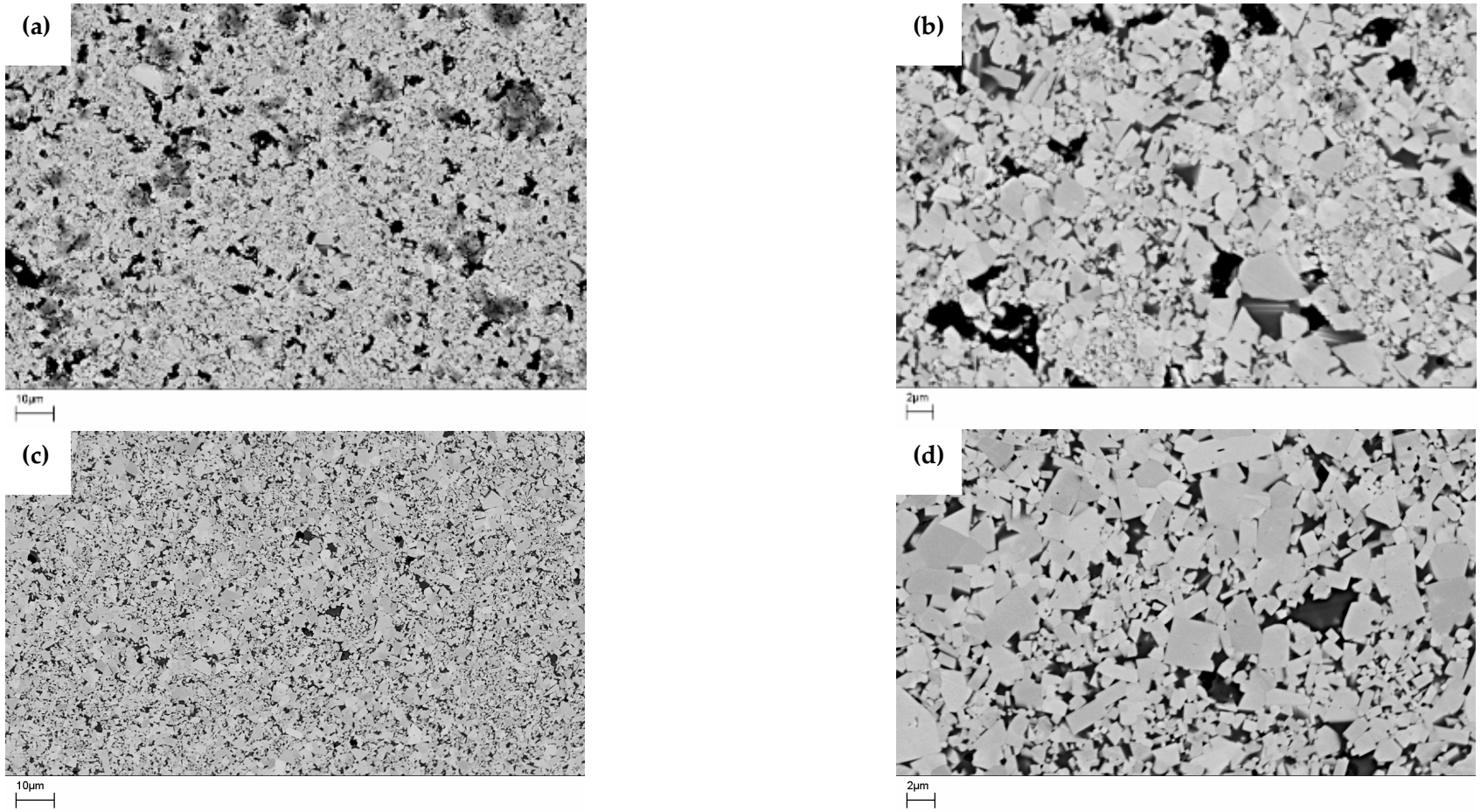

Fig. 5.31 SEM micrographs of pressureless sintered (1390°C/60 min) samples prepared from powder ball milled for (a, b) 30 min; (c, d) 60 min

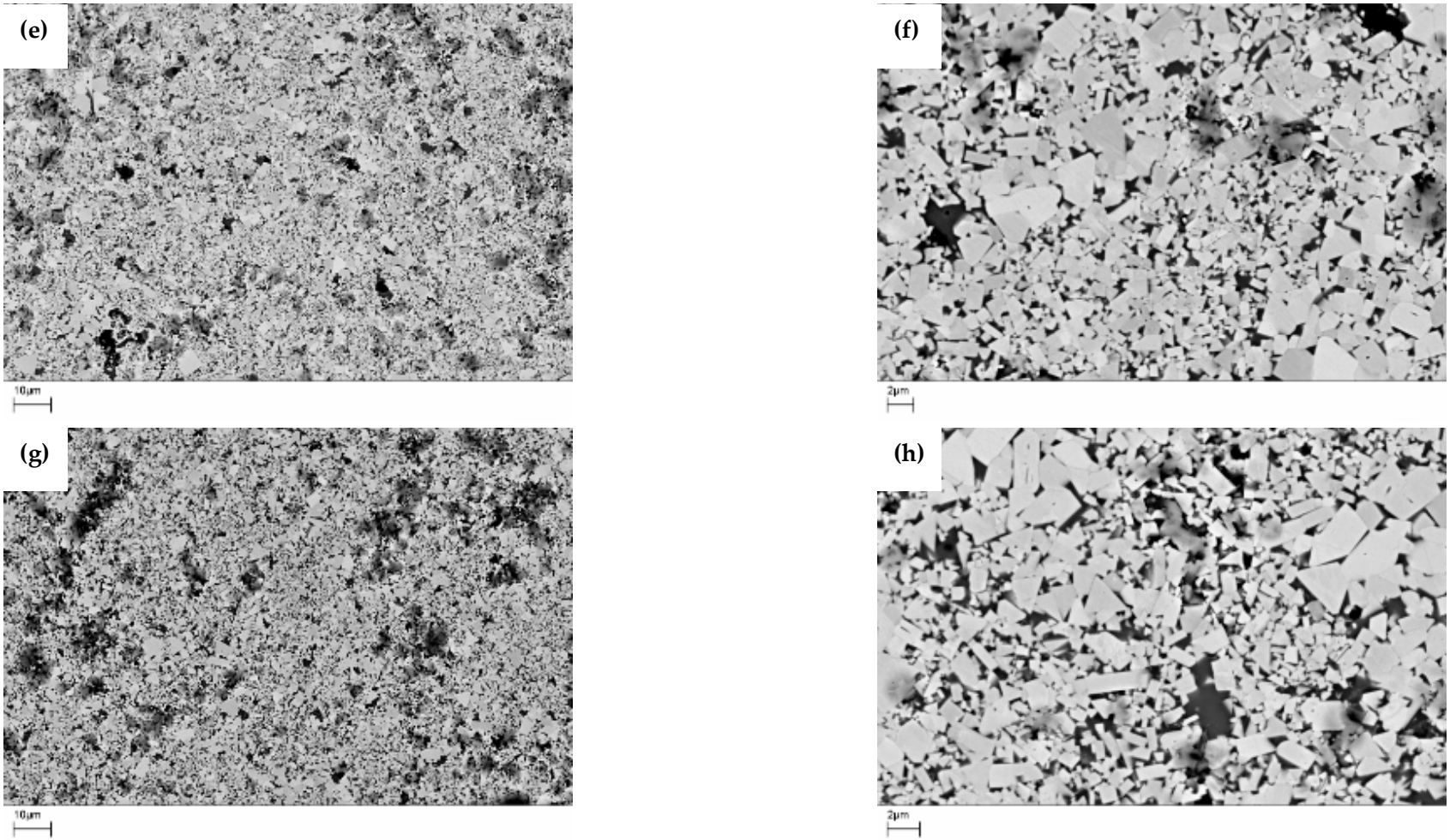

Fig. 5.31 cont'd SEM micrographs of pressureless sintered (1390°C/60 min) samples prepared from powder ball milled for (e, f) 180 min and (g, h) 300 min.

Clearly, the elevated temperature and isothermal hold time had a significant effect on WC grain growth. Grain growth in nanostructured materials appears to follow the traditional, phenomenological laws. A number of studies (Ganapathi, Owen and Chokshi 1991; Vergnon, Astier and Teichner 1974; Boutz *et al*. 1990) have confirmed the general relationship:

$$G^N - G_0^N = kt \tag{5.16}$$

where G is the instantaneous grain size, G_0 is the initial grain size, N is the grain size exponent (ranging from two to four), k is a rate constant, and t is time. The rate constant, k, is generally proportional to the diffusivity, $D_0 \exp(-Q/RT)$, and this gives the temperature dependence of grain growth (Mayo, Chen and Hague 1996). Eq. 5.9 shows that, in the ideal case, grain growth depends on temperature and time but, more importantly, it reveals what grain growth does not depend on (at least, not directly) or are simply not considered; microstructural parameters such as pore size, green density, or agglomerate size. The latter parameters can affect grain growth by altering the value of N in eq. 5.9 (Vergnon, Astier and Teichner 1974), but the effect is a weak one. The majority of the milled powders achieved relatively high green densities, Fig. 5.12 with the exception of the powder milled for 300 min. Usually, densification rate improves with a smaller particle size, giving higher final densities for a fixed processing cycle (Eremenko, Naidich and Lavrinenko 1970). In the rearrangement stage during LPS, a

small particle size improves the rate of rearrangement because of a large capillary force even though the amount of interparticle friction is increased. Likewise, in the solution-reprecipitation stage, a small particle size improves the densification rate (Froschauer and Fulrath 1976). As a high green density should reduce pore size, one could postulate that pore size has little bearing on grain growth as shown by the WC grain size measurements in Table 5.6. Mean WC grain size, measured by linear intercept, decreases with increasing milling time, Fig. 5.32, from 1.08 μm for 30 min milling to 0.85 μm for 300 min milling.

Table 5.6

Mean WC grain size after pressureless sintering (1390°C/60 min) measured by linear intercept.

Milling time (min)	Mean WC grain size (μm)
30	1.05
60	0.97
180	0.88
300	0.85

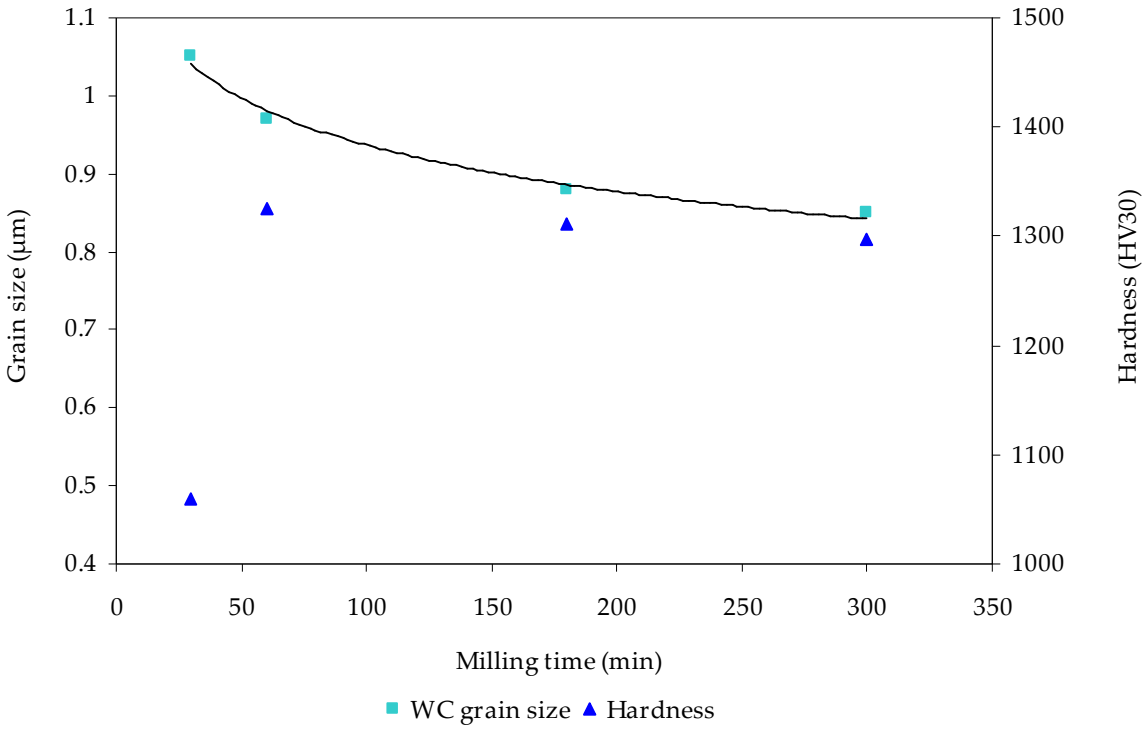

Fig. 5.32 Mean WC grain size and hardness as a function of milling time after pressureless sintering at 1390°C/60 min.

5.3.2 Effect of milling time on densification and microstructure after sinter-HIP

Generally speaking, the application of an external pressure to a powder compact results in a direct increase in the driving force of densification and an increase in densification kinetics. In sinter-HIP processing, a powder compact is first sintered or raised to an elevated temperature where diffusion can reduce or eliminate open porosity. Then, both pressure and heat are applied to the compact to fully consolidate the material. The driving force of densification under an external pressure is determined by the pressure

itself and also the contact area relative to the cross-sectional area of the particles (Kang 2005).

The relative density of the WC-10Co powders ball milled for 30, 60, 180, and 300 min after sintering at 1390°C/60 min followed by 5 min at 40 MPa pressure are shown in Fig. 5.33. As the samples were sintered using an industrially-based, sinter-HIP process, it was not possible to change the process cycle. Relative density seems to follow the same trend as that exhibited from pressureless sintering (Fig. 5.27), showing a sharp increase after 30 min ball milling, almost reaching theoretical density after 60 min ball milling and then decreasing sharply to ~ 96% after 300 min milling. It is interesting to note that both sintering processes show that the optimal ball milling time to achieve the highest level of densification is 60 min. This result clearly shows how quickly the 'ideal' conditions of MA were reached and that milling beyond this 'limit' serves no beneficial purpose. However, whereas hardness of the WC-10Co material also peaked for the 60 min milled powder after pressureless sintering, the results from sinter-HIP indicate a decreasing trend with the highest level of hardness achieved for 30 min milling, Fig. 5.36. Initially, this suggests that the supplementary application of pressure that took place during the latter stages of the sintering process was sufficient to generate a more homogeneous structure than that achieved from pressureless sintering, with further milling only leading to microstructural coarsening. During the sinter-HIP process, it is generally understood that the structure is homogeneously compacted and there is no displacement of the Co binder into the voids when typical pressures of 6-10 MPa are used (Upadhyaya 1998). This pressure is below that necessary to overcome capillary action, but above that

necessary for gross structural movement (Lueth 1985). This prevents any voids or porosity from being filled with Co but instead, fills them with the surrounding structure by gross movement.

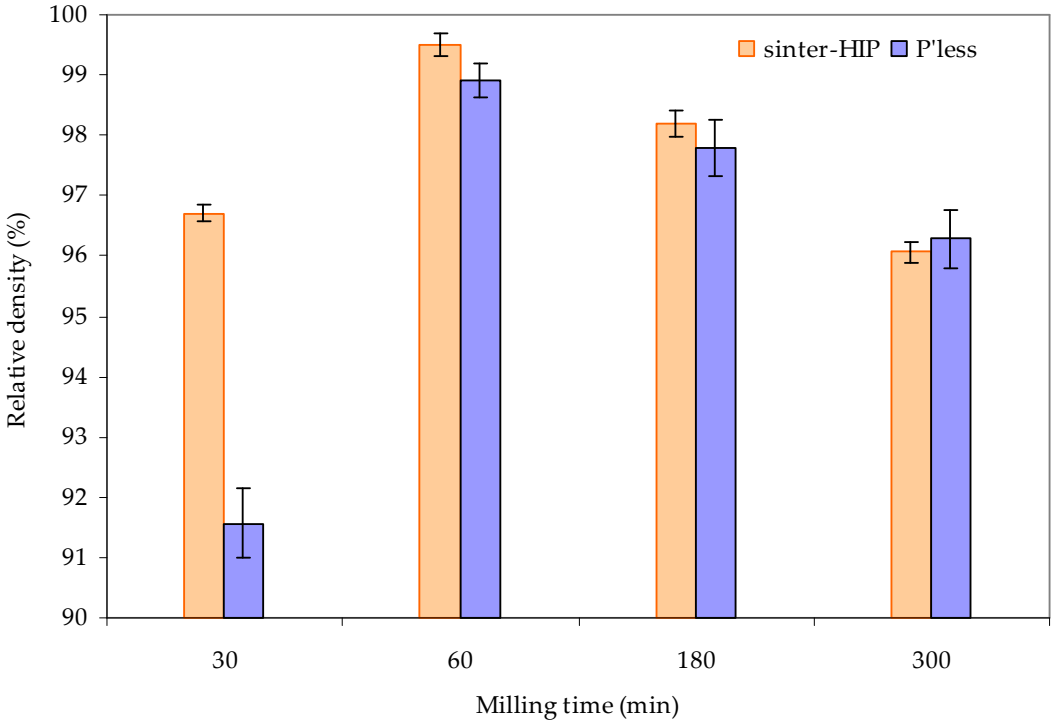

Fig. 5.33 Relative density as a function of milling time for the WC-10Co grade sinter-HIP'd at 1390°C/60 min.

However, an SEM micrograph of the 30 min ball milled sample shows that the high pressure used in this study (40 MPa) did cause Co pooling, Fig. 5.34. Co pools are porosity voids that are filled by Co through the HIP operation. This prevents the loss of strength of a porosity hole (Jawitz 1997). Energy dispersive X-ray analysis (EDX) of the

area shown in Fig. 5.34, estimated the Co level to be ~ 14.5 wt% with ~ 68 wt% of W in solid solution.

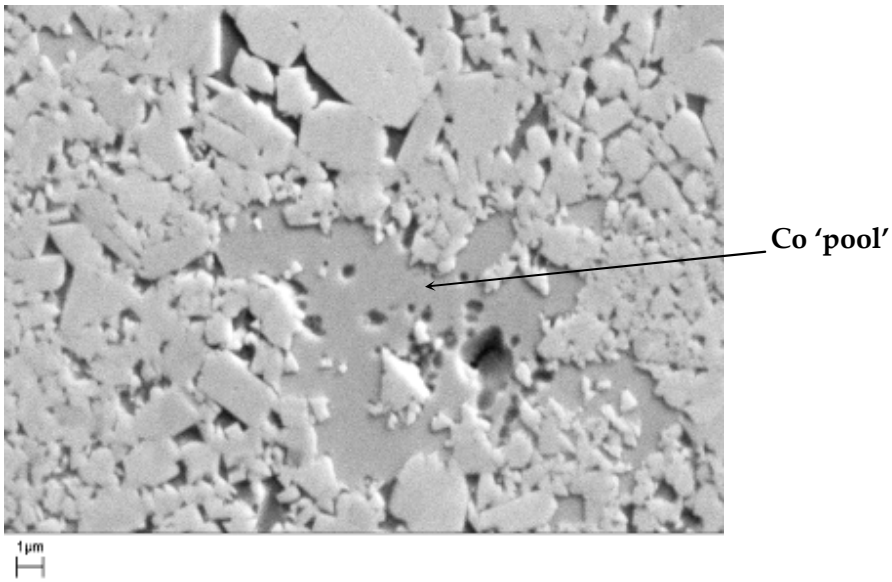

Fig. 5.34 SEM micrograph (BSD) of the 30 min milled material after sinter-HIP showing an area of Co pooling.

Further analysis of the microstructure for the 30 min milled sample, Fig. 5.35 (a, b), shows a non-uniform microstructure and a wide WC particle size distribution, with an average grain size of 1.41 μm, which shows that considerable WC grain growth has occurred due to the elevated temperature and external pressure. Hardness decreases at a much faster rate with milling time, Fig. 5.36, compared to the same samples pressureless sintered. This suggests that HIP had a significant effect on the final stage of LPS of the milled powders, serving only to accelerate the microstructural changes associated with this stage, including grain size, grain shape, and binder phase distribution. In the case of

hardmetals, complete densification is achieved during the first two sintering stages (see Chapter 3). Prolonged holding of the compact leads to microstructural changes, including further growth of the hard WC particles. In the hardmetal system where high solid solubility is present, all three stages of sintering overlap. However, at any particular stage, densification by a particular mechanism is so predominant that it can completely overshadow other simultaneously occurring events (German 1985). Complete densification takes place only when the liquid phase is sufficient enough to form continuity throughout the compact, i.e. at around 50-60 volume percent. Residual porosity of the 30 min milled sample after sinter-HIP is shown in Fig. 5.37, with porosity level rated at A08 according to ISO 4505:1978. In Fig. 5.38 it can be seen that WC grain growth is increased by the sinter-HIP process compared to pressureless sintering for the shorter milling times, whereas the growth rate is reduced for longer milling times.

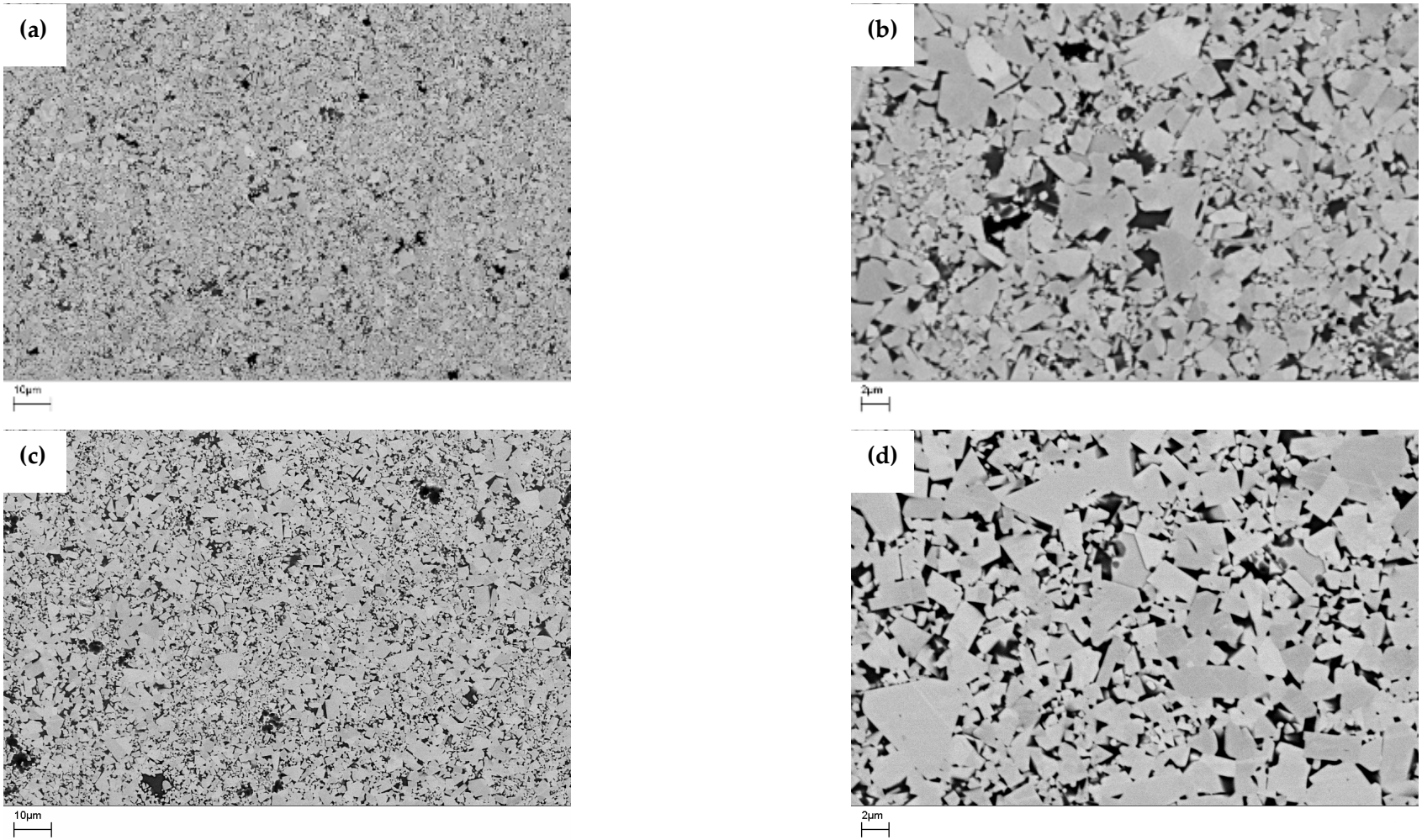

Fig. 5.35 SEM micrographs of sinter-HIP'd (1390°C/60 min) WC-10Co samples prepared from powder ball milled for (a, b) 30 min; (c, d) 60 min;

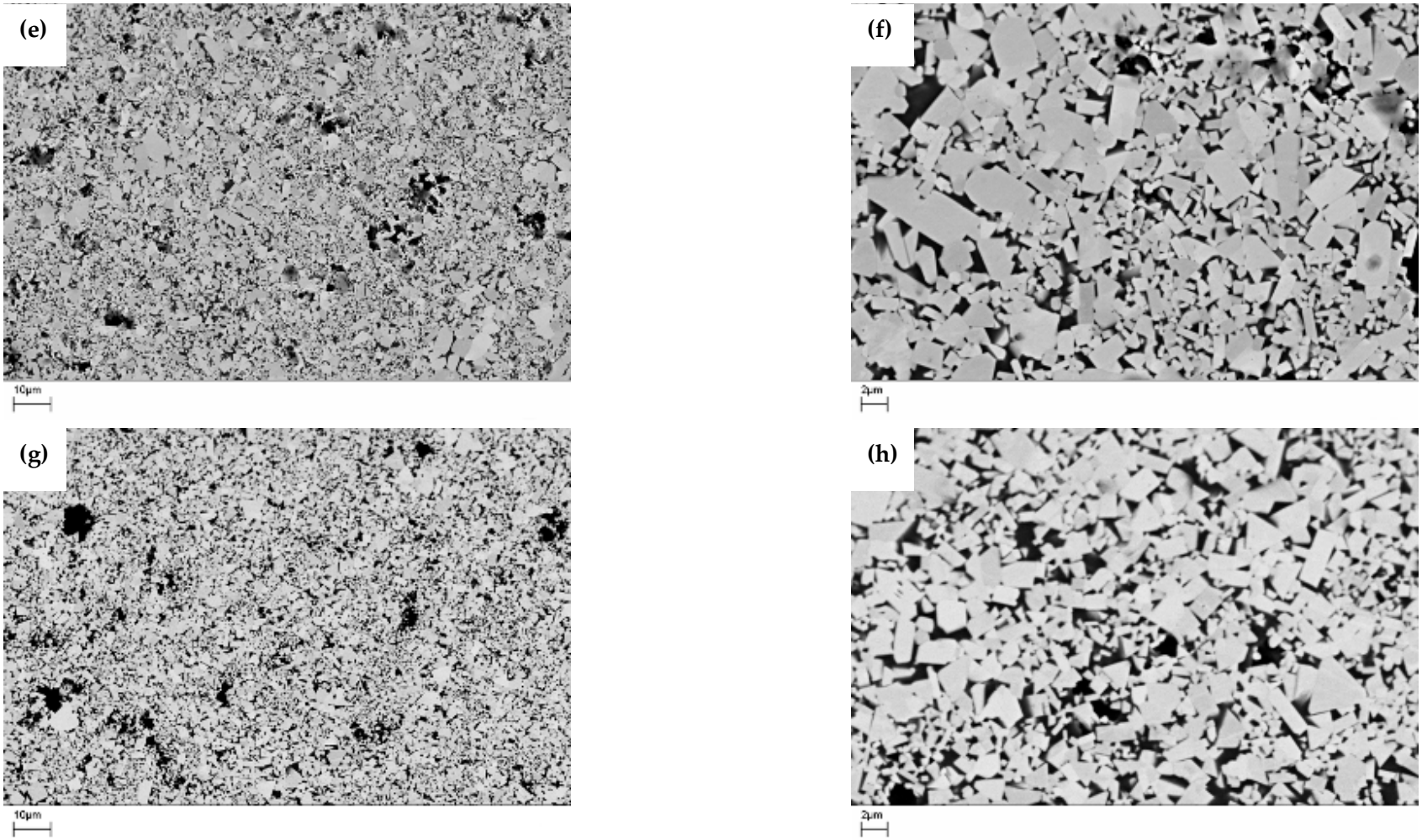

Fig. 5.35 cont'd SEM micrographs of sinter-HIP'd (1390°C/60 min) WC-10Co samples prepared from powder ball milled for (e, f) 180 min; and (g, h) 300 min.

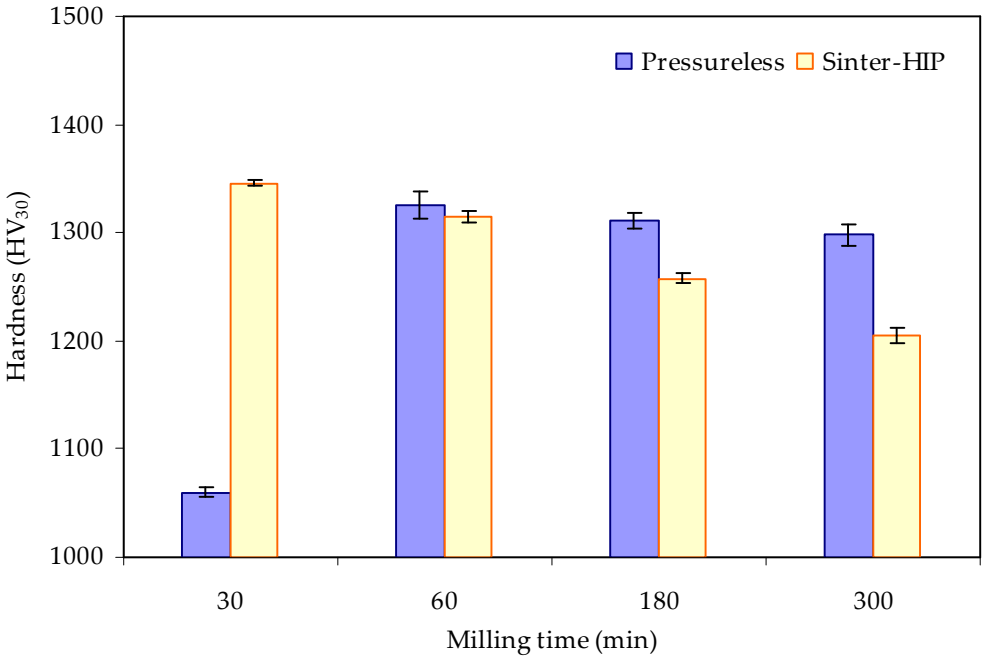

Fig. 5.36 Relative density and hardness as a function of milling time for WC-10Co after sinter-HIP.

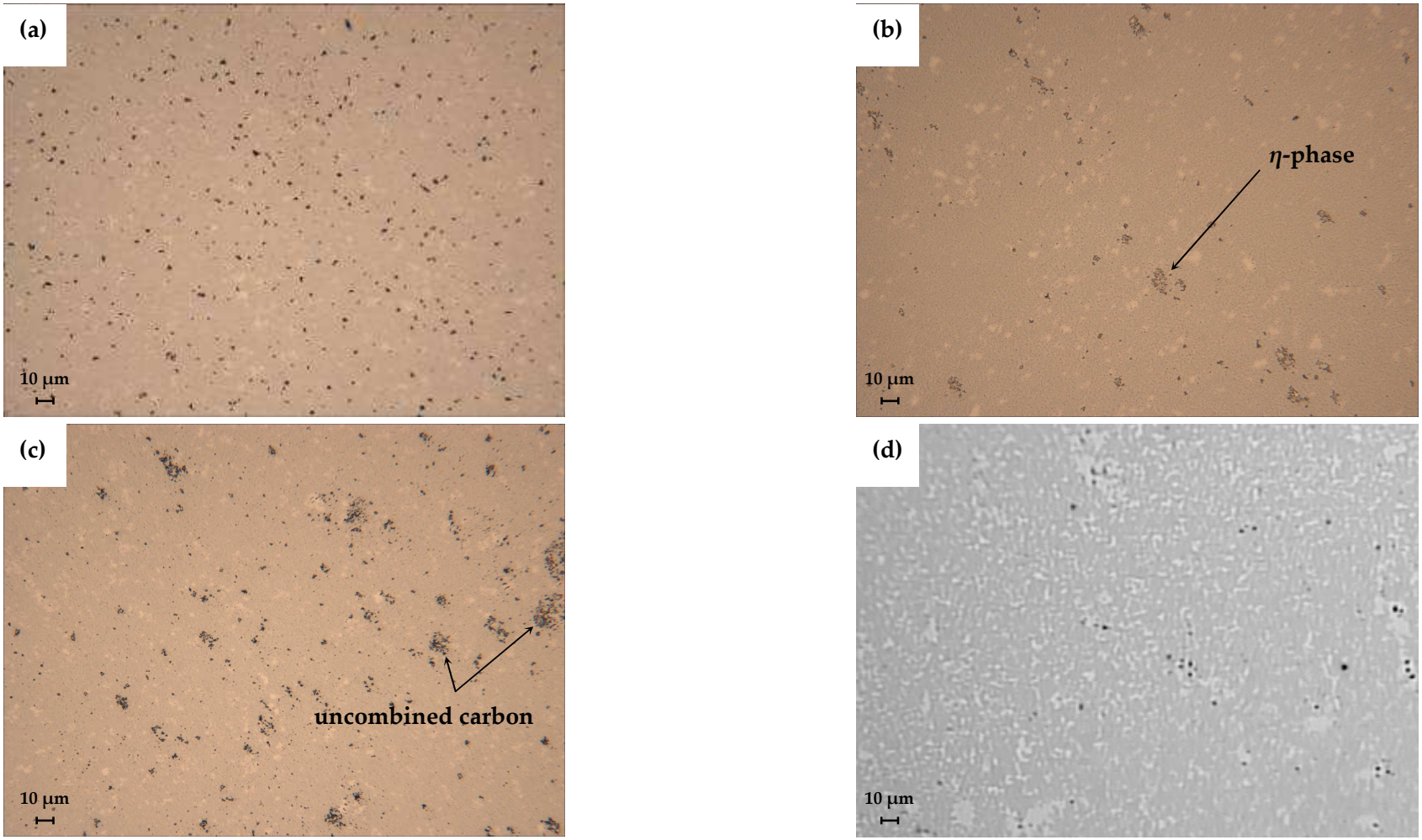

Fig. 5.37 Optical micrographs of WC10Co sinter-HIP'd at 1390°C/60 min after (a) 30 min, (b) 60 min, (c) 180 min and (d) 300 min ball milling.

Coercivity values, Fig. 5.39, also show similar behaviour to those obtained from pressureless sintering, with coercivity decreasing linearly with milling time and increasing WC grain size. However, the coercive force measurement for 180 min milling does not represent the decreasing trend in WC grain size. This measurement was affected by the uncombined carbon (graphite phase) that was precipitated during cooling, Fig. 5.37, as coercivity decreases with increasing carbon content (Fang and Eason 1993). Once again, the coercive force measurement for the 300 min milled material was affected by Fe pick-up. During LPS, coarsening of the microstructure occurs in parallel with densification, with the results between 30 and 60 min milling supporting that theory. During grain growth, the smaller grains preferentially dissolve and reprecipitate on the large grains. The growth behaviour of WC-Co alloys is believed to be a solution and reprecipitation process controlled by interfacial reactions (Exner 1983). Although WC grain size distribution is still wide, there did not appear to be any discontinuous grain growth. Grain size distribution has been attributed to the milling conditions and the initial size distribution of the WC powders (Exner *et al*. 1978). Porosity rating for the 60 min milled material was < A06 but there also appeared to be η-phase (Co_3W_3C) present, which is typically formed due to carbon deficiency through graphite precipitation. The presence of this third phase was also detected by magnetic saturation measurements, as shown in Fig. 5.40.

Table 5.7

Mean WC grain size after sinter-HIP and pressureless sintering (1390°C/60 min).

	Sinter-HIP			Pressureless	
Milling time (min)	Linear intercept mean WC grain size (μm)	EBSD mean WC grain size (μm)	Hardness (HV30)	Linear intercept mean WC grain size (μm)	Hardness (HV30)
30	1.41	-	1346	1.05	1059
60	1.32	-	1298	0.97	1326
180	0.91	0.83	1258	0.88	1311
300	0.84	0.74	1205	0.85	1298

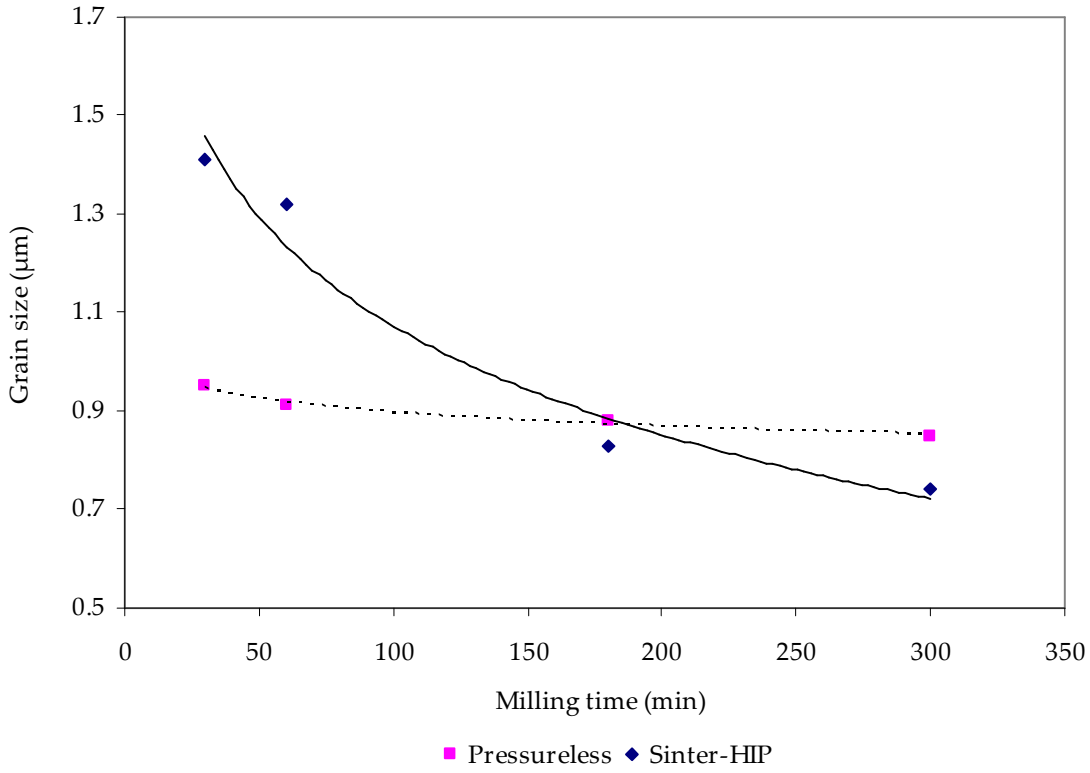

Fig. 5.38 Mean WC grain size as a function of milling time after sinter-HIP at 1390°C/60 min.

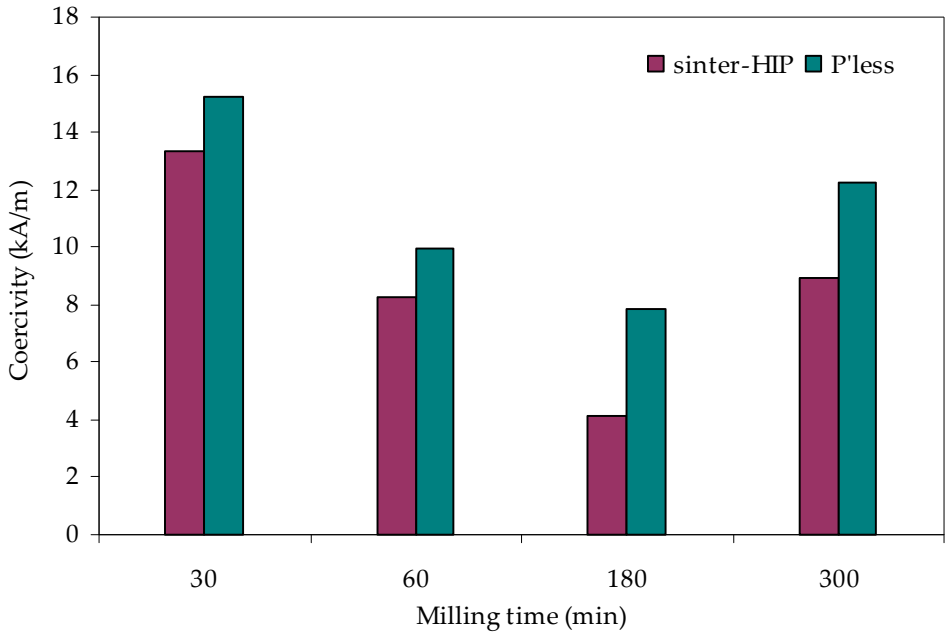

Fig. 5.39 Coercivity as a function of milling time for WC-10Co sinter-HIP'd at 1390°C/60 min.

Measurement of magnetic saturation (moment) was used as an indirect method of determining the Co content and the amount of W dissolved in the Co binder phase of the sintered samples, to establish the effects of the processing route on the WC-10Co composition. The saturation value of Co decreases linearly (Roebuck and Almond 1998; Freytag, Walter and Exner 1978) with the addition of W and is not affected by the amount of C in solution. If the Co in the hardmetal contains W in solution then the saturation value for the hardmetal can be calculated because (Roebuck and Almond 1998; Freytag, Walter and Exner 1978)

$$\sigma_B = \sigma_{Co} - 0.275 m_W \tag{5.17}$$

where σ_{Co} is the magnetic moment/unit wt of pure Co, σ_B is the magnetic moment/unit wt of the Co binder phase and m_W is the wt% W dissolved in Co. The decrease in the saturation value can be represented by

$$4\pi\sigma_B = 4\pi\left(\sigma_{Co} - 0.275 m_w\right) \tag{5.18}$$

where $4\pi\sigma_{Co}$ is 202 μT m^3 kg^{-1} (Bozorth 1951). When $4\pi\sigma_B$ attains a value of about 160 μT m^3 kg^{-1} or 16.0 emu/g (mass magnetisation), η-phase begins to form and so the range 202-160 μT m^3 kg^{-1} for the magnetic saturation (or 12.8-16.1 μT m^3 kg^{-1} magnetic moment) of the Co phase defines the two-phase field in WC-10wt%Co hardmetals. Given the

magnetic saturation data from each of the milling times, Fig. 5.40, then this would suggest the presence of binder phase solutes for each sample, which does not agree entirely with the micrographs observed in Fig. 5.37 and certainly not in the quantities suggested. Incorporating the magnetic saturation data from 60 min milling, for example, into calculations for the W content dissolved in the binder gives $4\pi\sigma_B$ = 11.7/0.10 = 117 μT m^3 kg^{-1}, therefore

$$m_W = \frac{202-117}{4x\pi x0.275} = 24.6wt\%$$

This result clearly indicates that additional binder phase solutes have affected the results, particularly Fe, as shown in Fig. 5.40, making precise calculations difficult. The effect of Fe on magnetic moment is opposite to that for W at about half the strength. An equation relating the change in magnetic moment of the binder phase with W additions (Roebuck 1996)

$$\sigma_B = \sigma_{Co} + Am_W \qquad (5.19)$$

has been suggested for elements other than W with A having a value of +0.13 μT m^3 kg^{-1} for Fe (Bozorth 1951). However, even with this correction the result is inordinately high at 19.3 μT m^3 kg^{-1}. When expressed as a percentage of the maximum expected for a nominally pure Co binder phase, the saturation is 69%, which is very low compared to

values obtained in other studies of ~ 90-91% (Shi, Shao and Duan 2007). This may have occurred due to a calibration issue. Calibrated reference samples, which have been measured in equipment with known field strength, should be used for accurate measurements and care should be taken with the geometry and dimensions of the test piece in relation to the field direction.

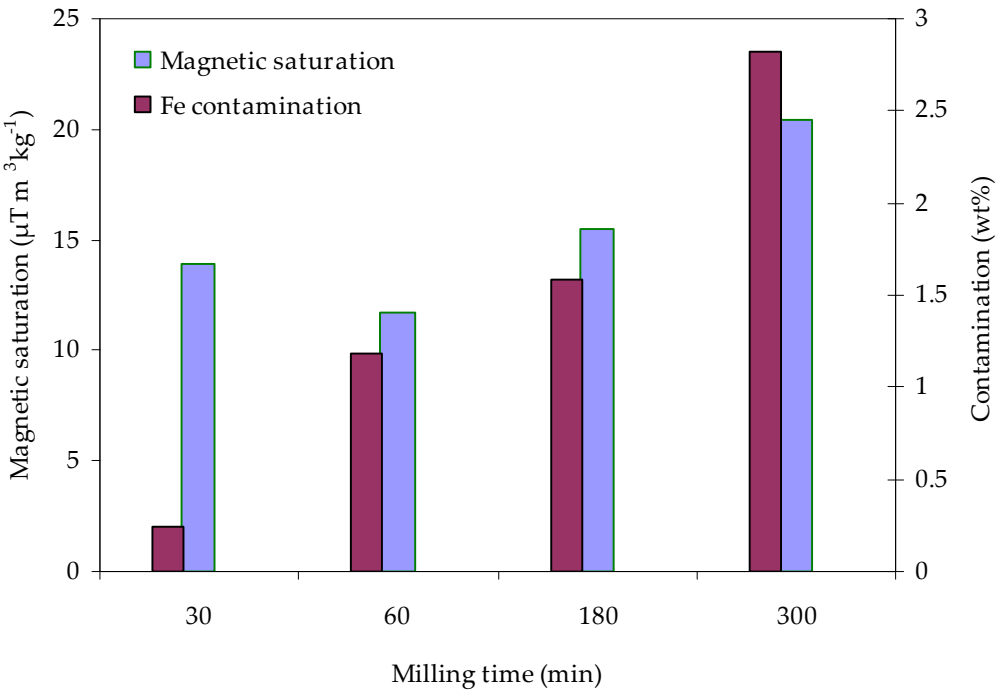

Fig. 5.40 Effect of ball milling time on the magnetic saturation of WC-10Co after sinter-HIP (1390°C/60 min).

The presence of η phase may have occurred due to vacuum sintering as part of the sinter-HIP process. The carbon content may change during sintering as high vacuum sintering tends to be slightly decarburising (Sands and Shakespeare 1966). Also, from

TG/DSC measurements, Fig. 5.20, some carbon could have been removed from the composition in the form of CO_2 and CO. During processing, variations in the initial composition of the starting WC-Co mixture result from the reactions involving C and O_2 adsorbed on the surfaces of the powder particles. From Fig. 5.37, the morphology of the η phase seems to be one of finely dispersed particles, which indicates low carbon deficiency. The fine, irregular shape observed in this study agrees with other reported work of carbon deficient WC-Co alloys (Cho, Lee and Chung 1996).

Magnetic saturation shows a sharp increase after 60 min milling and continues to increase over 20 μT m^3 kg^{-1} after 300 min milling, which, according to Fig. 3.3 estimates the Co content to be ~ 12.5wt%. However, Fig. 5.40 clearly shows that the resulting increase is due to Fe contamination from ball milling. Uncombined carbon often appears as clusters or rosettes (From and Sandström 1996), as is the case with 180 min milling, shown by an optical micrograph in Fig. 5.41. This excess carbon could have been caused by the preparation process prior to ball milling.

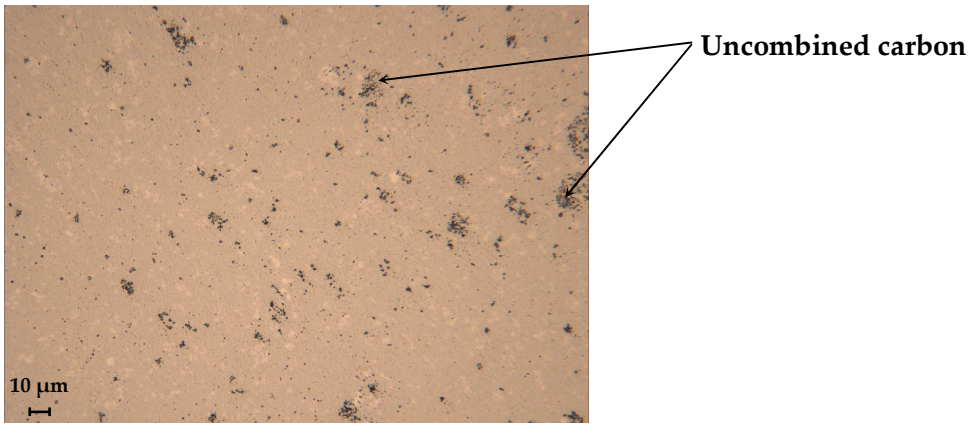

Fig. 5.41 Optical micrograph of uncombined carbon for a WC-10Co grade after 180 min ball milling followed by sinter-HIP.

WC grain size distribution after sinter-HIP was investigated using the electron backscatter diffraction (EBSD) technique for the 180 and 300 min milled material. A series of EBSD maps for the 180 min milled material are shown in Fig. 5.42. Colours represent the WC crystallographic orientation according to the inverse pole figure (IPF) colouring shown in Fig. 5.45. Non-indexed areas, either from the Co matrix or regions of WC that produced kikuchi patterns too poor to be indexed, are shown in white, Fig. 5.45 (b). Standard noise reduction routines were used to remove single isolated pixels and to identify originally non-indexed pixels where such zero-solutions are surrounded by a minimum of 4 other pixels of the same orientation. The sizes of WC grains were obtained from the orientation map, Fig. 5.42 (b) by the linear intercept method. The ability to precisely define the nature of the boundaries constitutes a significant advantage over imaging techniques where the visibility of a boundary is a function of the technique. The WC grain size distribution for the 180 min milled material is shown in Fig. 5.42. WC size distribution is wide with a number of grains > 4 μm. Mean grain size was determined at 0.83 μm. EBSD pattern maps from the 300 min milled material are shown in Fig. 5.45 with the grain size distribution shown in Fig. 5.44. Increased ball milling has improved the refinement of the microstructure resulting in a narrower size distribution and a reduced size range with the largest grains ~ 3 μm. Mean grain size has also been reduced to 0.74 μm. However, the pattern maps shown in Fig 5.45 also highlight the detrimental effects of prolonged milling on the microstructure, including contamination (mis-indexed phases) and macropores, which will inevitably affect mechanical properties.

Grain refinement has been a topic of intensive research for several decades. The driving force behind these enduring efforts is the enhancement of strength as the grain size decreases, as described by the empirical Hall–Petch (H-P) relationship (Hall 1951; Petch 1953)

$$\sigma_y = \sigma_i + k_y D^{-1/2} \tag{5.20}$$

where σ_y is the yield strength of a polycrystalline material, σ_i is the overall resistance of the lattice to dislocation movement, D is the average grain diameter, and k_y is the H-P slope measuring the relative strengthening contribution of grain boundaries. Eq. 5.13 has been found to be applicable to a wide range of coarse-grained ($D \geq$~1 μm) materials and ultrafine-grained (100 nm < D < 1 μm) materials (Chinh, Gubicza and Langdon 2007; Furukawa *et al*. 1996). The relationship between hardness and average WC grain size of the sintered samples is shown in Fig. 5.46, revealing that the Hv – $d^{-1/2}$ relationship in this study does not follow normal H-P behaviour as reported in other work for WC-10wt%Co with increasing hardness with decreasing WC grain size (Shi, Shao and Duan 2007; Cha *et al*. 2001; Roebuck, Gee and Morrell 2006) as shown in Fig. 5.47, but instead exhibits decreasing strength with decreasing WC grain size (increasing milling time). This unusual behaviour most likely stems from the synthesis process itself, more specifically, the high mechanical energy generated by the horizontal ball mill, and the subsequent difficulties in pressing a homogenous green compact with increasing milling

time. This type of mill supplies the highest relative velocity of grinding media amongst the different types of mills (section 2.2.3) and a high level of kinetic energy transfer to the powder. The rate at which the grain size decreases during milling is related to the deformation energy provided by milling. The results shown in Table 5.2 along with the data shown in Fig. 5.48, suggest that the optimum processing conditions for the material composition used in this study is ~ 60 min cyclic milling. The characteristics of crystal refinement and development of nanostructures during ball milling suggest that grain size decreases with milling time, reaching a minimum grain size, d_{min} that is a characteristic of each metal (Eckert *et al*. 1992; Oleszak and Shingu 1996). The data obtained in this study seems to support the concept that d_{min}, ~ 20 nm for this study, is governed by a balance between the hardening rate introduced by dislocation generation and the recovery rate arising from dislocation annihilation and recombination. It would also seem reasonable to assume that the severe deformation generated by this type of ball mill, coupled with the increasing levels of contamination, Fig. 5.11, could have caused the vacancy diffusion of impurity atoms. Concentrations of vacancies higher than equilibrium can be produced by extensive plastic deformation (Seitz 1952; Friedel 1969). The concept of vacancy production via plastic deformation was utilized to account for the occurrence of serrated flow in solid-solution alloys (Russell 1963; Mohamed, Murty and Langdon 1974). Serrated flow, referred to as dynamic strain ageing, was explained in terms of repetitive interaction between diffusing solute atoms and moving dislocations. In the temperature range where serrated flow was observed, the diffusivity of solute atoms (or impurity atoms) is too low to enable them to keep up with moving

dislocations. However, it has been suggested (Cottrell 1953) that the diffusion coefficient is enhanced as a result of the production of vacancies by straining.

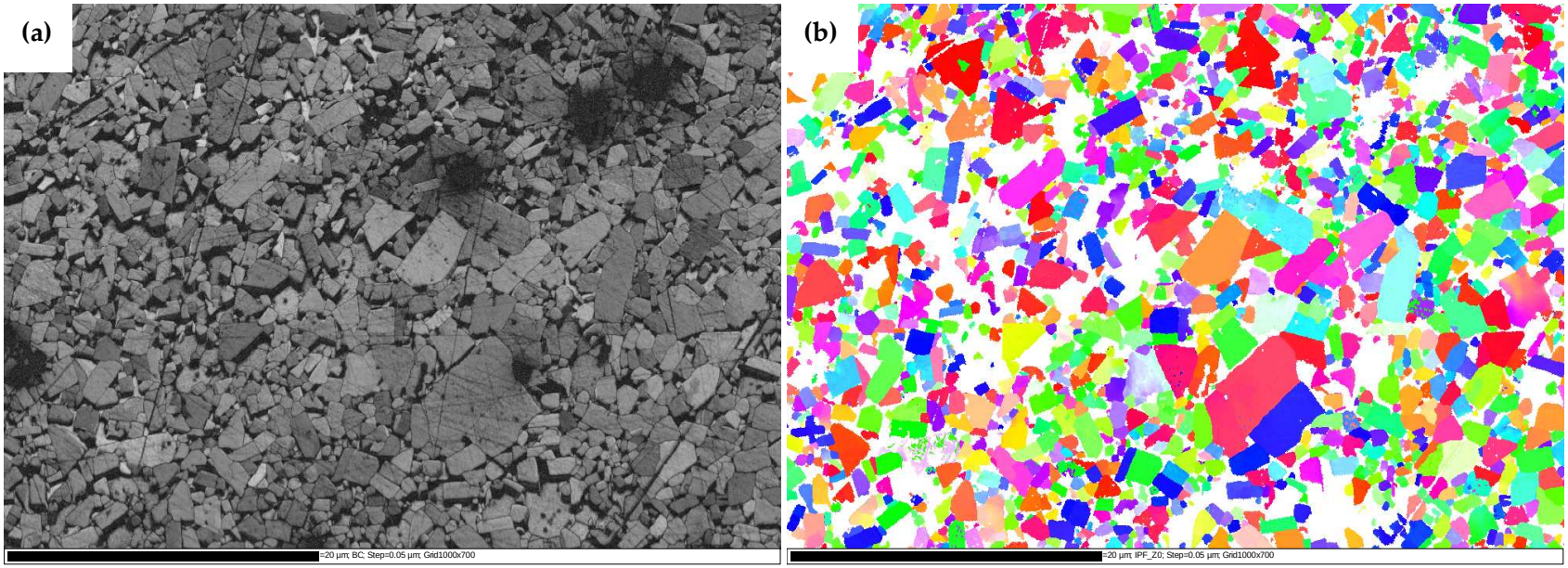

Fig. 5.42 EBSD maps of 180 min milled WC-10Co after sinter-HIP, showing (a) diffraction pattern quality map; (b) orientation colour map of the WC phase; (c) pattern quality map of WC phase (red) and cubic-Co (yellow); (d) pattern quality map of cubic-Co and mis-indexed phase.

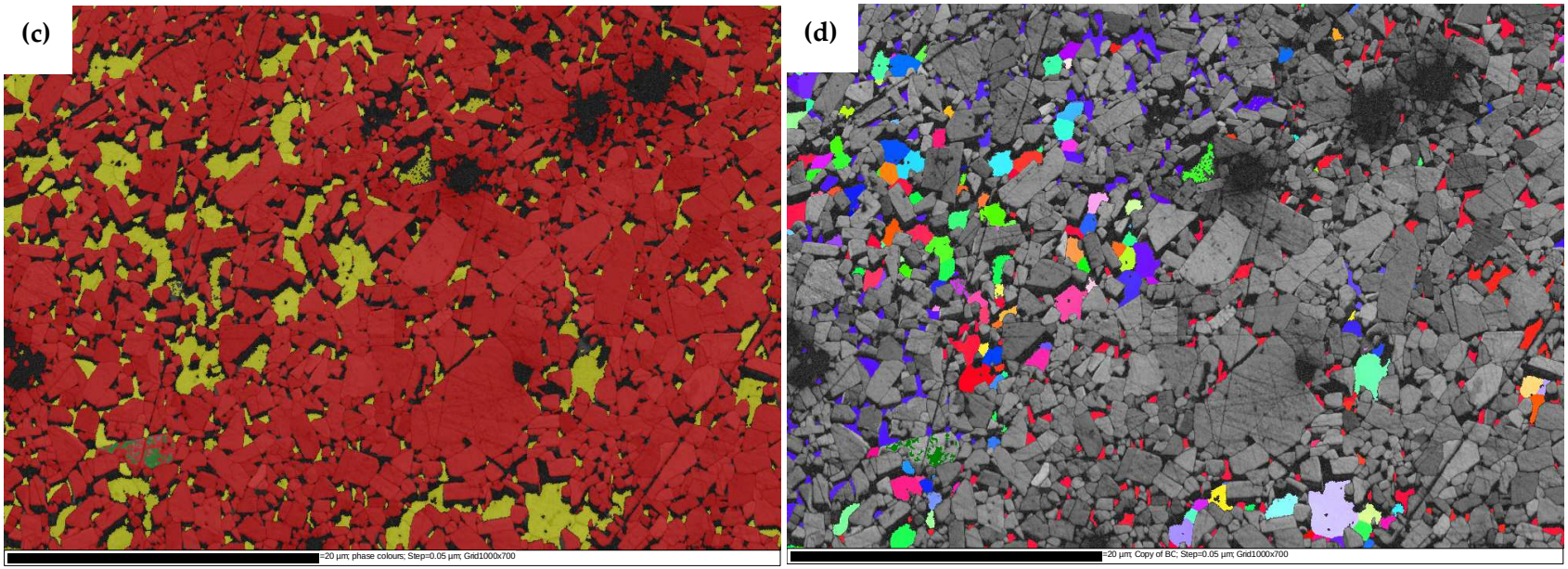

Fig. 5.42 cont'd EBSD maps of 180 min milled WC-10Co after sinter-HIP, showing (c) pattern quality map of WC phase (red) and cubic-Co (yellow); (d) pattern quality map of cubic-Co and mis-indexed phase.

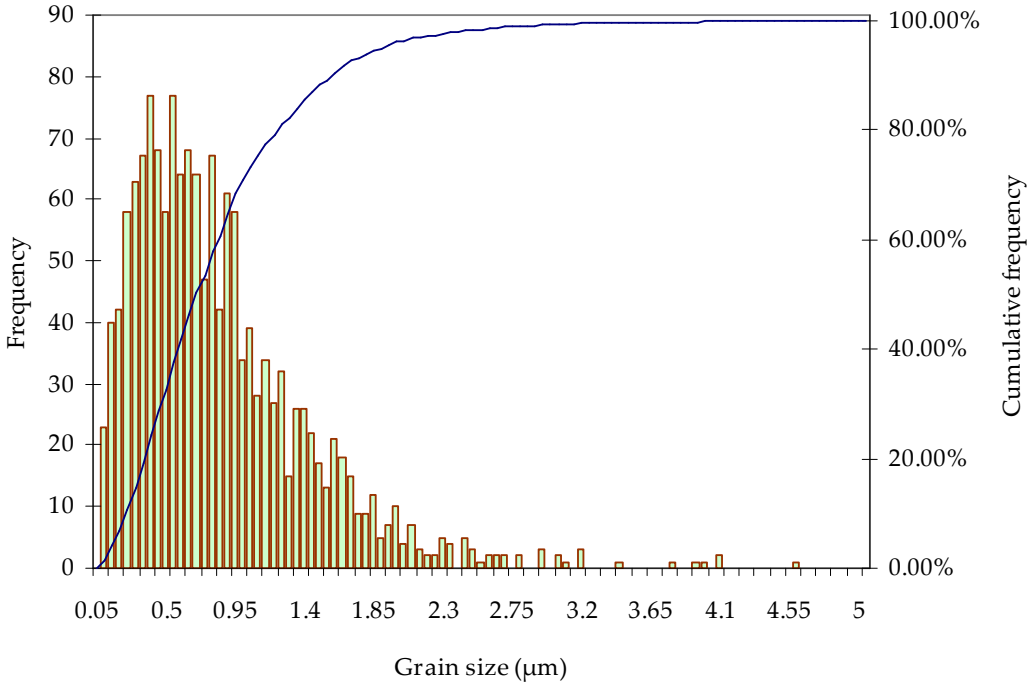

Fig. 5.43 WC grain size distribution from EBSD for WC-10Co, 180 min milled material after sinter-HIP.

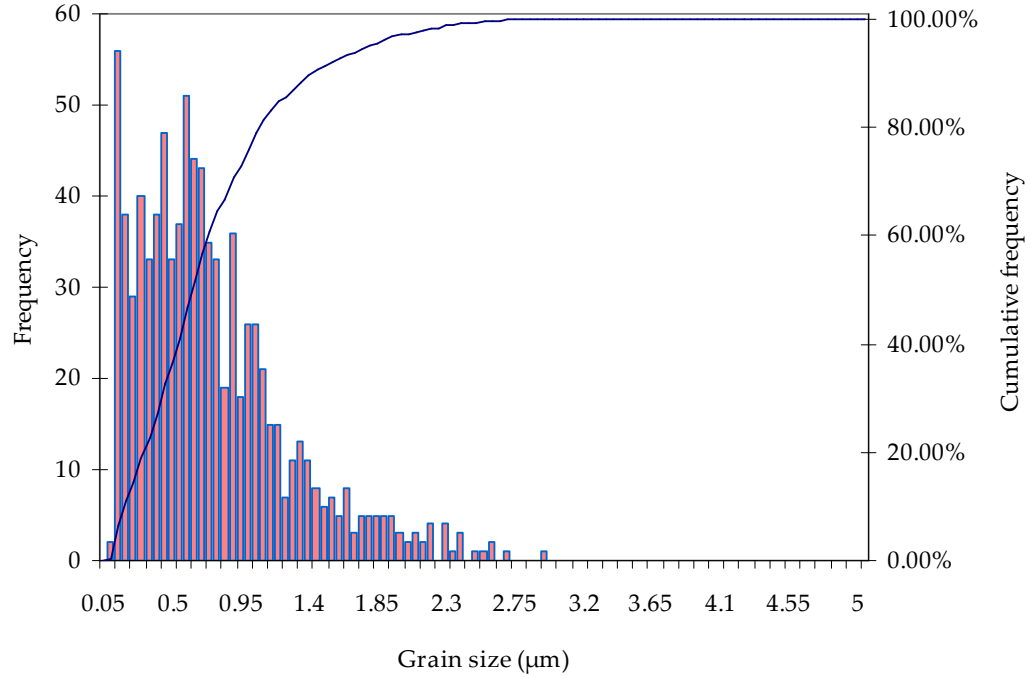

Fig. 5.44 WC grain size distribution from EBSD for WC-10Co, 300 min milled and sinter-HIP'd.

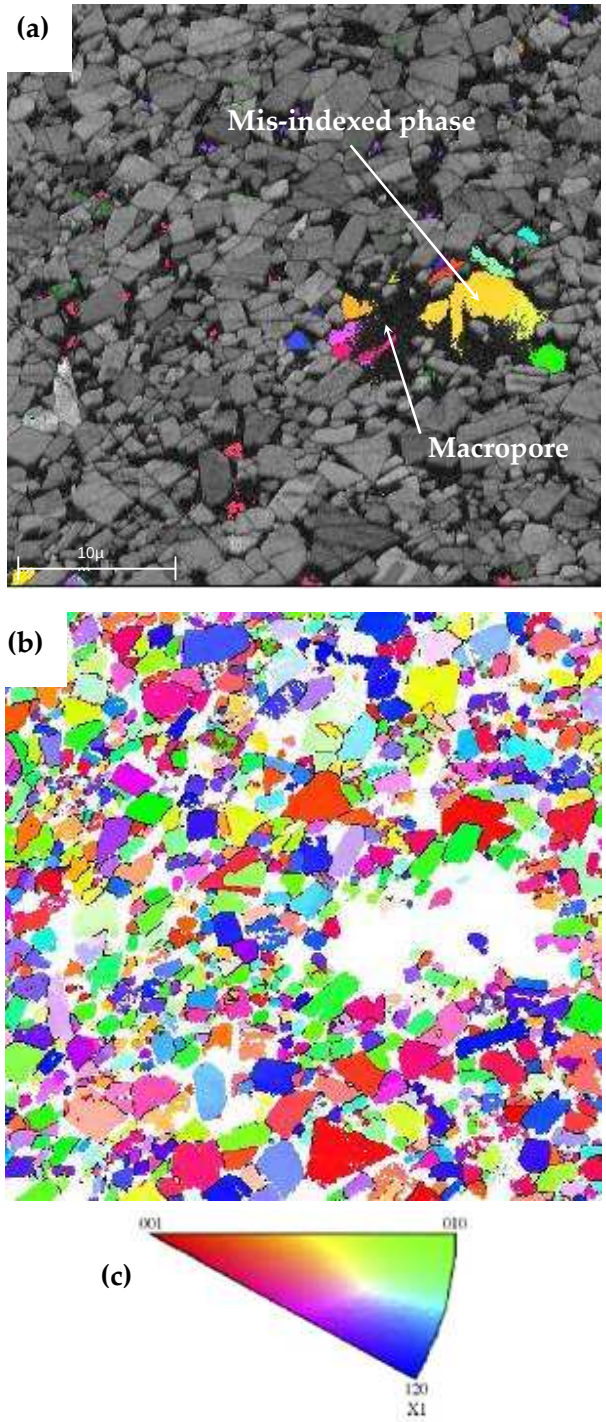

Fig. 5.45 EBSD maps of 300 min milled WC-10Co after sinter-HIP, showing (a) diffraction pattern quality map showing mis-indexed phase; (b) noise reduced, IPF colouring showing WC crystallographic orientation according to the inverse pole figure (c).

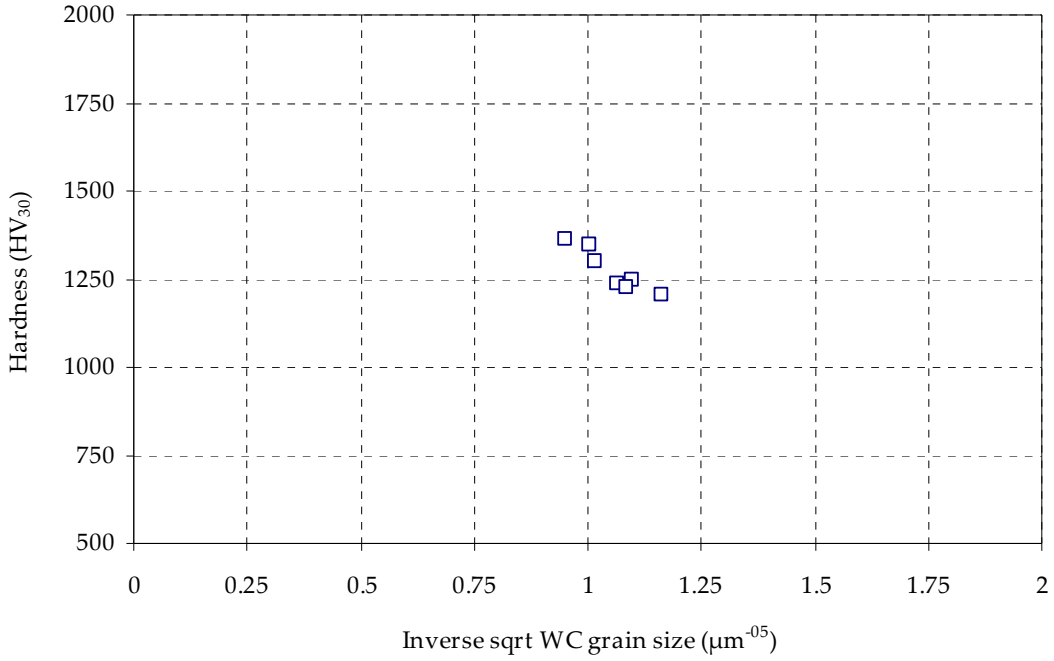

Fig. 5.46 Hardness as a function of the inverse square root of WC grain size ($d^{-0.5}$) for WC-10wt%Co data from this study.

Fig. 5.47 Hardness as a function of the inverse square root of WC grain size ($d^{-0.5}$) for WC-10wt%Co data from the National Physical Laboratory (Roebuck, Gee and Morrell 2001).

The increasing rate of hardness of the milled powders with milling time, observed by the decreasing level of green density, Fig. 5.48, and particle size distribution, Fig. 5.7 has also affected densification dynamics during sintering. Generally speaking, with all else being constant, the sintered density normally increases with green density or increased packing density as less work is required in the sintering cycle, which is shown in Fig. 5.48. It is interesting to note that sintered density follows the general trend of green density and remains unaffected by the sintering process. It is clear that poor consolidation, as illustrated by the larger decrease in green density after 300 min milling,

has led to sintering difficulties. Poor consolidation would most likely result in a broad pore size distribution. Although this milling time resulted in the smallest average particle size, Fig. 5.9, these small particles may well have clustered together and sintered into dense regions, leaving difficult-to-sinter large pores between the clusters. The presence of pores, Fig's 5.26 and 5.37, has clearly affected the mechanical strength of the materials and it is assumed that the reduction in strength could be affected by both the size and number of pores and also by the presence of impurities. The strength-reducing effect would most likely arise from the increased concentration of stress around a pore and would differ for an empty pore from one filled by an impurity.

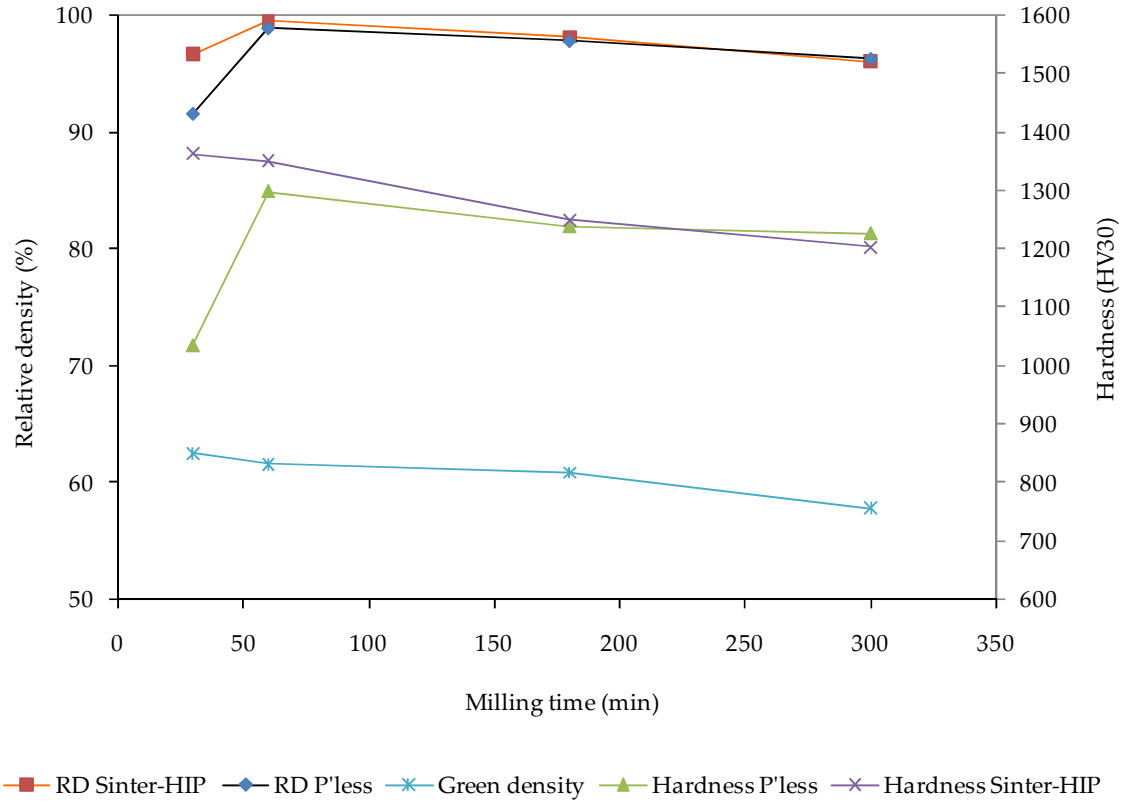

Fig. 5.48 Sintered density and hardness in relation to green density of ball milled WC-10Co.

Densification behaviour of the 30 min milled powder, Fig. 5.48 stems from its wide particle size distribution, Fig. 5.7. A wide initial particle size distribution has the greatest impact on the final stage of sintering. It upsets the balance between pinning and separation of grain boundaries and pores, allowing grain growth to initiate earlier in sintering, resulting in a lower final density (Chapell, Ring and Birchall 1986).

As demonstrated in Fig. 5.48, green density of the milled powders is a major determinant of the sintered density. The packing and sintering behaviour of the powders is further demonstrated in Fig. 5.49. A bimodal particle size distribution is observed after

30 min milling, Fig. 5.7, which has improved green packing density because the smaller particles are able to fit into the voids between the larger particles. Shrinkage is at its lowest when the large particle content is at its highest (minimum milling time) but this leads to restrained densification by the small particles, as shown in Fig. 5.48. After 30 min milling, the powder particle size distributions revert to those of monosized powders (Fig. 5.7) and sintering shrinkage increases with decreasing particle size (increasing milling time) and varies inversely with green density.

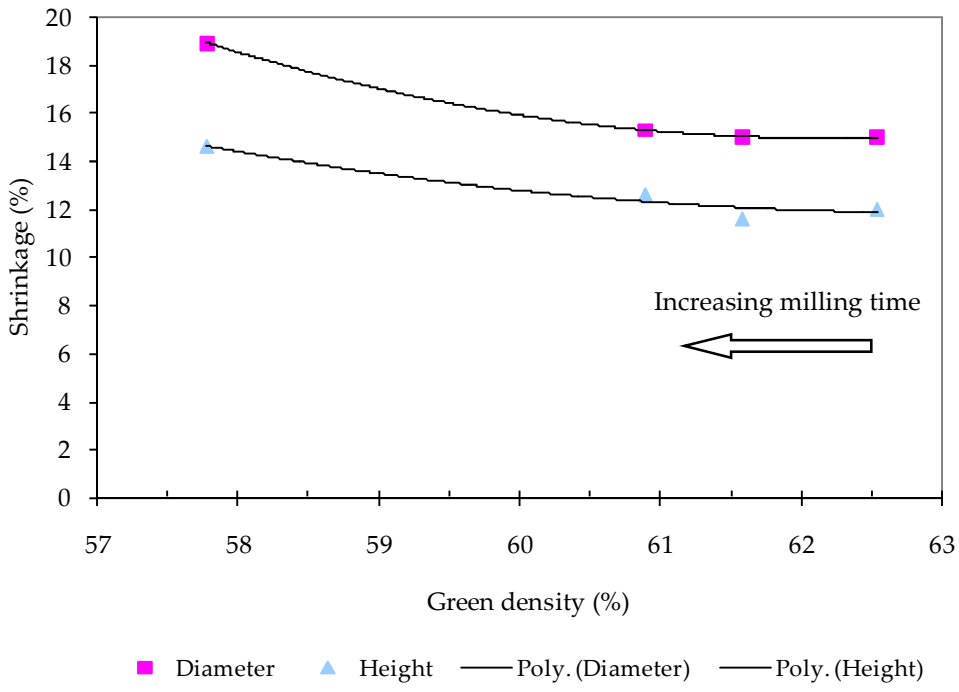

Fig. 5.49 Shrinkage behaviour of the pressed compacts after sinter-HIP at 1390°C/60 min. Data points fitted with a 2nd order polynomial.

5.3.3 Effect of milling time and sintering technique on mechanical properties

The mechanical properties of WC-Co hardmetals, such as hardness and fracture toughness, are dependent on the materials' microstructural parameters. Clearly there are other microstructural features that can affect hardness, such as the precise carbon/tungsten content of the binder phase, the contiguity of the carbide network and the size distribution and possible variations in shape of the WC grains (Lee and Gurland 1978). There is a general inverse trend of hardness against fracture toughness for WC-Co hardmetals, indicated by fracture toughness data (W_K) obtained from tests on a wide range of WC-Co hardmetals at the National Physical Laboratory (Roebuck and Almond 1988) and published data from Sandvik Hard Materials (Brookes 1992), Fig. 5.50.

For the purpose of this study, 'toughness' refers to the Palmqvist fracture toughness, W_K, obtained by measuring the total lengths of cracks emanating from the four corners of a Vickers hardness indentation (see section 4.5.6). Fracture toughness describes the ability of a material to withstand crack propagation. The failure of these materials normally initiates at pre-existing defects. Fracture toughness is one of the main properties incorporated in the design of hardmetal cutting tools due to the high risk of brittle fracture.

Fig. 5.50 Palmqvist toughness/hardness property map for a range of WC-Co materials (Roebuck and Almond 1988).

An empirical method for determining an estimate of fracture toughness from Vickers hardness testing was first developed by Palmqvist in 1962. Later, several authors (Anstis *et al*. 1981; Lawn *et al*. 1980; Niihara, Morena and Hasselman 1982; Niihara 1983; Shetty *et al*. 1985; Laugier 1987) have used the same technique to develop a number of relations between K_{IC} (plane strain fracture toughness), load (P), indentation diagonal (a), crack length from the centre of the indentation (c), Young's modulus (E) and Vickers hardness number (HV) of a material. The numerous indentation fracture models reported in the literature are classified into two groups. In one group it is assumed that the cracks that form from the Vickers indentation marks are well developed, radial-median, ''half-

penny''-shaped cracks, and in the other group it is assumed that radial Palmqvist cracks are formed. WC-Co hardmetals with Co volume fractions ≥ 5% do not develop "half-penny" cracks as a result of Vickers indentation (Shetty *et al*. 1985). Instead, the cracks are of the Palmqvist type, i.e. four independent, shallow surface cracks at the corners of the Vickers hardness impression, Fig. 5.51. In this study, the equation developed by Palmqvist (1962), eq. 5.14, was preferred because it presupposes no knowledge of other mechanical properties of the hardmetal. However, for comparative purposes, the data was also examined using the equation developed by Anstis *et al*. (1981), eq. 5.15.

$$W_K = A\sqrt{HV}\sqrt{W_G} \quad \text{(MN m}^{-3/2}\text{)} \tag{5.21}$$

where A is a constant of value 0.0028, HV is the Vickers hardness in N mm^{-2} and W_G is in N mm^{-1}.

$$K_{IC} = A\left(\frac{E}{H}\right)^{1/2}\left(\frac{P}{C_O^{3/2}}\right)^2 \tag{5.22}$$

where A is a constant of value 0.016±0.04, E is Young's modulus in MPa, H is the Vickers hardness in N mm^{-2}.

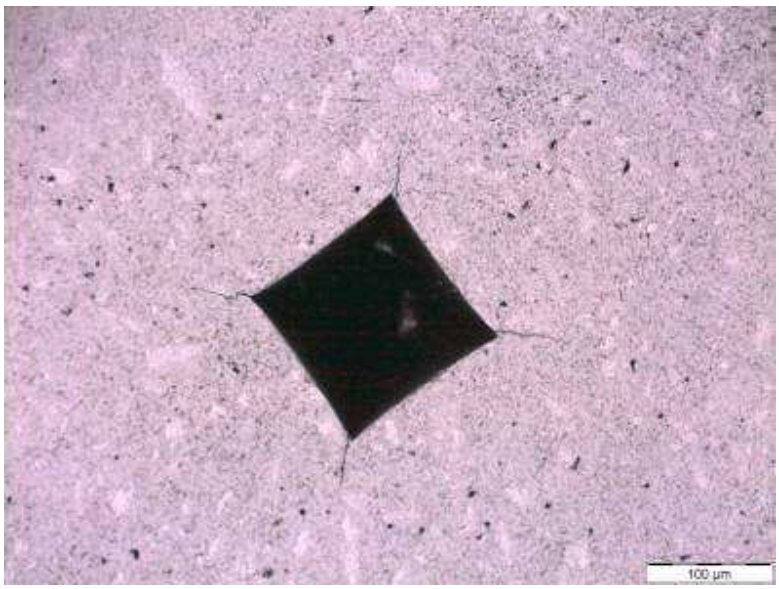

Fig. 5.51 Vickers hardness indentation (HV30) from a 60 min ball milled sample showing microcracks formed at each corner.

The hardness and fracture toughness of the pressureless sintered (1390°C/60 min) WC-10Co material is shown in Fig. 5.52. The W_k values were calculated from eq. 5.14 and are shown in Table 5.8, with the results based on ten indentations to provide reasonable statistics. Despite this, the considerable scatter in the results makes it difficult to form any reasonable conclusions about the relationship between fracture toughness and hardness for the pressureless sintered materials. Again, this seems to point towards effects from non-uniform consolidation. The relationship between fracture toughness and milling time is, in general, a detrimental one. Fracture toughness is higher for the 30 min milled sample due to the material's low hardness value and the deflection of cracks caused by the high number of pores. Toughness decreases after 60 min milling reaching a maximum value of 12 $MN.m^{-3/2}$ with a corresponding hardness of 1226 HV30. These

values are similar to those reported by others for WC-10Co materials (Roebuck and Almond 1988) and also to those involving MA as the synthesis process (Mi and Courtney 1998). The values obtained in this study were somewhat expected, given the WC grain size measurements, and are typical of conventional, coarse grained WC-10Co materials. Fracture toughness of WC-Co materials is known to increase as mean WC grain size and binder phase mean free path increase (Dusja, Parilak and Slesar 1987). The fracture toughness values obtained using eq. 5.11 (Anstis) are considerably higher than those from eq. 5.10, which pushes them outside of the typical range expected for coarse-grained WC-10Co.

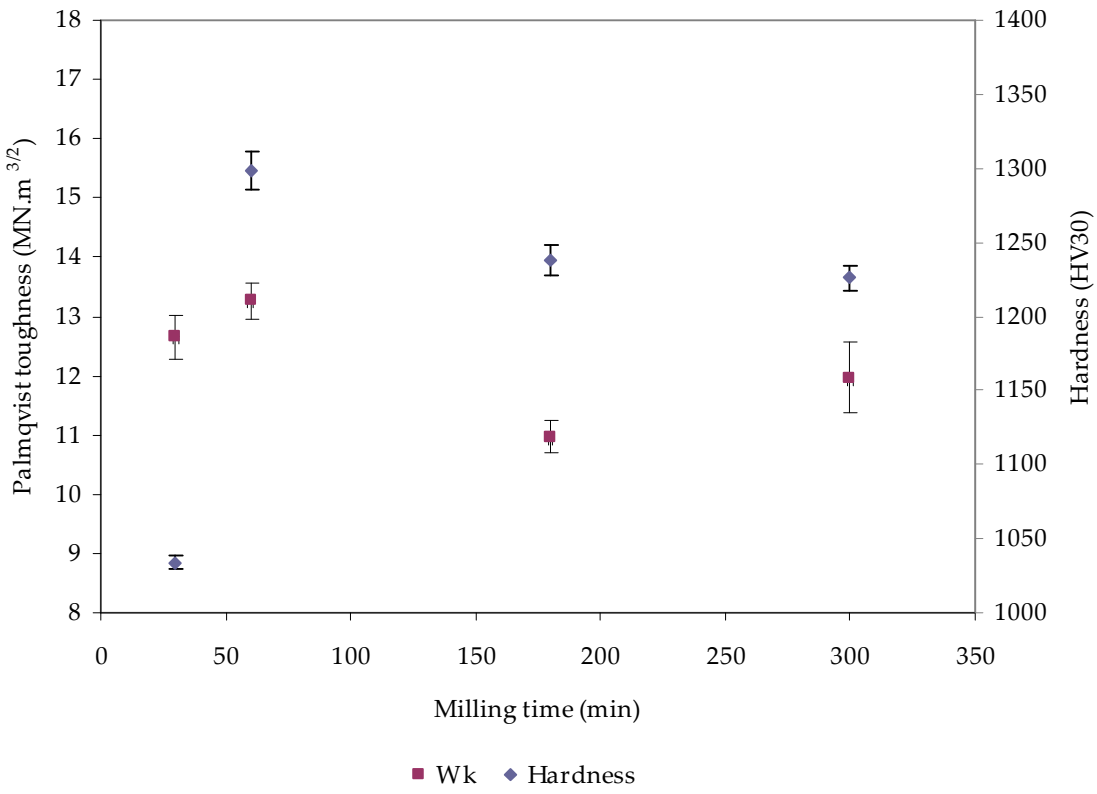

Fig. 5.52 Effect of milling time on the fracture toughness of WC-10Co pressureless sintered at 1390°C/60 min.

Table 5.8

Fracture toughness results after pressureless sintering at 1390°C/60 min.

Milling time (min)	Hardness mean value (HV30)	W_k (MN $m^{-3/2}$)	S.D.	K_{IC} (Anstis) (MN.$m^{-3/2}$)
30	1034	12.7	± 0.29	19.0
60	1298	13.1	± 0.16	18.0
180	1238	11.0	± 0.19	15.5
300	1226	11.6	± 0.51	16.4

S.D. – standard deviation

Fracture toughness behaviour of the WC-10Co materials after sinter-HIP (1390°C/60 min) processing is shown in Fig. 5.53 and Table 5.9, with the results showing that the effects of mean WC grain size and binder phase mean free path are much more pronounced. W_K increases with increasing milling time and decreasing hardness, but the rate of increase and the actual values obtained are significantly higher. W_K reaches 14.9 MN.$m^{3/2}$ after 300 min milling but the hardness level has dropped to 1203 HV30. Surprisingly, the material milled for 60 min, which exhibited some η-phase, still achieved a W_K value of 13.7 MN.$m^{3/2}$, as carbon deficiency is known to reduce fracture toughness (Upadhyaya 1998). There did not seem to be any significant reduction in the rate of W_K increase for the 180 min milled material, despite the excess carbon level. The effect of excess carbon is generally thought to be somewhat less than that of carbon deficient alloys. This has been attributed to improvements in WC grain size and binder phase distribution, which is brought about by increased binder phase fluidity (Bolton

and Keely 1982). Fracture toughness values using eq. 5.11 were again much higher than those from eq. 5.10, which, given the narrow hardness range obtained in this study, suggests that the relationship derived by Anstis *et al*. (1981) may be more suitable to hardmetals with a higher HV30 range. Fracture toughness data (using eq. 5.10) from both sintering techniques is overlaid with those obtained in the literature (Roebuck and Almond 1988; Brookes 1992) and is shown in Fig. 5.54. The data from sinter-HIP clearly fits much more closely than those obtained after pressureless sintering. These values should not be excluded as they may still be within the limits of scatter for these types of materials, which can be due, not only to real differences in materials, but also to the difficulties of measuring the values from which "toughness" is calculated.

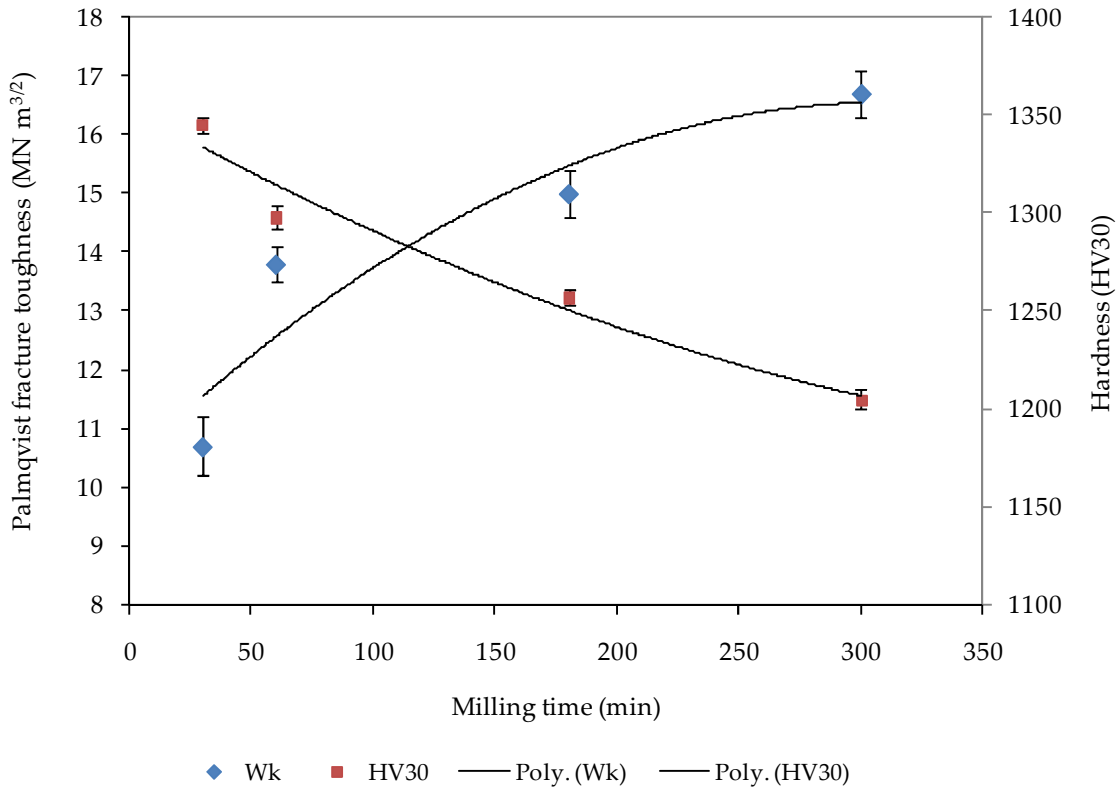

Fig. 5.53 Effect of milling time on the fracture toughness of WC-10Co after sinter-HIP at 1390°C/60 min. Data points fitted with a 2nd order polynomial.

Table 5.9

Fracture toughness results from sinter-HIP at 1390°C/60 min and pressureless sintering.

Milling time (min)	Sinter-HIP W_K (MN. $m^{-3/2}$)	S.D.	Sinter-HIP K_{IC} (Anstis) (MN. $m^{-3/2}$)	P'less W_K (MN. $m^{-3/2}$)	P'less K_{IC} (Anstis) (MN. $m^{-3/2}$)
30	11.1	± 0.48	14.3	12.7	19.0
60	13.7	± 0.24	18.7	13.1	18.0
180	14.9	± 0.31	20.2	11.0	15.5
300	16.1	± 0.33	21.8	11.6	16.4

S.D. – standard deviation

Fig. 5.54 Fracture toughness results from sinter-HIP at 1390°C/60 min and pressureless sintering overlaid with those of Roebuck and Almond (1988).

The transverse rupture strength (TRS) of the ball milled WC-10Co materials, consolidated by pressureless sintering and sinter-HIP, is shown in Fig. 5.55 with the average result of six type B samples for each technique listed in Table 5.10. TRS is an ultimate strength property, which is used as a standard in the hardmetal industry (Upadhyaya 1998). TRS is a combination of shear strength, compressive strength, and tensile strength and is used as a general measure of the toughness of the sintered material. When a WC-Co composite contains significant porosity, the strong correlation between its TRS and fracture toughness is obvious. The pores are viewed as existing

defects of which, the critical size is related to the critical stress and fracture toughness by (Fischmeister 1981; Exner, Walter and Pabst 1974):

$$K_{IC} = A\sigma_r \sqrt{a_c} \tag{5.23}$$

where a_c is the critical defect size, σ_r is the rupture strength, and A is a geometry related constant. When the porosity level is very low or negligible, the relationship between TRS and fracture toughness is not so straight forward. In fact, it has been shown that strength reaches an asymptotic value as the defect size, *a*, becomes equal or less than the size of a characteristic value (Roebuck 1995). Further, the flexural strength and fracture toughness are completely different concepts in the context of solid mechanics. TRS is a static tensile property whilst fracture toughness is a measure of the resistance of a material to crack propagation. Therefore, the relationship between them must be examined accordingly. TRS reaches a peak after 60 min ball milling for both sintering techniques with higher values realised for each milled material after sinter-HIP. Interestingly, the results from both techniques follow the same trend, despite the fact that a deleterious phase of η and graphite was present in the 60 and 180 min milled samples, respectively, after sinter-HIP. Despite the presence of η-phase, the higher TRS achieved by the 60 min milled sample was probably due to its high relative density and therefore, lower residual porosity, thereby reducing the nature and distribution of this type of defect within the microstructure. Fractography analysis of WC-10Co is reported to occur from closed pores near the surface rather than open pores (Cha *et al*. 2007).

Given the nature of the sinter-HIP process, the TRS values are lower than expected and are considerably below those quoted for other sinter-HIP and pressureless sintering work, as shown in Table 5.10.

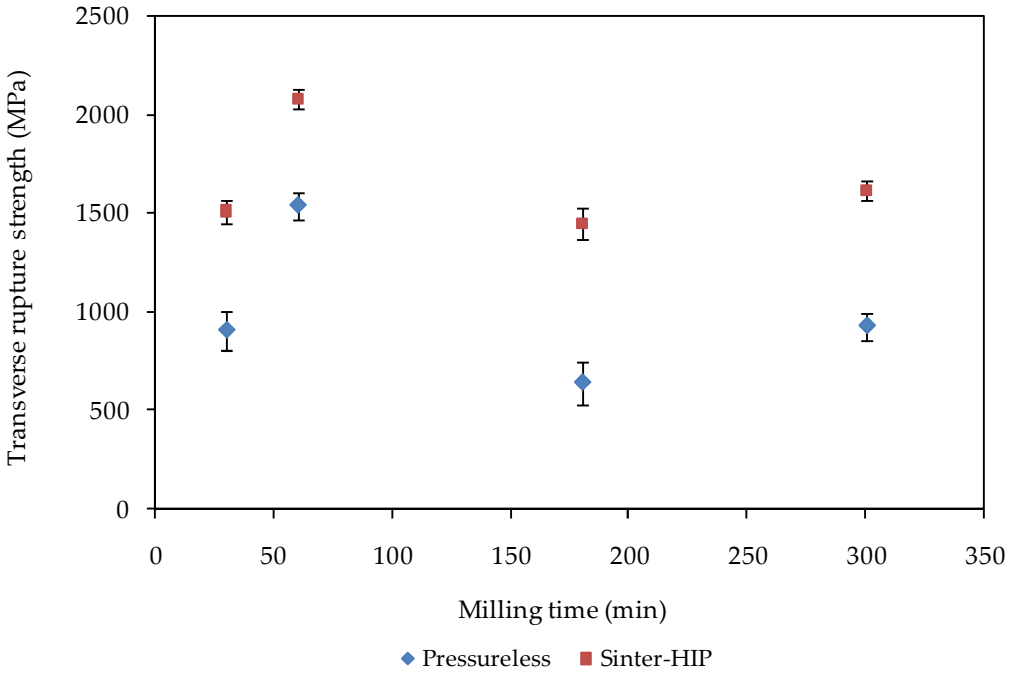

Fig. 5.55 Effect of ball milling time of the transverse rupture strength of WC-10Co, sintered by pressureless sintering and sinter-HIP.

Table 5.10

Transverse rupture strength of WC-10Co after pressureless sintering and sinter-HIP.

Milling time (min)	Sintering conditions	TRS – p'less (MPa)	S.D.	TRS – sinter-HIP (MPa)	S.D.	Ref.
30	1390°C/60 min	907	± 105	1505	± 69	This work
60	1390°C/60 min	1538	± 73	2079	± 57	This work
180	1390°C/60 min	642	± 113	1448	± 83	This work
300	1390°C/60 min	929	± 79	1614	± 52	This work
1440	VS/1400°C/60 min	1820	-	-		Sánchez et al. (2005)
1440	VS+HIP/1440°C/60 min	-	-	3120		Sánchez et al. (2005)
1440	VS/1380°C/45 min	2300	-	-		Shao et al. (2003)
1440	sinter-HIP/1380°C/45 min	-	-	3430		Shao et al. (2003)

* VS = vacuum sintering; S.D. – standard deviation

Strength has also been compromised by substantial growth of the WC grains. As grain separation increases, the grains provide less restriction to plastic flow and strength decreases. The defect role is suppressed at high volume fractions of solid (Exner and Gurland 1970). Thus, grain growth must be controlled to optimise properties. The relationship between the two sets of data is a curious one. TRS of WC-10Co hardmetals is reported to decrease with decreasing WC grain size (Cha *et al*. 2007; Lindau 1977; Pickens and Gurland 1978; Sigl and Fischmeister 1988; Lueth 1974; Sadahiro and Takatsu 1981). From Table 5.7, the milled materials after sinter-HIP show higher, average WC grain sizes compared to those from pressureless sintering. Both sets of materials show, in general, the same level of densification after sintering at 1390°C for 60 min with the majority of samples from pressureless sintering showing higher hardness and lower fracture toughness. If one views the fracture process during TRS testing as consisting of crack initiation and propagation processes with the ideal case when the effects of porosity are negligible, then the crack initiation process will dominate when the hardness is high and the fracture toughness is low. Therefore, the higher the hardness, then the higher the stress that is needed for crack initiation and, hence, the higher the TRS, Fig. 5.55. It is clear that other factors are influencing the fracture process for both types of sintered materials. The TRS of these materials is sensitively dependent on two major factors. The first factor is an extrinsic flaw where the fracture is initiated and the second factor is an intrinsic resistance to propagate the crack, i.e. fracture toughness. The effect of these factors on the TRS is dependent on the loading condition during the test

because it is affected not only by flaw size, but also by the location and distribution of flaws (Cha *et al*. 2007). As the densification results, Fig. 5.48, seemed to show that the mechanical properties of both materials were closely related to the structure formed during green pressing, then the fractured surfaces of the TRS samples were examined to search for further evidence. SEM micrographs of some of the TRS fracture surfaces are shown in Fig. 5.56. The fractographs confirm the critical importance placed on a uniform green structure in order to obtain reliable and consistent strength measurements. It is clear that the scale of the defects could not be compensated for during sintering, thereby resulting in the low rupture strength values. The defects were most likely caused by density gradients during pressing due to die wall friction and the poor compressibility of as-milled powder, and, to some extent, the length to width ratio of the green compact, all of which combined to cause delamination of the compacts' structure during sintering.

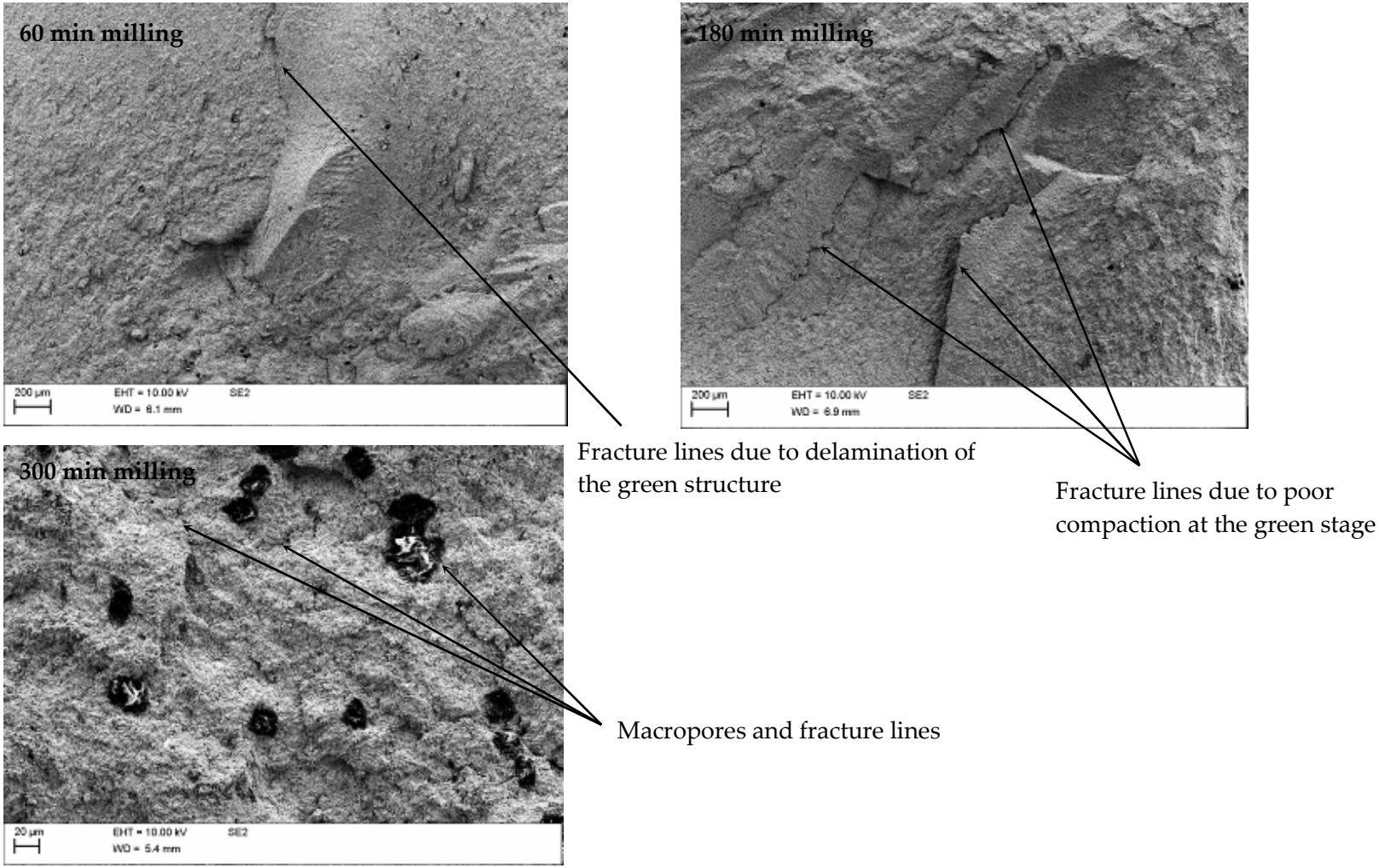

Fig. 5.56 SEM fractographs of some of the sinter-HIP TRS fracture surfaces.

5.3.4 Effect of milling temperature on densification and microstructure using pressureless sintering

The powder milled for 60 min at -30°C was pressureless sintered at 1390°C in order to allow a direct comparison with the 60 min RT milled powder. The powder milled at RT gave a relative density of 98.6% after pressureless sintering compared to almost theoretical (99.9%) for the low temperature milled powder, Fig. 5.57. The driving force associated with pressureless sintering is the reduction of surface energy from the surfaces of the internal pores. More than 50% of densification in hardmetals is achieved before the eutectic temperature of the pseudobinary WC-Co system is reached (Bargtsson, Johannesson and Lindau 1973). It is advantageous to reduce O_2 from the pores as much as possible during solid state heating otherwise at higher temperatures when the pores are closed the escape of CO gas is difficult (Amberg, Nylander and Uhrenius 1974). The TG/DSC data, Fig. 5.21, shows that the powder milled at -30°C underwent significant weight loss, which was complete by ~ 1100°C whilst the RT milled powder showed less weight loss, with completion at ~ 1300°C due to the level of impurities from milling pick up, Fig. 5.11. Impurities can have a significant effect on the existence of a continuous WC skeleton in the WC-Co microstructure (Uhrenius, Agren and Haglund 1996). According to the generally adopted proposal (Gurland 1959), the degree of skeleton formation can be quantitatively defined by the ratio of grain boundary area to total interface of the carbide grains (termed 'contiguity'). Co diffuses

out on to the carbide surfaces at < 1000°C and the agglomeration of the carbides starts at these temperatures. At 1100°C, a pronounced change in the pore structure was observed. After a further increase in temperature, the finer carbide particles start to dissolve and the binder becomes alloyed with tungsten and carbon. Grain growth of coarser WC particles takes place and a facetted WC structure of the coarser carbide is formed at 1200°C. Contiguity of the carbide phase after solid state sintering at 1250°C was reported to be ~ 0.3 (Uhrenius, Agren and Haglund 1996).

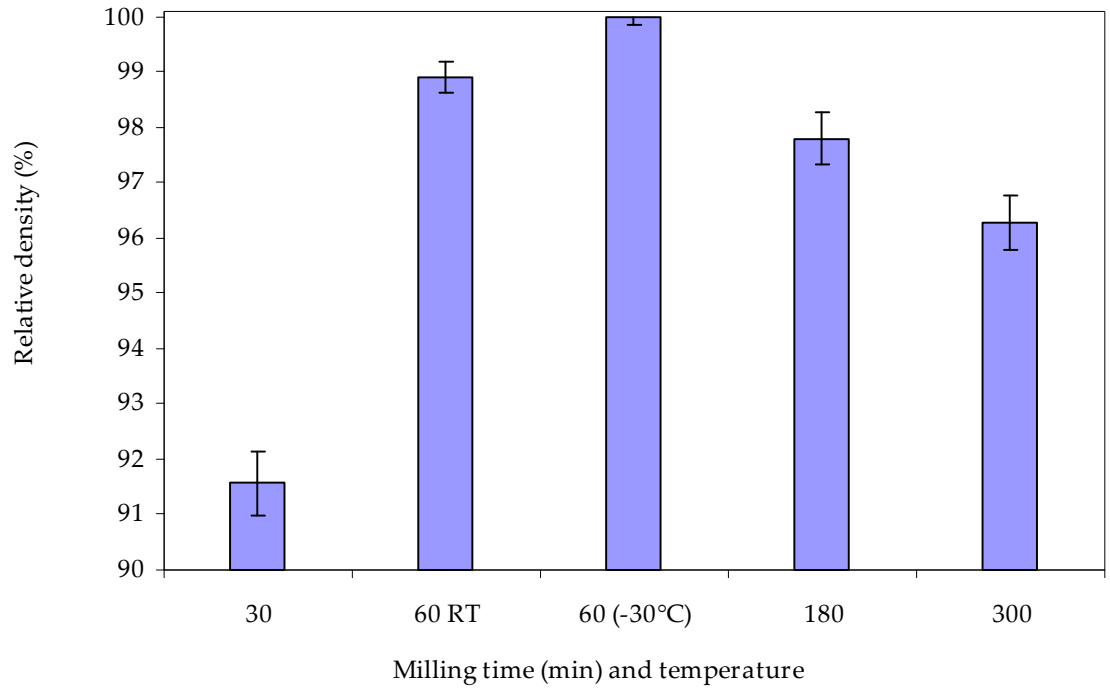

Fig. 5.57 Relative density as a function of milling time and temperature for WC10Co after pressureless sintering.

In general, high densities are not possible for this sintering technique as the final densification of powder compacts is strongly affected by the sintering atmosphere because the atmospheric gas is entrapped within pores as they become isolated (Kang 2005). Full densification is impossible with a slow diffusing or inert gas unless a high external pressure is applied (Coble 1962; Paek, Eun and Kang 1988). However, the powder milled at -30°C shows remarkable densification behaviour under pressureless conditions.

In Fig. 5.58, the residual porosity of the RT and -30°C milled powders after pressureless sintering can be seen, with a number of pores still remaining. Porosity rating for these materials is A06 and A04, respectively with no sign of any precipitates. Sintering behaviour can also suffer if the nanocrystalline powder is agglomerated. The powder milled at -30°C achieved close to full densification after pressureless sintering aided, to a certain degree, by its less agglomerated structure, Fig. 5.17.

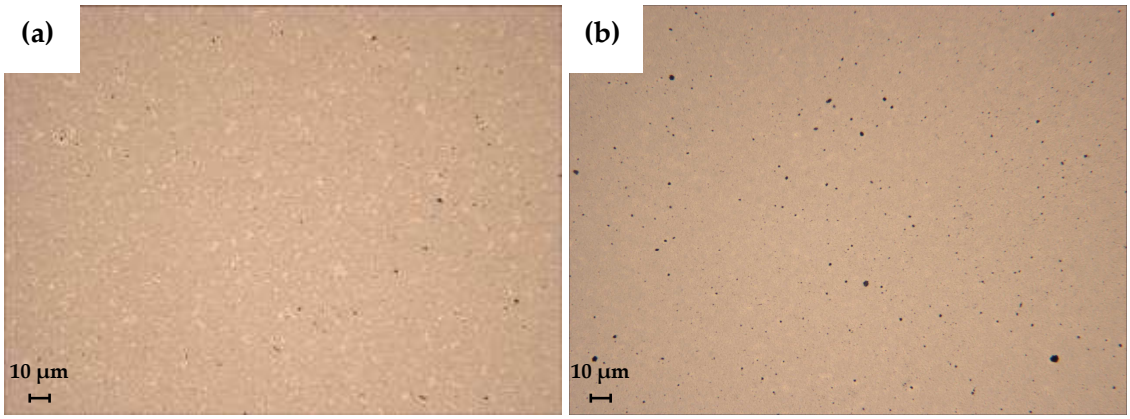

Fig. 5.58 Optical micrographs of WC-10Co for the (a) -30°C milled and (b) RT milled samples after pressureless sintering (1390°C/60 min).

Both powders exhibited considerable grain coarsening after pressureless sintering due to the elevated temperature and isothermal hold time, with the -30°C milled powder exhibiting a similar mean WC grain size of 0.91 μm compared to 0.97 μm for the RT milled powder. At the final stage of sintering, densification is interrelated with grain growth in the presence of pores. Densification rate decreases with increasing grain size and also increasing sintering time (Kang and Jung 2004). The small decrease in mean WC grain size observed by the linear intercept method for the -30°C milled material was also detected by the coercivity measurement, as shown in Fig. 5.59. As previously stated, coercivity increases with decreasing grain size and also decreasing Co content. Both factors contribute together, as well as individually, to a higher number of WC-Co interfaces, whilst at the same time controlling the thickness of the Co interlayer. A higher quantity of interfaces obstructs domain wall movement by pinning and causes higher coercivity values (Topić *et al*. 2006).

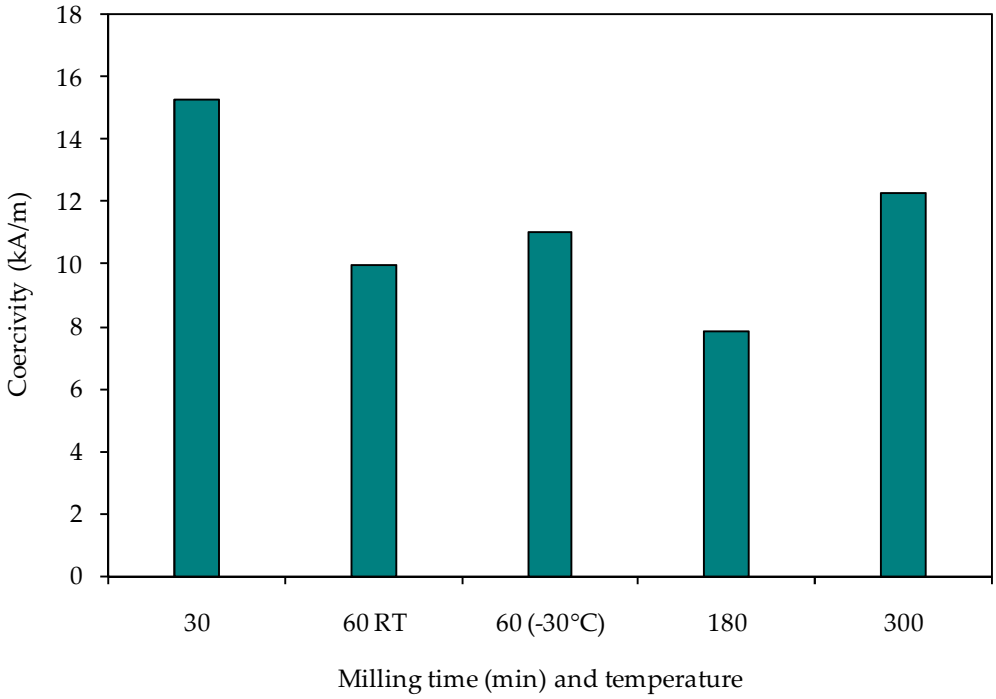

Fig. 5.59 Coercivity as a function of milling time and temperature for WC-10Co after pressureless sintering (1390°C/60 min).

SEM micrographs of the microstructures of the RT and -30°C milled samples after pressureless sintering are shown in Fig. 5.60. The microstructure of the low temperature milled sample shows a more uniform structure with a narrower grain size distribution but both samples exhibit considerable WC grain coarsening, which is reflected in the hardness values shown in Fig. 5.61. The RT and -30°C milled samples achieved hardness values of 1298 and 1337 HV30, respectively. Hardness increased slightly for the low temperature milled material due to the slight decrease in WC grain size. During deformation, the hard grains provide strengthening to the matrix and decrease the

dislocation motion. A high contiguity aids the hardness because of greater rigidity from solid-solid contacts (German 1985). Carbide particles form a partially connected structure with long range continuity through direct carbide-carbide contacts (Lee and Gurland 1978). For high mechanical properties and resistance to fracture, the matrix-carbide grain interface must be strong, which necessitates that the interface is free from precipitates, impurities and pores (Amberg, Nylander and Uhrenius 1974; Luyckx 1975). The weak links associated with liquid phase sintered materials are typically the pores and points of solid-solid contact, which give contiguity to the product (Chermant and Osterstock 1976).

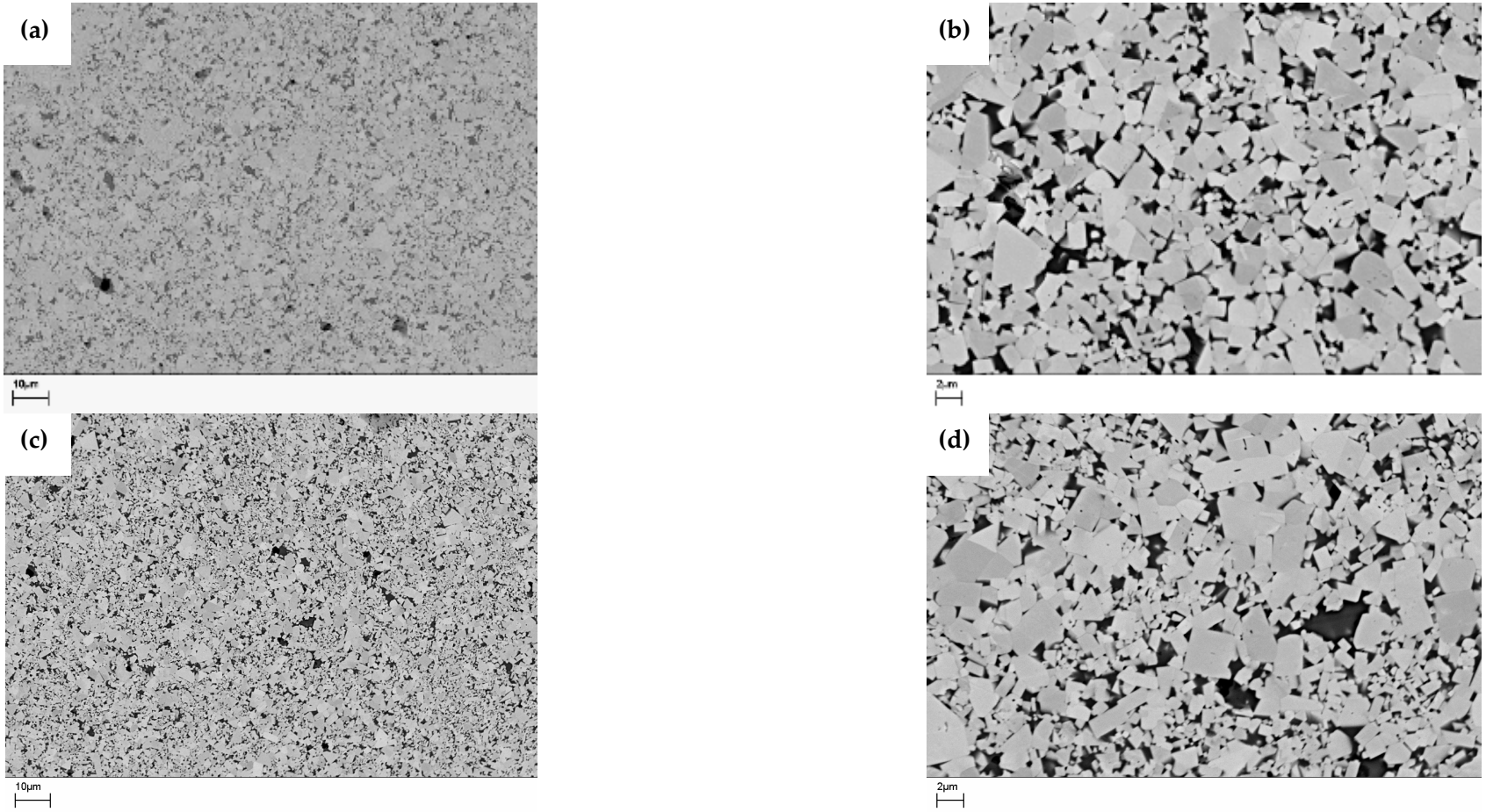

Fig. 5.60 SEM micrographs of the powders milled at (a) and (b) -30°C and (c) and (d) RT after pressureless sintering at 1390°C for 60 min.

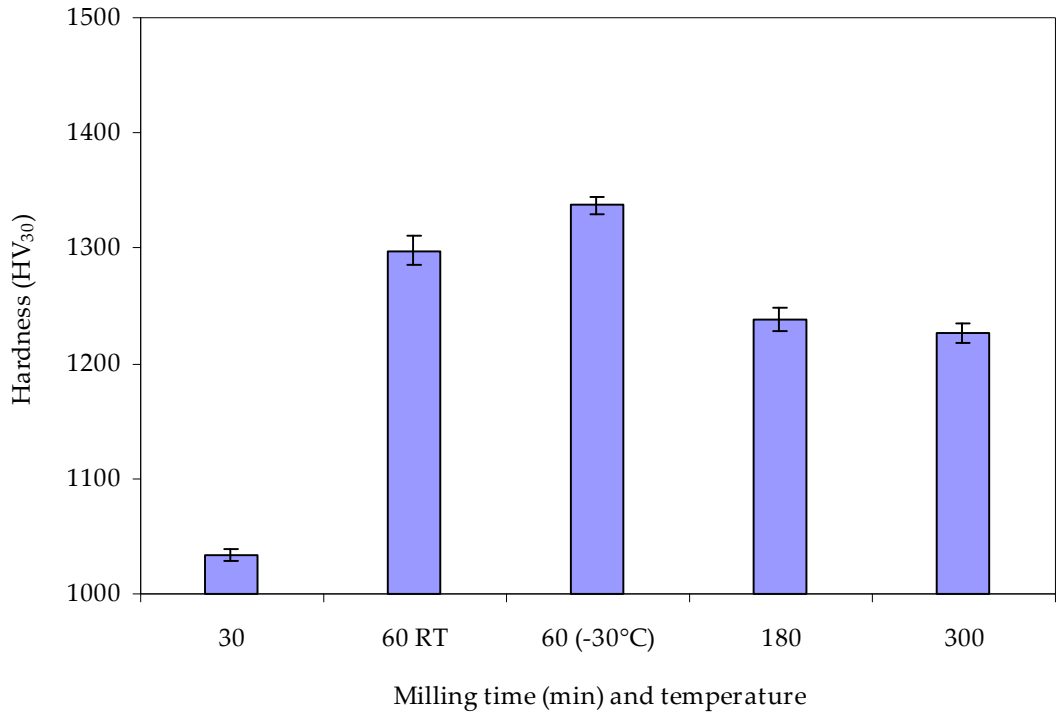

Fig. 5.61 Hardness as a function of milling time and temperature for WC-10Co after pressureless sintering (1390°C/60 min).

Unfortunately, these weak links dominate fracture and as a consequence it is desirable to have a low contiguity, small grain size and large grain separation to increase the fracture toughness (Peters 1979; Cherniavsky 1982). Interestingly, fracture toughness of the low temperature milled material, Fig. 5.62 and Table 5.11, does not follow established behaviour as the material exhibits higher fracture toughness and hardness with a smaller mean WC grain size. Fracture toughness of WC-Co alloys is known to increase as binder phase volume fraction, mean carbide grain size, and binder mean free path are increased (Dusja, Parilak and Slesar 1987). If the interface between the WC grain and matrix is 'clean' then further deformation is possible prior to failure (German 1985),

which could account for the increased toughness for the low temperature milled material as it shows significantly less contamination from the milling media, Fig. 5.22.

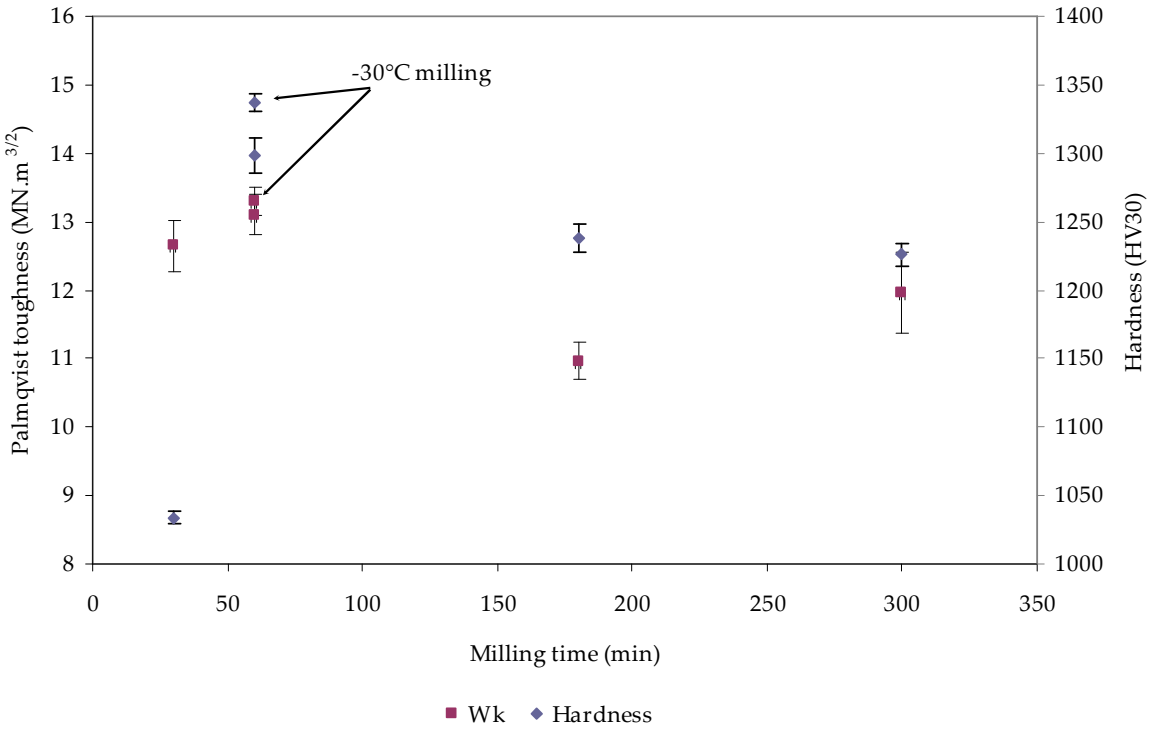

Fig. 5.62 Fracture toughness as a function of milling time and temperature for WC-10Co after pressureless sintering (1390°C/60 min).

Table 5.11

Fracture toughness results after pressureless sintering at 1390°C/60 min.

Milling time (min)	W_k ($MN.m^{-3/2}$)	S.D.	K_{IC} (Anstis) ($MN.m^{-3/2}$)
30	12.7	± 0.29	19.0
60	13.1	± 0.16	18.0
60 (-30°C)	13.3	± 0.21	18.0
180	11.0	± 0.19	15.5
300	11.6	± 0.51	16.4

5.3.5 Effect of milling temperature on densification and microstructure using sinter-HIP

Near theoretical density was observed by sintering the low temperature milled material under the application of an external pressure, Fig. 5.63. For comparison purposes, densities achieved from RT milling using pressureless and sinter-HIP processes are also shown. The densification level of the 60 min, -30°C milled material was uninfluenced by pressure-assisted sintering, which is not the case for the vast majority of the RT milled materials with all but one showing increased levels of densification using sinter-HIP. Optical micrographs of the -30°C milled material after sinter-HIP are shown in Fig. 5.64. Residual porosity for this material is rated at A02 but the micrograph and low magsat

value of 11.4 emu g^{-1} indicate the presence of η-phase, which was well dispersed and below the level observed in the 60 min RT milled powder.

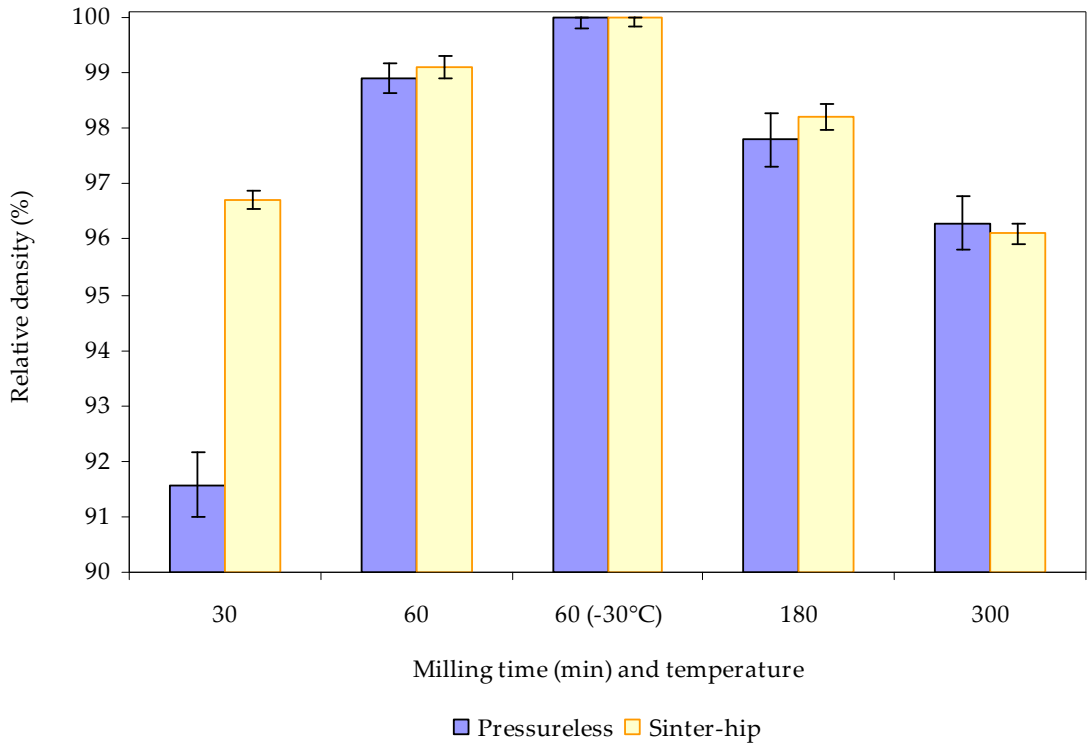

Fig. 5.63 Effect of ball milling temperature on densification using sinter-HIP (1390°C/60 min + 5 min at 40 MPa).

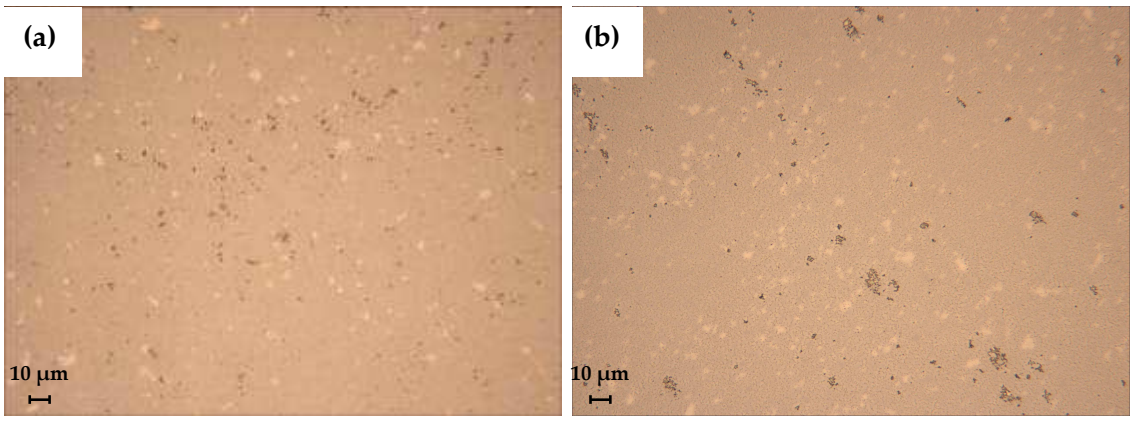

Fig. 5.64 Optical micrographs of WC-10Co for the (a) -30°C milled and (b) RT milled samples after sinter-HIP.

The presence of this third phase could have been due to the reactions involving CO, observed during TG/DSC measurements. These high CO reactions, coupled with carbon activity in the furnace atmosphere, may well have increased carbon deficiency. Coercivity increased to 9.11 kA/m compared to 8.2 kA/m for the 60 min RT milled material, Fig. 5.65. Typically, coercivity increases with increasing carbon content (Freytag and Exner 1977) but in this case the low temperature milled material exhibited a carbon deficiency phase, which suggests that the increase in coercive force is due to a decrease in WC grain size (Stjernberg 1970). This is confirmed by the increase in hardness with the low temperature milled material reaching 1363 HV30 compared to 1350 for the RT milled material, Fig. 5.66. This value is comparative with that of a conventional WC-10Co material with a 'medium' grain size structure classification (Scussel 1992).

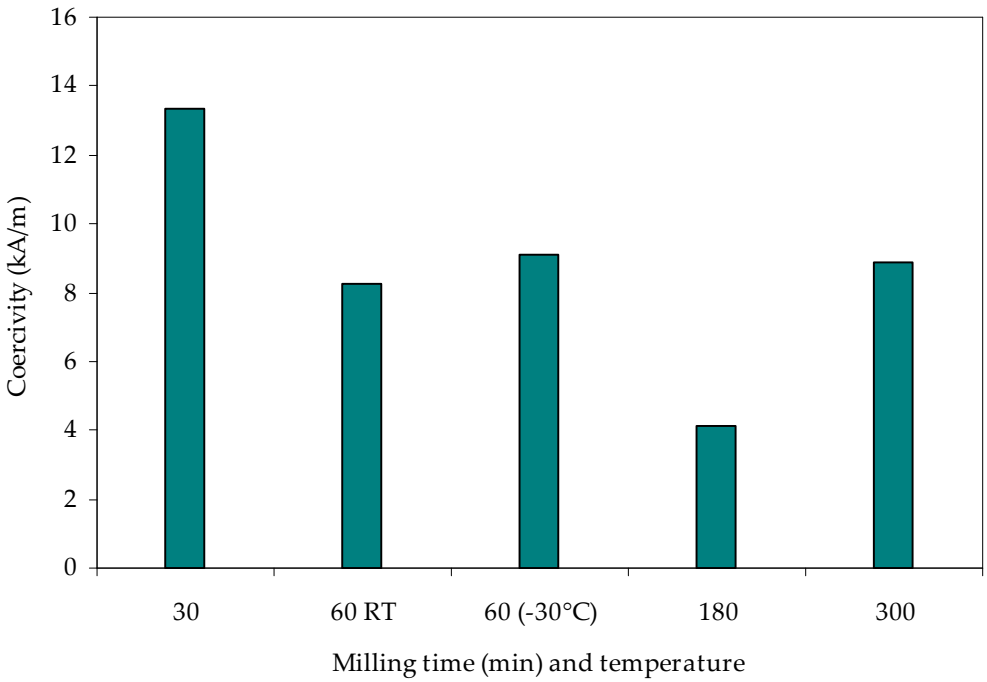

Fig. 5.65 Coercivity as a function of milling time and temperature for WC-10Co after sinter-HIP.

The hardness of the carbide and matrix phases are functions of particle size d, and binder mean free path λ, and are empirically related (Gurland 1979):

$$H_{WC} = 1382 + 23.1 d^{-1/2} \text{ (kg/mm}^2\text{)} \quad (5.24)$$

$$H_{M} = 304 + 12.7 \lambda^{-1/2} \text{ (kg/mm}^2\text{)} \quad (5.25)$$

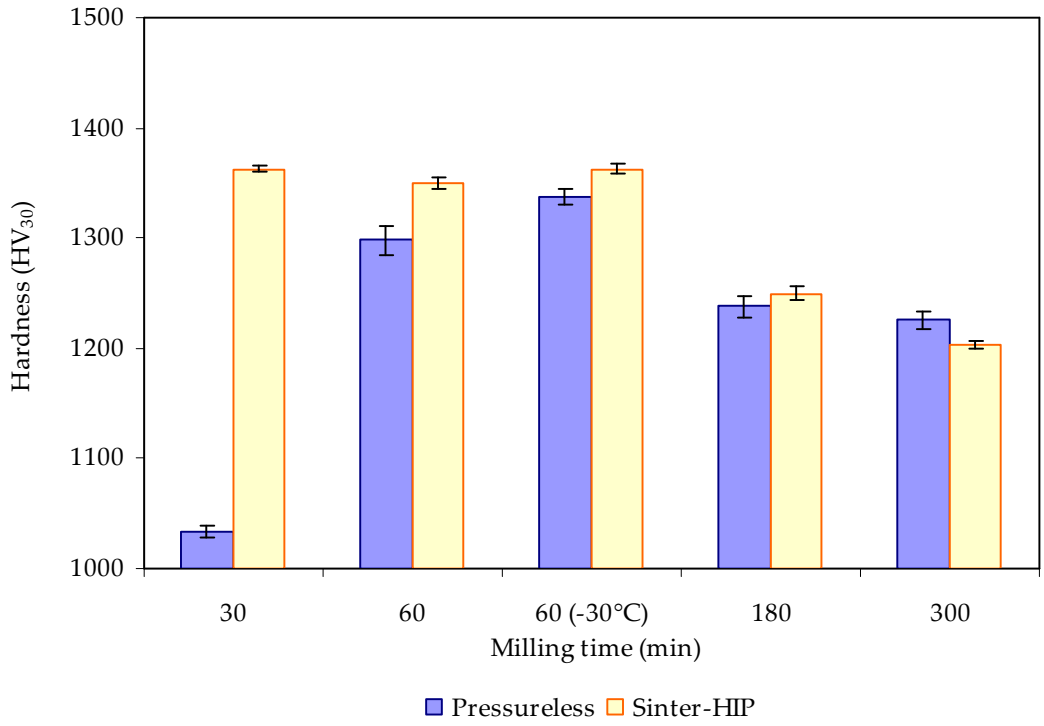

Fig. 5.66 Effect of milling temperature and time on hardness of WC-10Co after pressureless and sinter-HIP.

The SEM micrographs of the sinter-HIP'd WC-10Co material after 60 min milling at -30°C are shown in Fig. 5.67 (a, b), with 60 min RT milling also shown for comparative purposes. The low temperature milled material shows a more homogenous structure with a narrower WC grain size distribution, although significant WC grain growth has taken place. Nevertheless, linear intercept measurements for the -30°C milled material indicated a smaller average WC grain size of 1.17 μm compared to 1.32 μm for the RT milled material, Fig. 5.68. WC grains grow during solid and liquid phase sintering by dissolution of small grains in the Co-binder and reprecipitation on larger WC-grains. Grain growth and densification of nanostructured WC-Co powders operate concurrently

during heat- up to solid state temperatures and a large fraction of densification takes place at solid-state temperatures. Rapid densification and grain growth are partially attributed to the surface energy anisotropy of tungsten carbide (Fang *et al*. 2005). There did not appear to be any localised WC discontinuous grain growth in either sample. It was therefore assumed that continuous grain growth occurred due to the elevated sintering temperature and isothermal hold time. The high temperature and hold time had a detrimental effect on mechanical properties, as hardness levels were lower than conventional WC-10Co materials. During pressure-assisted sintering, pore curvature dominates the driving force for densification when grain sizes are 2 – 3 nm. With larger grains (~100 nm), the applied pressure has the more significant effect. At intermediate grain sizes (~20 nm), the effects of both variables are comparable (Padmanabhan and Hahn 1996). The application of an external pressure can increase mechanical properties due to the elimination of large pores (Qvick 1988). However, somewhat unexpectedly, the hardness of the -30°C milled material did not increase above that obtained by pressureless sintering, Fig. 5.63. Sintered density and hardness values of the -30°C milled powder are higher than those reported for a WC-9.8Co cryomilled composition containing a grain growth inhibitor (Lee *et al*. 2003).

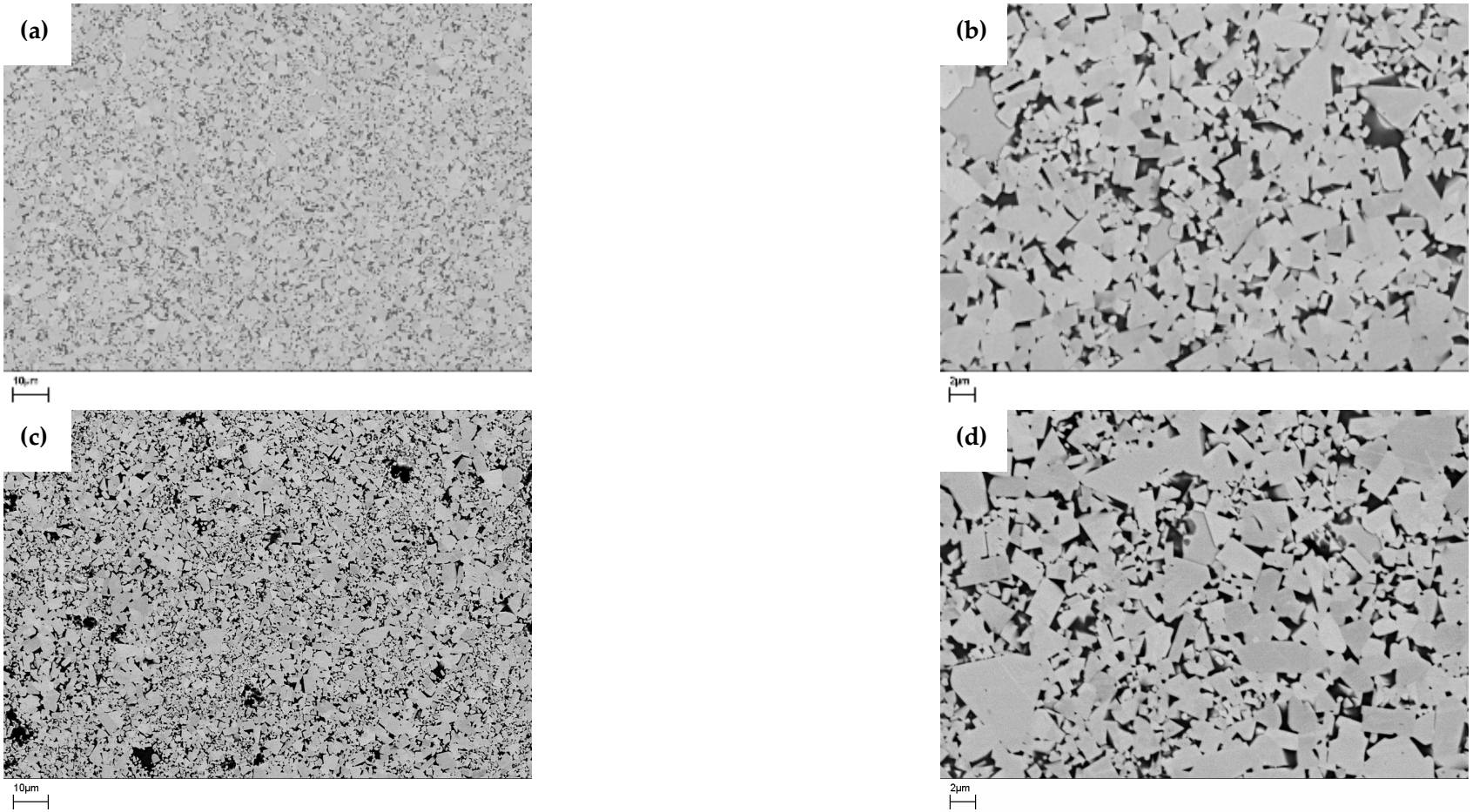

Fig. 5.67 SEM micrographs of the WC-10Co materials from (a), (b) 60 min milling at -30°C and (c), (d) 60 min at RT after sinter-HIP.

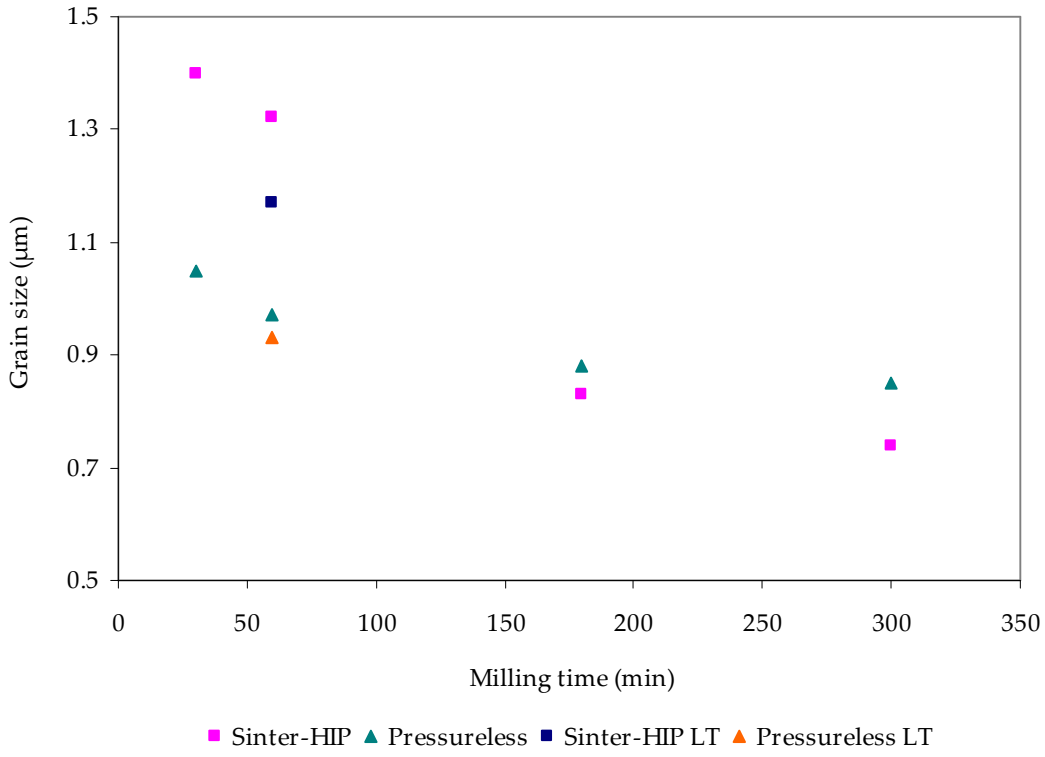

Fig. 5.68 Mean WC grain size as a function of milling time and temperature (LT -30°C) after sinter-HIP and pressureless sintering at 1390°C/60 min.

Palmqvist fracture toughness of the low temperature milled material, determined from Vickers hardness measurements using eq. 5.14, followed the same trend as that observed from sinter-HIP of the RT materials, with fracture toughness increasing with decreasing hardness, Fig. 5.69 and Table 5.12, but with a higher hardness from that achieved from pressureless sintering. The low temperature milled material shows a smaller, average WC grain size, which suggests that the number of interfaces has increased, thereby decreasing the binder mean free path (MFP). As already mentioned, fracture toughness increases with increasing mean WC grain size and MFP, but this

material does not follow this trend. Milling at -30°C and pressureless sintering at 1390°C for 60 min results in a WC grain size of 0.92 μm and a W_K value of 13.3 $MN.m^{3/2}$ compared to a WC grain size of 0.97 μm and a W_K value of 13.0 $MN.m^{3/2}$ for 60 min RT milling. The difference is increased even further after sinter-HIP with -30°C milling resulting in a WC grain size of 1.17 μm and a W_K value of 14.5 $MN.m^{3/2}$ compared to a WC grain size of 1.32 μm and a W_K value of 13.7 $MN.m^{3/2}$ after RT milling. The loss of carbon for both the -30°C and RT milled material did not have an effect on fracture toughness, which does not conform to general understanding as carbon deficiency is known to have a detrimental effect on toughness (Andrén 2001).

The low temperature milled material achieved a higher strength after sinter-HIP compared to the 60 min RT milled material, Fig. 5.70 and Table 5.13, but the value obtained is considerably below that of a conventional, fine-grained WC- 10Co material, typically ~3100 MPa, but is also below that of a coarser-grained material (~ 2760 MPa) (Scussel 1992). Material defects, including pores, inclusions, and large grains can all cause premature failure (Exner and Gurland 1970), but Co content is the most important variable in producing hardmetals of different qualities (Upadhyaya 1998). This material exhibits near theoretical density and showed virtually negligible amounts of impurities after milling. The improved microstructure of this material would also serve to reduce premature failure. Therefore, the most viable explanation for the low TRS value for the -30°C milled material is a reduced level of Co. The magsat for the -30°C milled material after sinter-HIP was 11.3 emu g^{-1}, which is significantly below the magsat for WC-10Co of 16 emu/g. From the interrelationship between carbon and Co shown in Fig. 3.3, a

value of 11.3 emu/g falls below the carbon range for a 10% Co composition, which does not correspond with the level of η-phase observed for this material. It seems more likely that the level of Co has changed during the powder processing stage, thereby altering the final composition below that of a 10wt% WC-Co alloy. TRS is known to decrease with decreasing Co content (Doi, Fujiwara and Miyake 1969; Gurland 1963; Gurland 1955; Engle 1942).

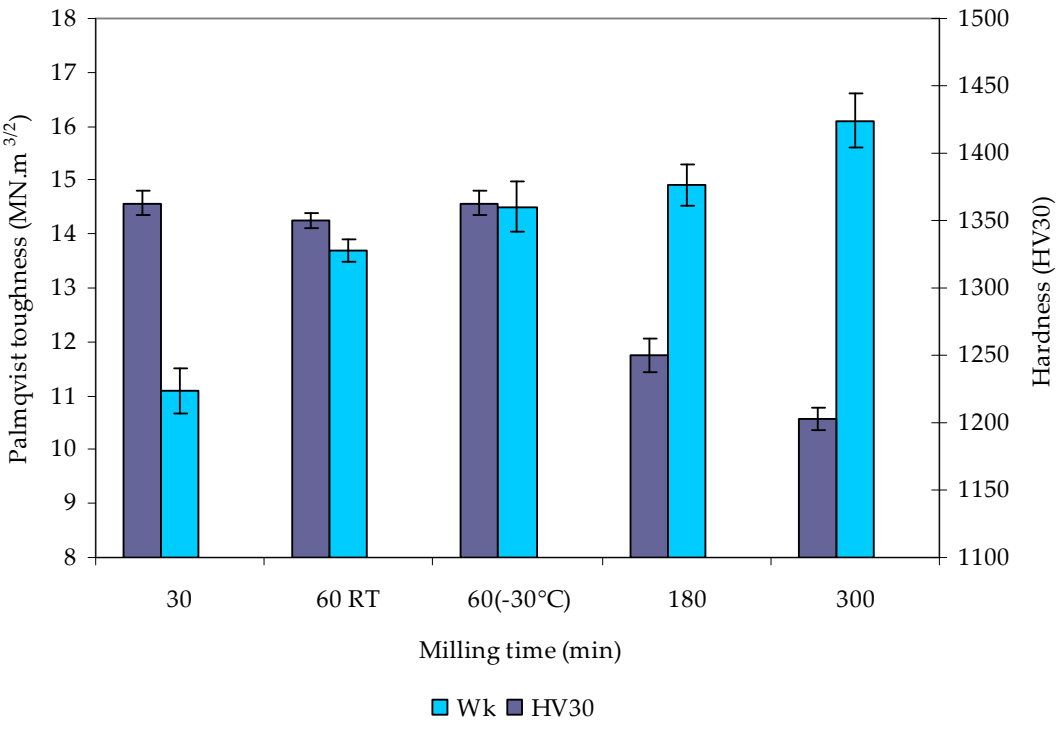

Fig. 5.69 Effect of ball milling temperature and time on the fracture toughness of WC-10Co after sinter-HIP.

Table 5.12

Fracture toughness results from low temperature milling after sinter-HIP at 1390°C/60 min and pressureless sintering.

	Sinter-HIP	S.D.	Sinter-HIP	P'less	P'less
Milling time (min)	W_K (MN. $m^{-3/2}$)		K_{IC} (Anstis) (MN. $m^{-3/2}$)	W_K (MN. $m^{-3/2}$)	K_{IC} (Anstis) (MN. $m^{-3/2}$)
30	11.1	± 0.48	14.3	12.7	19.0
60	13.7	± 0.24	18.7	13.1	18.0
60 (-30°C)	14.5	± 0.38	19.1	13.3	18.0
180	14.9	± 0.31	20.2	11.0	15.5
300	16.1	± 0.33	21.8	11.6	16.4

S.D. – standard deviation

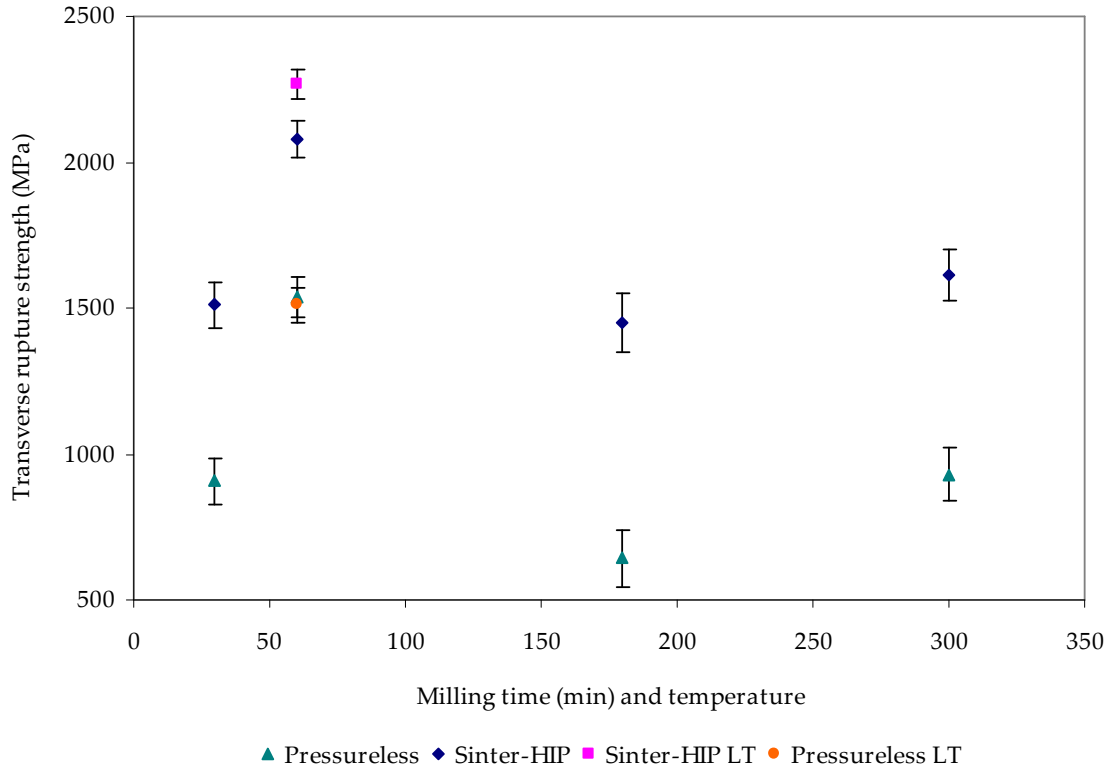

Fig. 5.70 Effect of ball milling temperature on the transverse rupture strength of WC-10Co after sinter-HIP.

Table 5.13

Transverse rupture strength of low temperature milled WC-10Co after pressureless sintering and sinter-HIP.

Milling time (min)	TRS – pressureless (MPa)	S.D.	TRS – sinter-HIP (MPa)	S.D.
30	906.7	± 105	1505.2	± 69
60	1538.3	± 73	2078.7	± 57
60 (-30°C)	1510.4	± 66	2265.2	± 83
180	641.7	± 113	1447.7	± 52
300	928.9	± 79	1614.4	± 61

S.D. – standard deviation

5.4 Effect of grain growth inhibitor

5.4.1 Effect of grain growth inhibitor on WC-Co eutectic temperature

The heating scans of the WC-10Co-1VC powders after 60, 180, and 300 min ball milling can be seen in Fig. 5.71. The doped powders exhibit the same trend as the undoped WC-10Co powders with the onset of melting reduced with increasing milling time, but to lower temperatures, which shows that the melting temperature (T_m) of WC-Co-VC is further decreased. The onset of melting for the 60, 180, and 300 min milled samples is 1306°C, 1293°C, and 1283°C, respectively, thereby lowering the WC-Co eutectic reaction by ~ 30°C for the case of 300 min milling. This is consistent with other work (Luycks and Alli 2001; Taniuchi, Okada and Tanase 1997) and fits within the solidus-liquidus lines calculated for the WC-10Co-1VC phase diagram, Fig. 3.7. The stored enthalpy is considerably reduced by the addition of VC compared with the undoped powders, Fig. 5.10, which suggests that the inhibitor has slowed down the rate of recovery and the relaxation processes within the grain boundaries. During milling, the inhibitor is distributed onto the surfaces of the WC grains, thus impeding coalescence during LPS. In general, coalescence is favoured in those cases where there are low misorientation angles between the grains and a high dihedral angle, apart from large grain size differences (Upadhyaya 1998). For a low dihedral angle, as in the case of the WC-Co system, the motion of the boundary through the small grain increases the system energy since the area of the grain boundary increases. Thus, there is an energy barrier for

impeding coalescence, and the simultaneous action of solution-reprecipitation from small to large grain is favoured (German 1985).

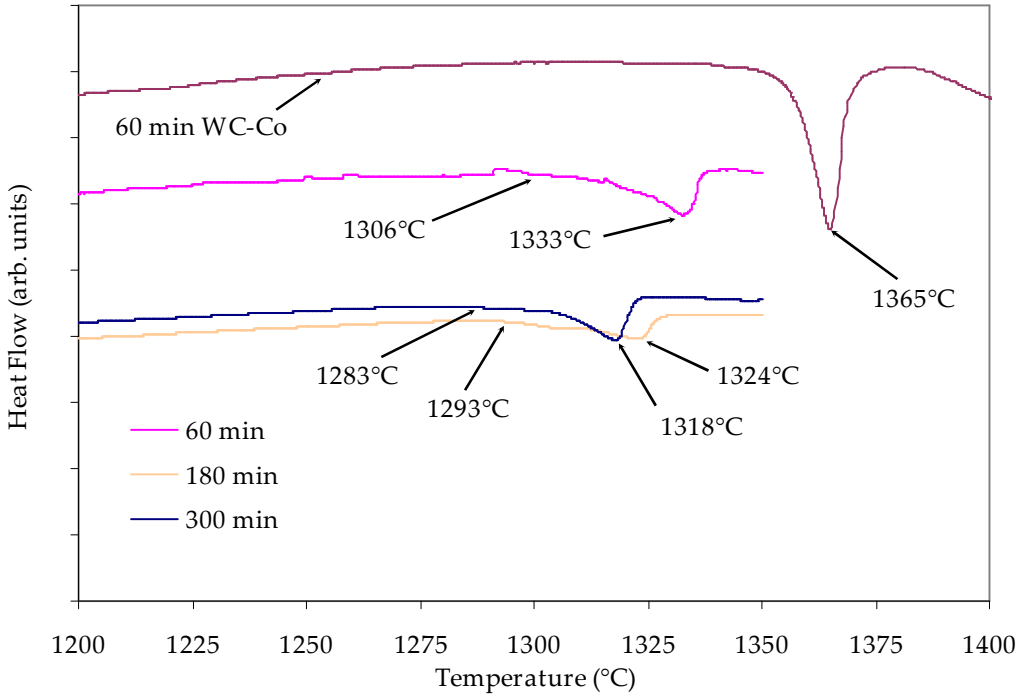

Fig. 5.71 DSC heating scans of WC-10Co-1VC powders after ball-milling for 60, 180, and 300 min.

5.4.2 Effect of inhibitor on green density

Single-ended pressing of the ball milled WC-10Co-1VC powders at 250 MPa shows that the addition of VC reduced green density by ~ 3.5%, with density levels following the same trend as the undoped powders and decreasing with increasing ball milling time, Fig. 5.72. In this study, the binder phase was kept constant at 10wt% and the hard WC phase was altered accordingly to include 1wt% of inhibitor, which gives the same

fraction of hard phase. The lower levels observed for the doped powders may be due to the coarseness of the VC starting powder with the green densities suggesting inadequate processing times to refine the VC particle sizes. The starting size of the particles was > 10 μm, Fig. 5.6, which is significantly larger than the starting sizes of both WC and Co. because of this, a minimum processing time of 30 min was not incorporated into the milling matrix for the doped powders as it was anticipated that such a short milling time would be insufficient for uniform particle deformation.

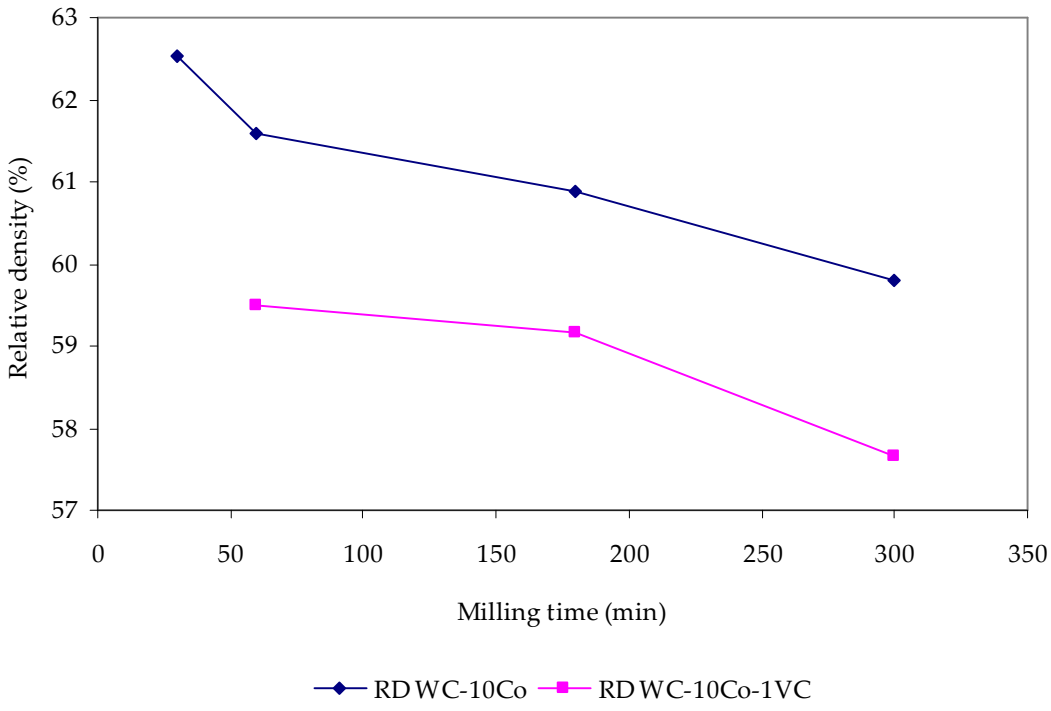

Fig. 5.72 Effect of ball milling time on the compaction behaviour of WC-10Co-1VC powders.

After 300 min ball milling of the doped powder composition, an SEM micrograph, Fig. 5.73, shows one of many large particles of VC, approximately 5 μm diameter, still remaining in the powder. This type of hard particle would hinder compaction mechanisms, including the initial sliding and rearrangement of particles and could also affect the applied force. During the course of compaction in a single action press, interaction between friction and the applied load at the die walls, as well as the resistance of the reinforcement particles against applied pressure, reduce the transmitted force from the upper punch to the lower punch (Chen 1991). This effect is more pronounced for composite powders containing higher amounts of reinforcement particles, which will be further exaggerated with the inclusion of large VC particles. These large particles could also cause a density gradient through the green compact.

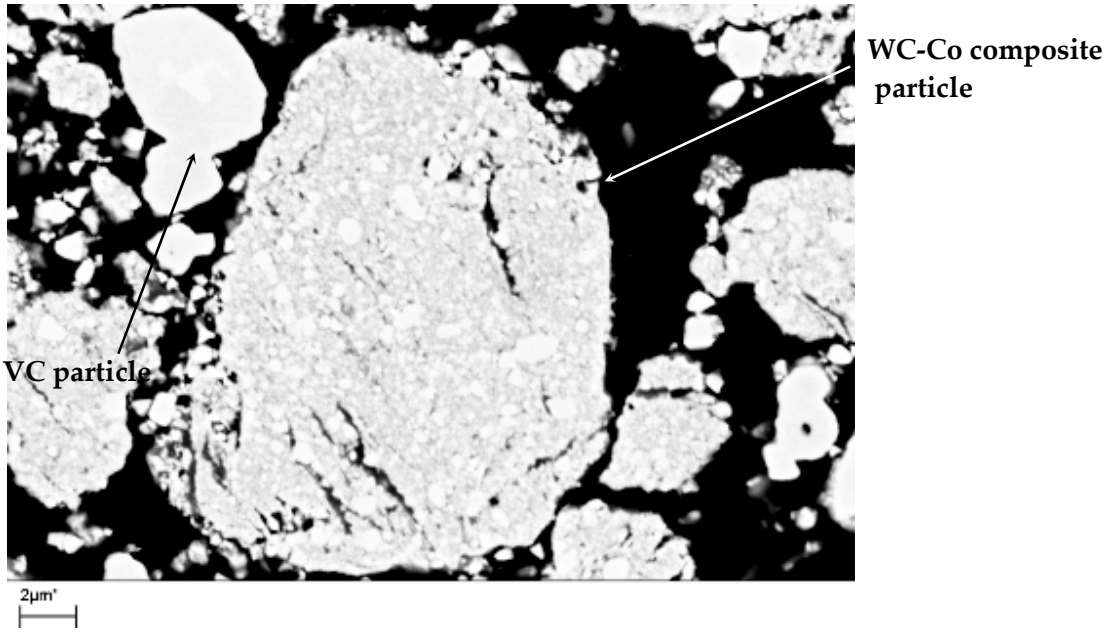

Fig. 5.73 SEM micrograph of WC-10Co-1VC powder after 300 min ball milling showing a large fragment of VC.

5.4.3 Effect of inhibitor and milling time on densification and microstructure using pressureless sintering

Compacts from the 180 min milled WC-10Co-1VC powder were pressureless sintered for 60 min at temperatures between 1355°C and 1420°C. VC is known to be effective at limiting continuous WC grain growth for a WC-10Co composition from the eutectic temperature up to 1575°C (Morton, Wills and Stjernberg 2005). From Fig. 5.74, the doped material achieved a higher relative density at 1355°C that the undoped material, with values of 84% and 78.9%, respectively. This effect does not conform to other reported work where the opposite effect was found for a nanocrystalline WC-10Co-1VC composition (Fang *et al*. 2005). After 1355°C, densification of the doped material is retarded. With increasing temperature, the rate of densification changes quite dramatically for both materials with the undoped material approaching 98% by 1390°C whilst the doped material reaches 89% TD. Sintering temperature was increased by 30°C for the doped material, which increased density to ~ 93%. This clearly shows the effect of VC on retarding densification. Extrapolating the relative density data indicated that a considerable increase in temperature would be required in order to reach near theoretical, which would have a detrimental effect on microstructural coarsening, therefore further temperature increases were not applied. Hardness increased linearly with densification for the doped material, reaching ~ 1000 HV30 at 1390°C compared to ~ 1200 HV30 for the undoped material. An increase in sintering temperature of 30°C resulted in an increase in hardness to ~ 1200 HV30. Despite this increase, hardness

remains substantially lower than values quoted in the literature of ~ 1800 HV30 for WC-10Co-VC sintered at 1400°C (Morton, Wills and Stjernberg 2005; Kleiner-Bicherl *et al.* 2006).

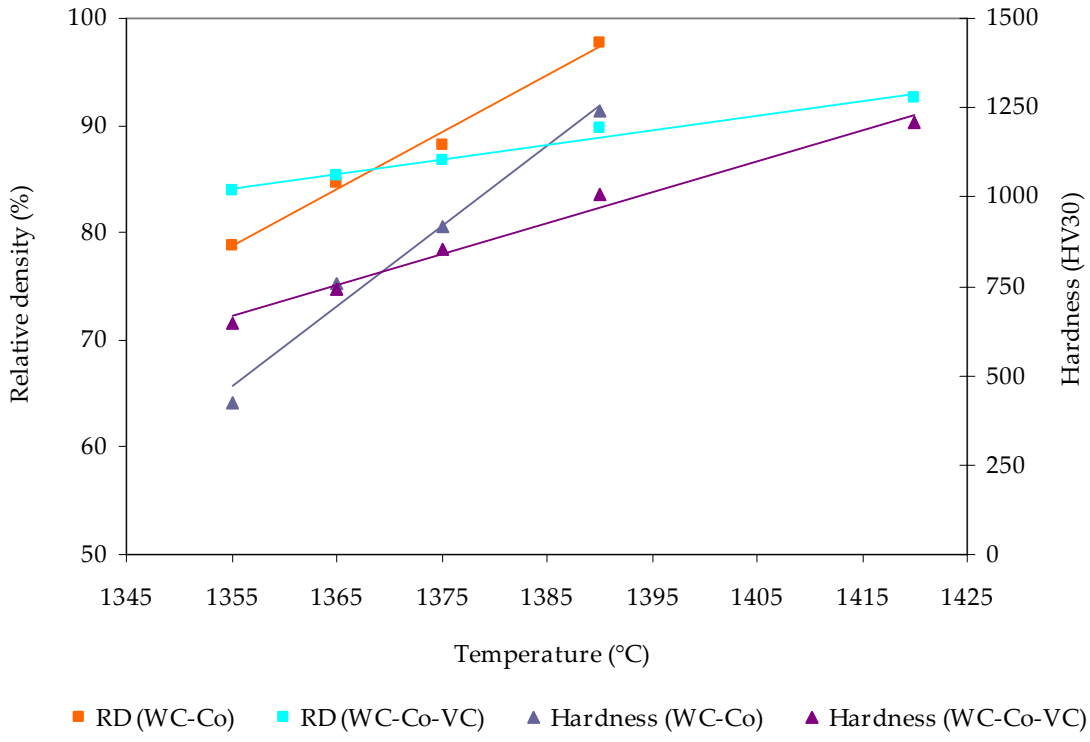

Fig. 5.74 Relative density and hardness as a function of sintering temperature for WC-10Co-1VC ball milled for 180 min and cold compacted at 250 MPa.

The 60 and 300 min ball milled materials were sintered at 1390°C for 60 min to allow a direct comparison with the undoped materials. Relative density decreases almost linearly with increasing ball milling time, as shown in Fig. 5.75. With such low levels of densification, residual porosity was expectedly high, Fig. 5.76, which is a direct result of

a number of critical factors with the first of these being the ineffectiveness of the synthesis process to break down the large VC particles. Given the coarseness of the VC powder particles, consideration was given to modifying the process sequence to pre-mill the VC powder in order to reduce the particle size to a much finer size before being added with the starting WC-10Co powder mix. The reason this route was not followed is due to the high levels of powder contamination observed during milling of the undoped powders and, therefore, it was decided to keep milling times to a minimum. The second factor is the lower relative density values achieved at each milling time compared to those observed after milling of the undoped powders, coupled with the densification retardation effects of VC, which led to higher required sintering temperatures to achieve near theoretical density, as shown in Fig. 5.74. Porosity ratings for the 60, 180, and 300 min milled materials are all rated at >A08 (see 4.5.3). The phenomenon of Co migration during sintering is dependent on the ability of the cobalt phase to wet the WC interfaces. This wetting behaviour is, in turn, strongly influenced by the grain growth inhibitor. It is known that VC inhibits the diffusion and migration of Co onto the WC grains at temperatures below the liquidus, which is attributed to low W solubility in the Co/V phase thereby decreasing the affinity of the Co binder for the WC grains (Taniuchi, Okada and Tanase 1997). This reduced affinity and migration behaviour may explain the higher porosity levels.

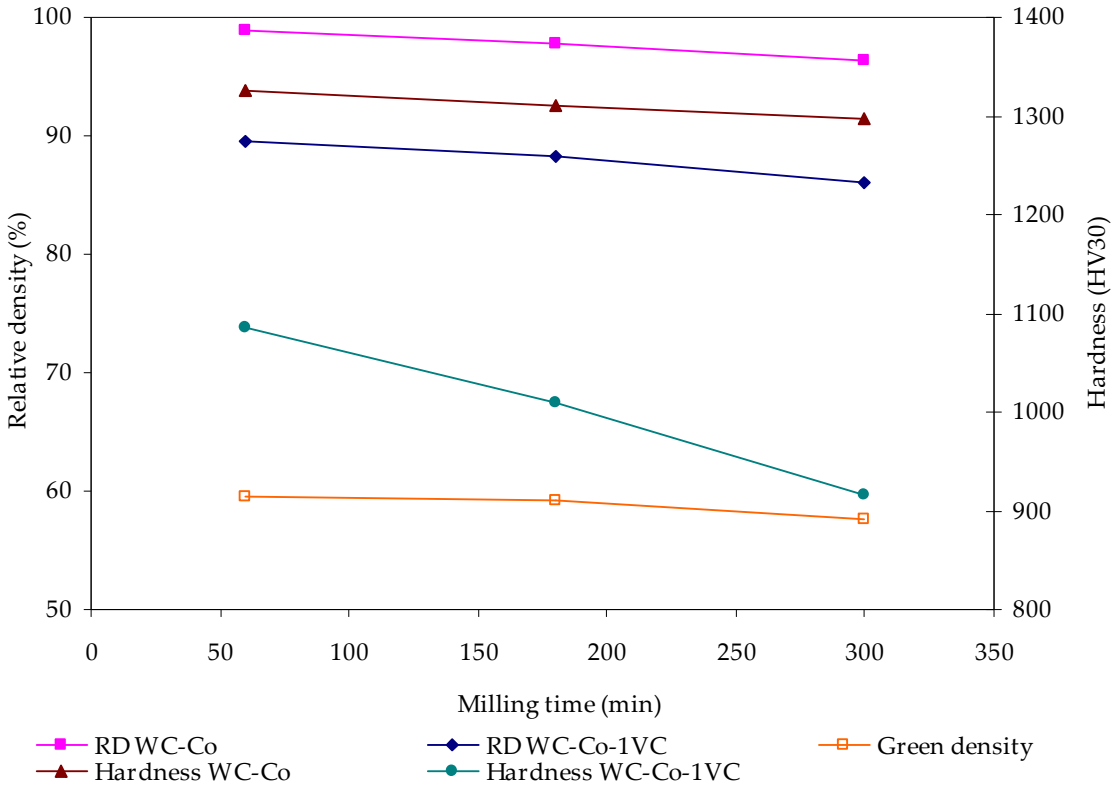

Fig. 5.75 Relative density and hardness of pressureless sintered (1390°C/60 min) WC-10Co-1VC as a function of milling time.

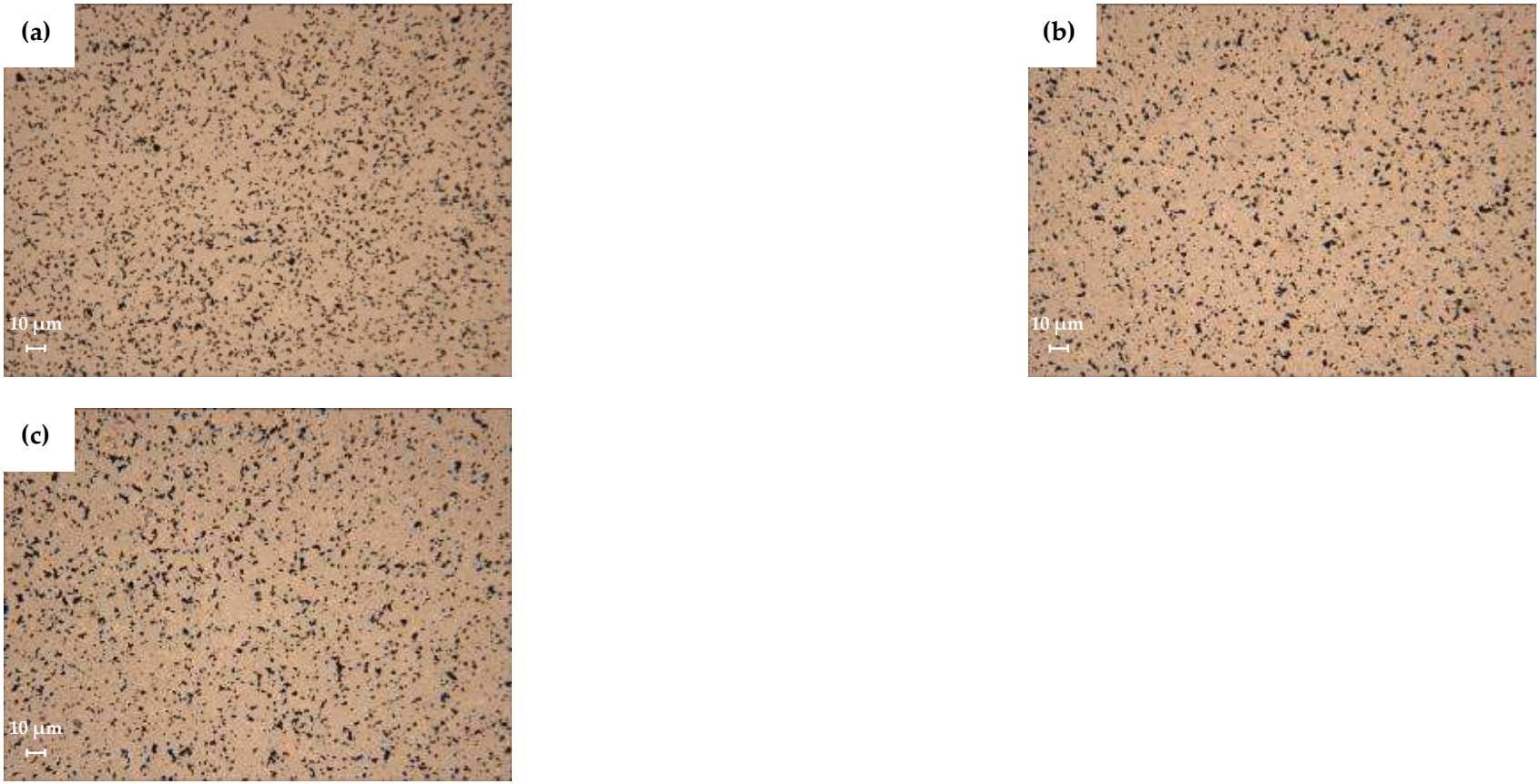

Fig. 5.76 Optical micrographs of WC-10Co-1VC pressureless sintered at 1390°C/60 min after (a) 60 min, (b) 180 min, and (c) 300 min.

The decreasing level of hardness with milling time corresponds with decreasing levels of densification, as shown in Fig. 5.75. It is also apparent that hardness of the doped material is more sensitive to milling time with a higher rate of decreasing hardness for a corresponding decrease in densification. Densification is strongly dependent on particle size with the onset of the rapid densification stage much faster for nanosize powders than ultrafine and fine powders (Fang *et al*. 2005). The entire temperature range of sintering during heating up was shown to shift proportionally to lower temperatures as the particle size decreased, which suggests that similar densification mechanisms are operating for nanocrystalline and micron-sized powders, although the activation energy for densification decreases significantly with a decrease in particle size (Groza 2007). However, with the doped materials, higher activation energy was required to improve densification, which suggests that powder particle sizes were coarser than those obtained from ball milling the undoped powders.

SEM micrographs of the sintered structures after pressureless sintering at 1390°C are shown in Fig. 5.77. The most striking observation is the inhomogeneity of the structures, which is most likely caused by inadequate mixing and dispersion of the inhibitor. One of the prerequisites of using grain growth inhibitors is a very homogeneous distribution of the inhibitor (Rabitsch and Veitsch 2007). The microstructures from all three milling times are very inhomogeneous, especially so for the 180 min milled material. The structure of the material after 300 min milling seems to have improved slightly but clearly, the ball milling times used in this study were not sufficient to uniformly reduce the VC particles. A slight improvement after 300 min milling suggests that the inhibitor

had only just started to become distributed at this stage, which, given the starting particle size of the inhibitor, does not seem unreasonable. There does not appear to be any γ phase present in the microstructures, which shows the high solubility of VC in Co, with all the VC being dissolved in the binder during sintering.

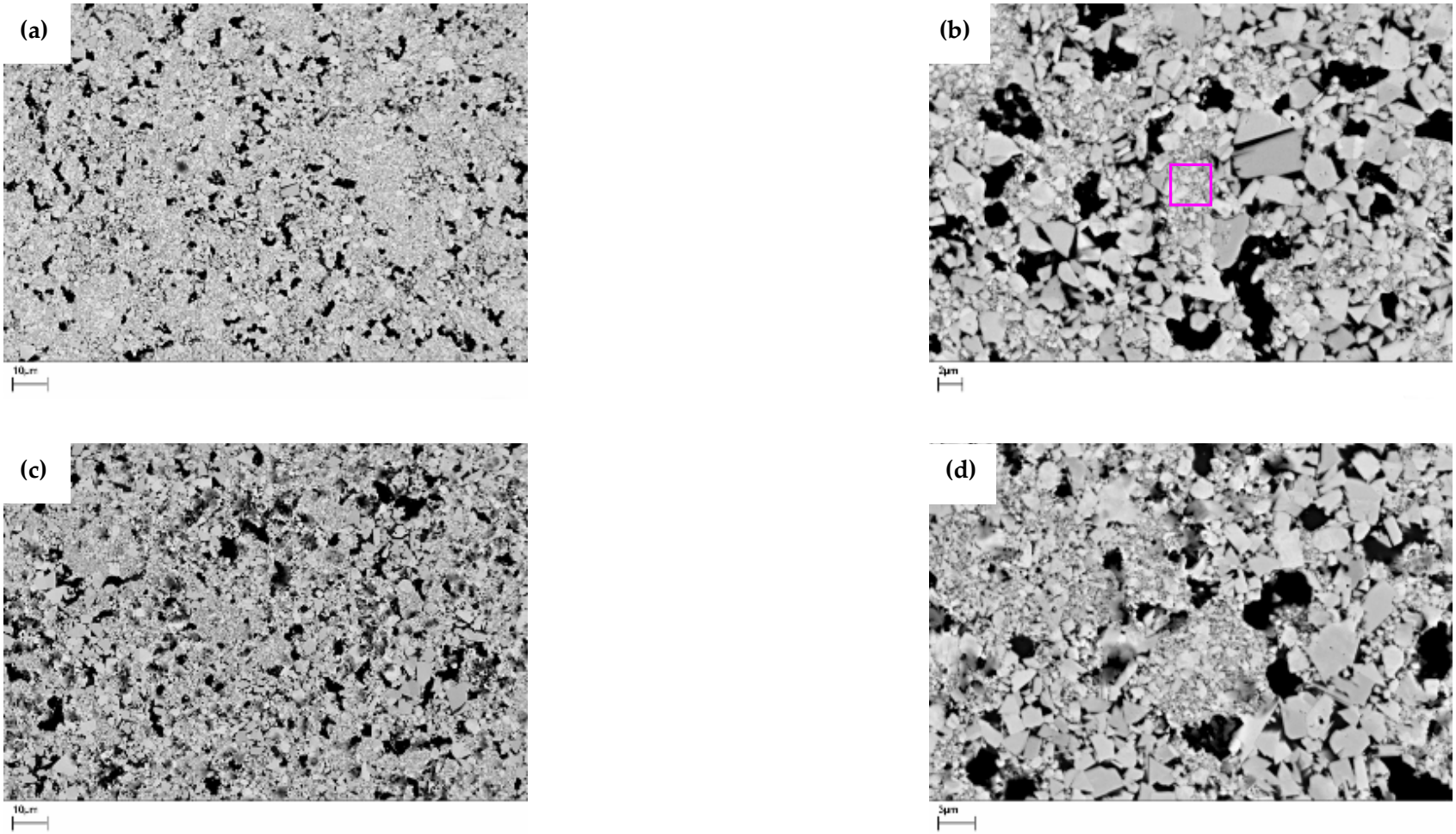

Fig. 5.77 SEM micrographs of pressureless sintered (1390°C/60 min) WC-10C-1VCo samples prepared from powder ball milled for (a), (b) 60 min; (c), (d) 180 min.

Fig. 5.77 cont'd SEM micrographs of pressureless sintered (1390°C/60 min) WC-10C-1VCo samples prepared from powder ball milled for (e), (f) 300 min.

EDX analysis of one of the poorly distributed areas from the 60 min milled material, highlighted in Fig. 5.77 (b), shows VC in combination with impurity element Fe, Fig. 5.78. One positive aspect of the microstructures is that WC grain growth has been reduced compared to the undoped microstructures. The SEM micrograph from 300 min milling, Fig. 5.77 (f), seems to show a large WC grain, ~ 6 μm surrounded by grains of ~ 2 μm. This suggests that discontinuous grain growth has occurred in the material. Inhomogeneous distribution of the inhibitor is known to cause this effect (Rabitsch and Veitsch 2007).

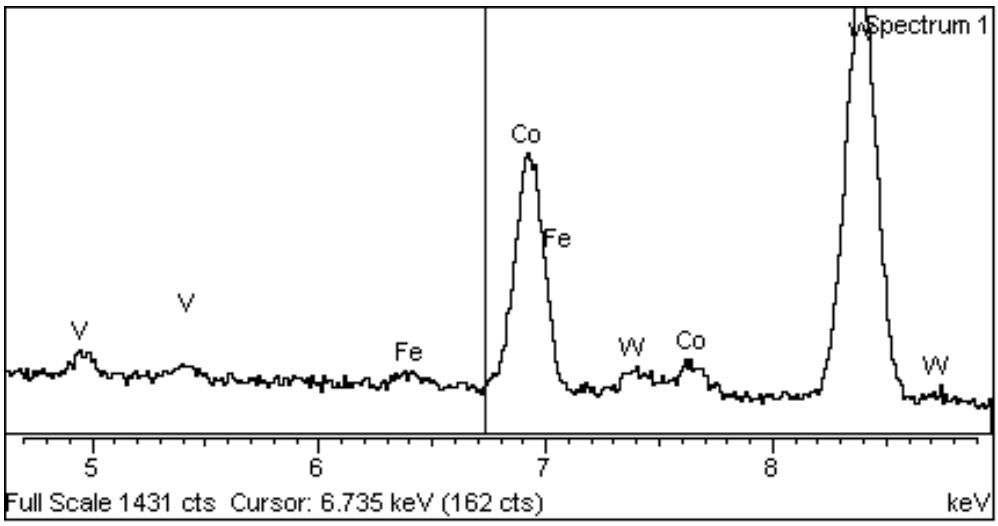

Fig. 5.78 EDX analysis of the highlighted area shown in Fig. 5.76 (b).

5.4.4 Effect of inhibitor and milling time on densification and microstructure using sinter-HIP

The 60, 180, and 300 min ball milled doped samples were sintered using the same process cycle as the undoped samples. Somewhat surprisingly, the application of an external pressure did not improve densification levels, Fig. 5.79, with the doped materials exhibiting similar values of relative density with milling time as those obtained from pressureless sintering. The 60 min milled material shows a significant increase in hardness compared to the sinter-HIP'd, undoped material, achieving 1463 HV30, which is surprising given that RD is < 90%. However, closer inspection of the microstructure, Fig. 5.82 (b), shows certain regions containing a much finer average WC grain size of < ~ 0.5 μm, which would explain the higher hardness value. Hardness then decreases sharply after 60 min milling, which corresponds with the inhomogenous microstructures, Fig. 5.82 (d) and (f), and larger average WC grain sizes. A faster decrease in hardness is observed after 60 min milling than the undoped material and falls to 1115 HV30 after 300 min milling compared to 1205 HV30 for the undoped material. This behaviour relates back to green pressing and the inhomogenous, lower density green compacts produced as a result of the inadequate processing strategy to deal with the large VC starting particles.

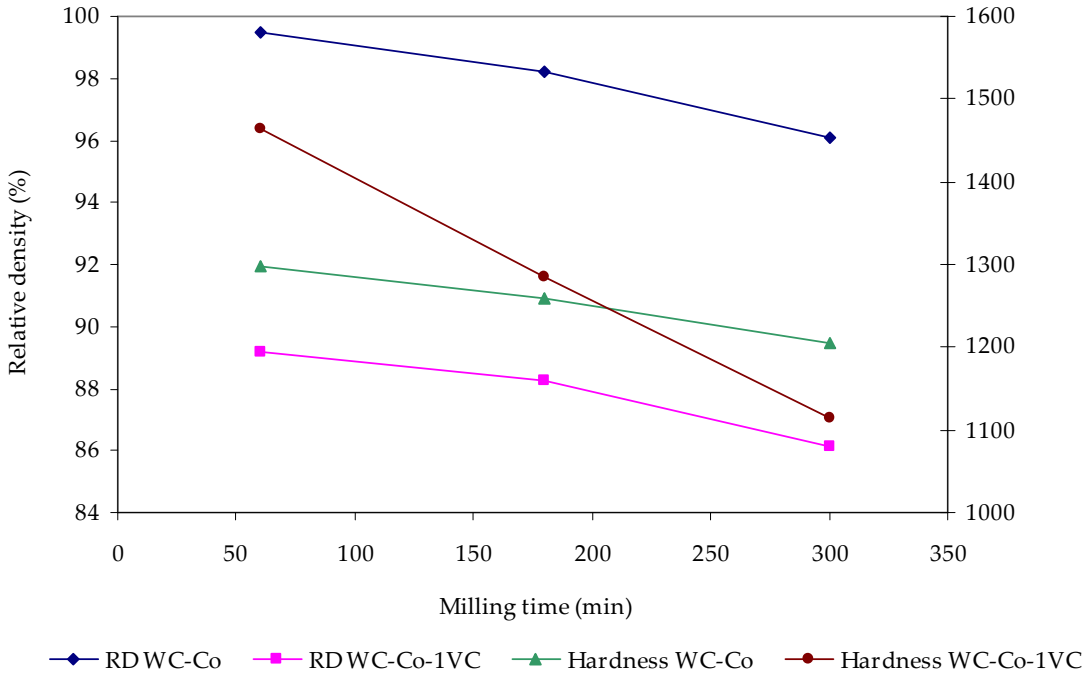

Fig. 5.79 Relative density and hardness of sinter-HIP'd WC10Co1VC, as a function of milling time.

Given the microstructures obtained from pressureless sintering then it seems reasonable to assume that the application of an external pressure has merely served to exaggerate the effects of the poorly distributed, partially deformed grain growth inhibitor. Residual porosity, as one would expect from the low density values, is > A08 for each material and is shown in Fig. 5.80 but is somehat improved when compared with the levels obtained from pressureless sintering, Fig. 5.76, with a reduced level of type B porosity (section 4.). The application of an external pressure during liquid phase sintering will aid pore collapse (Kingery, Woulbroun and Charvat 1963; Spriggs and Dutta 1974). The liquid cannot sustain a shear stress and therefore, it lubricates particle

sliding as induced by an external pressure. The difference in porosity levels between the two techniques could be due to pore stability and the increased levels of WC grain growth induced by the external pressure. According to the concept of pore stability, pores that cannot shrink during solid state sintering may satisfy their shrinkage condition with grain growth (Kang 2005) and it has also been proposed that abnormal grain growth could contribute to the shrinkage of large pores (Xue 1989). A pore which does not satisfy its shrinkage condition can shrink after abnormal grain growth. However, questions remain as to whether such a contribution is realistic. Nevertheless, given the SEM micrographs (Fig. 5.82), a link between pore stability and grain growth is a reasonable assumption.

The shortest milling time produced the optimum levels of hardness and density for the undoped material, as shown in Fig. 5.79. The effect of VC has been theorised on the basis of its solubility in the liquid Co phase during sintering and its effects on limiting the dissolution of W and C in liquid Co (Sadangi *et al*. 1999; Lay, Thibault and Hamar-Thibault 2003). During liquid phase sintering, solution-reprecipitation is one of the primary mechanisms of grain growth. Limiting the dissolution of W and C in the liquid phase will consequentially slow grain growth. The high hardness of the 60 min milled material suggests that WC grain size is at its smallest at this point, and subsequently increases as shown by the decreasing rate of hardness, although caution has to be applied to the hardness measurements due to the high levels of porosity and the possibility of the indentation partially 'collapsing' during loading. Furthermore, it is difficult to separate out hardness vs density vs grain growth relations.

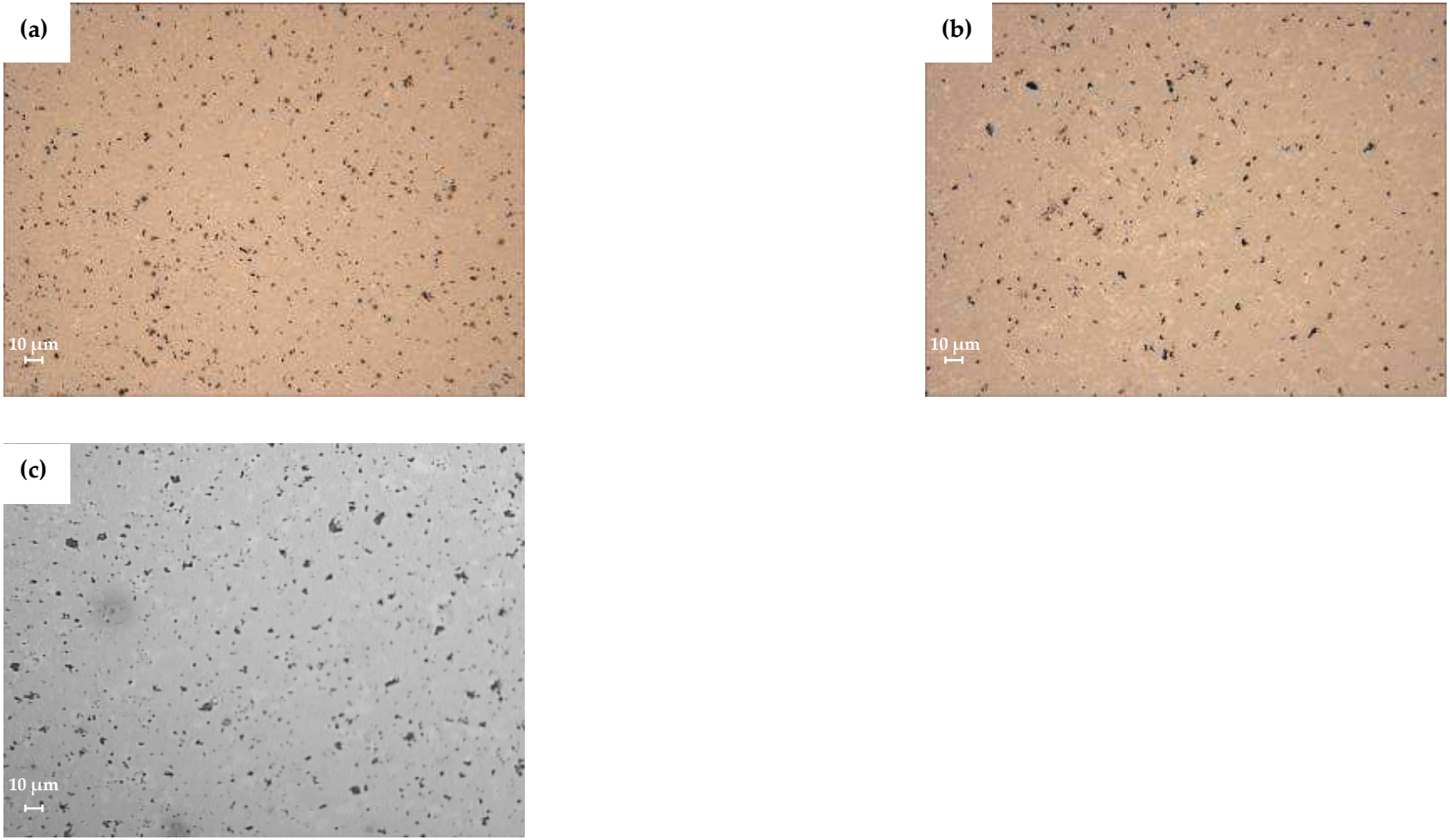

Fig. 5.80 Optical micrographs of WC-10Co-1VC sinter-HIP'd at 1390°C/60 min after (a) 60 min, (b) 180 min, and (c) 300 min.

Magnetic coercivity can provide a characterisation tool for indirectly checking WC grain size. The coercive force required to demagnetise a WC/Co hardmetal is primarily related to the Co/WC interphase area, because magnetic domain walls are pinned by these phase boundaries. The Co/WC interphase area is inversely related to the WC grain size. For smaller values of the latter, the interphase area increases and consequently so does the coercivity. However, in this study, a physical-based model of the relationship between coercivity and inverse grain size could not be established due to the influence of Fe that was picked up during extended ball milling (180 and 300 min). With this in mind, measurements of coercivity were used purely to show trends with increasing milling time, Fig. 5.81, where coercivity of the doped material is observed to follow the same trend of the undoped material from both sinter-HIP and pressureless sintering. Coercivity reaches 17.4 kA m^{-1} after 60 min milling for the doped material with hardness also at its highest. After further milling (180 min), both properties fall quite dramatically with coercivity falling to 7.3 kA m^{-1} and hardness to 1250 HV30, which suggests a significant increase in WC grain size. This is clearly shown by the SEM micrographs in Fig. 5.82. There is a substantial increase in grain size for the 180 min milled material with a number of very coarse grains, ~ 4 μm, present in the microstructure. As expected from the level of Fe pick up, Fig. 5.11, coercivity then shows an increase for the 300 min milled material, achieving 15 kA m^{-1} whilst hardness falls to 1203 HV30. However, the average WC grain size and distribution seems smaller and more uniform after 300 min milling, which may account for a proportion of the observed increase in coercivity. Once again, caution should be applied to the coercive force measurements, not only because of Fe

pick up but also from the level of porosity in the doped materials. The effects of porosity on coercive force include; (i) magnetization per unit volume decreases with increasing porosity; (ii) the pores can either increase or decrease the coercive force (it is determined by the relative shapes between the pores and the magnetic particle; (iii) unless the number of the pores is very small, there is a linear relationship between coercive force and porosity; (iv) the influence of number of pores on the coercive force is small; (v) coercivity is insensitive to the pore size variation (Chang and Shyu 1990).

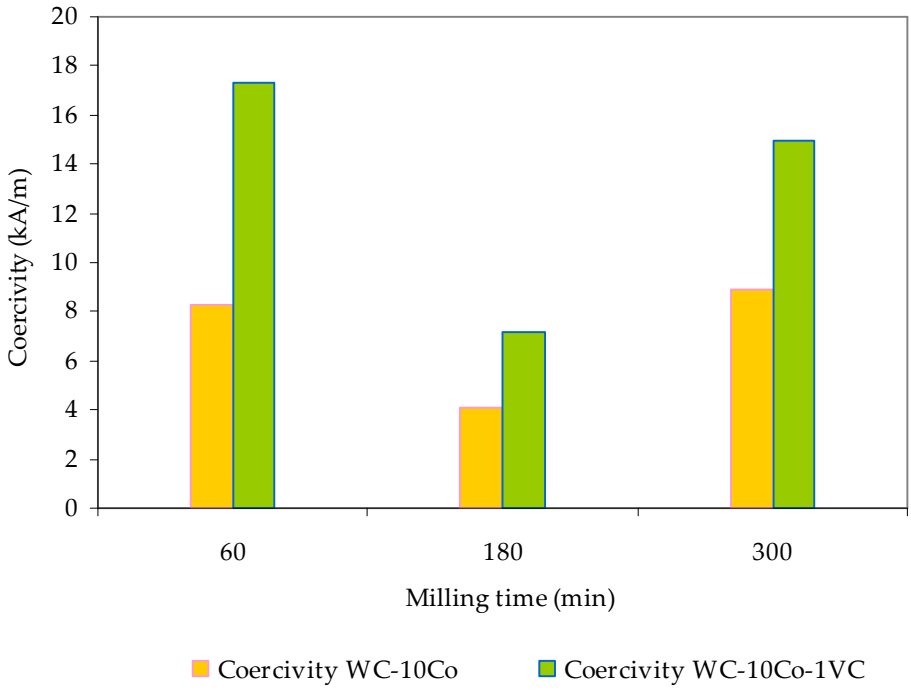

Fig. 5.81 Coercivity as a function of milling time for WC-10Co-1VC sinter-HIP'd at 1390°C/60 min.

EDX analysis of the highlighted area in Fig. 5.82 (f) also confirms a high Fe contamination level, Fig. 5.83. One way of minimising the contamination from the grinding medium and the vessel is to use the same material for the vessel and grinding medium as the powder being milled. Despite this, there will still be some wear and tear of the grinding medium, which will subsequently be incorporated into the powder. Thus, even though contamination from impurity elements will be minimised, the chemistry of the final powder will be different from the starting powder. This can be compensated for if one has knowledge of the extent of increase of the metallic content in the final powder. Given the prohibitively expensive cost of manufacturing a complete vessel from hardmetal, an alternative solution would involve the application of a hardmetal liner on the internal surface of the vessel.

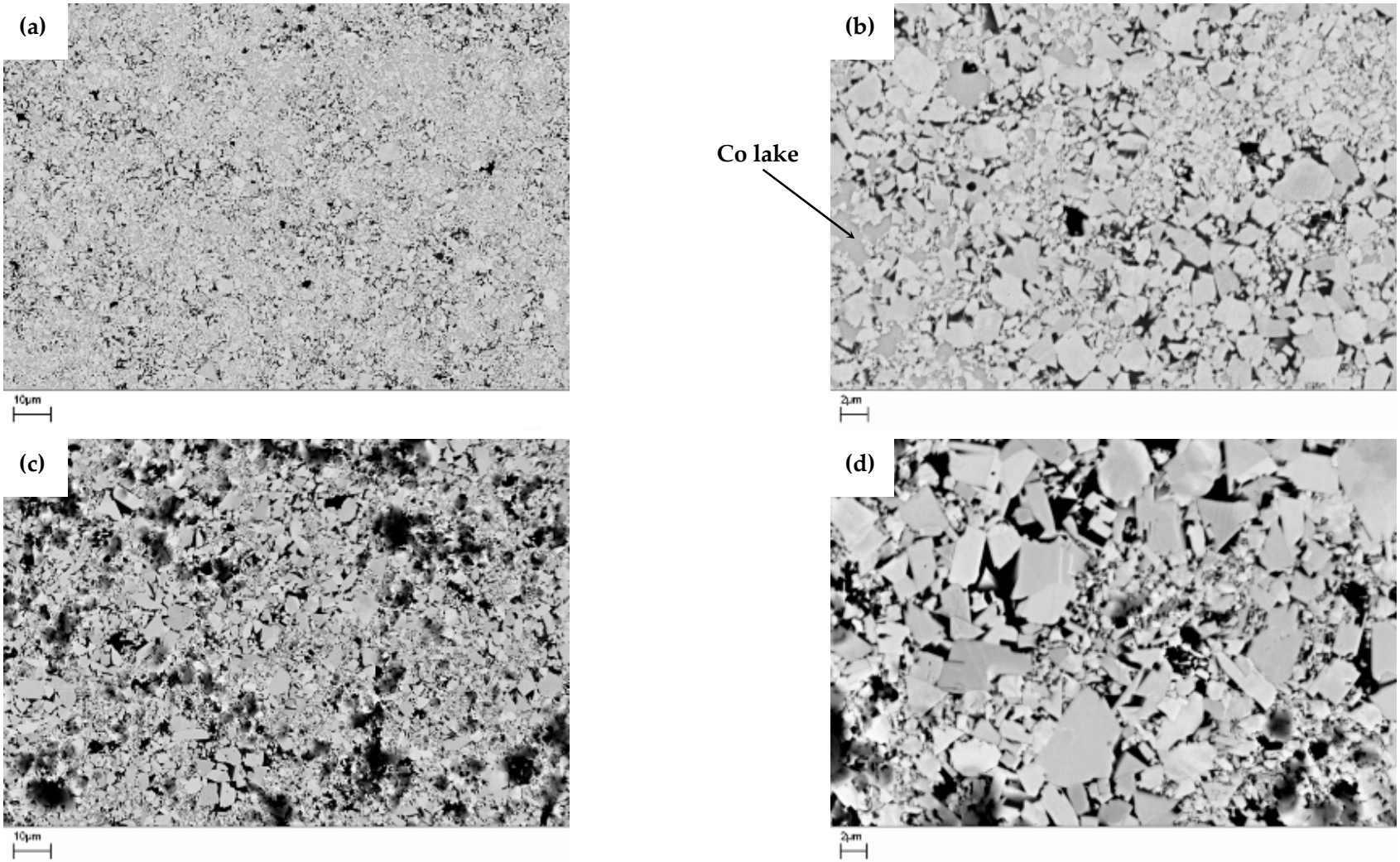

Fig. 5.82 SEM micrographs of WC-10Co-1VC sinter-HIP'd for ball milling times of (a, b) 60 min and (c, d) 180 min.

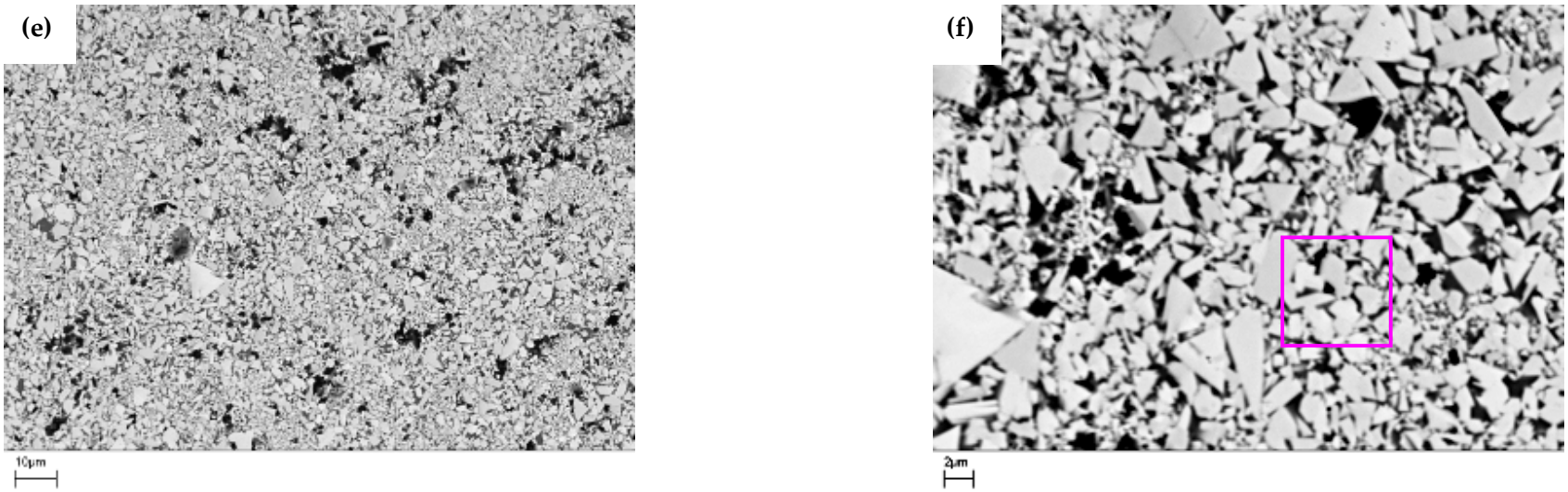

Fig. 5.82 cont'd SEM micrographs of WC-10Co-1VC sinter-HIP'd for ball milling times of (e, f) 300 min.

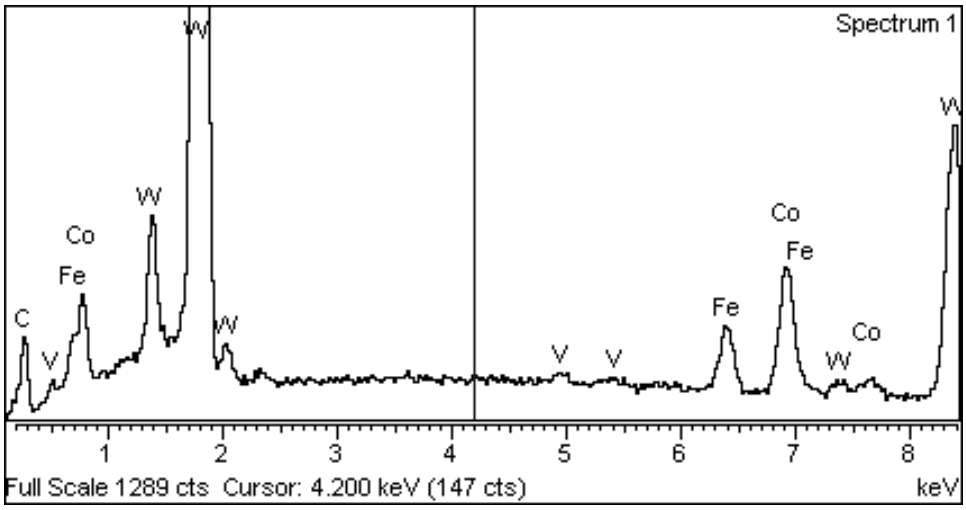

Fig. 5.83 EDX analysis of the highlighted area shown in Fig. 5.81 (f).

An EBSD band contrast map shows some of the remaining, precipitated VC phase (blue colour), Fig. 5.84, with IPF colouring according to Fig. 5.45. VC is added to WC-Co in very small amounts, typically, no more than 1 wt%. This small amount is thought to fully dissolve in the binder during sintering, but it has been found that during cooling, VC precipitates as nanoparticles of (V,W)C (Egami, Ehira and Macida 1993). The diffusion of WC into the Co binder phase is controlled by the VC content. VC also has to be dissolved into the binder phase then precipitated at the WC/Co grain boundaries (Arenas *et al*. 1999; Chabretou, Allibert and Missiaen 2003). Average WC grain size of the 300 min milled material was determined by measuring ~ 1250 grains using EBSD and found to be 0.53 μm, which compares favourably with the average grain size of 0.74 μm for the undoped material, Fig. 5.44. Grain size distribution, Fig. 5.85, shows a wider

distribution with a number of grains > 4 μm, which is consistent with the SEM micrographs shown in Fig. 5.82. Although there is evidence of discontinuous grain growth, the effectiveness of adding VC to suppress WC grain growth is clearly visible. The mechanism of grain size reduction in VC-doped WC-Co is thought to be related to the segregation of VC at the WC/Co or WC/WC interfaces (Taniuchi, Okada and Tanase 1997).

(a)

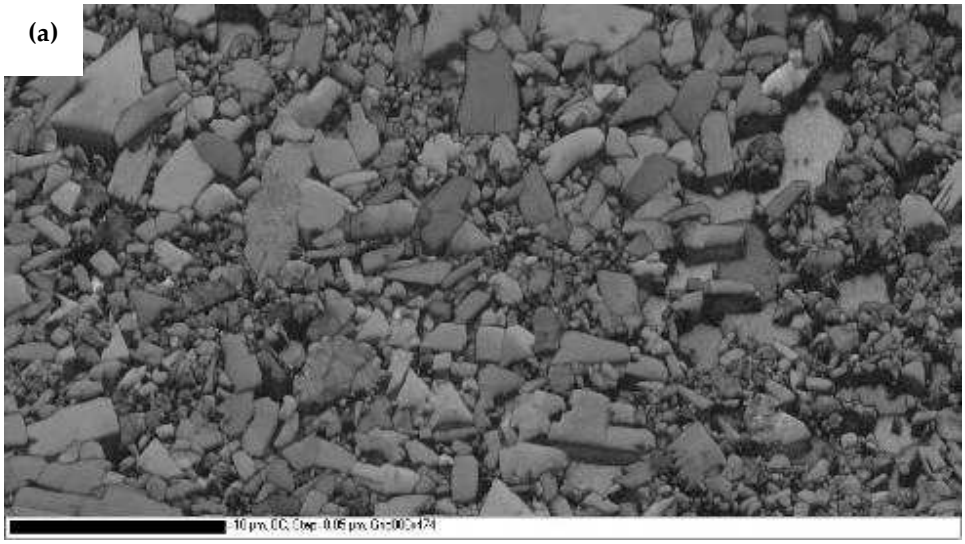

(b)

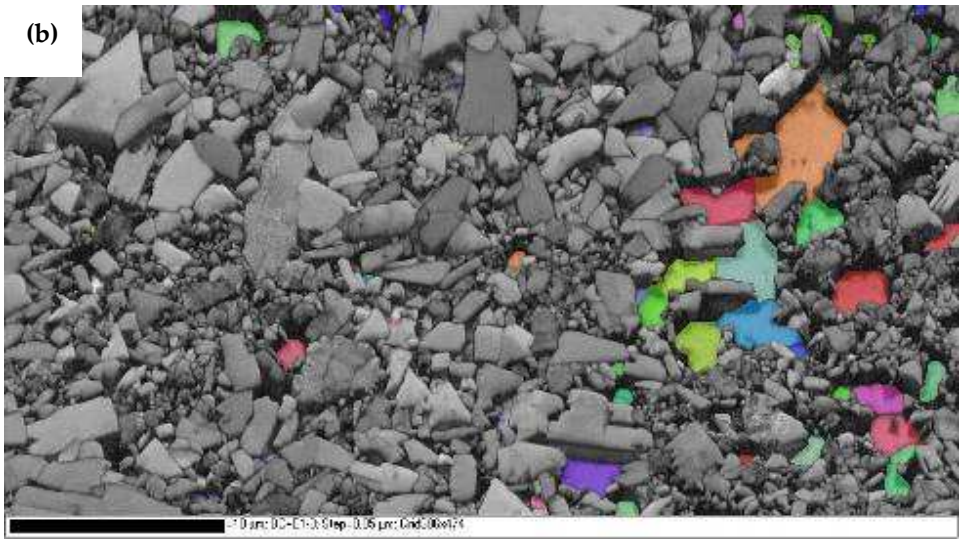

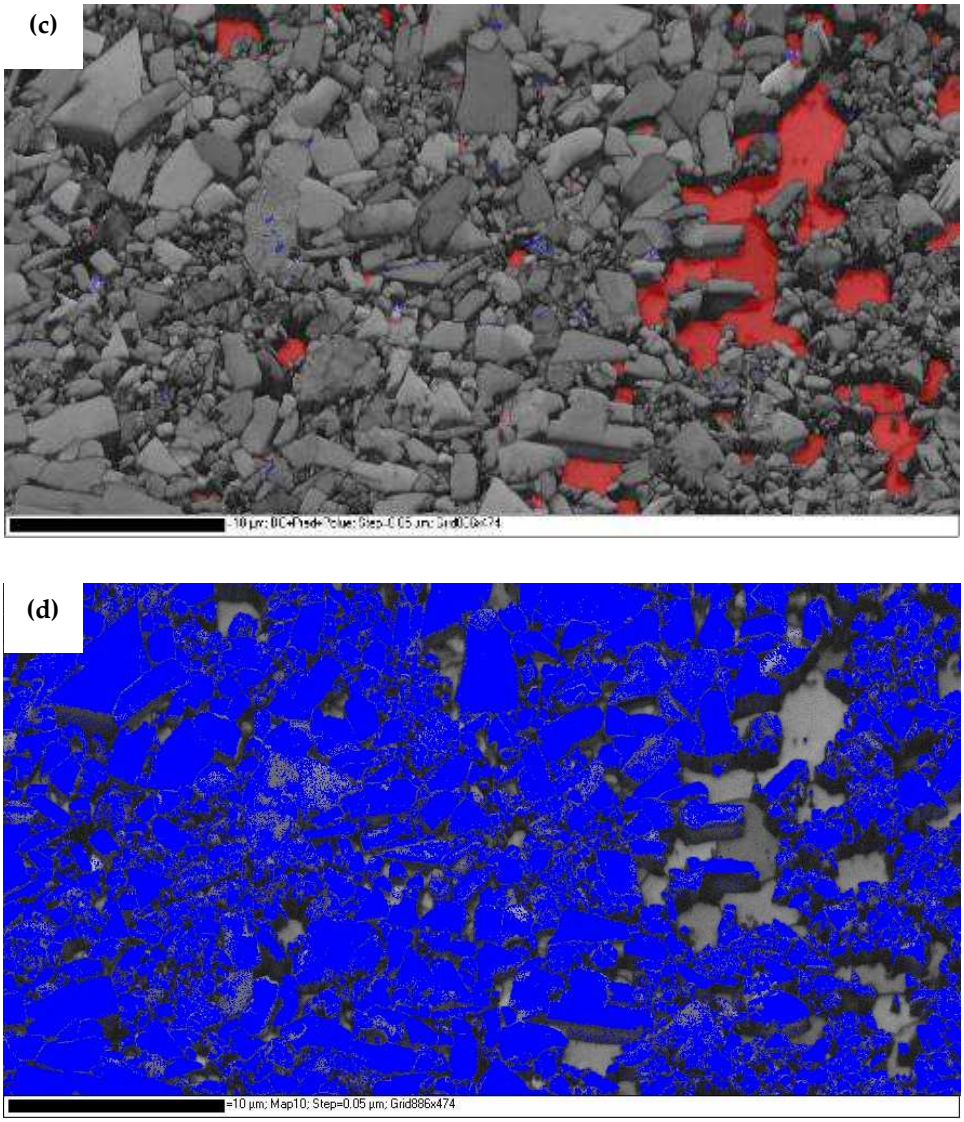

Fig. 5.84 EBSD maps of 300 min milled WC-10Co-1VC after sinter-HIP, showing (a) diffraction pattern quality map after noise reduction; (b) IPF pattern quality map of the Co phase; (c) pattern quality map of cubic-Co (red) and VC (blue); (d) band contrast map of WC phase (blue).

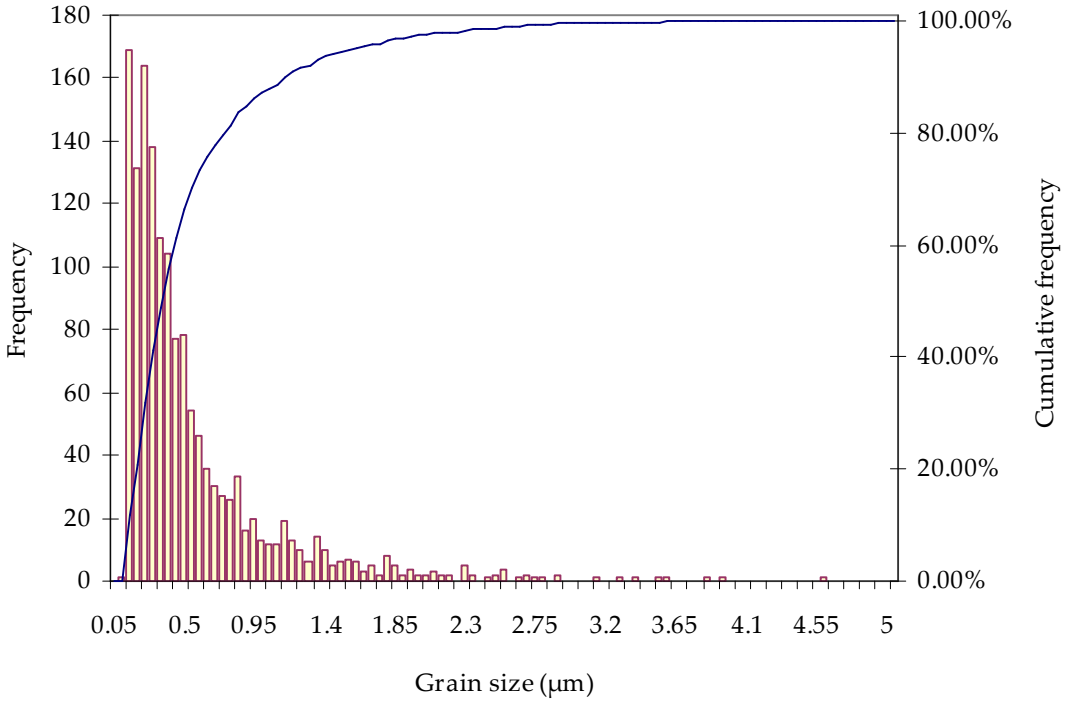

Fig. 5.85 WC grain size distribution from EBSD for WC-10Co-1VC, ball milled for 300 min and sinter-HIP'd at 1390°C for 60 min.

5.4.5 Effect of inhibitor and milling time on mechanical properties

The fracture toughness behaviour for both the doped and undoped materials after pressureless sintering are shown in Fig. 5.86 and Table 5.14, with Fig. 5.86 (b) showing the results after sinter-HIP. When V segregates on the WC/Co or WC/WC interfaces, the solid/liquid interfacial energy is decreased, and the process of smaller WC grains dissolving due to their higher dissolution potential and re-precipitating after diffusion through the binder on coarser WC grains is greatly reduced along with the coarsening of WC grains. The lower the interfacial energy, the finer the WC grain size and therefore,

the higher the hardness. The highest hardness is achieved for the 60 min milled material as it exhibits the most uniform and finest microstructure of the three milled, doped variants, with hardness decreasing with increasing milling time. Fracture toughness of the doped, pressureless sintered samples follows the generally observed trend of WC-Co materials (Fig. 5.54), increasing with decreasing hardness, compared to the inconsistent behaviour of the undoped, pressureless materials. However, the behaviour indicated in Fig. 5.86 (a) and (b) should be viewed with caution given the levels of residual porosity, as crack propagation may have been prematurely arrested by pores. The maximum hardness achieved is considerably lower than other, similar reported work where, for a similar WC grain size (2-4 μm), VC and binder content, ~ 1700 (HV30) was attained (Ngernbamrung *et al*. 2008). Upon first inspection, fracture toughness appears to compare well with the figures stated in other reported work (Ngernbamrung *et al*. 2008) of ~ 11 $MN.m^{-3/2}$, but it should be noted that this figure was achieved with a much higher hardness. It seems reasonable to assume that the fracture toughness/hardness relationship (Fig. 5.50) for WC-Co materials would be similar for VC-doped WC-Co, as the parameter controlling crack resistance is the binder mean free path (Luyckx and Allli 2001). Therefore, with the respective hardness values achieved in this study the expected fracture toughness would be ~ 14-15 $MN.m^{-1/5}$. The large difference in toughness may be due to the amount of inhibitor used in this study as ultra-fine grained WC-Co cemented carbides (<0.5 μm) require a VC/Co weight ratio of 5 wt% for optimal properties (Upadhyaya 1996). Moreover, it is reported that a VC/Co ratio >10% leads to embrittlement due to (V,W)C precipitation at the WC-Co interface (Schubert, Bock and

Lux 1993) and in typical metal cutting grades containing less than 10% Co, a higher level of VC (> 0.6%) results in a drastic reduction in the toughness (Upadhyaya, Sarathy and Wagner 2001). A comparison of the results calculated from the two equations for determining fracture toughness, Table 5.14, shows considerable difference with the results from the Anstis et al. equation significantly higher than those from the Shetty et al. equation. Interestingly, the difference is reduced for the highest hardness (60 min milling, sinter-HIP), which suggests that each equation gives a better correlation for a certain hardness range.

(a)

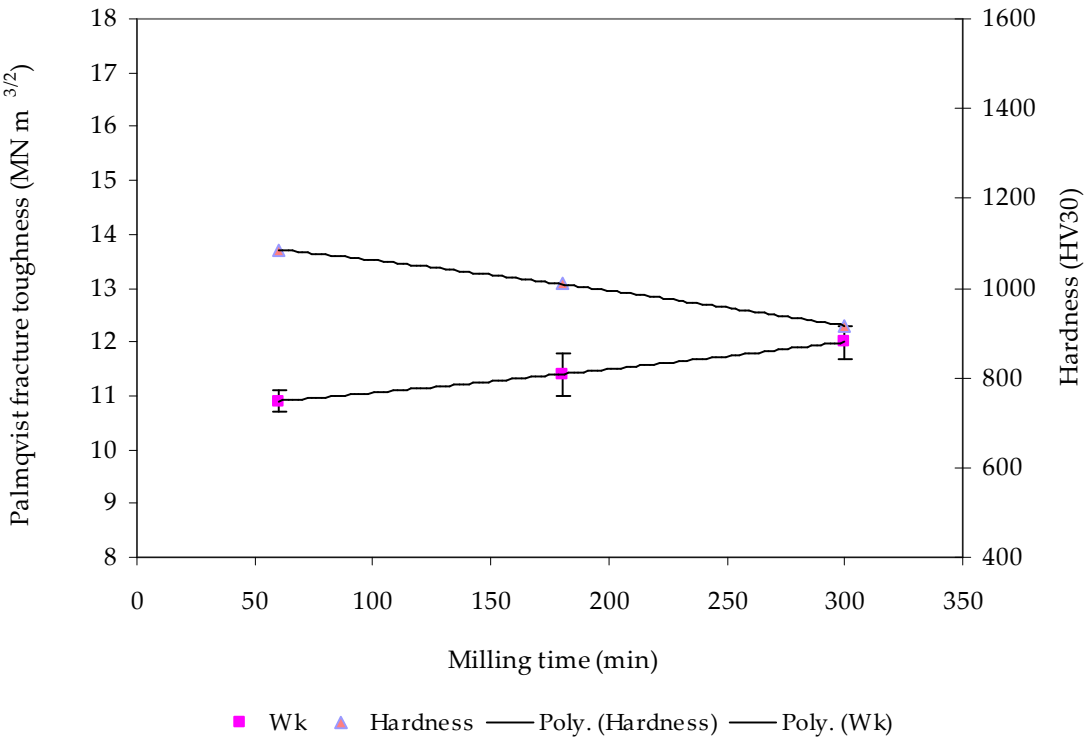

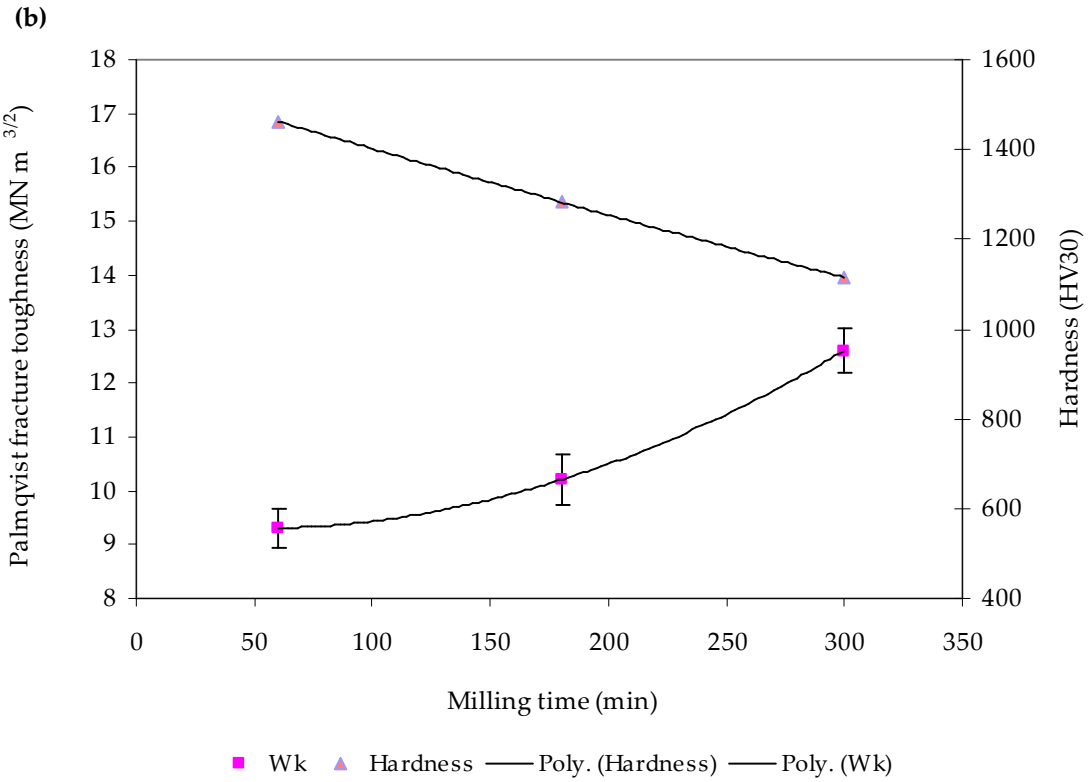

Fig. 5.86 Effect of inhibitor and ball milling time on the hardness and fracture toughness of WC-10Co-1VC after (a) pressureless sintering and (b) sinter-HIP.

Table 5.14

Fracture toughness results of WC-10Co-1VC material after pressureless sintering and sinter-HIP at 1390°C/60 min.

	Sinter-HIP	S.D.	Sinter-HIP	P'less	S.D.	P'less
Milling time (min)	W_K (MN. $m^{-3/2}$)		K_{IC} (Anstis) (MN. $m^{-3/2}$)	W_K (MN. $m^{-3/2}$)		K_{IC} (Anstis) (MN. $m^{-3/2}$)
60	9.3	± 0.32	11.2	10.9	± 0.19	16.4
180	10.2	± 0.48	13.9	11.4	± 0.37	18.0
300	12.6	± 0.42	18.4	12.0	± 0.31	18.8

The lower W_K values of the doped material suggest that the material possesses a poor, intrinsic resistance to crack propagation inevitably caused by the high volume fraction of porosity, which is confirmed by the transverse rupture strength (TRS) results, Fig. 5.87 and Table 5.15. The material reaches a maximum TRS of 1300 MPa, which is considerably lower than a TRS of 3780 MPa reported in similar work (Shi *et al*. 2006). For comparison purposes, results from both sintering techniques have been plotted to highlight the combination of VC doping and sintering process. The general trend exhibited by the materials is fairly representative of the microstructural aspects of each material and process with the sinter-HIP processed materials performing better than those from pressureless sintering due to their improved homogeneity and therefore, a reduced number of flaws. During pressureless sintering, residual macropores can result from irregularities in the initial particle arrangement or from void formation due to differential sintering in the vicinity of undestroyed agglomerates of fine powders (Kaysser *et al*. 1988). Both sets of results from the two techniques are affected by the inhomogenous green compacts, which could have been improved by incorporating a spray drying or granulating technique to improve the flow and compaction of the milled powders. Interestingly, the effect of milling time is less exaggerated for the doped materials. There is a significant amount of scatter with the TRS results, which is primarily due to the size and distribution of flaws caused by inadequate green pressing.

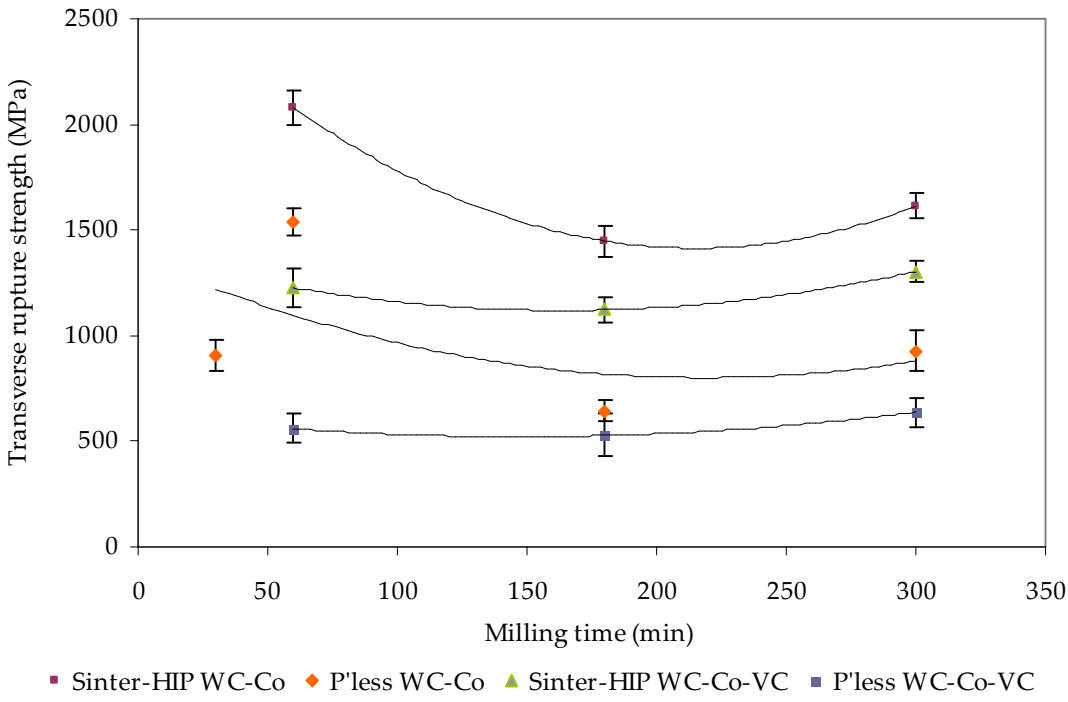

Fig. 5.87 Effect of inhibitor and ball milling time on the transverse rupture strength of WC-10Co-1VC for both pressureless and sinter-HIP. Data fitted with 2nd order polynomials.

Table 5.15

Transverse rupture strength of WC-10Co-1VC after pressureless sintering and sinter-HIP.

Milling time (min)	TRS – pressureless (MPa)	S.D.	TRS – sinter-HIP (MPa)	S.D.
60	560.1	± 77	1226.3	± 121
180	527.89	± 118	1122.8	± 58
300	637.79	± 68	1304.3	± 52

S.D. – standard deviation

5.5 Consolidation of milled WC-10Co powder using spark plasma sintering (SPS)

The SPS technique is a relatively new sintering technique that allows the preparation of fully dense materials at lower sintering temperatures and shorter holding times (min) than the extended holding times (hours) and temperatures normally used in conventional sintering. SPS provides significant advantages to the processing of materials into configurations previously unattainable. SPS consists, essentially, of a combination of high temperature, high axial pressure, and low-mode (low voltage, high current) field (plasma) assisted sintering (Munir, Anselmi-Tamburini and Ohyanagi 2006). The field component is associated with electric current passed through a powder specimen. The electric field generates Joule heat, which provides the conditions of hot compaction; the current also enhances densification and can improve the final grain

structure in quite a remarkable way. This approach significantly shortens processing and enhances the performance time and quality wise. In particular, it carries the potential of maintaining the nano-features in nanopowder-based materials after consolidation (Munir, Anselmi-Tamburini and Ohyanagi 2006; Nishimura *et al*. 1995; Nygren and Shen 2003).

Based on the results from pressureless and sinter-HIP processing, two mechanically alloyed powders, namely 60 min RT and 60 min -30°C, were chosen for the majority of the SPS experiments. The 300 min milled powder was also processed for the first set of SPS conditions, Table 5.16, in order to establish the effect of milling time. Shrinkage rate of the 300 min milled powder, sintered for 10 min at 1100°C under an applied pressure of 50 MPa, is shown in Fig. 5.88. The powder starts to densify around 800°C with maximum shrinkage at ~ 1000°C. For comparison purposes, the shrinkage behaviour of the 60 min RT and -30°C milled powders, sintered using the same parameters, is also shown. It should be noted that these two powders were held under an axial pressure of 100 MPa. The low temperature milled powder starts to densify around 980°C whereas the onset of densification is at 1005°C for the RT milled powder. This suggests that milling at -30°C has enhanced the densification kinetics for WC-10Co nanostructured powder. The low temperature milled powder exhibits slightly higher shrinkage compared to the RT milled powder but both are considerably below the maximum shrinkage shown by the 300 min milled powder. Maximum shrinkage rate is attained before the isothermal hold temperature. The total shrinkage exhibited by the three nanostructured powders appears significantly higher compared to similar SPS studies

(Cha *et al*. 2003; Huang *et al*. 2008), which may be due to the cold worked particle structure and their low green densities observed at 50 and 100 MPa compaction pressures, Fig. 5.12. For compacts with less than 60% theoretical density, percent shrinkage is high (Lardner, Spriggs and Wood 1972). Relative density of the 300 min milled material after sintering follows the same trend as that observed during pressureless and sinter-HIP, exhibiting a value of 85.6 %, whilst the RT and -30°C materials reached 94.3% and 94.7%, respectively. Residual porosity of the three samples is shown in the optical micrographs, Fig. 5.89 with Fig. 5.90 showing the microstructures of the three sintered materials.

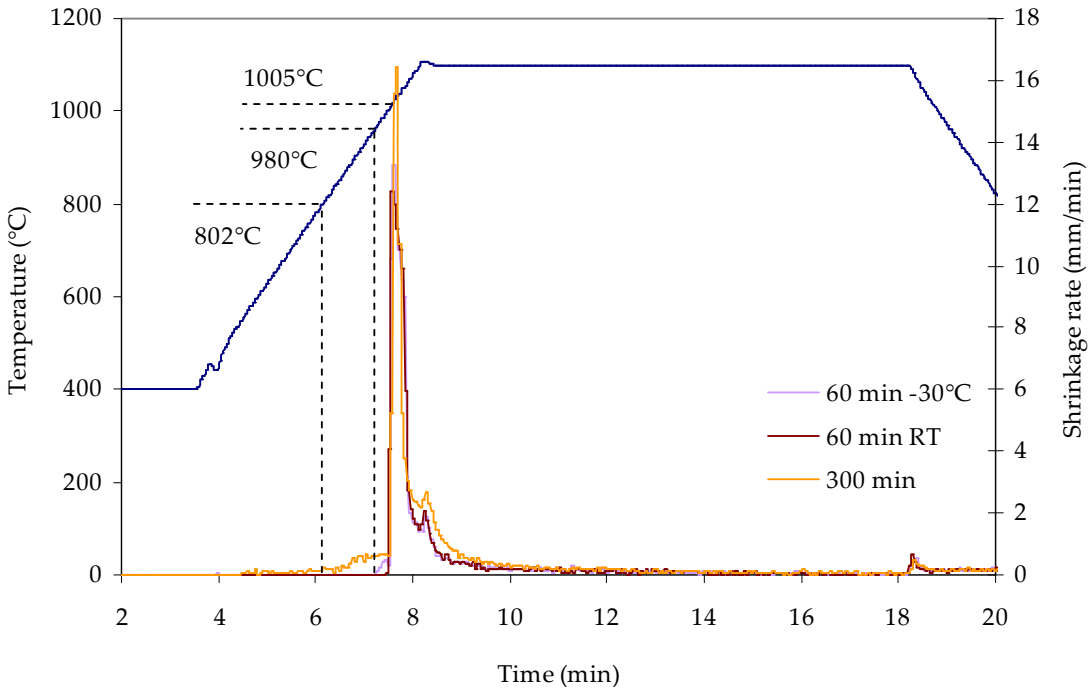

Fig. 5.88 Shrinkage behaviour of the ball milled WC-10Co powders during SPS for 10 min at 1100°C.

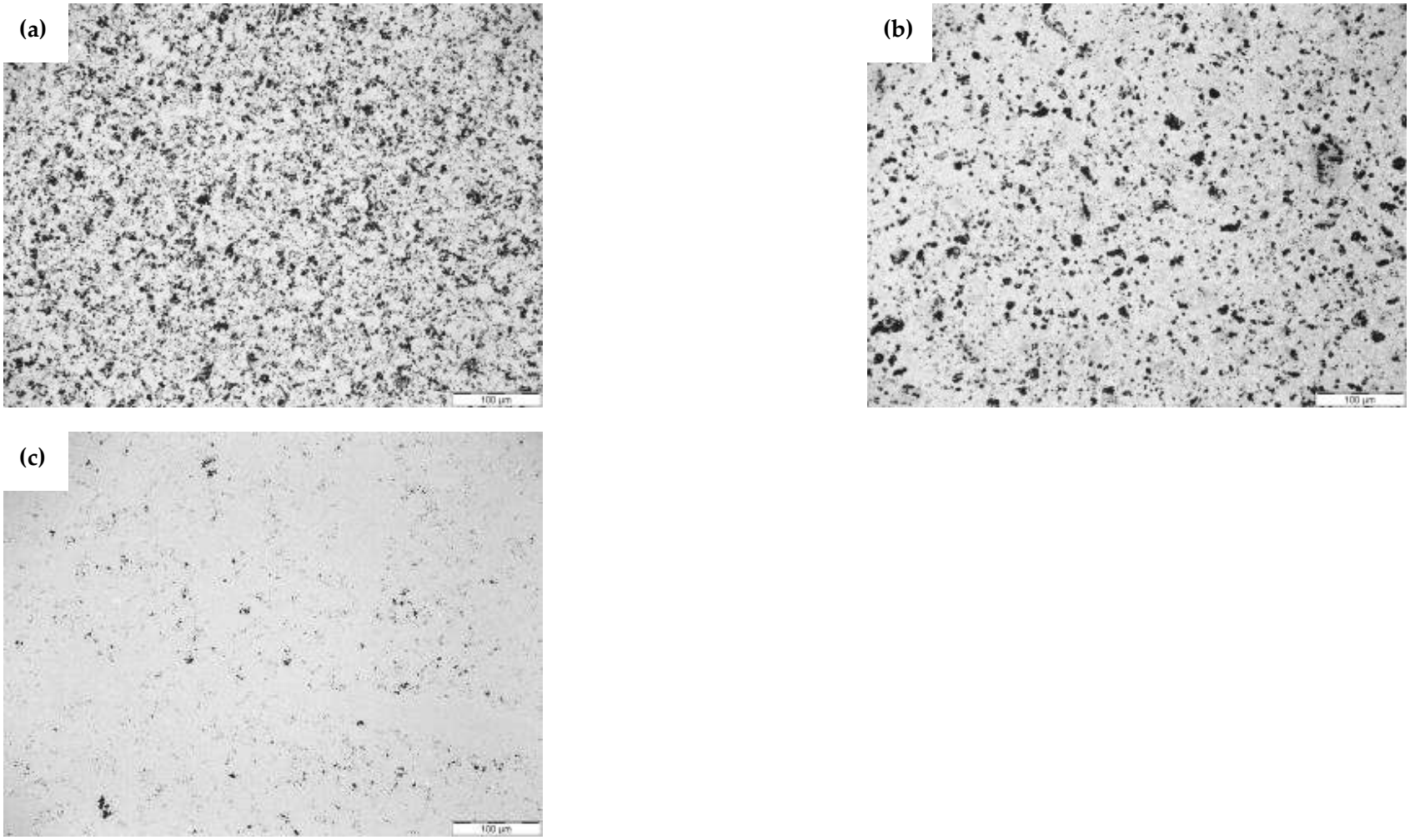

Fig. 5.89 Optical micrographs of (a) 300 min, (b) 60 min RT, and (c) 60 min -30°C milling of WC-10Co after SPS for 10 min at 1100°C.

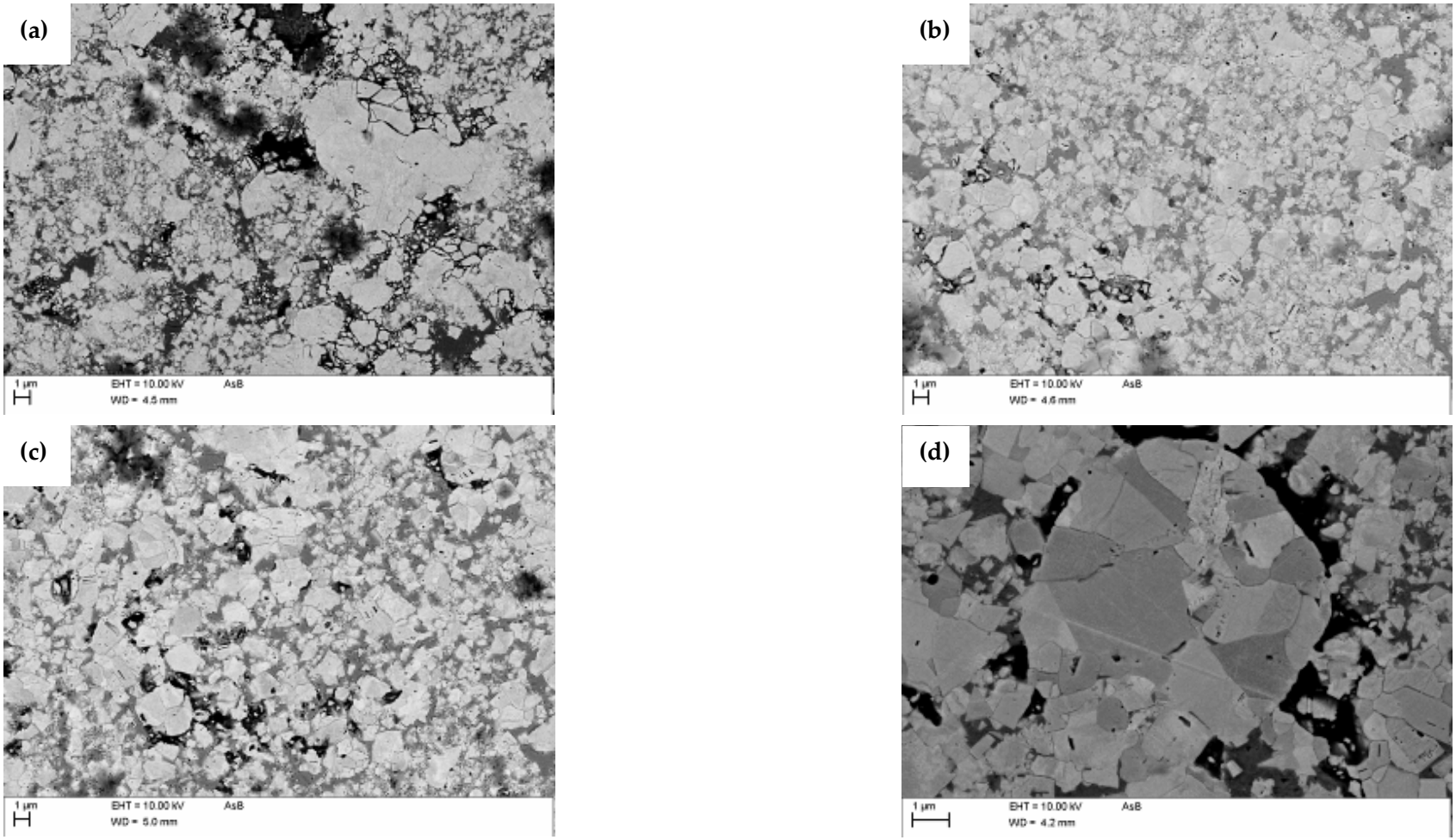

Fig. 5.90 SEM micrographs of (a) 300 min with 50 MPa axial pressure, (b) 60 min RT, (c) and (d) 60 min -30°C milling with 100 MPa axial pressure after SPS for 10 min at 1100°C.

Both 60 min milled materials exhibit similar structures with wide, WC grain size distributions with a number of WC grains ~ 2-3 μm. Considerable WC grain growth appears to have taken place, even though the sintering temperature was significantly below the onset of liquidus, which is substantially lower than the LPS sintering techniques. It is evident that the WC grains have changed from an equi-axed to a facetted, platelet shape after SPS for 10 min at 1100°C. The 300 min milled material, Fig. 5.89 (a), shows a non-uniform distribution of Co along with areas of nano-sized (< 0.2 μm) and coarse (2.5-6.0 μm) WC grains. An interesting phenomenon observed with the low temperature milled SPS material is shown in Fig. 5.89 (d). The microstructure shows a number of particles containing much coarser grains than the majority of the sample with the actual particle itself retaining a degree of residual sphericity from milling (Fig. 5.17), which suggests that the particle was only modestly deformed during SPS. This suggests that reduced deformation of the particles led to formation of the coarse grains.

A major part of grain coarsening and facetting of WC grains proceeds during solid-state sintering prior to the formation of a liquid (Haglund 1998; Petersson 2004; Allibert 2001; Gille, Leitner and Roebuck 1996). WC solid solubility in Co is known to become significant from 1100°C (Allibert 1999) with WC dissolution beginning at about 800°C (Haglund and Agren 1998). Solid-state shrinkage occurs due to Co spreading onto WC particles and rearrangement of the particles as they dissolve in the binder, thereby becoming facetted (Haglund, Agren and Uhrenius 1998; Roure 1996; Agren *et al*. 1996; Missiaen and Roure 1998; Schubert, Bock and Lux 1999). Co spreading occurs from 1100°C (Haglund, Agren and Uhrenius 1998) but readily contributes to the early stage of

densification for very fine powders (Schubert, Bock and Lux 1999). Recent theoretical approaches (Agren *et al*. 1996; Missiaen and Roure 1998) propose creep of the Co binder as the local process driving solid state rearrangement. However, the above mentioned, more conventional characteristics are somewhat different to the densification mechanism of WC-Co powders in the early stages of the SPS process. It was shown that at ~ 800°C, morphological changes occur in the powder where the sintering necks form, and local melting at the surface of particles is observed (Liu *et al*. 2008). At ~ 1000°C, more melting features are found at the surfaces of particles. With a further increase in the sintering temperature, ~ 1200°C, near TD is approached. As the sintering temperatures are much lower than the melting temperature of Co (1495°C), melting of the Co film surrounding the WC particles indicates that an extraordinarily high temperature is generated at the particle surface, which is higher than the melting point of Co. Accordingly, an inhomogeneous temperature distribution should exist in the WC-Co composite particles at the stage of neck formation.

Hardness and fracture toughness (W_K) values for the three materials after SPS at 1100°C for 10 min are given in Table 5.16. Although relative densities for the 60 min RT and -30°C materials are below those achieved from pressureless and sinter-HIP, hardness values are higher at 1433 and 1478 HV30, respectively. The given increase in hardness is not matched by a similar decrease in W_K, as the RT and -30°C materials achieved 9.2 and 10.1 $MN.m^{3/2}$, respectively. Coercive force measurements, Fig.'s 5.59 and 5.65, indicate that the higher hardness achieved by the low temperature milled powder was achieved by grain size refinement. The hardness value obtained for the -

30°C milled material is comparable with other reported work of ~ 1500 HV30 (Cha, Hong and Kim 2003) but the RT milled material has not performed as well. W_K values are higher than those reported in the literature for SPS WC-10Co (Cha, Hong and Kim 2003). Based on these initial findings, the -30°C milled material was used for the remaining SPS experiments.

In order to try and improve densification, the sintering temperature was increased to 1150°C with the isothermal hold time reduced to 5 min to try and minimize WC grain growth. Shrinkage behaviour of the material is shown in Fig. 5.91 with the SEM micrographs shown in Fig. 5.92. The change in temperature caused a slight decrease in densification, falling from 13.73 to 13.64 g cm^{-3}. Macro-pores are also visible in the microstructure. More surprisingly is the effect on the hardness level, which increased from 1478 to 1541 HV30 despite a decrease in coercive force. The increased temperature may have provided additional strengthening to the WC skeletal structure, which, in turn, provided strengthening to the matrix and decreased the dislocation motion during deformation.

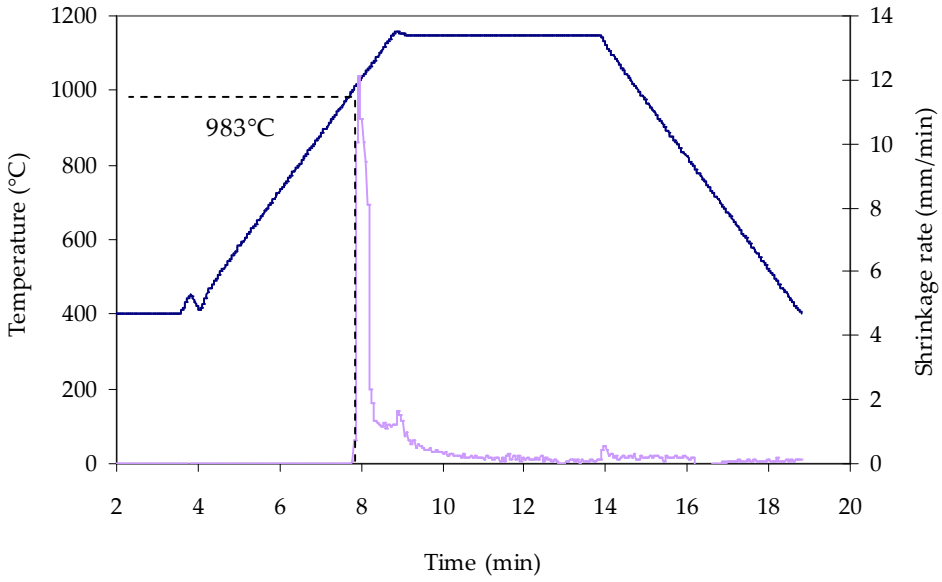

Fig. 5.91 Shrinkage behaviour of the -30°C ball milled WC-10Co powder during SPS for 5 min at 1150°C under 100 MPa pressure.

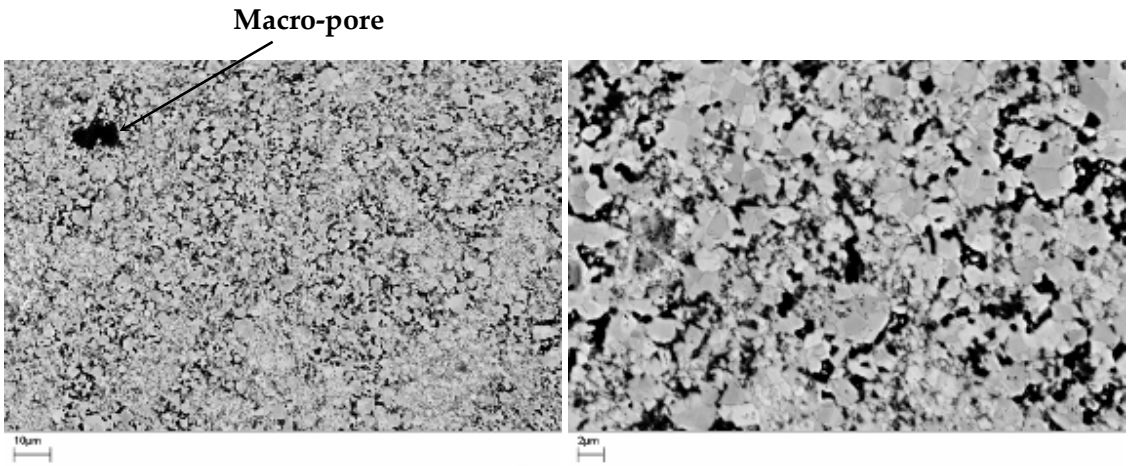

Fig. 5.92 SEM micrographs of -30°C ball milled WC-10Co after SPS for 10 min at 1150°C under 100 MPa pressure.

Sintering temperature was increased to 1200°C in order to maximise densification but minimise grain growth with an isothermal hold time of 3 min. Heating rate was doubled from 150°C min^{-1} to 300°C min^{-1} and cooling rate was reduced to 100°C min^{-1} to prevent any cracking due to the mismatch of thermal expansion coefficients of WC and Co. The shrinkage behaviour of the powder is shown in Fig. 5.93, and the SEM micrographs are shown in Fig. 5.94. Doubling the heat up rate has reduced the total amount of shrinkage from ~ 12 mm to ~ 8 mm. Although the microstructure suggests an increased level of densification over the sample sintered at 1150°C, the density measurement does not support this and, in fact, shows a small decrease. Coercive force suggests an increase in WC grain size but the hardness result does not follow the typical Hall-Petch relationship between hardness and grain size, as hardness increased from 1541 to 1557 HV30. Densification rate of WC-Co during SPS is thought to depend on the average heating rate rather than on the temperature history (Gillia and Bouvard 2000). Spark-plasma sintering results in extremely high heating rates, which enable powder systems' higher sinterability and cause highly non-uniform local and effective temperature distributions. These distributions impact vacancy concentrations (providing conditions for thermal diffusion), cause local melting within interparticle contact areas, and create thermal stresses, which stimulate dislocation creep. These phenomena instigate, in turn, accelerated diffusion and densification rates during spark-plasma sintering. The second group is related to the direct impact of an electromagnetic field on the diffusion mass transport through electromigration, ponderomotive forces, electroplasticity mechanisms, "pinch" effect, and dielectric breakdown of oxide films

(cleansing effect) including defect generation at grain boundaries (Olevsky, Kandukuri and Froyen 2007).

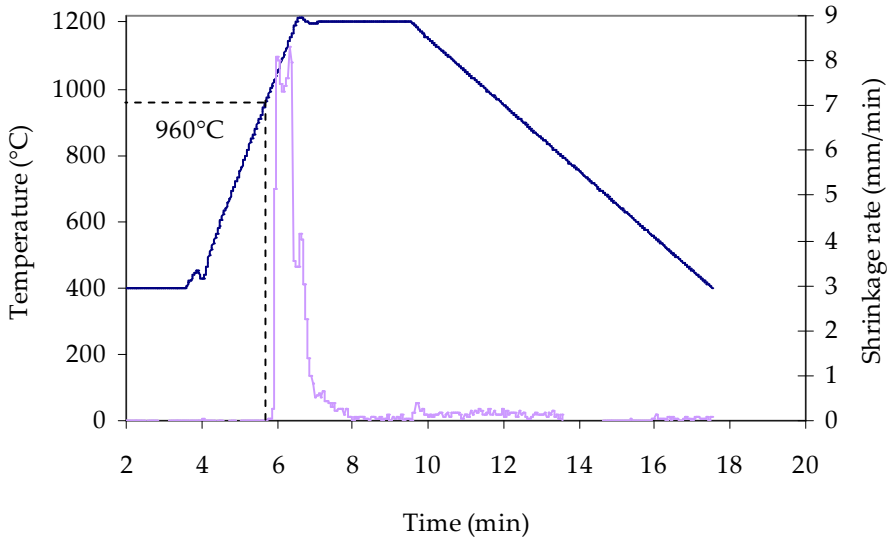

Fig. 5.93 Shrinkage behaviour of the -30°C ball milled WC-10Co powder during SPS for 3 min at 1200°C under 100 MPa pressure.

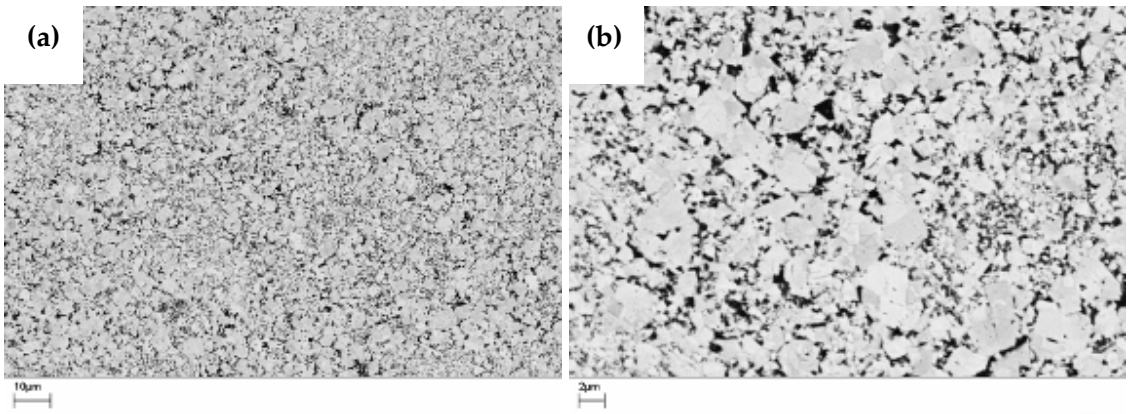

Fig. 5.94 SEM micrographs of -30°C ball milled WC-10Co after SPS for 3 min at 1200°C under 100 MPa pressure.

Table 5.16

Mechanical properties of WC-10Co ball milled materials after SPS.

Powder prep.	SPS parameters	Density ($g\ cm^{-3}$)	TD (%)	Hardness HV30	Coercivity (kA^{-1})	W_K ($MN.m^{3/2}$)	Ref.
MA 300 min	1100°C/10min/50 MPa	12.41	85.6	804	23.2	-	This work
MA 60 min	1100°C/10min/100 MPa	13.67	94.3	1433	9.1	9.2	This work
MA -30°C 60 min	1100°C/10min/100 MPa	13.73	94.7	1478	15.1	10.1	This work
MA -30°C 60 min	1150°C/5min/100 MPa	13.64	94.1	1541	14.8	10.7	This work
MA -30°C 60 min	1200°C/3min/100 MPa	13.63	94.0	1557	14.0	11.3	This work
MA 1440 min	1100°C/10min/100 MPa	14.21	98.0	1500	-	11.0	(Cha *et al.* 2003)

5.6 Summary of the discussion

The work undertaken in this study concerns the synthesis of nanostructured hardmetal (WC-10wt%Co) powders by ball milling at room temperature and low temperature, and the consolidation of said powders. From an industrial standpoint, ball milling is the commonly applied comminution method in the hardmetals industry. This operation is carried out mainly to blend the carbides with the auxiliary binder metal. The mechanical properties and the elimination of porosity from the sintered products are largely associated with the uniformity of cobalt distribution. This can be assured only when the ball milled admixture is uniform. The prime objective of ball milling, apart from particle size reduction, is to ensure that every carbide particle is coated with cobalt. In addition, it creates new active surfaces and an increased defect structure of both carbides and metal binder. It is important to understand the effect of a change in ball milling parameters on the sintered microstructure and properties of the bulk material, if the use of nano-scale powders is to become more than just consigned to niche markets.

5.6.1 Ball milling time

The influence of a change in ball milling time and the interrelation between particle size and melting temperature has been obtained for WC-10Co alloys, with and without grain

growth inhibitor. VC grain growth inhibitor, and ball milling times ranging from 30 min to 300 min were evaluated.

A balance in the mechanisms of MA appeared to be reached after 60 min high-energy ball milling using variable rotation rates and repetitious circulation. No microstructural or mechanical property-related advantage was found by extending the MA time beyond 60 min for either the VC-doped or undoped alloys. X-ray analysis showed that the average WC domain size was reduced to 21 nm after 60 min milling and 27 nm after 300 min milling with negligible levels of WC mean square strain. Although extending the milling time beyond 60 min did lead to a reduction in the mean particle size, this only served to reduce green density levels to 61.9% at 400 MPa pressure for the 300 min milled powder compared to 64% for the 60 min milled powder. There is difficulty in compacting fine, irregular powders because of large, interparticle frictional forces. Green density increased linearly with compaction pressure for the range 100-400 MPa for each milling time, Fig. 5.95. Green density levels for the VC-doped powders were lower than the undoped powders, decreasing to ~ 57% after 300 min milling. A reduction in particle size through extended milling time did lower the onset temperature of the WC-Co eutectic reaction from 1344°C for 60 min milling to 1312°C for 300 min milling, Fig. 5.96. A further reduction was observed for the VC-doped alloys, lowering the onset temperature from 1306°C for 60 min milling to 1283°C for 300 min milling. Extended milling time also increased the level of powder contamination from the milling media, with Fe pick-up increasing from 0.25 wt% for 30 min milling to 2.75 wt% for 300 min milling.

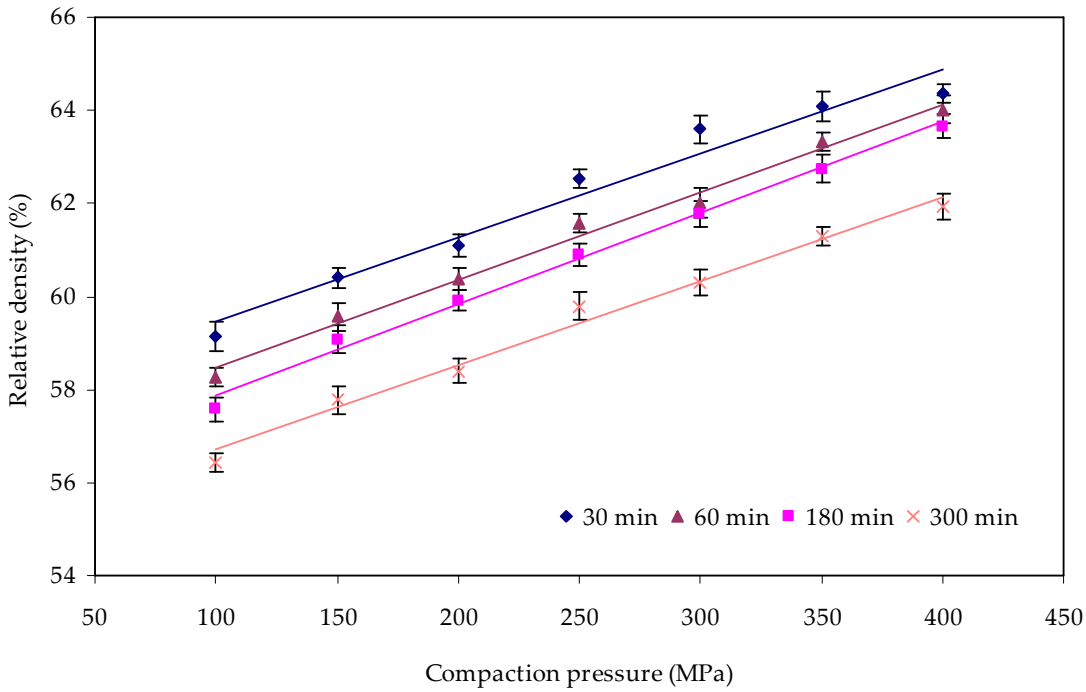

Fig. 5.95 Effect of compaction pressure on the relative density of WC-10Co powders ball milled for 30, 60, 180, and 300 min.

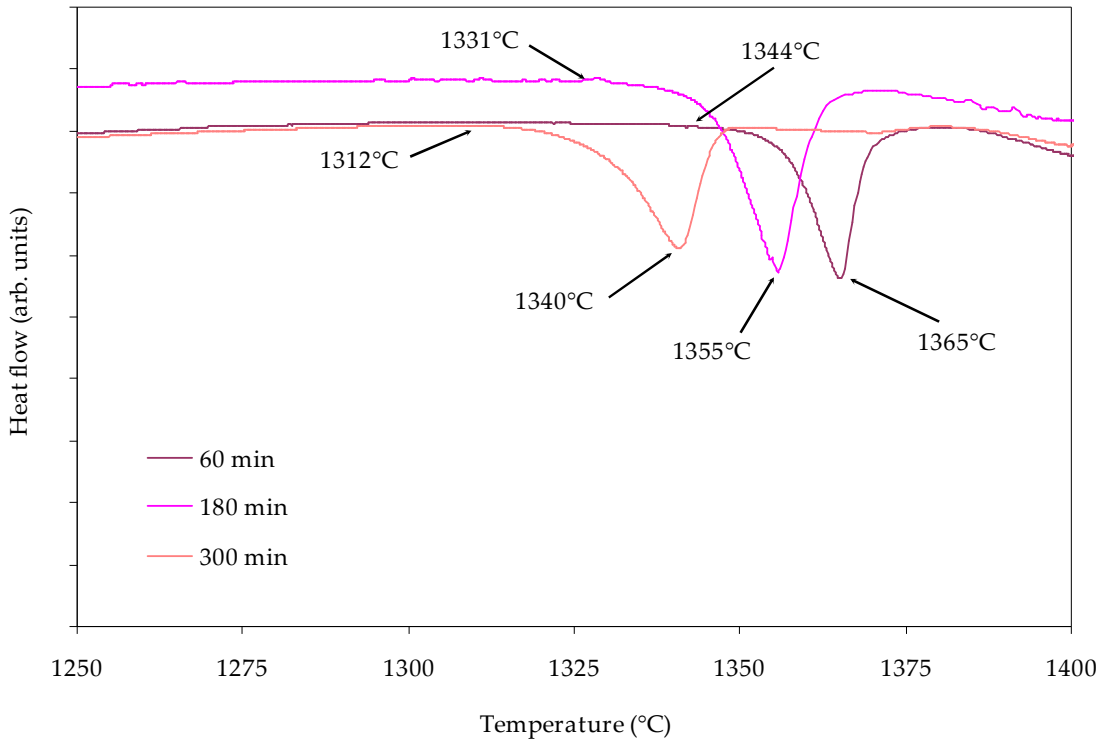

Fig. 5.96 DSC heating scan of the WC-10Co powders after ball milling for 60, 180, and 300 min with the onset and completion of melting shown for each powder.

5.6.2 Effect of milling temperature

Ball milling a further WC-10wt%Co composition for 60 min at -30°C using the same milling profile as that used for the room temperature (RT) milling study, has yielded very interesting results.

The morphology of the particles produced after low temperature milling appeared quite different to the 60 min RT milled powder, showing less irregularity and higher levels of deformation, Fig. 5.97 (a). Particle size analysis showed a smaller mean particle

size for the low temperature milled powder compared to the RT milled powder. Thermal analysis showed only a small difference in the onset temperature with the RT powder the lower of the two. A larger release of energy was observed for the -30°C milled powder, which suggested a higher level of stored energy in the particles. The thermal analysis scans were quite different in terms of weight loss with the -30°C milled powder exhibiting a higher loss, and the scans also revealed a number of weight changes had taken place, which were much more exaggerated for the -30°C milled powder. The temperatures of the weight changes suggested the decomposition of CO_3O_4, CO_2, or CO. Interestingly, XRF analysis showed much reduced levels of contamination for the -30°C milled powder with Fe pick-up at a negligible level. The morphology and structure of the particles aided cold compaction, as a green density of 65.5% was obtained for the -30°C milled powder at 400 MPa pressure compared to 64% for the RT milled powder.

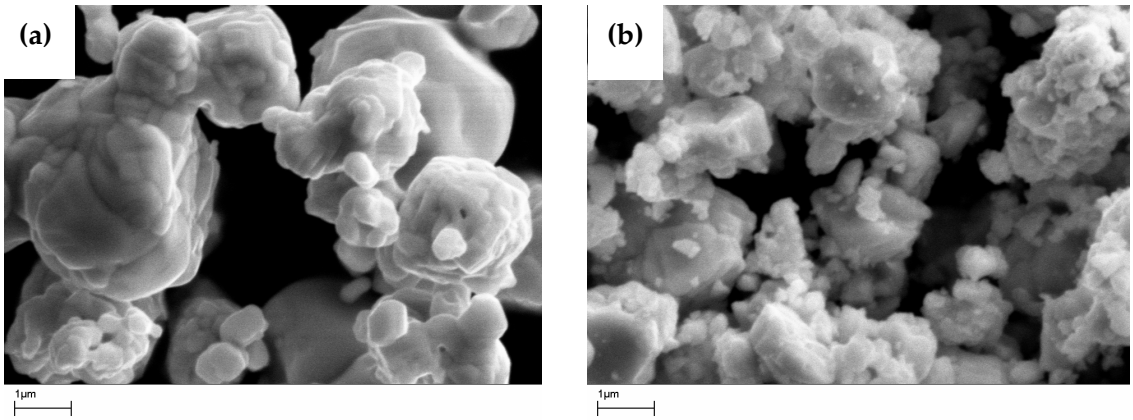

Fig. 5.97 SEM micrographs of the WC-10Co powders after 60 min milling at (a) -30°C and (b) RT.

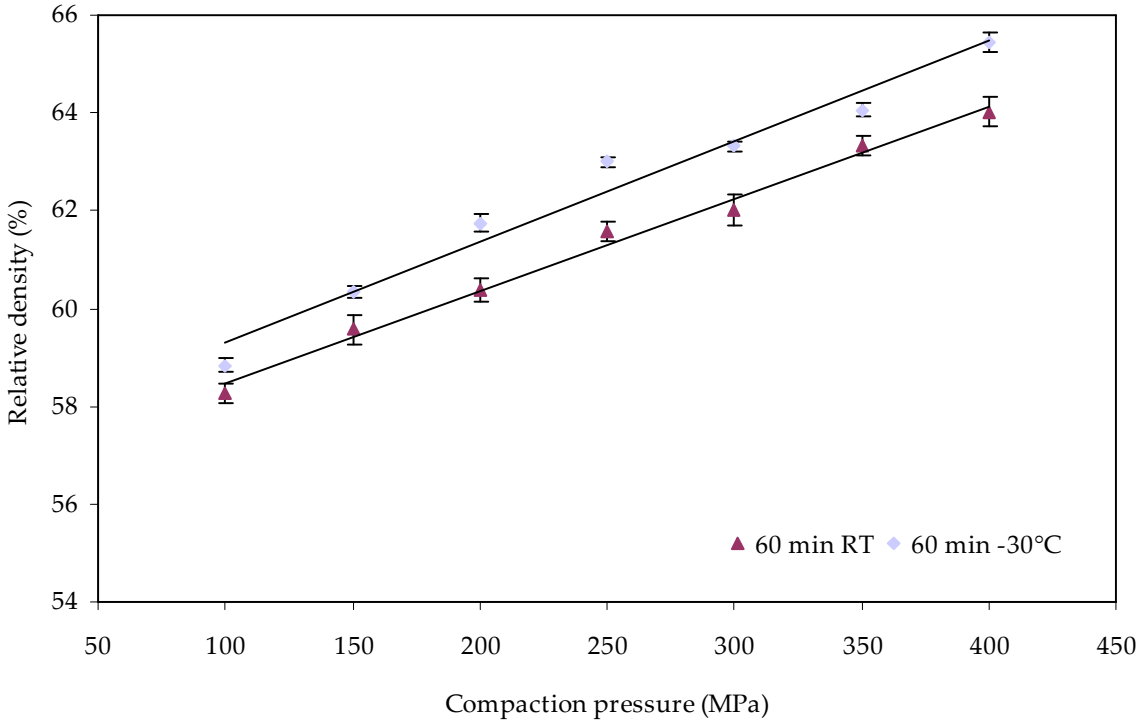

Fig. 5.98 Effect of compaction pressure on the relative density of WC-10Co powders ball milled for 60 min at -30°C and RT.

5.6.3 Consolidation of nanostructured hardmetal powders using conventional and non-conventional methods

The influence of pressure and temperature on the densification rate and mechanical properties of the mechanically alloyed powders have been established. Optimum levels of densification were observed for both the 60 min RT and -30°C milled powders, with the latter achieving close to theoretical density after pressureless sintering at 1390°C for 60 min. This temperature was used to allow a direct comparison with an industrial-based, sinter-HIP process. Densification was affected by increased milling time,

decreasing to ~ 96% for the 300 min milled material. Hardness levels reached a peak of 1298 HV30 for the 60 min milled material and then decreased to 1226 HV30 for the 300 min milled material, Fig. 5.99. The increased level of densification exhibited by the low temperature milled material resulted in a hardness value of 1337 HV30. However, microstructural analysis of both RT and -30°C milled materials showed that substantial WC grain growth had taken place due to the elevated temperature and isothermal hold time.

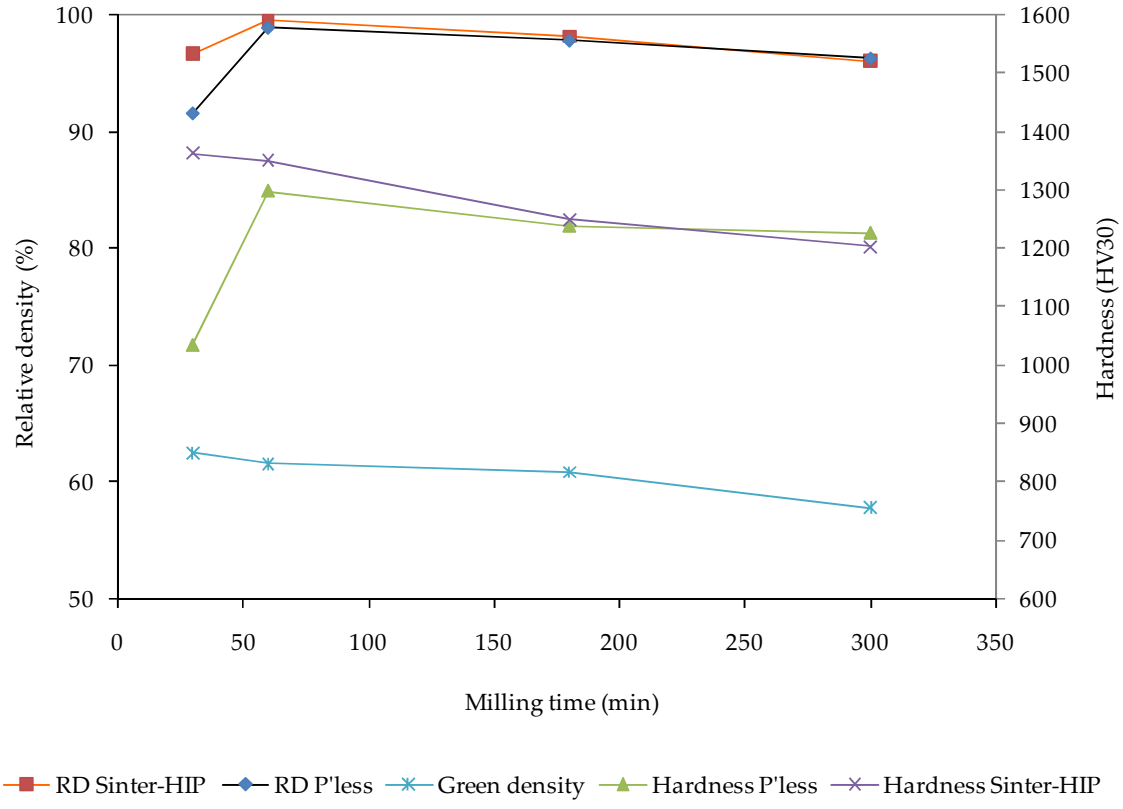

Fig. 5.99 Sintered density and hardness in relation to green density of ball milled WC-10Co.

Indirect measurements of WC grain size by coercive force revealed a similar value for both materials, which was confirmed by linear intercept measurements. Magnetic measurements were affected by ferromagnetism, caused by Fe pick-up during milling. The relationship between hardness and average WC grain size of the sintered samples, Fig. 5.100, revealed that the Hv – $d^{-1/2}$ relationship in this study does not follow normal H-P behaviour as reported in other work for WC-10wt%Co with increasing hardness with decreasing WC grain size (Shi, Shao and Duan 2007; Cha *et al*. 2001; Roebuck, Gee and Morrell 2006), but instead exhibits decreasing strength with decreasing WC grain size (increasing milling time). This unusual behaviour most likely stems from the synthesis process itself, more specifically, the high mechanical energy generated by the horizontal ball mill, and the subsequent difficulties in pressing a homogenous green compact with increasing milling time.

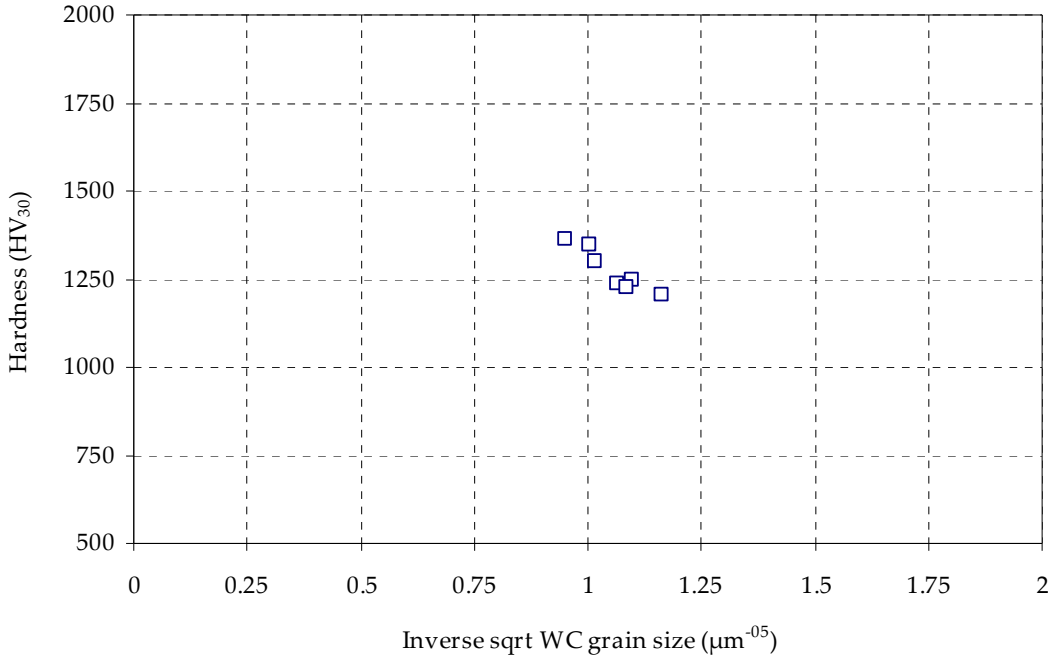

Fig. 5.100 Hardness as a function of the inverse square root of WC grain size ($d^{-0.5}$) for WC-10wt%Co data from this study.

The considerable scatter in the Palmqvist fracture toghness (W_K) results made it difficult to form any reasonable conclusions about the relationship between fracture toughness and hardness for the pressureless sintered materials. Again, this seemed to point towards effects from non-uniform consolidation. The relationship between fracture toughness and milling time was, in general, a detrimental one. Fracture toughness was higher for the 30 min milled sample due to the material's low hardness value and the deflection of cracks caused by the high number of pores. Toughness decreased after 60 min milling reaching a maximum value of 12 MN.m$^{-3/2}$ with a corresponding hardness of 1226 HV30. These values are similar to those reported by others for WC-10Co materials (Almond and Roebuck 1988) and also to those involving MA as the synthesis process (Mi

and Courtney 1998). The -30°C milled material was the exception, exhibiting a higher W_K with higher hardness due to its improved structure at both the green and sintered stages.

Fracture toughness behaviour of the WC-10Co materials after sinter-HIP (1390°C/60 min) processing, Fig. 5.101, showed that the effects of mean WC grain size and binder phase mean free path were much more pronounced. W_K increased with increasing milling time and decreasing hardness, but the rate of increase and the actual values obtained were significantly higher. W_K reached 14.9 $MN.m^{-3/2}$ after 300 min milling but the hardness level dropped to 1203 HV30. Surprisingly, the material milled for 60 min, which exhibited some η-phase, still achieved a W_K value of 13.7 $MN.m^{-3/2}$.

The VC-doped materials did not respond well to pressureless sintering, showing reduced levels of densification with increased milling time compared to the undoped materials. The doped materials also showed a reduction in the densification rate with increasing temperature, which was probably caused by an alteration in the interfacial energy or interference with the interfacial dissolution and reprecipitation steps. Optimum densification and properties were once again observed for the 60 min milled material, which exhibited a relative density of 89.5% and a hardness of 1086 HV30. These results were considerably below those reported in the literature, mainly due to the differences in the starting particle sizes between WC, Co and VC and the subsequent non-uniform distribution and deformation of VC during ball milling. There was evidence that discontinuous grain growth had occurred in the 300 min milled material, which was probably caused by compositional differences in the powder compact or

coarse carbides acting as 'seeds' for rapid grain coarsening for a small fraction of the WC grains.

A further set of the mechanically alloyed samples were processed using sinter-HIP at a temperature of 1390°C, followed by 5 min at 40 MPa pressure. The addition of a high isostatic pressure during sintering aided densification levels and pore collapse for the 30, 60 and 180 min milled materials to 96.7, 99.5% and 98.2%, respectively, Fig. 5.99. However, the 300 min material showed a slight decrease to 96%. Rearrangement processes play a larger role in densification. In the rearrangement stage, the rate of densification increases as the capillary force increases. Sinter-HIP also caused additional microstructural coarsening for the 30, and 60 min milled materials with enlargement due to a solution-reprecipitation process. Co pooling was observed for the 30 min milled material caused by nonuniform distribution of the binder during milling. Optical micrographs of the 60 min milled materials showed slight carbon deficiency (η-phase), less so for the low temperature milled material, which was probably caused by slight decarburisation during the vacuum sintering stage of sinter-HIP. On the whole, sinter-HIP had a detrimental effect on hardness levels with only the material from the shortest milling time showing an increase. The remaining materials exhibited the same decreasing trend with increasing milling time as that observed from pressureless sintering but at a faster rate. This suggested that sinter-HIP had exaggerated the effects of 'over-milling', for example, high levels of contamination, and reduced green density. WC mean grain size decreased with increased milling time, which followed the same trend as that from pressureless sintering. Electron backscatter diffraction (EBSD) of the

300 min milled sample estimated mean WC grain size to be 0.74 μm compared to 0.85 μm for the pressureless sintered material. The low temperature milled material exhibited a smaller WC grain size after sinter-HIP compared to the RT milled material, achieving 1.47 μm and 1.62 μm, respectively. Fracture toughness values were higher as a result of the WC grain sizes and binder mean free path, and increased with decreasing hardness. Once again, the low temperature milled material countered that relationship and showed increased W_K with increased hardness. Analysis of the fracture surfaces of broken TRS testpieces graphically demonstrated the reasons for the low levels of material strength, including delamination of the green structure, fracture lines, and macro-pores. It was clear that the root cause of the low mechanical properties achieved from both sintering techniques was due to the inhomogeneity introduced during green pressing, as the powders were not spray dried or granulated.

Sinter-HIP did not improve densification levels for the VC-doped materials but had a detrimental effect, with densification values reduced, on average, by ~ 10% compared to the undoped, sinter-HIP'd materials, which was approximately the same difference found after pressureless sintering. Optimum mechanical properties were achieved by the 60 min milled material with hardness measured at 1463 HV30 for 90% relative density, which represented a hardness increase of ~ 12% over the undoped material. The high hardness was attributed to the reduced, mean WC grain size, which was shown by the highest coercive force value of 17.4 kA m^{-1}. Hardness decreased at a higher rate with milling time compared to the undoped material even though WC grain growth had been reduced by the inhibitor, with a mean grain size of 0.53 μm determined by EBSD for the

300 min milled material compared to 0.74 μm for the equivalent, undoped material. W_K values were lower than the undoped material and considerably below reported values. This was due to the amount of inhibitor used as fine-grained WC-Co cemented carbides require a VC/Co weight ratio of 5 wt% for optimal properties. The high VC/Co ratio used in this study led to embrittlement due to (V,W)C precipitation at the WC-Co interface. The poor crack resistance was also demonstrated by the low TRS values, which reached a maximum of 1300 MPa.

Microstructural aspects of the materials were affected by a number of factors including; (i) slow heating rates, (ii) high temperature, (iii) and long hold times of the conventional sintering techniques. A non-conventional technique of spark plasma sintering (SPS) densified the 60 min milled materials at 1100°C with a hold time of 10 mins with a heat up rate of 150°C min^{-1}. Both materials achieved ~ 94% relative density with improved hardness levels compared to those achieved for conventional sintering, Fig. 5.101. A higher hardness was observed for the low temperature milled material. SEM micrographs showed significant WC grain growth had taken place even though the sintering temperature was well below the onset temperature of the WC-Co eutectic (1320°C). This suggested that rapid heating had accelerated densification during sintering due to the early activation of consolidation diffusion mechanisms. Surface diffusion contributes to the evolution of the pore surface curvature, thereby influencing the intensity of grain-boundary diffusion during the early stages of sintering. The interaction of the surface and grain-boundary diffusion is one of the major mechanisms enabling the impact of heating rates on the consolidation kinetics during SPS. The results

also suggested that a high solubility of WC in Co existed well below the eutectic temperature, which helped in surface smoothing of the particles leading to an enhanced rearrangement in the solid state. An increase in sintering temperature to 1150°C with a shorter hold time of 5 mins resulted in a slight drop in relative density but an increase in hardness to 1541 HV30 for the low temperature milled material, with a corresponding decrease in W_K. Relative density continued to decrease with increased temperature but at a much lower rate due to the higher heating rate of 300°C min^{-1}. Hardness reached 1557 HV30 with a W_K of 11.3 $MN.m^{-3/2}$, which compared favourably with the results from conventional sintering.

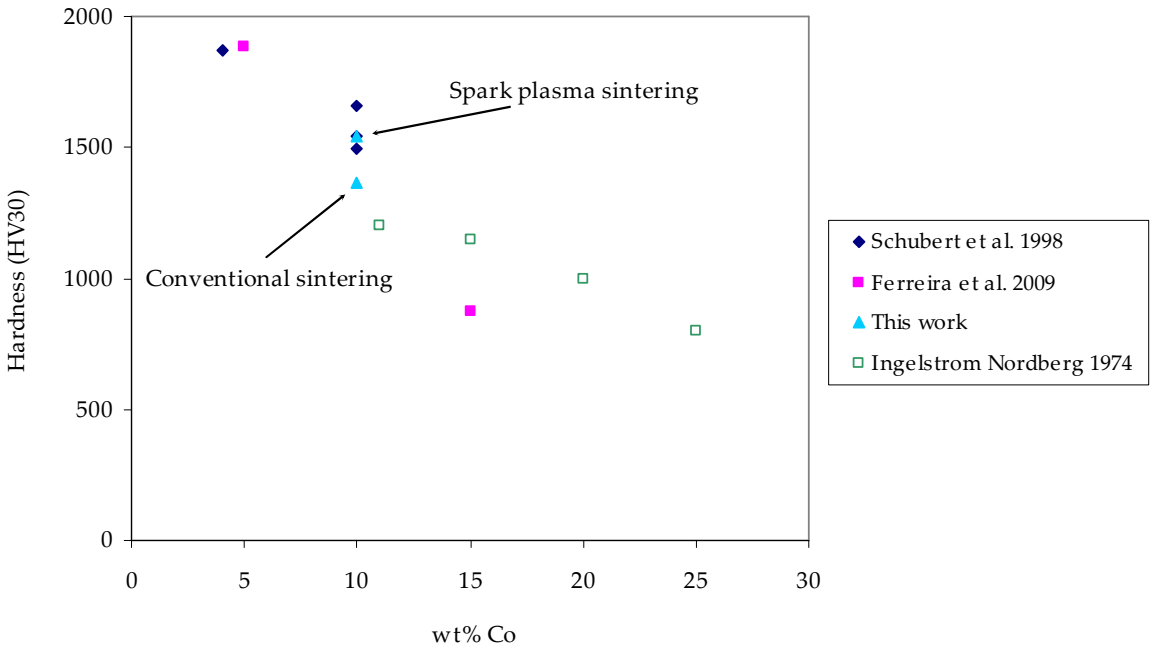

Fig. 5.101 Comparison of the hardness levels achieved for the MA processed and sintered powders with those reported in the literature.

6. Conclusions

1. Nanostructured WC-10wt%Co powder was synthesised after 60 min cyclic milling at room temperature with an average WC domain size of 21 nm and mean square strain of 6 x 10^{-4}, measured by X-ray diffraction line broadening. WC domain size showed a slight increase with milling time, which may be due to dynamic recovery during extended milling caused by thermal processes, as the size increased to 27 nm after 300 min ball milling.
2. Composite WC-Co particles with a homogeneous distribution of superfine (<0.5 μm) WC grains in the Co matrix were formed after 60 min of milling. Extended ball milling (300 min) reduced the mean particle size from 0.148 μm for 60 min milling to 0.117 μm, Fig. 5.8. Particle size distribution showed more nanosized (<0.2 μm) particles were generated with increasing milling time. This, along with the particle morphological results, Fig. 5.6 (g), suggested that the actual particles being measured were non-agglomerated, single particle fragments from the ball milling process. Particle size measurements also suggested that the milling 'limit' was reached under 300 min, as a five-fold increase in ball milling time shifted the mean particle size by just 0.03 μm. This small reduction in the mean particle size with milling time suggested strong interparticle bonding in the agglomerates, i.e. hard agglomerates.
3. Thermal analysis showed that the onset temperature of the WC-Co eutectic was reduced with increased milling time with an onset temperature of 1344°C, 1331°C,

and 1312°C recorded after 60, 180, and 300 min milling, respectively. Grain boundary stored energy increased after 60 min milling up to 180 min ball milling. After further milling (300 min), the energy release decreased to a level below that of the powder milled for 60 min, which, along with the larger WC domain size from 300 min milling, suggested that MA steady-state equilibrium was reached between 60 and 180 min.

4. Powder contamination from the milling media increased with increased milling time with Fe content measured at ~ 3wt% after 300 min ball milling. The reason for a high amount of Fe contamination during milling is due to the difference in hardness between the stellite milling medium and the WC powders. Controlling the purity of the powders is a key requirement if the promise of nano-hardmetals is to be realised. With the high surface area of nanoscale particles, there is a high risk of the impurity elements in the surroundings being absorbed onto their surfaces.
5. Green density increased linearly with compaction pressure between 100 and 400 MPa for all the milled powders. It was possible to exceed 60% relative density for all the ball milled powders, provided that compaction pressure was > 300 MPa, Fig. 5.11. Increased ball milling time resulted in decreased levels of green density, which was a direct result of the increase in average surface area of the particles resulting in an increase in inter-particle friction. A phenomenological compaction equation was used to show the compaction behaviour of the powders with ball milling time, Fig. 5.14. Plastic deformation behaviour showed a gradual decrease with milling time up to 180 min milling, which suggested that the levels of cold work from the MA

mechanisms (repeated welding, fracturing, and re-welding of powder particles) were of sufficient intensity, even after 30 min, to have a gradual effect on the hardness of the powder particles. After prolonged ball milling (300 min), the curve showed a sharp decrease, which indicated an increased level of cold work, producing more brittle powder particles. This was consistent with the morphological changes shown in Fig. 5.6. The curve in Fig. 5.14 also showed that the MA mechanisms did not reach equilibrium.

6. In direct comparison, a WC-10wt%Co composition was MA at -30°C for 60 min with the aid of a refrigerated bath. Average WC domain size, determined by X-ray line broadening, was 26 nm compared to 21 nm for the powder milled at RT. The measured rms-strain in the WC lattice was higher for the powder milled at -30°C. The higher value of mean square strain suggested that milling at a lower temperature reduced the rate of dynamic recovery.
7. The morphology of the particles from -30°C milling showed increased deformation with a slightly rounded morphology. The particles also seemed to show a high degree of flattening, which suggested an imbalance between the mechanisms of MA. Particle size measurements of the low temperature milled powder showed a smaller mean particle size of 0.129 μm compared with 0.148 μm for the RT, 60 min milled powder.
8. The powder milled at -30°C showed increased relative density with increased pressure, showing higher values at each pressure. At 400 MPa pressure, the powder milled at RT gave a relative density of 64% compared with 65.5% for the powder

milled at -30°C. The higher relative density achieved by the powder milled at low temperature was a result of its flattened, slightly rounded morphology, as it allowed higher mechanical interlocking between particles.

9. From a TGA/DSC scan (Fig. 5.19), the powder milled at low temperature showed a greater enthalpy release, which suggested a higher level of grain boundary stored energy in the particles. The powder milled at -30°C showed a higher weight loss, reaching ~ 0.9% compared with ~ 0.7% for the RT milled powder. The derivative of weight loss showed a number of thermal events occurred for both powders, although the events for the low temperature milled powder were significantly increased and also shifted to higher temperatures. Without mass spectroscopy it was unclear whether this change represented the decomposition of CO_3O_4, CO_2, or CO.
10. Wear of the milling media was considerably reduced by lowering the MA process temperature to -30°C with almost undetectable levels of Fe after 60 min milling with stellite media compared with 1.2wt% Fe after 60 min at RT. This suggested that low temperature milling could help to lower powder surface and interface contamination levels, which are of particular concern for nanostructured materials.
11. Initial densification levels of the RT milled powders, after pressureless sintering for 60 min at 1355°C, showed an inverse relationship with green density, Fig. 5.24. The 300 min milled powder with the lowest green density and, therefore the smallest particle size, showed the highest level of densification after sintering and reached ~ 93% TD compared with ~ 76% for the 60 min milled powder, which showed a larger particle size. Densification and hardness reached optimum levels for the 60 min

milled powder after pressureless sintering for 60 min at 1390°C with 99% TD and 1326 HV30, respectively. Both properties decreased with increased milling time with the 300 min milled powder achieving ~ 96% TD and 1298 HV30, respectively. WC grain size measurements showed that, overall, increased milling time resulted in a decrease in average WC grain size. However, decreasing WC grain size with decreasing hardness does not follow the typical Hall-Petch relationship between these two features. The elevated temperature and isothermal hold time had a detrimental affect on the microstructures, causing considerable WC grain growth with the 60 min milled powder, for example, exhibiting an average WC grain size of 0.97 μm after 60 min at 1390°C, Table 5.4.

12. Densification levels after sinter-HIP followed the same trend as that observed from pressureless sintering with the 60 min milled powder reaching close to TD, then decreasing to ~ 96% for the 300 min milled powder. The most noticeable difference in densification levels between the two processes was that exhibited by the 30 min milled powder, which increased to ~ 97% TD with the application of an external pressure. Hardness decreased linearly with milling time after sinter-HIP with the highest hardness achieved after 30 min milling, Fig. 5.35. This suggested that the application of an external pressure was sufficient to generate a uniform structure with the lowest increase in WC grain size. Grain size measurements showed that, in fact, WC grain size was coarser for the 30 min milled powder after sinter-HIP. Also, SEM analysis showed that Co distribution was non-uniformly dispersed with areas of Co 'pooling' observed in the microstructure, Fig. 5.33. Therefore, the reason for the

high hardness value was most probably due to the localised, finely structured areas of WC, Fig. 5.34 (b).

13. Deleterious phases of eta (η) and graphite were observed after sinter-HIP for the 60 min and 180 min milled powders, respectively. Eta phase was probably formed during cooling and caused by the sinter-HIP process itself as the vacuum stage tends to be slightly decarburising. The excess carbon phase could have been caused by the milling preparation stage, which involved 'coating' the milling media using an identical composition, designed to minimise contamination levels during milling.
14. Electron backscatter diffraction (EBSD) patterns of the 180 and 300 min milled powders after sinter-HIP showed that increased ball milling resulted in a slightly narrower WC grain size distribution and a smaller mean grain size of 0.74 μm compared to 0.83 μm for 180 min milling.
15. From the numerous relationships developed between fracture toughness, load, indentation diagonal, crack length etc., eq. 4.5 was preferred because it presupposes no knowledge of other mechanical properties of the hardmetal. W_K increased with increased milling time and decreased hardness for both sintering techniques but this effect was much more pronounced for the sinter-HIP materials. W_K reached 11.6 $MM.m^{-3/2}$ with 300 min milling after pressureless sintering but reached 16.1 $MN.m^{-3/2}$ for the same material after sinter-HIP, which was due to the effect of mean WC grain size and binder phase mean free path. Sinter-HIP clearly showed a higher change in toughness for a given increase in hardness compared to pressureless sintering, Fig. 5.49. However, the toughness results for the materials produced in this study

indicated that unless the test material is particularly homogenous, there is a large scatter of results that are microstructure dependent. The test was inappropriate for some of the poorly densified materials.

16. Low temperature milling enhanced densification levels with the cylindrical compact approaching TD for both pressureless sintering (60 min at 1390°C) and sinter-HIP. This was probably due to a more homogenous green compact, lower level of impurities, and the complete loss of entrapped gases during solid state sintering, Fig. 5.20. The improved powder purity enhanced the existence of a continuous WC skeleton. Milling at -30°C resulted in a slightly smaller average WC grain size of 0.91 μm after pressureless sintering to that obtained for the RT material. Microstructural analysis showed a more uniform structure and a narrower grain size distribution for the low temperature milled material but both materials exhibited considerable grain coarsening, which was reflected in the low hardness values. Despite the low hardness levels, the improved homogeneity of the low temperature milled material and lower WC grain size resulted in a higher hardness value of 1363 HV30 compared to 1326 HV30 for the RT milled material.
17. Fracture toughness of the low temperature milled material, Fig. 5.57, did not follow established behaviour as the material exhibited higher fracture toughness with higher hardness from pressureless and sinter-HIP techniques, achieving 13.3 $MN.m^{-3/2}$ and 14.5 $MN.m^{-3/2}$, respectively, despite the presence of η phase. This did not conform to general understanding as carbon deficiency is known to have a detrimental effect on toughness. Strength levels increased and were the highest

amongst all the milled materials, irrespective of the sintering process, due to the low level of porosity and other inclusions but the values obtained were significantly below those of typical, fine-grained WC-10Co materials. This was probably due to the low level of binder as determined by magnetic saturation measurements, the quantity of which may have altered during the synthesis stage.

18. Addition of 1wt% vanadium carbide (VC) inhibitor to the WC-10Co composition proved beneficial in lowering the onset temperature of the WC-Co eutectic. With increased milling time, the onset was shifted from 1306°C for 60 min milling to 1283°C for 300 min milling. The large difference in starting sizes of the VC powder (> 10 μm), WC (~ 3.5 μm) and Co (~1.5 μm) powders led to non-uniform dispersion of the inhibitor during milling with a number of ~ 5 μm diameter VC particles still remaining after 300 min milling. This, in turn, led to green densities < 60% TD, irrespective of milling time due to hindrance of the compaction mechanisms, including the initial sliding and rearrangement of particles. These large particles may have also caused density gradients through the compact as densification levels were severely affected for both sintering techniques, reaching less than 90% TD. The non-uniform dispersion of the inhibitor led to an inhomogeneous sintered structure for all the milled variants, with discontinuous WC grain growth occurring with extended milling (180 and 300 min), which was much more exaggerated after sinter-HIP. The inhibitor was effective in reducing the average WC grain size with EBSD indicating a grain size of 0.53 μm for the 300 min milled, sinter-HIP variant compared to 0.74 μm for the undoped material. The general trend in mechanical properties of the materials

was fairly representative of their microstructural features and consolidation process with the sinter-HIP processed materials performing better than those from pressureless sintering due to their improved homogeneity and therefore, a reduced number of flaws.

19. Analysis of the fracture surfaces of the TRS testpieces revealed that the mechanical properties of both materials were closely related to the structure formed during green pressing. It was clear that the scale of the defects could not be compensated for during sintering, thereby resulting in the low rupture strength values. The defects were most likely caused by density gradients during pressing due to die wall friction and the poor compressibility of as-milled powder, and, to some extent, the length to width ratio of the green compact, all of which combined to cause delamination of the compacts' structure during sintering.
20. Spark plasma sintering (SPS) showed that the onset of shrinkage (densification) was dependent upon particle size with the powder from 300 min milling showing an onset temperature of ~ 800°C compared to ~ 1000°C for the 60 min milled powder. The low temperature milled powder showed an onset temperature of 980°C, which suggested that low temperature milling provided enhanced densification kinetics. Densification levels followed the same trend as those observed during conventional sintering with relative density decreasing with increased milling time, but with an exaggerated effect, as the difference in density for the 60 min and 300 min materials was higher with values of 94.3% and 85.6% TD, respectively. The low temperature milled powder reached a higher relative density of 94.7%. Improved levels of

hardness were also shown by this material, achieving 1478 HV30 compared to 1433 HV30 for the RT milled material. Coercive force measurements indicated a substantial difference in the level of grain growth between the two 60 min milled materials with the -30°C milled material showing a value of 15 kA^{-1} compared to 9 kA^{-1} for the RT material.

21. SPS temperature was increased to aid densification and the hold time reduced to 5 min to minimise WC grain growth of the low temperature milled material, but the changes had a detrimental effect on both features reducing relative density to 94.1% TD and coercivity to 14.8 kA^{-1}. Despite this, hardness increased to 1541 HV30, which did follow conventional behaviour of decreasing hardness with increasing grain size. The increased temperature may have provided additional strengthening to the WC skeletal structure, which, in turn, provided strengthening to the matrix and decreased the dislocation motion during deformation. A further increase in temperature to 1200°C and a reduction in hold time to 3 min caused the same decreasing effects on densification and coercivity, with values of 94% and 14 kA^{-1}, respectively. Hardness continued to increase and reached 1557 HV30.

7. Suggestions for future work

7.1 Low temperature milling

From the results of this study, there seems little to be gained from trying to improve microstructural/mechanical property relationships by ball milling longer than 60 min. Also, there is little point in developing the undoped, room temperature milled powders with traditional consolidation processes due to uncontrolled levels of WC gain growth.

It is clear that the results of low temperature ball milling need further investigation in order to verify the promising aspects of this particular part of the study. These include the very low levels of contamination, increased green density, low levels of porosity, uniform microstructure, and improved mechanical properties. Additional work should include ball milling below -30°C, as the current system is capable of operating at temperatures to -45°C. This would determine whether any further beneficial effects are obtained by reducing the milling temperature still further. Although the microstructure and mechanical properties represent those of a medium grade WC-10wt%Co (1.3-2.5 μm) after conventional liquid phase sintering, the material's behaviour in response to non-conventional sintering should be further investigated. Hardness levels >1500 HV30 were achieved without any dopant, despite significant WC grain growth. Clearly, the powder will require doping with an inhibitor if further significant gains in hardness are to be realised but careful consideration should be given to the method of introduction.

7.2 Addition of the inhibitor

This study confirmed that a very homogeneous distribution of the grain growth inhibitor, and binder, is an essential prerequisite in controlling WC grain growth in hardmetals. These constituents should be distributed as uniformly as possible within the WC to achieve as stable a sintering behaviour and as uniform a microstructure as possible. Sub-micron carbides experience most of their sintering shrinkage before the binder melts. Binder or inhibitor heterogeneities within the compact will therefore give local concentrations (or depletions) that are too long range to be neutralised by solid state diffusion. This provides an opportunity for localised WC grain growth or coalescence during the heating stage of the sinter cycle. At the binder eutectic temperature, these larger grains act as "seeds" for further more rapid growth by Ostwald ripening. The results from VC doping also showed that inhomogeneous distribution of the inhibitor caused discontinuous grain growth, due to the coarse and agglomerated starting powder. It is clear that mechanical mixing of the coarse inhibitor with WC and Co did not provide the required uniform dispersion in this case. Future work should concentrate on either adding an inhibitor of comparable fineness (<1 μm) with WC and Co at the start of milling or pre-doping the WC powder particles by a chemical route or by coating them. The chemical route would involve adding the inhibitor as a salt in solution and using methods of controlled precipitation or adsorption to disperse the inhibitor on to the surfaces of the WC particles. The inhibitor would then

be reduced *in situ* with hydrogen in a furnace. The aim, depending on the degree of dispersion and the reducing conditions, would be to create adherent nanoscale particles.

7.3 Alternative binder to Co

Co continues to dominate the hardmetals market as a binder for WC-Co due to its unique properties. The reasons for this are some unique properties of Co and the Co-W-C ternary system, including the high solubility of WC in Co that varies strongly with temperature, and also the favourable properties of Co itself (high hardness, yield stress, toughness and strength). However, Co also exhibits a number of shortcomings namely, poor corrosion resistance, erratic cost levels, and environmental toxicity.

The cost picture is continually fluctuating; the price of Co doubled in 2006 from around $12/lb to $24/lb with trading in early 2008 reaching a record high of over $40/lb (Cobalt development institute 2008).

The safety of Co is attracting considerable interest as a hazardous metal, use of which is affected by the new EU regulation of chemicals, REACH, which came into force on 1st June 2007. REACH (Registration, Evaluation and Authorisation of Chemicals), will place a duty on companies that manufacture, import and use chemicals in the EU to assess the risks arising from their use and manage any risks identified. Unsurprisingly, this has generated considerable reaction by UK hardmetal producers who view the legislation as unworkable (Powdermatrix technology roadmap 2004), given the critical role of Co in hardmetals. Dispensation will be inevitable for its continued use as a binder until

alternative, cost effective binders that can offer optimised carbon content with equivalent mechanical properties can be developed.

It has been known for some time that hardmetal powder in breathable form can provoke negative health effects if inhaled. The so called "hardmetal lung", which is a specific type of lung fibrosis occurring only after exposure to hardmetal dust, is an acknowledged occupational disease in Germany (Gries, Prakash 2007). However, it is not well understood why a combination of WC with Co impacts more on health, especially on the lung, compared to Co or WC alone. Historically, relatively little attention has been paid to the hardmetal industry by various scientific or governmental health authorities. However, during the past few years, several extraordinary events have taken place that have the potential to significantly impact the global hardmetal industry.

In October 2003, the International Agency for Research on Cancer (IARC) determined that "Co metal with WC was evaluated as probably carcinogenic to humans (Group 2A) on the basis of limited evidence in humans for increased risk of lung cancer". The IARC based their findings on two studies on hardmetal workers in Europe that suggested exposure to WC-Co was associated with an increase in deaths amongst these workers from lung cancer. In May 2004, a request for public comment was published by the United States Department for Health and Human Services, which listed 21 substances that they proposed for listing on the "Report of Carcinogenesis". Included in that report was "Co/WC metal manufacturing". The report is a "congressionally mandated listing" of "substances that are either (i) known human carcinogens or may reasonably be anticipated to be human carcinogens, and (ii) to which a significant number of persons

residing in the United States are exposed". Finally, last year the German Research Foundation (DFG) concluded the following; "WC and Co-containing hardmetals were classified as carginogenic in humans and, therefore, placed in carcinogenicity category 1". These 3 independent bodies based their claims around the findings of a small number of epidemiological studies conducted in Europe. In a review of these studies, the Cobalt development institute (CDI) found a statistically weak correlation and also suggested that certain cofounders for lung cancer (e.g. smoking history) were not adequately accounted for. As a result, the hardmetal industry may face substantial regulation based upon incomplete scientific data.

Given that the specific nature of Co is responsible for adverse health effects, it has been shown that a mixture of WC with Fe powder has no cytotoxic effects (Gries, Prakash 2007), which was established from an acute inhalation study performed on rats. A partial replacement of 10 % Co in WC-Co by 5% Fe, using Co and Fe powder milled together with WC in an attritor mill, lead to a reduction in toxicity by about 50%. When the same nominal composition (WC-Co5%Fe5%) was produced as a composite with WC, whereby Fe and Co were formed as an alloyed phase, mortality at the same concentration (1 mg/l) dropped from 30% to zero, and remained at zero, even at 5 mg/l. A blend of WC with a fine alloy powder (51%Fe, 49%Ni) showed no inhalation toxicity at 0.5 nor 5 mg/l. These results clearly show that inhalation toxicity of Co in contact with WC can be largely reduced if not eliminated, if it is alloyed with Fe. This finding is of great significance for the safe handling and production of hardmetal powders.

In order to meet the necessary requirements for processing WC-based hardmetals by liquid phase sintering, the alternative binder element should wet the carbide and have solubility for WC. The carbide surfaces must be easily wetted to develop a continuous binder to minimise carbide/carbide interfaces for optimum properties. The elements of the transition metal group, Fe, and Ni show similar behaviour and more or less meet the above requirements (Prakash 1993). Both metals effectively wet WC (Samsonov et al. 1968; Ramqvist 1969; Oberacker, Prakash 1978) and the solubility of WC in Fe and Ni at 1250°C was found to be 7 and 12 wt % respectively compared to 22 wt % for Co (Edwards, Raine 1952).

Hardmetals with Fe-based binders have been commercialised in some areas due to performance advantages over Co bound hardmetals, but they are still under prejudice because their development had been in times of high Co prices or low Co availability. Their given name was "substitute", which is often associated with "inferior". Recent work has shown that the most promising combinations for Fe/Ni/Co bonded hardmetals have been found when the binder phase structure is mainly martensitic, Table 8.1.

Besides the cost-effective nature of alternative binders, other benefits have emerged. For example, investigations by Prakash (1979) on Fe/Ni/Co alloys showed that cemented tungsten carbides with Fe-rich binders resulted in improved properties, such as increased hardness, abrasive wear resistance, toughness, and strength compared to Co-bonded hardmetals, Table 8.1. Similar findings have also been reported by Polini et al. (2006), who obtained hardmetals with comparable mechanical properties to those of conventional Co-cemented carbides.

Future work should focus on developing a 10wt%, Fe-rich Fe/Ni/Co based binder, which will allow a direct comparison with the results already obtained in this study for a 10wt% Co binder level. All the powders should be of equivalent fineness and be uniformly mixed and dispersed before MA with WC. The Fe-rich binder should prove advantageous in terms of sintering, as the onset temperature of the WC-Fe/Ni/Co eutectic should be lower than that of conventional WC-Co.

Table 7.1

Mechanical properties of alternative Fe-based binders for WC.

Binder	WC starting particle size (μm)	Binder (wt.%)	Binder ratio (wt.%)	Density (g/cm^3)	Hardness HV	TRS (MPa)	Type of binder powder	Ref.
Co	0.8	9	-	14.70	1608			(Gille *et al*. 2000)
Fe/Ni/Co	2	9	30:30:40	14.54	1245	2760	Pre-alloyed	(Polini *et al*. 2006)
Fe	-	10	-		1812	-	M. mixed	(Wittmann *et al*. 2002)
Fe/Ni/Co	0.8	9	75:15:10	14.55	1817	-	Pre-alloyed	(Gille *et al*. 2000)
Fe/Ni/Co	2.5	20	20:20:60	13.41	870	3289	M. mixed	(Gille *et al*. 2000)
Fe/Ni/Co	2.5	20	20:20:60	13.51	900	3510	Pre-alloyed	(Gille *et al*. 2000)
Fe/Ni/Co	0.6	10	-	-	1648	-	M. mixed	(Gries, Prakash 2007)

M.Mixed – mechanically mixed

References

AGREN, J., BRANDT, J., HAGLUND, S. and UHRENIUS, B. (1996) Modelling of solid state sintering of cemented carbides. *In*: GERMAN, R.M. and MESSING, G.L., (eds.). *Proceedings of sintering technology*, *New York, 1996*, pp.149-156.

AHN, J.P., HUH, M.Y. and PARK, J-K. (1997) Effect of green density on subsequent densification and grain growth of nanophase SnO_2 powder during isothermal sintering. *Nanostructured Materials*, **8**(5), pp. 637– 643.

AJDELSZTAJN, L., HULBERT, D., MUKHERJEE, A. and SCHOENUNG, J.M. (2007) Creep deformation mechanism of cryomilled NiCrAlY bond coat material. *Surface and Coatings Technology*, **201**(24), pp. 9462-9467.

ALLIBERT, C.H. (1999) Liquid volume fraction involved in liquid phase sintering of cemented carbides WC-Co. *in*: EPMA, (eds.). *Third conference on advances in hard materials production*, *EURO PM99, Shrewsbury, 1999*, pp. 183-189.

ALLIBERT, C.H. (2001) Sintering features of cemented carbides WC-Co processed from fine powders. *International Journal of Refractory Metals and Hard Materials*, **19**, pp. 53-61.

ALMOND, E.A. and ROEBUCK, B. (1988) Identification of optimum binder phase compositions for improved WC hard metals. *Materials Science and Engineering*, **105-106**(1), pp. 237-248.

AL-QURESHI, H.A., GALIOTTO, A. and KLEIN, A.N. (2005) On the mechanics of could die compaction for powder metallurgy. *Journal of Materials Processing Technology*, **166**, pp. 135-143.

AL-QURESHI, H.A., SOARES, M.R.F., HOTZA, D., ALVES, M.C. and KLEIN, A.N. (2008) Analyses of the fundamental parameters of cold die compaction of powder metallurgy. *Journal of Materials Processing Technology*, **199**(1-3), pp. 417-424.

AMBERG, S. and DOXNER H. (1977) Porosity in cemented carbides. *Powder Metallurgy*, **20**(1), pp. 1–10.

AMBERG, S., NYLNADER, E.A. and UHRENIUS, B. (1974) The influence of hot isostatic pressing on the porosity of cemented carbide. *Powder Metallurgy International*, **6**, pp. 178-180.

ANDRÉN, H.O. (2001) Microstructures of cemented carbides. *Materials & Design*, **22**(6), pp. 491-498.

ANTOLOVICH, S.D. and ANTOLOVICH, B.F. (1996) An introduction to fracture mechanics. *In* ASM handbook, fatigue and fracture, **19**, pp. 371-80.

ARATO P. BARTHA, L., PORAT, S., BERGER, S. and ROSEN, A. (1998) Solid or liquid phase sintering of nanocrystalline WC/Co hardmetals. Nanostructured Materials, **10**(2), pp. 245-55.

ARENAS F., de ARENAS, I.B., OCHOA, J. and CHO, S.-A. (1999) Influence of VC on the microstructure and mechanical properties of WC–Co sintered cemented carbides. *International Journal of Refractory Metals and Hard Materials*, **17**(1-3), pp. 91-97.

BACK, S.-H., LEE, G.-H., KANG, S. (2005) Effect of cryomilling on particle size and microstrain in a WC-Co alloy. *Materials Transactions*, **46**, pp. 105-110.

BALZAR, D. (1999) Voigt-function model in diffraction line-broadening analysis. Microstructure analysis from diffraction. *in*: SNYDER, R.L., BUNGE, H.J. and FIALA, J. (eds.), International Union of Crystallography.

BARGTSSON, B., JOHANNESON, T. and LINDAU, L. (1973) *Plansee berichte für Pulvermetallurgie*, **21**, p. 110.

BENJAMIN, J. S. (1970) Dispersion strengthened superalloys by mechanical alloying. *Metallurgical Transactions*, **1**, pp. 2943-2951.

BENJAMIN, J.S. (1976) Mechanical alloying. *Scientific American*, **234**(5), pp. 40-48.

BERG, H.V.D. (2007) Market demands for new applications. *in*: *Proceedings of EURO PM2007, Toulouse, France, 15-17 October.*

BETTERIDGE W. (1982) Cobalt and its alloys. New York: John Wiley & Sons.

BEVER, M.B., HOLT, D.L. and TITCHENER, A.L. (1973) The stored energy of cold work. Progress in Materials Science, **17**, pp. 5-177.

BHATTACHARYA, A.K. and ARZT, E. (1993) Plastic deformation and its influence on diffusion process during mechanical alloying. *Scripta Metallurgica et Materialia*, **28**(4), pp. 395-400.

BIRRINGER R. (1989) Nanocrystalline materials. *Materials Science and Engineering A*, **117**, pp. 33-43.

BLOOR, D. and CAHN, R.W. (1994) *The encyclopedia of advanced materials*. Oxford: Pergammon Press Inc.

BOCK, A., SCHUBERT, W.D. and LUX, B. (1992) Inhibition of grain growth on submicron cemented carbides. *Powder Metallurgy International*, **24**(1) pp. 20-26.

BOLTON, D. and KEELEY, R.J. (1982) Effects of non-stoichiometric carbon contents on the fracture toughness of WC–Co hardmetal alloys. *International Journal of Refractory Metals and Hard Materials*, **1**, pp. 103–111.

BOUTZ, M. M., THEUNISSEN, G. S. A. M., WINNUBST, A. J. A. and BURGGRAAF, A. J. (1990) Grain growth during sintering of nanocrystalline Y and/or Ce-doped tetragonal zirconia. *in*: Superplasticity in Metals, Ceramics, and Intermetallics. *Proceedings: Materials Research Society Symposium*, MAYO, M.J., KOBAYASHI, M. and WADSWORTH, J., (eds.), Pittsburgh 1990, **196**, pp. 87–92.

BOYLE, J.F., MANAS-ZLOCZOWER, I. and FEKE, D.L. (2005) Hydrodynamic analysis of the mechanisms of agglomerate dispersion. *Powder Technology*, **153**, pp. 127-133.

BRISCOE, B.J. and ROUGH, S.L. (1998) The effects of wall friction on the ejection of pressed ceramic parts. *Powder Technology*, **99**, pp. 228-233.

BROOK, R.J. (1969) Pore-grain boundary interactions and grain growth. *Journal of the American Ceramic Society*, **52**(1), pp. 56–57.

BROOKES, K.J.A. (1992) World directory and handbook of hardmetals and hard materials, 5th ed, Internatioanl Carbide Data, UK.

BROOKES, K.J.A. (2002) Through the looking glass - the rather odd world of hardmetals. *Metal Powder Report*, **57**(5), pp. 28-29.

BRUKER (2003) AXS Bruker DIFFRACplus TOPAS/TOPAS R/TOPAS P V2.1. Technical Reference, Germany.

CAHN, R.W. (1992) Nanostructures Come of Age. *Nature*, **359**, pp. 591–592.

CALKA, A., NIKOLOV, J.I. and NINHAM, B.W. (1993) *in*: Mechanical alloying for structural applications, deBARBADILLO, J.J. et al., (eds.). Materials Park, OH: ASM International, 1993, p. 189-195.

CAMPBELL, S.J. and KACZMAREK, W.A. (1990) Mössbauer spectroscopy applied to materials and magnetism. *in*: LONG, G.J. and GRANDJEAN, F. (eds.), New York, Plenum press, p. 273.

CARROLL, D.F. and CONNER, C.L. (1997) Processing of superfine WC powders into high quality WC/Co materials. *in*: McKOTCH, R. and WEBB, R., (eds.). Advances in Powder Metallurgy & Particulate Materials. Princeton, NJ, Metal Powder Industries Federation, 1997.

CARROLL, D.F. (1997) Processing and properties of ultra®ne WC/Co hard materials. *in*: KNERINGER, P., RODHAMMER, P. and WILHARTITZ, P., (eds.). Proceedings of the 14th International Plansee Seminar, vol. 2, Reutte, Plansee AG, 1997, pp. 168-182.

CASTEX, L., LEBRUN, J.L., MAEDER, G., SPRAUEL, J.M. Détermination de constraintes résiduelles par diffraction des rayons X, vol. 22, Publications scientifiques et techniques de l'ENSAM, Paris, 1981, p. 51.

CHA, S.I., HONG, S.H., HA, G.H. and KIM, B.K. (2001) Mechanical properties of WC–10Co cemented carbides sintered from nanocrystalline spray conversion processed powders. *International Journal of Refractory Metals and Hard Materials*, **19**(4-6), pp. 397-403.

CHA, S.I., HONG, S.H. and BYUNG, K. (2003) Spark plasma sintering behavior of nanocrystalline WC–10Co cemented carbide powders. *Materials Science and Engineering A*, **351**(1-2), pp. 31-38.

CHABRETOU, V., ALLIBERT, C.H. and MISSIAEN, J.M. (2003) Quantitative analysis of the effect of the binder phase composition on grain growth in WC-Co sintered materials. *Journal of Materials Science*, **38**(12), pp. 2581-2590.

CHANG, C.-R. and SHYU, J.P. (1990) Effects of Porosity on Coercive Force of Particulate Medium. *Chinese Journal of Physics*, **28**(1), pp. 29-36.

CHAPELL, J.S., RING, T.A. and BIRCHALL J.D. (1986) Particle size distribution effects on sintering rates. *Journal of Applied Physics*, **60**, pp. 383-391.

CHEN, Y.C. and DAEHN, G.S. (1991) The thermal cycling deformation of a particle reinforced metal matrix composite: comparison between a model and experimental observations. *Scripta Materialia*, **25**(7), pp. 1543-1548.

CHEREMISINOFF, N.P. (1990) *in: Handbook of ceramics and composites, synthesis and properties*, vol.1, Marcel Dekker Inc.

CHERMANT, J.L. and OSTERSTOCK, F. (1976) Fracture toughness and fracture of WC-Co composites. *Journal of Materials Science*, **11**, pp. 1939-1951.

CHERNIAVSKY, K.S. (1982) Stereology of cemented carbides. *Science of Sintering*, **14**, pp. 1-12.

CHIN, Z.-H. and PERNG, T.-P. (1997) Instant Formation of TiN by Reactive Milling of Ti in Nitrogen. *Material Science Forum*, **235-238**, pp. 121-126.

CHO, K.H., LEE, J.W. and CHUNG, I.S. (1996) A study on the formation of anomalous large WC grain and the eta phase. *Materials Science and Engineering A*, **209**(1), pp. 298-301.

CHUNG, K.H., HE, J., SHIN, D.H. and SCHOENUNG, J.M. (2003) Mechanisms of microstructure evolution during cryomilling in the presence of hard particles. *Materials Science and Engineering A*, **356**(1-2), pp. 23-31.

COBLE, R.L. (1962) Sintering alumina: effect of atmospheres. *Journal of the American Ceramic Society*, **45**, pp. 123-27.

COELHO, A. (2007) TOPAS V4 academic user's manual. Bruker AXS Inc., WI, USA.

Da SILVA AGP, SCHUBERT WD, LUX B. (2001) The Role of the Binder Phase in the WC-Co Sintering. *Materials Research*, **4**(2), p. 59.

DAUB, H.W., DREYER, K., HAPPE, A., HOLZHAUER, D. and KASSEL, D. (1995) Performance potential of superfine and ultrafine grained hardmetals and their manufacture. *in*: Pulvetechnologische Wege in die Zukunft. Germany: Deutsche Gesellscaft for Metallkunde, pp. 285-306.

DAVIS, R.M., McDERMOTT, B. and KOCH, C.C. (1988) Mechanical alloying of brittle materials. *Metallurgical Transactions*, **19A**, pp. 2867-2874.

DEHOFF, R .T. and RHINES, F.N. (1968) Quantitative Microscopy. New York: McGraw-Hill.

DOI, H., FUJIWARA, Y. and MIYAKE, K. (1969) *Transactions of the Metallurgical Society of the American Institute of Mining, Metallurgical and Petroleum Engineers*, **2**, p. 1457.

DUSJA, J., PARILAK, L. and SLESAR, M. (1987) Fracture characteristics of ceramic and cermet cutting tools. *Ceramics International*, **13**(3), p. 133-137.

EGAMI, A., EHIRA, M. and MACHIDA, M. (1993) *Proceedings of the 13th International Plansee Seminar*, BILDSTEIN, H. and ECK, R. (eds.), Metallwerk Plansee Reutte, 1993, vol.3, p. 693.

EL-ESKANDARANY, M.S. (1998) Mechanical solid state mixing for synthesizing of SiC_p/Al nanocomposites. Journal of Alloys and Compounds, 279, pp. 263-271.

EL-ESKANDARANY, M.S. (2000) Fabrication of nanocrystalline WC and nanocomposite WC–MgO refractory materials at room temperature. *Journal of Alloys and Compounds*, **296**(1-2), pp.175-182.

EL-ESKANDARANY, M.S. (2001) Mechanical alloying for fabrication of advanced engineering materials. New York: Noyes Publications.

EL-ESKANDARANY, M.S., SUMIYAMA, K., AOKI, K. and SUZUKI, K. (1992) Reactive ball mill for solid state synthesis of metal nitrides powders. *Materials Science Forum*, **801**, pp. 88-90.

EL-ESKANDARANY, M.S., MAHDAY, A.A., AHMED, H.A. and AMER, A.M. (2000) Synthesis and characterizations of ball-milled nanocrystalline WC and nanocomposite WC–Co powders and subsequent consolidations. *Journal of Alloys and Compounds*, **312**, pp. 315-325.

ENGLE, E.W. (1942) *Powder Metallurgy*. Ohio: ASM.

EREMENKO, V.N., NAIDICH, Y.V. and LAVRINENKO, I.A. (1970) *Liquid phase sintering*. New York: Consultants Bureau.

ESAWI, A.M.K. (2005) From nanopowders to finished products – the route towards application. *in*: *Proceedings of the 12th International Conference on Composites/Nanoengineering*, ICCE-12, August 1 – 6, 2005, Tenerife, Spain.

EVANS, A.G. (1982) Structural reliability: a processing dependent phenomenon. *Journal of the American Ceramic Society*, **65**, pp. 127-137.

EXNER, H.E. (1979) Physical and chemical nature of cemented carbides. *International Metals Review*, **24**, pp. 149-173.

EXNER, H.E. (1983) Qualitative and quantitative interpretation of microstructures in cemented carbides. *in*: *Science of Hard Materials*, Viswanadham, R.K., Rowcliffe, D.J. and Gurland, J. (eds.), Plenum Press, New York, pp. 233–262.

EXNER, H.E. and GURLAND, J. (1970) A review of parameters influencing some mechanical properties of tungsten carbide-cobalt alloys. *Powder Metallurgy*, **13**, pp. 13-31.

EXNER, H.E., WALTER, A., WALTER, P. and PETZOW, G. (1978) Auswirkung der wolframkarbid-ausgangspulver auf gesinterte wolframkarbid-kobalt-hartmetalle. *Metallwissenschaft und Technik*, **32**(5), pp. 443–448.

FALKOVSKY, V.A., KLYACHKO, L.I and GLUSHKOV, V.N. (2001) *in*: *Proceedings of the 15th International Plansee Seminar on Hard Materials*, KNERINGER, G., RÖDHAMMER, P. and WILDNER, H. (eds.), vol. 2, Plansee AG, Tyrol, Austria, 2001, pp. 29–34.

FANG, Z. and EASON, J.W. (1993) Nondestructive evaluation of WC-Co composites using magnetic properties. *International Journal of Powder Metallurgy*, **29**(3), pp. 259-265.

FANG, Z. and EASON, J.W. (1995) Study of nanostructured WC-Co composites. *International Journal of Refractory Metals and Hard Materials*, **13**(5), pp. 297-303.

FANG, Z., MAHESHWARI, P., WANG, X., SOHN, H.Y., GRIFFO, A. and RILEY, R. (2005) An experimental study of the sintering of nanocrystalline WC–Co powders. *International Journal of Refractory Metals and Hard Materials*, 23, pp. 249-257.

FAROOQ, M.U. and KLEMENT, U. (2004) EBSD characterization of carbide -carbide boundaries in WC–Co composites. *Journal of Microscopy*, **213**(3), pp. 306–312.

FAUDOT, F., GAFFET, E. and HARMELIN, M. (1993) Identification by DSC and DTA of the oxygen and carbon contamination due to the use of ethanol during mechanical alloying of Cu-Fe powders. *Journal of Materials Science*, **28**(10), pp. 2669-2676.

FECHT, H.J. (1994) Nanophase materials by mechanical attrition: synthesis and characterization. *in*: HADJIPANAYIS, G.C. and SIEGEL, R.W. (eds.) *Nanophase Materials*, Dordrecht: Kluwer, p. 125.

FECHT, H.J. (1995) Nanostructure formation by mechanical attrition. *Nanostructured Materials*, **6**, pp. 33-42.

FISCHMEISTER, H.F. (1981) Development and present status of the science and technology of hard materials. *in*: Science of Hard Materials, VISWANADHAM, R.K., ROWCLIFFE, D.J. and GURLAND, J. (eds.), *Proceedings of the international conference on the science of hard materials*, 1981. New York: Plenum, pp. 1–42.

FISCHMEISTER, H.F. and EXNER H.E. (1965) Beobachtungen über den Mahlvorgang bei Hartmetallpulvern, *Planseeber Pulvermet* **13**, pp. 178–198.

FOGAGNOLO, J.B., VELASCO, F., ROBERT, M.H. and TORRALBA, J.M. (2003) Effect of mechanical alloying on the morphology, microstructure and properties of aluminium matrix composite powders. *Materials Science and Engineering A*, **342**, pp. 131-143.

FOUGERE, G. E., WEERTMAN, J.R., SIEGEL, R.W. and KIM, S. (1992) Grain-size dependent hardening and softening of nanocrystalline Cu and Pd. *Scripta Metallurgica et Materialia*, **26**(12), pp. 1879-1883.

FREYTAG, J. and EXNER, H.E. (1977) The influence of tungsten and carbon additions on the sintering and the magnetic properties of WC-12Co cemented carbides. *in*: Hausner, H.H. and Taubenblat, P.V. (eds.), *Modern developments in powder metallurgy*, Princeton: MPIF-APMI, 1977, vol.10, pp. 511–523.

FROSCHAUER, L. AND FULRATH, R.M. (1976) Direct observation of liquid-phase sintering in the system tungsten carbide-cobalt. *Journal of Material Science*, **11**, pp. 142–149.

GANAPATHI, S.K., OWEN, D.M., and CHOKSHI, A.H. (1991) The kinetics of grain growth in nanocrystalline copper. *Scripta Metallurgica et Materialia*, **25**(12), pp. 2699-2704.

GAO, L., LI, W., WANG, Z.H., ZHOU, J.X., CHAO, Z.J. and ZAI, Q.Z. (2001) Fabrication of nano Y–TZP materials by super-high pressure compaction. *Journal of the European Ceramic Society*, **21**(2), pp. 135-138.

GE, R. (1995) *Powder Metallurgy Science and Technology*, **6**(3), pp. 20-24.

GERMAN, R.M. (1985) *Liquid phase sintering*. New York: Plenum Press.

GERMAN, R.M. (1989) *Particle packing characteristics*. Princeton: Metal Powder Industry.

GERMAN, R.M. (1996) *Sintering theory and practice*. New York: Wiley- Interscience.

GERMAN, R.M. and OLEVSKY, E. (2005) Mapping the compaction and sintering response of tungsten-based materials into the nanoscale size range. *International Journal of Refractory Metals and Hard Materials*, **23**(4-6), pp. 294-300.

GILLE, G., LEITNER, G. and ROEBUCK, B. (1996) Sintering behaviour and properties of WC–Co hardmetals in relation to the WC powder properties. *in*: EURO PM96, pp. 195-210.

GILLE, G., BREDTHAUER, J., GRIES, B., MENDE, B. and HEINRICH, W. (2000) Advanced and new grades of WC and binder powder – their properties and application. *International Journal of Refractory Metals and Hard Materials*, **18**, (2-3), pp. 87-102.

GILLE, G., SZESNY, B., DREYER, K., van den BERG, H., SCHMIDT, J., GESTRICH, T. and LEITNER, G. (2002) Submicron and ultrafine grained hardmetals for microdrills and metal cutting inserts. *International Journal of Refractory Metals and Hard Materials*, **20**(1), pp. 3-22.

GILLE, G., SZESNY, B. and LEITNER, G. (1999) A new 0.4 mm WC powder as well as powder-related properties and sintering Behaviour of 0.6 to 30 mm WC-Co Hardmetals. *Journal of Advanced Materials*, **2**, p. 9.

GILLIA, O. and BOUVARD, D. (2000) Phenomenological analysis of densification kinetics during sintering: application to WC–Co mixture. *Materials Science and Engineering A*, **279**(1-2), pp. 185-191.

GILMAN, P.S. and BENJAMIN, J.S. (1983) Mechanical Alloying. *Annual Review of Materials Science*, **13**, pp. 279-300.

GILMAN, P.S. and NIX, W.D. (1981) The structure and properties of aluminum alloys produced by mechanical alloying: powder processing and resultant powder structures. *Metallurgical and Materials Transactions A*, **12**(5), pp. 813-824.

GLEITER, H. (2000) Nanostructured materials: basic concepts and microstructure *Acta Materialia*, **48**(1), pp. 1-29.

GOREN-MUGINSTEIN G.R., BERGER, S. and ROSEN, A. (1998) Sintering study of nanocrystalline tungsten carbide powders. *Nanostructured Materials*, 10(5), pp. 795-804.

GORKUNOV, E., ULYANOV, A. and CHULKINA, A. (2004) *in*: *Proceedings of the 16th World Conference NDT*, vol. 9, 2004.

GRAAT, P. (2004) X-ray diffraction – technical note 13. Philips Research. http://www.research.philips.com/technologies/projects/matanalysis/publications.html.

GREARSON, A., JAMES, M., TILLMAN, M., NORGREN, S. and GUSTAFFSON, P. (2005) The future of finer grain hard metals. *in*: *Proceedings of the 16th international plansee seminar*, KNERINGER, G., RÖDHAMMER, P. and WILDNER, H. (eds.), PLANSEE Holding AG, Reutte, Austria, pp. 314–338.

GREENWOOD, R.M., LORETTO, M.H. and SMALLMAN, R.E. (1982) The defect structure of tungsten carbide in deformed tungsten carbide-cobalt composites. *Acta Metallurgica,* **30**(6), pp. 1193-1196.

GROZA, J.R. and DOWDING, R.J. (1996) Nanoparticulate materials densification. *Nanostructured Materials*, **7**(7), pp. 749-768.

GROZA, J.R. (2007) Nanocrystalline powder consolidation methods. *in*: Koch, C.C. (ed.), *Nanostructured Materials: Processing, Properties, and Applications,* 2nd ed., William Andrew Inc., pp. 173–234.

GUILLERMET, A. F. (1988) Study of the thermodynamic properties of the Co–Fe–Ni–W–C system using CALPHAD techniques, Ph.D Thesis, Royal Institute of Technology, Stockholm.

GURLAND, J. and BARDZIL, P.B. (1955) *Transactions of the Metallurgical Society of the American Institute of Mining, Metallurgical and Petroleum Engineers*, **203**, p. 311-315.

GURLAND, J. (1963) *Transactions of the Metallurgical Society of the American Institute of Mining, Metallurgical and Petroleum Engineers*, **227**, pp. 1146-1150.

GURLAND, J. (1979) A structural approach to the yield strength of two-phase alloys with coarse microstructures. *Materials Science and Engineering*, **40**(1), pp. 59-71.

HAGLUND, S. and AGREN, J. (1998) W content in Co binder during sintering of WC-Co. *Acta Materialia*, **46**(8), pp. 2801-2807.

HAGLUND, S., AGREN, J. and UHRENIUS, B. (1998) Solid state sintering of cemented carbides - an experimental study. *Zeit Metallk*, **89**.

HAGLUND, S. (1998) Sintering of cemented carbides-experiments and modeling. Ph.D thesis, Royal Institute of Technology, Stockholm, Sweden.

HAGUE, D.C., and MAYO, M.J. (1997) Sinter-Forging of Nanocrystalline Zirconia: 1, Experimental. *Journal of the American Ceramic Society*, **80**, pp. 149–156.

HANSEN, J.D., RUSIN, R.P., TENG, M.-H. and JOHNSON, D.L. (1992) Combined-stage sintering model. *Journal of the American Ceramic Society*, **75**, pp. 1129–1135.

HARRIS, C.C. (1968) The application of size distribution equations to multi-event comminution processes. *Transactions of the American Society of Mining Engineers*, **241**, pp. 343-357.

HE, J., AJDELSZTAJN, L. and LAVERNIA, E.J. (2001) Thermal stability of nanocrystalline WC-Co powder synthesized by using mechanical milling at low temperature. Journal of Materials Research, 16(2), pp. 478-488.

HECKEL, R. W. (1961) Density - pressure relationships in powder compaction. Transaction of Metallurgical Society ofAIME**,** 221, p. 671.

HELLSING, M., HENJERED, A., NORDEN, H., and ANDREN, H. O. (1983) *in*: *Science of Hard Materals,* VISWANADHAM, R.K., ROWCLIFFE, D.J. and GURLAND, J. eds., Plenum Press, New York, p. 93.

HELLSTERN, E., FECHT, H. J., FU, Z. and JOHNSON, W. L. (1989) Structural and thermodynamic properties of heavily mechanically deformed Ru and AlRu. *Journal of Applied Physics*, **65**, p. 305.

HIBBS, M.K. and SINCLAIR, R. (1981) Room-temperature deformation mechanisms and defect structure of tungsten carbide. *Acta Metallurgica*, **29**(9), pp. 1645-1654.

HINNUBER J., RUDIGER O. and KINNA W. (1961) Powder Metallurgy 1961; **5**(8), p. 1.

HUANG, B.-L., PEREZ, R.J., CRAWFORD, P.J., NUTT, S.R. and LAVERNIA, E.J. (1996) The synthesis of nanocrystalline $Fe_{78}B_{13}Si_9$ by cryogenic high-energy ball milling of metglas. *Nanostructured Materials*, **7**(1-2), pp. 57-65.

HUANG, B.-L., PEREZ, R.J. and LAVERNIA, E.J. (1998) Grain growth of nanocrystalline Fe–Al alloys produced by cryomilling in liquid argon and nitrogen. *Materials Science and Engineering A*, **255**(1-2), pp.124-132.

HUANG, S.G., VANMEENSEL, K., LI, L., Van der BIEST, O. and VLEUGELS, J. (2008) Influence of starting powder on the microstructure of WC–Co hardmetals obtained by spark plasma sintering. *Materials Science and Engineering A*, **475**(1-2), pp. 87-91.

HUANG, J.Y., WU, Y.K. and YE, H.Q. (1996) Allotropic transformation of cobalt induced by ball milling. *Acta Materialia*, **44**(3), pp. 1201-1209.

HUMPHREYS, F.J. (2001) Texture analysis: macrotexture, microtexture and orientation mapping. *Journal of Microscopy*, **203**(2), pp. 231–232.

HUMPHREYS, F.J. (2004) Characterisation of fine-scale microstructures by electron backscatter diffraction (EBSD). *Scripta Materialia*, **51**, pp. 771–776.

HUMPHREYS, F.J. and BROUGH, I. (1999) High resolution backscatter diffraction with a field emission gun scanning electron microscope. *Journal of Microscopy* **195**, pp. 6-9.

HUMPHREYS, F.J. and HATHERLY, M. (1996) Recrystallization and Related Annealing Phenomena. Oxford: Pergamon.

HUPPMAN, W.J. and RIEGGER, H. (1975) Modelling of rearrangement processes in liquid phase sintering. *Acta Metallurgica*, **23**(8), pp. 965-971.

HWANG, S.J., NASH, P., DOLLAR, M. and DYMEK, S. (1992) The production of intermetallics based on NiAl by mechanical alloying. *Materials Science Forum*, **88-90**, pp. 611-618.

JAEGER, D.M. and JONES, A.R. (1994) Dispersoid Distribution in Iron based ODS alloys made by Mechanical Alloying. *in*: COUTSOURADIS, D. et al. (eds.), *Materials for Advanced Power Engineering*, *Part II*, Dortrecht: Kluwer Academic Publishers, pp. 1507-1514.

JAROENWORALUCK, A., YAMAMOTO, T., IKUHARA, Y., SAKUMA, T., TANIUCHI, T., OKADA, K. and T. TANASE (1998) Segregation of vanadium at the WC/Co interface in VC-doped WC-Co. *Materials Research Society*, **13**(9), pp. 2450-2452.

JAWITZ, M.W. (1967) *Printed circuit board materials handbook*. New York: McGraw-Hill Professional.

JIA, C-C., TANG, H., MEI, X.-Z., YIN, F.-Z. and QU, X.-H. (2005) Spark plasma sintering on nanometer scale WC–Co powder. *Materials Letters*, **59**(19-20), pp. 2566-2569.

JOHANSSON, T. and UHRENIUS B. (1978) Phase equilibria, isothermal reactions, and a thermodynamic study in the Co-W-C system at 1150 degree C. *Metal Science*, **12**(2), pp. 83-94.

JUNG, J. and KANG, S. (2005) Compaction as a critical factor for success in the sintering of ultra-fine WC-Co powders. *Journal of the American Ceramic Society*, **88** (11), pp. 3032–3036.

KALOSHKIN, S.D., TOMLIN, I.A., ANDRIANOV, G.A., BALDOKHIN, U.V. and SHELEKHOV, E.V. (1997) Phase transformations and hyperfine interactions in mechanically alloyed Fe-Cu solid solutions. *Materials Science Forum*, **235-238**, pp. 565-70.

KANG S-JL. (2005) *Sintering*. Oxford: Elsevier Butterworth-Heinemann.

KANG, S.-J.L and JUNG, Y.-ll. (2004) Sintering kinetics at final stage sintering: model calculation and map construction. *Acta Materialia*, **52**(15), pp. 4573-4578.

KANG, S.-J.L., KAYSSER, W.A., PETZOW, G. and YOON, D.N. (1984) Elimination of pores during liquid phase sintering of Mo-Ni. *Powder Metallurgy*, **27**, pp. 97-100.

KAWAKITA, K. and LÜDDE, K.-H. (1971) Some considerations on powder compression equations. *Powder Technology*, **4**(2), pp. 61-68.

KAYSSER, W.A., FRISCH, A., ASLAN, M. and PETZOW, G. (1988) Microstructural development during final stage HIPing. *in: Proceedings of the International conference on hot isostatic pressing of materials: applications and development*, Antwerp, Belgium, 25-27 Apr., 1988, pp. 2.1-2.9.

KAYSSER, W.A. and HUPPMANN, W.J. (1986) *Verlag-Schmid, Freiburg, Part II*. p. 1205.

KIM, B.K., HA, G.H., LEE, D.W., LEE G.G. and AHN, I.S. (1998) Chemical processing of nanostructured cemented carbide. *Advanced Performance Materials*, **5**(4), pp. 341-352.

KIM, H.C., SHON, I.J., GARAY, J.E. and MUNIR, Z.A. (2004) Consolidation and properties of binderless sub-micron tungsten carbide by field-activated sintering. *International Journal of Refractory Metals and Hard Materials*, **22**, pp. 257–264.

KIM, Y.D., CHUNG, J.Y., KIM, J. and JEON, H. (2000) Formation of nanocrystalline Fe–Co powders produced by mechanical alloying. *Materials Science and Engineering A*, **291**, pp. 17-21.

KINGERY, W.D., BOWEN, H.K. and UHLMAN, D. R. (1976) *Introduction to Ceramics*, 2nd ed., John Wiley & Sons.

KISHINO, J., NOMURA, H., SHIN, S.-G., MATSUBARA, H. and TANASE, T. (2002) Computational study on grain growth in cemented carbides. *International Journal of Refractory Metals and Hard Materials*, **20**(1), pp. 31-40.

KIS-VARGA, M. and BEKE, D.L. (1996) Phase transitions in Cu-Sb systems induced by ball milling. *Materials Science Forum*, **225-227**, pp. 465-470.

KLEINER-BICHERL, A., SCHUBERT, W.D., SCHÖN, A., BOCK, A. (2006) *WC-Co* hardmetals containing alumina dispersoids. *in: EURO PM 2006 Proceedings Volume 1-Hard Materials*, EPMA, (2006), pp. 69-75.

KOCH, C.C., PATHAK, D. and YAMADA, K. (1993) *in*: deBARBADILLO, J.J. et al., (eds.) *Mechanical alloying for structural applications*. Materials Park, OH: ASM International, pp. 205-212.

KOCH, C.C. (1997) Synthesis of nanostructured materials by mechanical milling: problems and opportunities. Nanostructured Materials, 9, pp. 13-22.

KUHN, E. (1984) Powder metallurgy. Ohio: ASM International.

KUMAI, S., KING, J.E. and KNOTT, J.F. (1991) Fatigue in SiC-particulate-reinforced aluminium alloy composites. *Materials Science and Engineering A*, **146**, pp. 317-326.

KWON, Y.-S., GERASIMOV, K.B. and YOON, S.Y. (2002) Ball temperatures during mechanical alloying in planetary mills. *Journal of Alloys and Compounds*, **346**(1-2), pp. 276-281.

LANGE, F.F., DAVIS, B.I. and AKSAY, I.A. (1983) Processing-related fracture origins: III differential sintering of ZrO_2 agglomerates in Al_2O_3/ZrO_2 composite. *Journal of the American Ceramic Society*, **66**(6), pp. 407-408.

LANGE, F.F. (1989) Powder processing science and technology for increased reliability. *Journal of the American Ceramic Society*, **72**, pp. 3-15.

LARDNER, E., SPRIGGS, G.E. and WOOD, G.A. (1972) *Powder Metallurgy*, **15**(30), p. 267.

LASSNER, E. and SCHUBERT, W.-D. (1999) *Tungsten: Properties, Chemistry, Technology of the Element, Alloys, and Chemical Compounds*. New York: Kluwer/Plenum Publishers.

LAU, M.L., JIANG, H.G., PEREZ, R.J., JUAREZ-ISLAS, J. and LAVERNIA, E.J. (1996) *in*: BOURELL, B,L. (ed.) TMS proceedings of processing and properties of nanocrystalline materials, p. 255.

LAUGIER, M.T. (1987) New formula for indentation toughness in ceramics. *Journal of Materials Science Letters*, **6**, pp. 355-356.

LAY, S., THIBAULT, J. and HAMAR-THIBAULT, S. (2003) Structure and role of the interfacial layers in VC rich WC–Co cermets. *Philosophy Magazine*, **83**(10), pp.1175–1190.

LEE, G.-H., PARK, S., KANG, S., CHUNG, K.-H. and LAVERNIA, E.J. (2003) Processing issues for cryomilled WC-Co nanopowders. *Materials Transactions*, **44**, pp. 1935-1941.

LEE, H.C. and GURLAND, J. (1978) Hardness and deformation of cemented tungsten carbide. *Materials Science and Engineering*, **33**, pp. 125-133.

LEE, J., ZHOU, F., CHUNG, K.H., KIM, N.J. and E.J. LAVERNIA (2001) Grain growth of nanocrystalline Ni powders prepared by cryomilling. *Metallurgical and Materials Transactions*, **32A**, pp. 3109-3115.

LEE, P.Y., YANG, J.L. and LIN, H.M. (1998) Amorphization behaviour in mechanically alloyed Ni—Ta powders. *Journal of Materials Science*, **33**(1), pp. 235-239.

LEE, S.-M., CHAIX, J.-M., MARTIN, C.L., ALLIBERT, C.H. and KANG, S.-J.L. (1999) Computer simulation of particle rearrangement in the presence of liquid. *Metals and Materials*, **5**, pp. 197-203.

LEE, S.-M. and KANG, S.-J.L. (2001) Evaluation of densification mechanisms of liquid phase sintering. *Zeitschrift Fur Metallkunde*, **92**, pp. 669-674.

LEITNER, G., GESTRICH, T. and GILLE G. (1997) Shrinkage, liquid phase formation and gaseous reactions during sintering of WC-Co hardmetals and correlation to the WC grain size. *in*: KNERINGER, G., RÖDHAMMER, P. and WILHARTITZ, P. eds. *Proceedings of the 14th International Plansee Seminar*, Plansee AG, Reutte, vol.2, pp. 86-89.

LINDAU, L. (1977) *in*: *Proceedings of the 4th international conference on fracture*, Waterloo, Canada, vol. 2, 1977, p. 21.

LINES, M.G. (2008) Nanomaterials for practical functional uses. *Journal of Alloys and Compounds*, **449**(1-2), pp. 242-245.

LINIGER, E. and RAJ, R. (1987) Packing and sintering of two-dimensional structures made from bimodal particle size distributions. *Journal of the American Ceramic Society*, **70**, pp. 843-849.

LOPEANDIA, A.F. and RODRIGUEZ-VIEJO, J. (2007) Size-dependent melting and supercooling of Ge nanoparticles embedded in a SiO_2 thin film. *Thermochimica Acta*, **461**, pp. 82-87.

LU, L. and LAI, M.O. (1998) *Mechanical alloying*. New York: Kluwer Academic Publishers.

LU, L. and LAI, M.O. (1995) Formation of new materials in the solid state by mechanical alloying. *Materials & Design*, **16**(1), pp. 33-39.

LUETH, R.C. (1974) Fracture mechanics of ceramics. *in*: Bradt, R.C. *et al*. (ed.) New York: Plenum Press, vol.2, p. 791.

LUO, P., NIEH, T.G., SCHWARTZ, A.J. and LENK, T.J. (1995) Surface characterisation of nanostructured metal and ceramic particles. *Materials Science and Engineering*, **A204**, pp. 59–64.

LUTON, M.J., JAYANTH, C.S., DISKO, M.M., MATRAS, S. and VALLONE, J. (1989) *in*: MCCANDLISH, L.E., POLK, D.E., SIEGEL, R.W. and KEAR, B.H., (eds.) *Materials Research Society Symposium Proceedings*, Pittsburgh, PA, 1989, p. 79.

LUYCKX, S.B. (1975) Role of inclusions in the fracture initiation process in WC-Co alloys. *Acta Metallurgica*, **23**, pp. 109-115.

LUYCKX, S.B. (2004) *WITS Research Showcase, "Materials science – cemented tungsten carbide."* <http://web.wits.ac.za/NR/rdonlyres/06D40843-A7DF-46CA-9CBE-6583DF3E9D78/0/Materials.pdf> (accessed May 15, 2006).

LUYCKX, S.B. and ALLI, M.Z. (2001) Comparison between V C and Cr C as grain refiners for WC-Co. *Materials and Design*, **22**, pp. 507-510.

LUYCKX, S.B, OSBORNE, C., CORNISH, L. and WHITEFIELD, D. (1996) Fine grained WC–VC–Co hardmetal. *Journal of Powder Metallurgy*, **39(**3), pp. 210–212.

LYNDON, J. and SWARTZENDRUBER, J. (1991) Properties, units and constants in magnetism. *Journal of Magnetism and Magnetic Materials*, **100**(1-3), pp. 573-575.

MAYO, M.J., CHEN, D.J. and HAGUE, D.C. (1996) Consolidation of nanocrystalline materials by compaction and sintering. *in*: EDELSTEIN, A.S. and CAMMARATA, R.C. (eds.) *Nanomaterials: Synthesis, Properties and Applications*. Bristol: The Institute of Physics, pp. 165–197.

McCANDLISH, L.E., KEAR, B.H. and BHATIA, S.J. (1994) Spray conversion process for the production of nanophase composite. US Patent, 5 352 269.

McCANDLISH, L.E., KEAR, B.H. and KIM, B.K. (1992) Processing and properties of nanostructured WC-Co. *Nanostructured Materials*, **1**(2), pp. 119-124.

MEREDITH, B. and MILNER, D.R. (1976) Densification mechanisms in the tungsten carbide-cobalt system. *Powder Metallurgy*, **1**, pp. 38-45.

MI, S. and COURTNEY, T.H. (1997) Synthesis of WC and WC-Co Cermets by Mechanical Alloying and Subsequent Hot Isostatic Pressing. *Scripta Materialia*, **38**(1), pp. 171-176.

MICHALSKI, A. and SIEMIASZKO, D. (2007) Nanocrystalline cemented carbides

sintered by the pulse plasma method. *International Journal of Refractory Metals and Hard Materials*, **25**(2), pp. 153-158.

MISSIAEN, J.M. and ROURE, S. (1998) A general morphological approach of sintering kinetics: application to WC-Co solid state sintering. *Acta Materialia*, **46**(11), pp. 3985-3993.

MOELLE, C., SCHMIDT, C., MÜLLER, K. and FECHT, H.J. (1996) Synthesis, compaction and properties of nanocrystalline attrited powder. *in*: BOURELL, D.L. (ed.) *Synthesis and processing of nanocrystalline powder*. The Minerals, Metals & Materials Society, pp. 121-131.

MORRELL, R. (1997) Flexural strength testing of ceramics and hardmetals. Measurement good practice guide, No.7, National Physical Laboratory.

MORSI, K., SHINDE, S. and OLEVSKY, E.A. (2006) Effect of nickel particle size on the compaction behavior of rotator mixed and mechanically alloyed nickel and aluminum powders. *Materials Science and Engineering: A*, **426**(1-2), pp. 283-288.

MORTENSEN, A. (1997) Kinetics of densification by solution-reprecipitation. *Acta Materialia*, **45**(2), pp. 749-758.

MORTON, C.W., WILLS, D.J. and STJERNBERG, K. (2005) The temperature ranges for maximum effectiveness of grain growth inhibitors in WC–Co alloys. *International Journal of Refractory Metals and Hard Materials*, **23**(4-6), pp. 287-293.

MOTYL, E.J. (1963) Spray drying ferrite powder. *Western Electric Engineer*, **7**(3), pp. 3-10.

MUNIR, Z.A., ANSELMI-TAMBURINI, U. and OHYANAGI, M. (2006) The effect of electric field and pressure on the synthesis and consolidation of materials: a review of the Spark Plasma Sintering method. *Journal of Materials Science*, **41**, pp. 763-777.

MURTY, G.S., KOCZAK, M.J. and FRAZIER, W.E. (1987) High temperature deformation of rapid solidification processed/mechanically alloyed Al---Ti Alloys. *Scripta Metallurgica*, **21**(2), pp. 141-146.

NELSON, R.J., and MILNER, D.R. (1972) Densification processes in the tungsten carbide cobalt system. *Powder Metallurgy*, **15**, pp. 347-363.

NGERNBAMRUNG, S., DATERAKSA, K., BOONYONGMANEERAT, Y., CHUANKRERKKUL, N. and SUJIROTE, K. Processing of ultrafine grained WC-Co

hardmetals for property enhancements. In: proceedings of the 3rd international conference on processing materials for properties (PMP-III), Dec 7-10, Bangkok, 2008.
NIESZ, D.E. (1996) A review of ceramic powder compaction. *Kona*, **14**, pp. 44-51.
NIIHARA, K., MORENA, R. and HASSELMAN, D.P.H. (1982) Evaluation of KIC of brittle solids by the indentation method with low crack-to-indent ratios. *Journal of Materials Science Letters*, **1**, pp. 13-16.
NIIHARA, K. (1983) A fracture mechanics analysis of indentation-induced Palmqvist cracks in ceramics. *Journal of Materials Science Letters,* **2,** pp. 221–223.
NISHIMURA, T., MITOMO, M., HIROTSURU, H. and KAWAHARA, M. (1995) Fabrication of silicon nit*ride nano-ceramics by spark plasma sintering.* Journal of Materials Science Letters, **14**(15), pp. 1046-1047.
NYGREN, M. and SHEN, Z.J. (2003) On the preparation of bio-, nano- and structural ceramics and composites by spark plasma sintering.
Solid State Sciences, **5**, pp. 125-131.
OGILVY, I.M., PERROTT, C.M. and SUITER, J.W. (1977) On the indentation fracture of cemented carbide Part 1 – survey of operative fracture modes. *Wear*, **43**, pp. 239–252.
OLESZAK, D. and SHINGU, P.H. (1996) Nanocrystalline metals prepared by low energy ball milling. *Journal of Applied Physics*, **79**(6), pp. 2975-2980.
OLEVSKY, E., KANDUKURI, S. and FROYEN, L. (2007) Analysis of mechanisms of spark-plasma sintering. *Key Engineering Materials*, **368-372**, pp. 1580-1584.
PADMANABHAN, K.A. and HAHN, H. (1996) Microstructures, mechanical properties and possible applications of nanostructured materials. *in*: BOURELL, D.L. (ed.) *Synthesis and processing of nanocrystalline powder*. The Minerals, Metals & Materials Society, p.21.
PAEK, Y.K., EUN, K.Y. and KANG, S.-J.L. (1988) Effect of sintering atmosphere on densification of MgO doped Al_2O_3. *Journal of the American Ceramic Society*, **71**, pp. 380-82.
PALMQVIST, S. (1962) Ribildungsarbeit bei Vickers-Eindrücken als Ma für die Zähigteit von hartmetallen. *Arch. Eisenhütternwes.*, 33, pp. 629-634.
PANELLI, R; AMBROZIO FILHO, F.A (1998) Compacting equation and its use to describe the powder consolidation behavior. *Powder Metallurgy*, v. 41, No. 2,

pp. 131-133.

PARK, H.H., KWON, O.-J. and YOON, D.N. (1986) The critical grain size for liquid flow into pores during liquid phase sintering. *Metallurgical and Materials Transactions A*, **17**(11), pp. 1915-1919.

PARK, J.-K, KANG, S.J-L., EUN, K.Y. and YOON, D.N. (1989) Microstructural change during liquid phase sintering of W−Ni−Fe alloy. *Metallurgical and Materials Transactions A*, **20**(5), pp. 837-845.

PARK, J.S., JOHNSON, J.L. and GERMAN, R.M. (2006) Advances in powder metallurgy and particulate materials. *In*: *proceedings of the 2006 international conference on powder metallurgy and particulate materials*, June 18-21, San Diego, California, 2006.

PAUL, A.V., GNYUSOV, S.F., IVANOV, Y.F., KUL'KOV, S.N. and KOZLOV, E.V. (1994) Structural-phase changes in hard alloy WC-steel 110G13 after dynamic loading. *Russian Physics Journal*, **37**(8), pp. 757-761.

PETERS, C.T. (1979) The relationship between Palmqvist indentation toughness and bulk fracture toughness for some WC-Co cemented carbides. *Journal of Materials Science*, **14**, pp.1619-1623.

PETERSSON, A. (2004) *Cemented carbide sintering: constitutive relations and microstructural evolution*. P.hD. Thesis, Royal Institute of Technology, Sweden.

PETZOW, G. and EXNER, H.E. (1976) Particle rearrangement in solid state sintering. *Zeitschrift Fur Metallkunde*, **67**, pp. 611-618.

PHUNG, X., GROZA, J., STACH, E.A., WILLIAMS, L.N. and RITCHEY, S.B. (1993) Surface characterization of metal nanoparticles. *Materials Science and Engineering A*, **359**(1-2), pp. 261-268.

PICKENS, J.R. and GURLAND, J. (1978) The fracture toughness of WC---Co alloys measured on single-edge notched beam specimens precracked by electron discharge machining. *Materials Science and Engineering*, **33**(1), pp. 135-142.

POPA, N.C. and BALZAR, D. (2002) An analytical approximation for a size-broadened profile given by the lognormal and gamma distributions. *Journal of Applied Crystallography*, **35**, pp. 338-346.

POQUILLON, D., LEMAITRE, J., BACO-CARLES, V., TAILHADES, P.H., and LACAZE, J. (2002) Cold compaction of iron powders—relations between powder morphology and mechanical properties. Part I: Powder preparation and compaction. *Powder Technology*, **126**, pp. 65-74.

PORAT, R., BERGER, S. and ROSEN A. (1996) Dilatometric study of the sintering mechanism of nanocrystalline cemented carbides. *Nanostructured Materials*, **7**(4), pp. 429-36.

PORAT, R. and MALEK, J. R. (1988) Binder mean free-path determination in cemented carbide by coercive force and material composition, *Israel Journal of Technology*, **24**,pp. 405–414.

PORTER, D.A. and EASTERLING, K.E. (1992) *Phase transformations in metals and alloys*. 2nd ed., Florida: CRC Press Inc.

QVICK J. (1988) Use of oxygen probes to study and control the atmosphere during reduction of tungsten oxide. *International Journal of Refractory Metals and Hard Materials*, **7**, pp. 201-205.

RABE, T. and WÄSCHE, R. (1995) Sintering behaviour of nanocrystalline titanium nitride powders. *Nanostructured Materials*, **6**(1-4), pp. 357-360.

RABITSCH, K. and VEITSCH, C. (2007) Strategies for grain growth inhibition in hard metals. *in*: *Proceedings of EURO PM2007*, Toulouse, France, 15-17 October 2007, EPMA.

RADLINSKI, A.P., CALKA, A., NINHAM, B.W. and KACZMAREK, W.A. (1991) Application of surface active substances in mechanical alloying. *Materials Science and Engineering* A, **134**, pp. 1346-1349.

ROEBUCK, B. and ALMOND, E.A. (1988) Deformation and fracture processes and the physical metallurgy of WC/Co hardmetal. *International Materials Review*, **33**(2), pp. 90-110.

ROEBUCK, B., BENNETT, E.G. and GEE, M.G. Grain size measurement methods for WC/Co hardmetals. *in*: *Proceedings of the 13th International Plansee Seminar*, May 24-28, 1993, Reutte, Austria, V2, pp. 273-292.

ROEBUCK, B. (1995) A model for the limiting strength of hardmetals. *Journal of Hard Materials*, **6**, pp. 1-15.

ROEBUCK, B. (1995) Terminology, testing, properties, imaging and models for fine grained hardmetals. *International Journal of Refractory Metals and Hard Materials*, **13**, pp. 265-279.

ROOSEN, A. and BOWEN, H.K. (1988) Influence of various consolidation techniques on the green microstructure and sintering behavior of alumina powders. *Journal of the American Ceramic Society*, **71,** pp. 970–977.

ROURE, S. (1996) *Densification de melanges de poudres WC-Co: de la compression au frittage*. Ph.D. Thesis, Institut Polytechnique de Grenoble, France.

ROURE, S. and MISSIAEN, J.M. (1995) Contribution of image analysis to solid state sintering of WC-Co. *Acta Stereology*, **14**(2), p. 215-222.

ROURE, S., BOUVARD, D., DORÉMUS, P. and PAVIER, E. (1999) Analysis of die compaction of tungsten carbide and cobalt powder mixtures. *Powder Metallurgy*, **42**(2), pp. 164-170.

SADAHIRO, T. and TAKATSU, S. (1981)A new precracking method for fracture toughness testing of cemented carbides. *in*: HAUSER, H.H., ANTES, H.W. and SMITH, G.D. (eds.) *modern developments in powder metallurgy*, vol. 14. New Jersey, Metal Powder Industries Federation, pp. 561–72.

SADANGI, R.K., McCANDLISH, L.E., KEAR, B.H. and SEEGOPAUL, P. (1998) Grain growth inhibition in liquid phase sintered nanophase WC/Co alloys. *in*: *Advances in powder metallurgy and particulate materials*, New Jersey, Metal Powder Industries Federation, pp. 1.51–1.60.

SAITO, T., TANIGUCHI, Y., KOBAYASHI, M. and KOBORI, K. (1998) Mechanical properties of disk reinforced cemented carbides. *in: Proceedings of the conference on powder metallurgy and particulate materials,* 1998, Las Vegas. New Jersey, Metal Powder Industries Federation, pp. 1–149.

SALIMON, A.I., KORSUNSKY, A.M and IVANOV, A.N (1999) The character of dislocation structure evolution in nanocrystalline FCC Ni-Co alloys prepared by high-energy mechanical milling. *Materials Science and Engineering A*, **271**(1-2), pp. 196-205.

SÁNCHEZ, J.M., ORDÓÑEZ, A., GONZÁLEZ, R. (2005) HIP after sintering of ultrafine WC–Co hardmetals. *International Journal of Refractory Metals and Hard Materials*, **23**, pp. 193-198.

SANDS, R.L. and SHAKESPEARE, C.R. (1966) *Powder metallurgy*. London: George Newnes Ltd.

SCHATT, W. and Wieters, K. (1997) Powder metallurgy-process and materials. 1st ed. Shrewsbury: EPMA.

SCHERRER, P. (1918) Bestimmung der grösse und der inneren struktur von kolloidteilschen mittels röntgenstrahlen. *Nachrichten der Gesellschaft Göttingen*, **26**, pp. 98-100.

SCHUBERT, W.D., BOCK, A. and LUX, B. (1993) General aspects and limits of conventional ultrafine WC powder manufacture and hard metal production. *in*: *Proceedings of the 13th International Plansee Seminar*, Metallwerk Plansee, Reutte, vol.4, pp. 283-305.

SCHUBERT, W.D., BOCK, A. and LUX, B. (1995) General aspects and limits of conventional ultrafine WC powder manufacture and hard metal production. *International Journal of Refractory Metals and Hard Materials*, **13**, pp. 281 296.

SCHUBERT, W.D., BOCK, A. and LUX, B. (1999) Aspects of ultrafine hardmetal sintering. *in*: ROSE, C.L. and THIBODEAU, M.H. (eds.) *Proceedings of the international conference on powder metallurgy and particulate materials*, vol.3, Vancouver, Canada, 1999, MPIF, pp. 23-36.

SCHWARZ, R. B, and KOCH, C. C. (1986) Formation of amorphous alloys by the mechanical alloying of crystalline powders of pure metals and powders of intermetallics. *Applied Physics Letters*, **49**, pp. 146-148

SCUSSEL, H.J. (1992) *Friction and Wear of Cemented Carbides*. ASM Handbook, ASM International, vol.18, p. 795.

SEO, O., KANG, S. and LAVERNIA, E. J. (2003) Growth inhibition of nano WC particles in WC-Co alloys during liquid-phase sintering. *Materials Transactions*, **44**(11), pp. 2339-2345.

SHAO, G.-Q., DUAN, X.-L., XIE, J.-R, YU, X.-H., ZHANG, W.-F. and YUAN, R.-Z. (2003) Sintering of nanocrystalline WC-Co composite powder. *Reviews on Advanced Materials Science*, **5**(4), pp. 281-286.

SHAPIRO, I.M. and KOLTHOFF, J. (1947) *Journal of Physical and Colloid Chemistry*, **51**, pp. 483-493.

SHETTY, D.K., WRIGHT, I.G., MINCER, P.N. and CLAUER, A.H. (1985) Indentation fracture of WC-Co cermets. *Journal of Materials Science*, **20**, pp. 1873-1882.

SHI, X.L., SHAO, G.Q., DUAN, X.L., XIONG, Z. and YANG, H. (2006) Characterizations of WC-10Co nanocomposite powders and subsequently sinterhip sintered cemented carbide. *Materials Characterization*, **57**(4-5), pp. 358-370.

SIGL, L.S. and FISCHMEISTER, H.F. (1988) On the fracture toughness of cemented carbides. *Acta Metallurgica*, **36**(4), pp. 887-897.

SIVAPRAHASAM, G., CHANDRASEKAR, S.B., and SUNDARESAN R. (2006) Microstructure and mechanical properties of nanocrystalline WC–12Co consolidated by spark plasma sintering. *International Journal of Refractory Metals and Hard Materials*, **25**(2), pp. 144-152.

SKRINJAR, O. and LARSSON, P-L. (2004) Cold compaction of composite powders with size ratio. *Acta Materialia*, **52**(7), pp. 1871-1884.

SNOWBALL, R.F., and MILNER, D.R. (1968) Densification processes in the tungsten carbide cobalt system. *Powder Metallurgy*, **11**(21) p. 2340.

SONI, P.R. (2000) *Mechanical alloying*. Cambridge: Cambridge International Science Publishing.

STIGLICH, J.J., YU, C.C. and SUDARSHAN, T.S. (1996) Synthesis of nano WC/Co for tools and dies. *in*: *Proceedings: International conference on tungsten refractory metals*, 1996, New Jersey, MPIF, pp. 229-236.

STJERNBERG, K. (1970) Some relationships between the structure and mechanical properties of WC-Co alloys. *Powder Metallurgy*, **13**(25), p. 1.

STOKES, A. R. and WILSON, A. J. C. (1942) *Proceedings of the Cambridge Philosophy Society*, **38**, p. 313.

SUN, J. and SIMON, S.L. (2007) The melting behaviour of aluminium nanoparticles. *Thermochimica Acta*, **463**, pp. 32-40.

SUN, J., ZHANG, F. and SHEN, J. (2003) Characterizations of ball-milled nanocrystalline WC–Co composite powders and subsequently rapid hot pressing sintered cermets. *Materials Letters*, **57**, pp. 3140-3148.

SUNDIN, S. and HAGLUND, S. (2000) A comparison between magnetic properties and grain size for WC/Co hard materials containing additives of Cr and V. *International Journal of Refractory Metals and Hard Materials*, 18(6), pp. 297-300.

SURYANARAYANA, C. (2001) Mechanical alloying and milling. *Progress in Materials Science*, **46**(1-2), pp. 1-184.

SWEENEY, S.M. and MAYO, M.J. (2002) Green density-based sintering predictions. *Journal of Materials Research*, **17**, pp. 89-97.

TAKACS, L. and PARDAVI-HORVATH, M. (1994) Nanocomposite formation in the Fe_3O_4-Zn system by reaction milling. *Journal of Applied Physics*, **75**(10), pp. 5864-5866.

TANAKA, T. and KOSUGI, M. (1988) Crystallographic study of the fatigue crack nucleation mechanism in pure iron. *in*: FONG, J.T. and FIELDS, R.J. (eds.) *Basic questions in fatigue*, Philadelphia, ASTM, pp. 98-119.

TANIUCHI, T., OKADA, K. and TANASE, T. (1997) Sintering behavior of VC-doped micro-grained cemented carbide. *in*: KNERINGER, G., RÖDHAMMER, P. and WILHARTITZ, P. (eds.) *Proceedings of the 14th International Plansee Seminar*, Reutte 1997, pp. 644-657.

THÜMMLER, G. and OBERACKER, E. (1993) *Introduction to Powder Metallurgy*. Cambridge: University Press.

TOPIĆ, I., SOCKEL, H.G., WELLMANN, P. and GÖKEN, M. (2006) The influence of microstructure on the magnetic properties of WC/Co hardmetals. *Materials Science and Engineering A*, **423**, pp. 306-312.

TROOST, K.Z., van der SLUIS, P. and GRAVESTEIJN, D.J. (1993) Microscale elastic-strain determination by backscatter Kikuchi diffraction in the scanning electron microscope. *Applied Physics Letters*, **62**(10), p. 1110.

TRUSOV, L.I., LAPOVOK, V.N. and NOVIKOV, V.I. (1989) Problems of sintering ultrafine powders. *in*: USKOKOVIC, D.P., PLAMOUR III, H. and SPRIGGS, R.M. (eds.) *Science of Sintering*, New York: Plenum Press, pp. 185–192.

TSURUTA, K., TOTSUJI, H. and TOTSUJI, C. (2000) Tight-binding molecular dynamics of ceramic nanocrystals using PC-based parallel machines. *Materials Research Society*, **581**, pp. 673–678.

TJONG, S.C. and CHEN, H. (2004) Nanocrystalline materials and coatings. *Materials Science and Engineering*, **R45**, pp. 1-88.

UHRENIUS, B. (1994) Evaluation of molar volumes in the Co-W-C system and calculation of volume fractions of phases in cemented carbides. *International Journal of Refractory Metals and Hard Materials*, **12**(3), pp. 121-127.

UNDERWOOD, E. E. (1970) *Quantitative Stereology*. Reading: Addison-Wesley Publishing Co., Inc.

UPADHYAYA, A., SARATHY, D. and WAGNER, G. (2001) Advances in alloy design aspects of cemented carbides. *Materials & Design*, **22**(6), pp. 511-517.

UPADHYAYA, G.S. (1996) *in*: *Nature and properties of refractory carbides*. New York: Nova Science Publishers Inc., p. 446.

VERGNON, P., ASTIER, M., and TEICHNER, S.J. (1974) Initial stage for sintering of ultrafine particles (TiO_2 and Al_2O_3). *in*: KUHN, W.E. (ed.) *Fine particles*. New Jersey: The Electrochemical Society, pp. 299-307.

WANG, G.M., CAMPBELL, S.J., CALKA, A. and KACZMAREK, W.A. (1997) Synthesis and structural evolution of tungsten carbide prepared by ball milling. *Journal of Materials Science*, **32**(6), pp. 1461-1468.

WANG, X., FANG, Z.Z. and SOHN, H.Y. (2008) Grain growth during the early stage of sintering of nanosized WC–Co powder. *International Journal of Refractory Metals and Hard Materials*, **26**(3), pp. 232-241.

WILSON, A.J.C. (1963) Mathematical theory of X-ray powder diffractometry. New York: Gordon & Breach.

WITKIN, D.B. and LAVERNIA, E.J. (2006) Synthesis and mechanical behavior of nanostructured materials via cryomilling. *Progress in Materials Science*, **51**(1), pp. 1-60.

WITTMANN, B., SCHUBERT, W.-D. and LUX, B. (2002) WC grain growth and grain growth inhibition in nickel and iron binder hardmetals. *International Journal of Refractory Metals and Hard Materials*, **20**(1), pp. 51-60.

WRONSKI, C.R.M. (1967) The size dependence of the melting point of small particles of tin. *British Journal of Applied Physics*, **18**, pp. 1731-1737.

WU, L., LIN, J., KIM, B.K., KEAR, B.H. and McCANDLISH, L.E (1993) Grain Growth Inhibition in Sintering of Nanostructured WC-Co Alloys. *in*: BILDSTEIN, H. and ECK, R. (eds.) *Proceedings of the 13th International Plansee Seminar*, Metallwerk Plansee, Reutte, 1993, vol. 3, pp. 667-679.

XUEMING, M.A. and GANG, J.I. (1996) Nanostructured WC-Co alloy prepared by mechanical alloying. *Journal of Alloys and Compounds*, **245**, pp. L30–L32.

YAMAMOTO, T., IKUHARA, Y., WATANABE, T., SAKUMA, T., TANIUCHI, Y., OKADA, K. and TANASE, T. (2001) High resolution microscopy study in Cr3C2-doped WC-Co. *Journal of Materials Science*, **36**(16), pp. 3885-3890.

YANG, Z.M., MAO, C.H. and DU, J. (2001) *Transactions of Nonferrous Metals Society China*. **11**, p. 529.

YAO, Z. G., STIGLICH, J. J. and SUDARSHAN, T. S. (1998) Nanosized WC-10Co holds promise for the future. *Metal Powder Report*, **53**(3), pp. 26–33.

ZHANG, F.L., SHEN, J. and SUN, J. (2004) The effect of phosphorus additions on densification, grain growth and properties of nanocrystalline WC–Co composites. *Journal of Alloys and Compounds*, **385**(1-2), pp. 96-103.

ZHANG, F.L., WANG, C.Y. and ZHU, M. (2003) Nanostructured WC/Co composite powder prepared by high energy ball milling. *Scripta Materialia*, **49**(11), pp. 1123-1128.

ZHANG, X., WANG, H., NARAYAN, J., and KOCH, C.C. (2001) Evidence for the formation mechanism of nanoscale microstructures in cryomilled Zn powder. *Acta Materialia*, **49**(8), pp. 1319-1328.

ZHAO, J. and HARMER, M. P. (1988) Effect of pore distribution on microstructural development: II, first and second generation pores. *Journal of the American Ceramic Society*, **71**(7), pp. 530-539.

ZHU, X.K., ZHANG, X., WANG, H., SERGUEEVA, A.V., MUKHERJEE, A.K., SCATTERGOOD, R.O., NARAYAN, J. and KOCH, C.C. (2003) Synthesis of bulk nanostructured Zn by combinations of cryomilling and powder consolidation by room temperature milling: optimizing mechanical properties. *Scripta Materialia*, **49**(5), pp. 429-433.

ZOZ, H. and ERNST, D. (1997) Mechanical alloying using cycle operation – a new way to synthesize CMB-materials. *in*: *5th international conference on advanced particulate materials and processes*, Florida, 1997.

ZOZ, H. (1995) Performance of the simoloyer. *in*: *4th international conference on powder metallurgy in aerospace, defence and demanding applications*, GOODWIN, P.S. and SCHWARZ, R.B (eds.), *Annaheim, Los Angeles, USA, May 8-10, 1995*.